Self-Consistent Green's Function Embedding for Advanced Electronic Structure Calculations based on a Dynamical Mean-Field Concept

Wael Chibani

vorgelegt von Diplom-Physiker
Wael Chibani
aus Casablanca

Dissertation
von der Fakultät II - Mathematik und Naturwissenschaften
der Technischen Universität Berlin
zur Erlangung des akademischen Grades
Doktor der Naturwissenschaften
Dr. rer. nat.

genehmigte Dissertation

Promotionsausschuss:
Vorsitzender: Prof. Dr. Mario Dähne
Gutachter: Prof. Dr. Patrick Rinke
Gutachter: Prof. Dr. Eckehard Schöll
Tag der wissenschaftlichen Aussprache: 14.12.2015

Berlin 2016

بِسْمِ ٱللَّهِ ٱلرَّحْمَٰنِ ٱلرَّحِيمِ

Für Hana ...

Contents

Zusammenfassung **vii**

Abstract **ix**

Introduction **1**

1 Theory of Interacting Particles **5**
1.1 The single particle Green's function . . . 7
1.1.1 Time-dependent perturbation theory . . . 8
1.1.2 The Green's function - a definition . . . 9
1.1.3 The single particle propagator . . . 10
1.1.4 The Dyson equation . . . 11
1.2 The self-energy . . . 12
1.3 The quasi-particle concept . . . 14
1.4 The electron-electron interaction . . . 16
1.4.1 The Hartree-Fock approximation . . . 17
1.4.2 The random phase approximation and the concept of screening 21
1.4.3 Hedin's equations and the GW approximation . . . 24
1.4.4 GW calculations for real systems . . . 26
1.5 Wave-function based approaches . . . 27

2 Kohn-Sham Density Functional Theory **31**
2.1 The Hohenberg-Kohn theorem . . . 31
2.2 The Kohn-Sham equations . . . 33
2.3 Local and semi-local approximations . . . 36
2.4 Hybrid functionals . . . 37
2.5 Connecting DFT and many-body perturbation theory - The Sham-Schlüter equation . . . 39
2.6 RPA exchange-correlation energy in a DFT framework . . . 40
2.7 Comparison to GW . . . 42

3 Embedding Schemes and the Dynamical Mean-Field Theory **45**
3.1 Conventional embedding schemes . . . 46
3.1.1 The ONIOM model . . . 46
3.1.2 The shell embedded-cluster model . . . 47
3.1.3 The cluster extrapolation scheme . . . 49
3.1.4 The embedded cluster theory . . . 50

3.1.5 Potential-functional embedding theory . . . 51
3.2 Dynamical Mean-Field Theory . . . 53
3.2.1 Scaling analysis in the limit $d \longrightarrow \infty$ . . . 53
3.2.2 Derivation of the dynamical mean-field equations . . . 57
3.2.3 Example of a single impurity Anderson model . . . 61
3.2.4 Extending DMFT to *ab-initio* methods: The LDA+DMFT approach . . . 63
3.2.5 Impurity solvers . . . 65

4 Real Space Dynamical Mean-Field Embedding 69
4.1 Numeric atom-centered orbitals in FHI-aims . . . 70
4.2 The Embedding Green's functions with NAOs . . . 71
4.2.1 The "on-site" Green's function for a periodic system . . . 73
4.2.2 The embedded Green's function . . . 75
4.3 The local self-energy . . . 76
4.3.1 The resolution of identity for NAOs . . . 77
4.3.2 Hybrid local self-energies . . . 78
4.3.3 The GW local self-energy . . . 79
4.4 The RDMFE self-consistency cycle . . . 79
4.5 Frequency and time grids . . . 87

5 Exploring Physical Quantities with the Real Space Dynamical Mean-Field Embedding 93
5.1 Evaluation of the density of states and the spectra . . . 93
5.1.1 Density of states of embedded Si unit cells . . . 95
5.1.2 Band structure of embedded Si unit cells . . . 102
5.2 Total energy calculation . . . 108
5.2.1 The Galitskii-Migdal equation for local Green's functions . . . 110
5.2.2 The embedded total energy as correction to the KS total energy 115
5.2.3 The RDMFE total energy . . . 116
5.2.4 Correlating the required size of the unit cell with the range of the interaction . . . 126
5.2.5 Calculating cohesive properties with RDMFE . . . 127
5.3 Physical properties for metals from RDMFE . . . 129
5.3.1 Cohesive properties for metals from RDMFE(GW) . . . 130
5.3.2 Band structures for metals from RDMFE(PBE0) . . . 130

Conclusions and perspectives 138

A The self-energy integral 141

Bibliography 145

Acknowledgments 162

Zusammenfassung

Die Elektronenstrukturtheorie ermöglicht es die berechneten elektronischen Eigenschaften (z.B. Bandstruktur und Gesamtenergie) realer Systeme mit denen aus dem Experiment zu vergleichen und erlaubt deren Vorhersage. Die Qualität der theoretischen Ergebnisse hängt allerdings von der verfügbaren Computerleistung ab. Dies spiegelt sich in dem hohen Rechenaufwand der fortgeschrittenen theoretischen Methoden wider, anhand derer die Elektronenstruktur von Materialien mit hoher Genauigkeit reproduziert werden kann. Folglich ist die Anwendbarkeit dieser Methoden auf kleine Systeme beschränkt.
Einbettungsmethoden bieten eine Möglichkeit fortgeschrittene theoretische Methoden auf größere Systeme auszuweiten. Die Grundidee eines jeden Einbettungsansatzes besteht darin, das zu untersuchende System in ein eingebettetes Teilsystem und dessen Einbettungsumgebung aufzuteilen. Hierbei wird das eingebettete System mit genaueren, aber rechenaufwändigeren Theorien als die Einbettungsumgebung beschrieben.
In diese Arbeit entwickle ich eine Einbettungsmethode für periodische Systeme. Diese erlaubt die Berechnung des physikalisch relevanten Teils, hier der Einheitszelle, mit Elektronenstrukturmethoden, welche (typischerweise) für periodische Systeme mit großem Rechenaufwand verbunden sind. Im Gegensatz hierzu wird der Rest des Systems mit der rechnerisch effizienteren Kohn-Sham Dichtefunktionaltheorie beschrieben. In Anlehnung an die *dynamical mean-field theory* (DMFT), wird die in dieser Dissertation eingeführte Einbettungsmethode mit Hilfe von selbstkonsistenten Greenschen Funktionen formuliert. Das Greensche Funktion Formalismus ermöglicht es die Hybridisierung zwischen der eingebetteten Region und der Umgebung auf natürlicher Weise darzustellen. Diese Beschreibung der Hybridisierung macht eine zusätzliche Sonderbehandlung der Einheitszellenatome, die an die Umgebung angrenzen, überflüssig. Dies ist ein entscheidender Vorteil gegenüber konventionellen Einbettungsmethoden.
Unsere *real space dynamical mean-field embedding* (RDMFE) Methode basiert auf zwei Dyson Gleichungen, wovon eine das eingebettete Teilsystem (hier die Einheitszelle) und eine weitere die periodische Umgebung beschreibt. Diese Dyson Gleichungen definieren zwei selbstkonsistente Zyklen, die ich in FHI-aims im Rahmen dieser Arbeit implementiert habe. Die Gesamtenergie und die Bandstruktur werden anschließend aus den resultierenden selbstkonsistenten Greenschen Funktionen berechnet. In der DMFT wird das eibgebettete System (typischerweise d- oder f-Elektronzustände) mit sehr genauen bis hin zu exakten Theorien berechnet. Im Gegensatz hierzu werden in der RDMFE Näherungen zur Berechnung der Einheitszelle herangezogen. Diese approximierte Beschreibung der eingebetteten Einheit-

szelle hat den Vorteil, dass zur Beschreibung des eingebetteten Systems kein korrelierter Unterraum benötigt wird, wie das für DMFT der Fall ist.
Um die Leistung von RDMFE zu zeigen, habe ich einfache Bulk-Systeme betrachtet und die eingebettete Einheitszelle mit Hybridfunktionale und die GW-Näherung der Vielteilchenstörungstheorie berechnet. Grundsätzlich kann aber jede Theorie, die über die GW-Näherung hinaus geht, verwendet werden. Ich habe gezeigt, dass die resultierenden Gesamtenergien und Zustandsdichten schnell mit den numerischen Rechenparametern konvergieren. Außerdem habe ich demonstriert, dass diese physikalischen Größen systematisch mit der Größe der eingebetteten Einheitszellen zu ihren periodischen Werte konvergieren. Das die RDMFE die wichtigsten Eigenschaften der "besseren" Theorie erfasst, habe ich am Beispiel des Plasmon Peaks in Bulk-Silizium dargestellt, wobei die Einheitszelle mit der GW-Näherung behandelt wurde.
Die zugrunde liegende Arbeit zeigt, dass die RDMFE verwendet werden kann um fortgeschrittene Elektronenstruktur Methoden für Systemgrößen anwendbar zu machen, die vorher so nicht erreichbar waren. Dies verspricht unzählige interessante Anwendungsmöglichkeiten in der Zukunft. Die Entwicklung von RDMFE ist daher ein bedeutender Schritt nach vorne auf dem Weg zur Anwendbarkeit sehr genauer Theorien auf periodische Systeme.

Abstract

Electronic structure theory is of fundamental importance for material science, since it enables the comparison of the calculated electronic properties (e.g. the band structure and the total energies) of real systems with the experimental findings and allows their prediction. The quality of the theoretical results depends, however, on the available computational power. This is reflected in the fact that advanced theoretical methods, that are able to reproduce the electronic structure of materials in a reasonable way, are computationally demanding. As a consequence, their applicability is limited to small systems.

Embedding schemes offer a way to extend advanced theoretical methods to large systems. The main idea behind every embedding scheme is to partition the system of interest into an embedded region and a surrounding. The embedded system is smaller and can then be treated with more accurate, and thus computationally more demanding, approaches than the surrounding.

In this thesis I present an embedding scheme for periodic systems that facilitates the treatment of the physically important part (here the unit cell) with advanced electronic-structure methods, that are computationally too expensive for periodic systems. The rest of the periodic system is treated with computationally more efficient approaches, e.g., Kohn-Sham density-functional theory, in a self-consistent manner.

The method is based on the concept of dynamical mean-field theory (DMFT) formulated in terms of Green's functions. The Green's function formalism facilitates a natural definition of the hybridization between the embedded system and the surrounding, so that no special treatment of the boundary atoms is required. This constitutes a major advantage over conventional embedding schemes used in quantum chemistry.

Our real space dynamical mean-field embedding (RDMFE) scheme features two nested Dyson equations, one for the embedded cluster and another one for the periodic surrounding. These Dyson equations define two self-consistency cycles that I have implemented in FHI-aims as a part of this thesis. The total energy, the density of states and the band structure are then computed from the resulting self-consistent Green's functions. Compared to DMFT, where the embedded system (usually d- or f-electron levels) is treated with essentially exact methods, I use in RDMFE approximate theories to calculate the embedded unit cell. RDMFE is thus free from the ambiguity in the definition of a correlated subspace that plagues DMFT.

To demonstrate the performance of RDMFE, I consider simple bulk systems and treat the embedded unit cell with hybrid functionals and many-body perturbation theory in the GW approximation for which periodic reference calculations are avail-

able. In principle, however, any beyond-GW approach can be used. I show that the resulting total energies and density of states converge well with the computational parameters. Moreover, I demonstrate that these quantities systematically converge to their periodic limit when increasing the size of the embedded unit cell. The ability of our method to capture key properties of the "better" theory is demonstrated for the example of the plasmon satellite in bulk Silicon, when the embedded unit cell is treated with the GW approximation.
The Analysis I give in this work reveals that RDMFE has the potential to make advanced electronic methods accessible for unprecedented system sizes offering a multitude of application possibilities. The development of our embedding scheme is thus a significant step towards making highly accurate theoretical approaches applicable to large systems.

Introduction

The electronic many-body problem is one of the most studied yet most challenging problems in condensed matter physics. Due to the long-range Coulomb interaction between electrons, the description of electronic systems is only possible in an approximated way. The development of approximations to understand and accurately describe electronic processes in condensed matter systems constitutes a very broad and simultaneously very active research field in theoretical physics. One of the earliest quantum mechanical approaches to the many-body problem is perturbation theory. The main virtue of perturbation theory is its controllability. In other words, one knows exactly what one has approximated and one knows how to improve upon this approximation. Hence, the theory is systematically improvable. In the model Hamiltonian community, the quantum mechanical concept of second quantization (also called occupation number formalism) is used to rewrite the many-body Hamiltonian in a simple form based on occupation number operators. This simplification allows the construction of model scenarios mimicking electronic processes with two or more electrons involved. Due to the drastic reduction in the electron number, these models can be solved with highly accurate numerical methods facilitating qualitative insight into the complex electronic interactions. In quantum chemistry, wave function based methods are favored due to their accurate description of real systems. In contrast to perturbative approaches, where the approximation affects the Hamiltonian, here the complexity of the problem is translated into the wave function. Hence, the configuration space, and with it the numerical cost, grows dramatically with the level of accuracy required to describe a given system. The application of such wave function based methods is thus limited to single atoms or small molecules. Conversely, the balance between accuracy and computational efficiency of density functional theory (DFT) with its local (i.e., local density approximation (LDA)) and semi-local (i.e., generalized gradient approximations (GGAs)) approximations has paved the way for DFT to become the method of choice for discribing large, real systems.

However, common density functional theory approximations (DFA) suffer from several limitations such as the self-interaction error [1, 2, 3], the lack of a derivative discontinuity in the exchange-correlation potential [4, 5, 6], the inaccurate description of van der Waals iteractions [7, 8, 9], or the absence of image effects [10, 11, 12]. These shortcomings limit the predictive power of LDA and GGAs, especially for localized electrons such as d- or f-electron systems [13, 14, 15, 16, 17] or for systems where charge transfer can occur as is the case for adsorbates on surfaces [18, 19, 20, 21]. Moreover, DFT is mainly a ground-state method and is of limited applicability

to excited states. While perturbation theory or wave function based methods can overcome some of these limitations, their applicability to real systems is limited by their high computational cost as mentioned previously. To overcome the *efficiency-accuracy* conundrum, much effort has been devoted to combine the best of both worlds, that is to merge local and semilocal DFT approximations (DFA) with advanced electronic methods [22, 23, 24, 25, 26, 27, 28, 29, 30, 31, 32, 33, 34, 35, 36].

In this work, I investigate the concept of embedding. Embedding is a divide-and-conquer approach, where the full system is divided into two parts: a small embedded region, which is treated with advanced, computationally demanding approaches, and an embedding environment that is treated with computationally more efficient approaches. Following this general principle, various embedding schemes have been developed in the past [22, 23, 24, 25, 26, 27, 28, 29, 30, 31, 32, 33, 34, 35, 36]. Depending on the background of the authors, they differ in area of application, on how they treat the coupling between the embedded region and the surrounding, and in the approaches used to describe the two regions. In (bio)chemistry, for example, one of the most popular embedding schemes combines quantum mechanics (QM) and classical molecular mechanics (MM). The embedded region is treated quantum mechanically and the surrounding by MM [23, 24, 26, 28, 29]. In surface science, fully quantum mechanical schemes are more prevalent, e.g., for the description of surface adsorbates. They divide space into regions for advanced and less advanced electronic-structure approaches and differ mostly on how these two regions are coupled, e.g. through maximal exchange overlap [22], density embedding [33] or cluster extrapolation [31, 32]. In the model Hamiltonian community, dynamical mean-field theory [25, 27, 30] offers a natural embedding framework by mapping an infinite, correlated lattice model into an impurity model coupled to a self-consistently determined mean-field bath [37]. When DFA is chosen as the mean-field, DMFT becomes material specific [30, 38, 39]. The embedding is achieved by means of Green's functions facilitating the calculation of spectra, band structures, but also phase diagrams. Recently, Zgid and Chan [34] proposed to use DMFT as an embedding framework for quantum-chemistry approaches such as the configuration-interaction method. They since proposed a simplified DMFT scheme based on density-matrix embedding to access static properties (e.g., the ground-state energy and its derivatives) [35].

The objective of the work presented in this thesis is to extend the DMFT concept to couple two *ab initio* regions. The idea is similar to that of Zgid and Chan [34], but I here explore the possibility of using DMFT as a general embedding scheme for advanced first-principles electronic-structure methods. These can be advanced DFT exchange-correlation functionals or Green's function based excited-state methods for example, approaches that go beyond the GW method [40], which are still computationally too expensive for large-scale systems. In contrast to previous DMFT schemes, the unit cell is treated as the local, embedded region, that is coupled to the rest of the periodic system via the DMFT formalism. The advantage of the present approach is that all electrons in the embedded region are treated on the same quantum mechanical footing.

This thesis is structured as follows: in Chapter 1, I introduce perturbation theory and the single particle Green's function as basic tools to approach the electronic many-body problem. For the two-body interaction, I step by step show how the accuracy is improvable by accounting for more electronic processes. Hence, I start with the simple Hartree-Fock approximation before I introduce the famous Hedin's equations and the concept of screening. Finally, I briefly tackle some prominent wave function based approaches, to motivate the next chapter. In Chapter 2, I turn to DFT and the related approximations and shortly discuss their performance. To conclude this Chapter, I show how the random phase approximation and *GW* can be combined with DFT to describe real systems. A review of some prominent *ab initio* embedding schemes is given in Chapter 3, before I give a more detailed discussion of DMFT and the derivation of the related Green's functions. I then address DMFT applications for real systems within the LDA+DMFT approach and briefly present some of the established impurity solvers. To close this Chapter, I present some examples, where DMFT is successfully applied. In Chapter 4 I present the concept of our real-space dynamical mean-field embedding (RDMFE) approach and its implementation in the all-electron Fritz-Haber-Institute *ab initio* molecular simulations code [41, 42, 43]. Here I discuss all the technical details of the methods related to the embedding Green's functions but also computational ones, such as the resolution of identity, the frequency grids and the required Fourier transforms. Finally, in Chapter 5 I discuss how physical quantities can be calculated from RDMFE. The density of states and the total energy from RDMFE are discussed and tests for hybrid density functionals and *GW* for representative elements are performed.

Chapter 1

Theory of Interacting Particles

Except for relativistic effects, the main physics and chemistry of a condensed matter system with N_e electrons and N_n nuclei, is captured by the many-body Hamiltonian

$$\begin{aligned}\hat{\mathcal{H}} = &-\frac{1}{2}\sum_{i}^{N_e}\frac{\nabla_i^2}{m_e} + \frac{1}{2}\sum_{i\neq j}^{N_e}\frac{1}{|\mathbf{r}_i-\mathbf{r}_j|} - \frac{1}{2}\sum_{i}^{N_e}\sum_{\nu}^{N_n}\frac{Z_\nu}{|\mathbf{r}_i-\mathbf{R}_\nu|} \\ &-\frac{1}{2}\sum_{\nu}^{N_n}\frac{\nabla_\nu^2}{M_\nu} + \frac{1}{2}\sum_{\nu\neq\mu}^{N_n}\frac{Z_\nu Z_\mu}{|\mathbf{R}_\nu-\mathbf{R}_\mu|},\end{aligned} \tag{1.1}$$

where Latin indices i, j label electronic coordinates and Greek indices ν, μ, nuclear ones. Correspondingly, $\mathbf{r}$ and $\mathbf{R}$ are electronic and nuclear coordinates, respectively. M_ν labels the mass of the nucleus with index ν, Z_ν its atomic number and m_e is the electronic mass. The first term in the Hamiltonian Eq. (1.1) describes the electronic kinetic energy, the second one the interactions between electrons and the third one the interaction between electrons and nuclei. The last two terms (second line of Eq. (1.1)) are pure nuclear terms, where the first term describes the kinetic energy of the nuclei and the second one the interaction between different nuclei. I use atomic units $M_\nu = m_e = e = \hbar = \frac{1}{4\pi\epsilon_0} = 1$, but write the masses m_e and M_ν esplicitly for clarity.

Most physical properties of a given system can be obtained by solving the time-independent Schrödinger equation

$$\hat{\mathcal{H}}\Psi(\{\mathbf{r}\},\{\mathbf{R}\}) = E\Psi(\{\mathbf{r}\},\{\mathbf{R}\}), \tag{1.2}$$

where $\Psi(\{\mathbf{r}\},\{\mathbf{R}\})$ is the wave function of the full system (i.e., electrons and nuclei) and E the corresponding eigenvalues. A common way to write the solution to Eq. (1.2) is the expansion

$$\Psi(\{\mathbf{r}_j\},\{\mathbf{R}_\nu\}) = \phi(\{\mathbf{r}_j\};\{\mathbf{R}_\nu\})\Lambda(\{\mathbf{R}_\nu\}), \tag{1.3}$$

where $\Lambda(\{\mathbf{R}_\nu\})$ are coefficients that depend on the nuclear coordinates only and $\phi(\{\mathbf{r}_j\};\{\mathbf{R}_\nu\})$ the electronic wave-functions at nuclear position $\mathbf{R}_\nu$, that solve the electronic Schrödinger equation $\hat{H}_e\psi = E_e\psi$ corresponding to the electronic Hamil-

tonian

$$\begin{aligned}\hat{H}_e = &-\frac{1}{2}\sum_i^{N_e}\frac{\nabla_i^2}{m_e} + \frac{1}{2}\sum_{i\neq j}^{N_e}\frac{1}{|\mathbf{r}_i-\mathbf{r}_j|} - \frac{1}{2}\sum_i^{N_e}\sum_\nu^{N_n}\frac{Z_\nu}{|\mathbf{r}_i-\mathbf{R}_\nu|}\\ &+\frac{1}{2}\sum_{\nu\neq\mu}^{N_n}\frac{Z_\nu Z_\mu}{|\mathbf{R}_\nu-\mathbf{R}_\mu|}.\\ =\ &\hat{T}+\hat{V}_{ee}+\hat{V}_{ext}\\ &+\hat{V}_{nn}. \end{aligned} \tag{1.4}$$

The ground state from such a solution to the Schrödiger equation, Eq. (1.2), contains matrix elements such as $\langle\phi_i|\nabla_\nu^2|\phi_j\rangle$ and $\langle\phi_i|\nabla_\nu|\phi_j\rangle$. Essentially, such matrix elements of the nuclear kinetic operator describe the dynamics of the lattice atoms within what is called electron-phonon coupling. They couple different electronic states ϕ_i and ϕ_j and are thus difficult to solve. Hence, approximations have to be considered at this point:

(i) The adiabatic (or Born-Oppenheimer) approximation [44]: Due to their much smaller mass, the electrons can be viewed as following the motion of the nuclei adiabatically. This means that transitions between ϕ_j and ϕ_i for $i \neq j$ are suppressed. Thus, matrix elements such as $\langle\phi_i|\nabla_\nu^2|\phi_j\rangle$ or $\langle\phi_i|\nabla_\nu|\phi_j\rangle$ vanish for $i \neq j$.

(ii) For the diagonal terms (i.e. $i = j$) however, only $\langle\phi_i|\nabla_\nu^2|\phi_i\rangle$ survives and can be roughly estimated to be

$$\langle\phi_i|\nabla_\nu^2|\phi_i\rangle \approx 10^{-4}\times\langle T_e\rangle, \tag{1.5}$$

where $\langle T_e\rangle$ is the kinetic energy of an electron.

With these approximations, the full many-body problem described by Eq. (1.2) can be seperated in an equation for electrons defined by the electronic Hamiltonian $\hat{H}_e$ in Eq. (1.4), and one for the nuclei given by

$$\left[-\frac{1}{2}\sum_\nu^{N_n}\frac{\nabla_\nu^2}{M_\nu}+\frac{1}{2}\sum_{\nu\neq\mu}^{N_n}\frac{Z_\nu Z_\mu}{|\mathbf{R}_\nu-\mathbf{R}_\mu|}+E_e^\nu\right]\Lambda_\nu = E_\nu\Lambda_\nu, \tag{1.6}$$

where E_e^ν is the electronic energy at the nuclear position ν. Equation (1.6) determines the coefficients Λ_ν and in practice it is replaced by the classical mechanical (Newtonian) equation of motion.
In contrast to Eq. (1.1) the electronic Hamiltonian Eq. (1.4) does not include the kinetic part of the nuclei and thus, the kinetic contribution comes only from the electrons. The nuclear coordinates $\mathbf{R}_{\mu,\nu}$ are not quantum operators anymore, but become parameters for the electronic Schrödinger equation.
In the Born-Oppenheimer approximation the electronic mass m_e is taken to be much smaller than that of the nuclei, so that one can consider the electrons as instantaneously (i.e., adiabatically) following the motion of the nuclei without getting excited

from the stationary state of the electronic Hamiltonian $\hat{H}_e$. Hence, for systems where electron-phonon coupling effects (i.e., non-adiabatic effects) are not important the Born-Oppenheimer approximation is well justified. However, the description of superconductivity for instance, where electron-phonon coupling is crucial, would not be possible within this approximation.

Solving the electronic Schrödinger equation is simple for the case of non-interacting electrons, i.e., $\hat{V}_{ee} = 0$. However, to describe real systems, electronic interactions are crucial, making the exact solution of the electronic Schrödinger equation an unfeasible task. This is mainly due to the long-range nature of the Coulomb repulsion between electrons. Hence, interacting electronic systems are strongly correlated "in the sense that every electron *feels* the presence" of every other one. The development of accurate approximations to describe real systems has been the driving force of a lot of fields in theoretical quantum physics and chemistry. One of the most prominent quantum mechanical tools that has been used extensively in condensed matter theory, is perturbation theory. It relies on the idea of partitioning the Hamiltonian in two parts: one part where one knows the solution exactly and another part (the perturbation), which includes all the complexity and where the solution is still to be found. Using quantum mechanical tools and physical intuition one can then rewrite the problem as a series expansion of the perturbation. Assuming that the perturbation is small enough so that at some part of the series it will become negligible, allows a truncation of the perturbation series. In this Chapter I will introduce an important tool of perturbation theory, that is the propagator theory which represents the foundation of the successful concept of Feynman diagrams. After a brief introduction into the propagator theory, the key approximations, such as Hartree-Fock [45, 46] and the random-phase approximation [47, 48, 43], will be discussed before presenting Hedin's equations [40] and the approximations related to them. This Chapter is mainly based on the books by Mattuck [49, 50], Fetter and Walecka [51] and the review article by Aryasetiawan and Gunnarsson [52].

1.1 The single particle Green's function

To start with, I would like to briefly remind the reader how the time evolution of states is defined. The time evolution of a state $|\psi(t_0)\rangle$ at time t_0 can be defined as is known from basic quantum mechanics lectures as

$$|\psi(t)\rangle = \hat{U}(t, t_0)|\psi(t_0)\rangle, \tag{1.7}$$

where I omit spatial coordinates for brevity. Inserting Eq. (1.7) in the Schrödinger equation yields

$$[i\frac{\partial}{\partial t}\hat{U}(t, t_0) - \hat{H}\hat{U}(t, t_0)]|\psi(t_0)\rangle = 0. \tag{1.8}$$

Since this must hold for every state $|\psi(t_0)\rangle$, one has

$$i\frac{\partial}{\partial t}\hat{U}(t, t_0) = \hat{H}\hat{U}(t, t_0). \tag{1.9}$$

Equation (1.9) is a differential equation with the following solution

$$\hat{U}(t,t_0) = 1 - i\int_{t_0}^{t} \hat{H}(t')\hat{U}(t',t_0)dt'. \tag{1.10}$$

For time-independent Hamiltonians one obtains the very simple formula

$$\hat{U}(t,t_0) = \exp[-i(t-t_0)\hat{H}]. \tag{1.11}$$

It is straightforward to show that the time evolution operator $\hat{U}(t,t_0)$ satisfies the following properties

$$\begin{aligned} \hat{U}(t_0,t_0) = 1,\ \hat{U}(t_2,t_0) &= \hat{U}(t_2,t_1)\hat{U}(t_1,t_0) \\ \hat{U}^{\dagger}(t,t_0) = \hat{U}(t_0,t) &= \hat{U}^{-1}(t,t_0). \end{aligned} \tag{1.12}$$

One can now look at a specific Hamiltonian and ask how it evolves in time under a given perturbation.

1.1.1 Time-dependent perturbation theory

Now I consider the following Hamiltonian

$$\hat{H} = \hat{H}_0 + \hat{V}(t), \tag{1.13}$$

where $\hat{H}_0$ is the unperturbed Hamiltonian and $\hat{V}(t)$ is a perturbing time-dependent potential. Using Eqs. (1.12), one can easily show that the Schrödinger equation can be written as

$$i\frac{\partial}{\partial t}\hat{U}_I(t,t_0) = \hat{V}_I(t)\hat{U}_I(t,t_0), \tag{1.14}$$

where $\hat{V}_I(t) = \hat{U}_0^{\dagger}(t,t_0)\hat{V}(t)\hat{U}_0(t,t_0)$ and $\hat{U}_I(t,t_0) = \hat{U}_0^{\dagger}(t,t_0)\hat{U}(t,t_0)$ with $\hat{U}_0(t,t_0) = \exp[-i(t-t_0)\hat{H}_0]$ being the time evolution operator corresponding to the unperturbed Hamiltonian $\hat{H}_0$.
Making use of the solution of the Schrödinger equation Eq. (1.10), the time evolution operator can be written in the useful form of a series expansion

$$\hat{U}(t,t_0) = \hat{U}_0(t,t_0) + \sum_{n=1}^{\infty} \hat{U}^{(n)}(t,t_0), \tag{1.15}$$

with $\hat{U}^{(n)}(t,t_0)$ given by

$$\begin{aligned} \hat{U}^{(n)}(t,t_0) = (\frac{1}{i})^n \int_{t_0}^{t} d\tau_n \int_{t_0}^{\tau_n} d\tau_{n-1} \quad ... \quad \int_{t_0}^{\tau_3} d\tau_2 \int_{t_0}^{\tau_2} d\tau_1 \\ \hat{U}_0(t,\tau_n)\hat{V}(\tau_n)\hat{U}_0(\tau_n,\tau_{n-1}) \quad ... \quad \hat{U}_0(\tau_3,\tau_2)\hat{V}(\tau_2)\hat{U}_0(\tau_2,\tau_1)\hat{V}(\tau_1)\hat{U}_0(\tau_1,t_0). \end{aligned} \tag{1.16}$$

In the case of a time-independent $\hat{V}$ one easily see that all terms in $\hat{U}$ only depend on $(t-t_0)$ and one can write

$$\hat{U}(t-t_0) = \hat{U}_0(t-t_0) + \sum_{n=1}^{\infty} \hat{U}^{(n)}(t-t_0). \tag{1.17}$$

1.1.2 The Green's function - a definition

I focus now only on such cases where the perturbation is purely static (i.e., $V = V(t=0)$). As discussed above, the time evolution operator contains the exponential function that is typically a rapidly oscillating function. Calculating integrals over such oscillating functions is not always easy. Instead a Fourier transformation to the frequency domain may be appropriate. But since the Fourier integral runs from $-\infty$ to ∞ the integration bound has to be fixed. Hence, the Green's functions [53] on the time axis is defined as

$$\begin{aligned} G^+(t) &= -i\Theta(t)\hat{U}(t), \\ G_0^+(t) &= -i\Theta(t)\hat{U}_0(t), \end{aligned} \tag{1.18}$$

where

$$\Theta(t) = \begin{cases} 0 & \text{if} \quad t \leq 0, \\ 1 & \text{if} \quad t > 0. \end{cases}$$

One can see that the Green's function differs from the time evolution operator only by specifying the integration bounds, which is done using the Heavyside function $\Theta(t)$. The " + " sign labels the retarded Green's function, which means that one "measures" the system after the interaction happens. Equivalently $G^-(t) = -i\Theta(t)\hat{U}(t)$ refers to the advanced Green's function, where the interaction happens after the system is measured.
For δ very small $G^+(t)$ corresponds to the Hamiltonian $\hat{H}$ and $G_0^+(t)$ is the one corresponding to $\hat{H}$. Recalling Eq. (1.9) for the time evolution operator and choosing $t_0 = 0$ one can derive a Schrödinger like equation for the Green's function using the relation $\hat{U}(0) = 1$

$$\begin{aligned} i\frac{\partial}{\partial t}\hat{G}^+(t) = \frac{\partial}{\partial t}\Theta(t)\hat{U}(t) &= \delta(t)\hat{U}(t) + \Theta(t)\frac{\partial}{\partial t}\hat{U}(t) \\ &\overset{Eq.((1.9))}{=} \delta(t)\hat{U}(0) + \frac{1}{i}\Theta(t)\hat{H}\hat{U}(t) \\ &= \delta(t) + \hat{H}G^+(t), \end{aligned} \tag{1.19}$$

which yields

$$\left(i\frac{\partial}{\partial t} - \hat{H}\right)\hat{G}^+(t) = \delta(t). \tag{1.20}$$

The upper definition of the Green's function makes it clear that the Green's function is an operator. A similar equation for G_0^+ can be derived

$$\left(i\frac{\partial}{\partial t} - \hat{H}_0\right)\hat{G}_0^+(t) = \delta(t), \tag{1.21}$$

for the non interacting Hamiltonian $\hat{H}_0$. One can now write Eq. (1.17) in terms of the Green's function as well

$$G^+(t) = G_0^+(t) + \sum_{n=1}^{\infty} G^{(n)}(t), \tag{1.22}$$

with

$$G^{(n)}(t) = \int_{-\infty}^{\infty} d\tau_n \int_{-\infty}^{\infty} d\tau_{n-1} \quad ... \quad \int_{-\infty}^{\infty} d\tau_2 \int_{-\infty}^{\infty} d\tau_1 \tag{1.23}$$
$$G_0^+(t-\tau_n)\hat{V}G_0^+(\tau_n-\tau_{n-1}) \quad ... \quad G_0^+(\tau_3-\tau_2)\hat{V}G_0^+(\tau_2-\tau_1)\hat{V}G_0^+(\tau_1-t_0).$$

Here I make use of the convolution theorem, i.e. the convolution of two functions is the product of their Fourier transform

$$F(t) = \int_{-\infty}^{\infty} d\tau_1 G_0^+(\tau_2-\tau_1)\hat{V}G_0^+(\tau_1) \xrightarrow{FT} F(\omega) = G_0^+(\omega)\hat{V}G_0^+(\omega). \tag{1.24}$$

It is then possible to rewrite Eq. (1.22) in the frequency domain and to obtain this common and very useful expression for the Green's function in terms of G_0^+ and $\hat{V}$ only

$$\begin{aligned} G^+(\omega) = G_0^+(\omega) + G_0^+(\omega)\hat{V}G_0^+(\omega) \quad &+ \\ G_0^+(\omega)\hat{V}G_0^+(\omega)\hat{V}G_0^+(\omega) \quad &+ \quad ... \end{aligned} \tag{1.25}$$

Substituting G for the time evolution operator in Eq. (1.18), one obtains

$$G^+(t) = -i\Theta(t)e^{-i\hat{H}t}. \tag{1.26}$$

Its Fourier transform is then

$$\begin{aligned} G^+(\omega) &= -i\int_0^{\infty} dt \exp\{i(\omega - \hat{H} + i\delta)t\} \\ &= (\omega - \hat{H} + i\delta)^{-1}. \end{aligned} \tag{1.27}$$

Further writing $G^+(\omega)$ in the basis $\phi_n(r)$ of the eigenstates with eigenvalues ϵ_n of the Hamiltonian $\hat{H}$ gives the following more common expression for the Green's function in the frequency and time domain respectively

$$\begin{aligned} G^+(\mathbf{r},\mathbf{r}',\omega) &= \sum_n \frac{\phi_n(\mathbf{r})\phi_n^*(\mathbf{r}')}{\omega - \epsilon_n + i\delta} \\ G^+(\mathbf{r},\mathbf{r}',t) &= \sum_n \phi_n(\mathbf{r})\phi_n^*(\mathbf{r}')e^{-i\epsilon_n t}\Theta(t). \end{aligned} \tag{1.28}$$

These representation is often referred to as the Lehmann representation of the Green's function.

1.1.3 The single particle propagator

To understand how Green's function theory is used to answer key physical questions one can imagine trying to look at a specific particle and asking the question:
"if this particle is at an initial state $|i(\mathbf{r}',t_0)\rangle$ at time t_0 and position $\mathbf{r}'$ what is the probability to find this same particle at a different time t and position $\mathbf{r}$ in the final

state $|f(\mathbf{r},t)\rangle$? Asking this question is the same as thinking of propagating a state that one can prepare to be $|i(\mathbf{r}',t_0)\rangle$ at time t_0, to a state $|f(\mathbf{r},t)\rangle$ at time t. Thus, I consider the initial and final states

$$|i(\mathbf{r}',t_0)\rangle = \psi^\dagger(\mathbf{r}')U(t_0,0)|0\rangle \tag{1.29}$$

and

$$|f(\mathbf{r},t)\rangle = \psi^\dagger(\mathbf{r})U(t,0)|0\rangle, \tag{1.30}$$

respectively, where $|0\rangle$ is the vacuum state and the field operators ψ, that play the role of creation ($\psi^\dagger$) or annihilation (ψ) operators.
The transition probability $W_{i\longrightarrow f}$ between these two states is given by

$$W_{i\longrightarrow f} = |\langle f(\mathbf{r},t)|U(t,t_0)|i(\mathbf{r}',t_0)\rangle|^2. \tag{1.31}$$

$W_{i\longrightarrow f}$ is proportional to the matrix element of the time evolution operator

$$\begin{aligned}\langle f(\mathbf{r},t)|U(t,t_0)|i(\mathbf{r}',t_0)\rangle &= \langle 0|\psi(\mathbf{r},t)\psi^\dagger(\mathbf{r}',t_0)|0\rangle \\ &\equiv iG^+(\mathbf{r},\mathbf{r}',t-t_0), \text{ for } t>t_0\end{aligned} \tag{1.32}$$

where the definition

$$\begin{aligned}\psi^\dagger(\mathbf{r}',t_0) &= U^\dagger(t_0,0)\psi^\dagger(\mathbf{r}')U(t_0,0) \\ \psi(\mathbf{r},t) &= U^\dagger(t,0)\psi(\mathbf{r})U(t,0),\end{aligned} \tag{1.33}$$

has been introduced.
Until now I have only worked with the propagator for the electrons. One can think of the same procedure to describe hole propagation. The difference between the electron and the hole propagator is essentially of causal nature. Hence, the hole propagator can be written as

$$iG^-(\mathbf{r},\mathbf{r}',t_0-t) = -\langle 0|\psi^\dagger(\mathbf{r}',t)\psi(\mathbf{r}',t_0)|0\rangle. \tag{1.34}$$

A way to write the particle and hole propagators together in one expression is

$$iG(\mathbf{r},\mathbf{r}',t-t_0) = \langle 0|\mathbf{T}\{\psi^\dagger(\mathbf{r},t)\psi(\mathbf{r}',t_0)\}|0\rangle, \tag{1.35}$$

with the time ordering operator $\mathbf{T}$ that is defined as follows

$$iG(\mathbf{r},\mathbf{r}',t-t_0) = \begin{cases}\langle 0|\psi(\mathbf{r},t)\psi^\dagger(\mathbf{r}',t_0)|0\rangle & \text{if} \quad t>t_0; \text{ electron} \\ -\langle 0|\psi^\dagger(\mathbf{r}',t_0)\psi(\mathbf{r},t)|0\rangle & \text{if} \quad t_0>t; \text{ hole}\end{cases}$$

which is a very commonly used definition of the propagator.

1.1.4 The Dyson equation

In the previous section I have derived the relation (1.27) for $\hat{H}$ and G. The same expression can of course be derived for $\hat{H}_0$

$$G_0^+(\omega) = (\omega - \hat{H}_0 + i\delta)^{-1}. \tag{1.36}$$

Using Eq. (1.36) and $\hat{H} = \hat{H}_0 + \hat{V}$ one can rewrite Eq. (1.27) as follows

$$\begin{aligned} G^+(\omega) &= (\omega - \hat{H}_0 - \hat{V} + i\delta)^{-1} \\ &= \left([G_0^+(\omega)]^{-1} - \hat{V}\right)^{-1}. \end{aligned} \tag{1.37}$$

Multiplying with $\left([G_0^+(\omega)]^{-1} - \hat{V}\right)$ one obtains

$$\left([G_0^+(\omega)]^{-1} - \hat{V}\right) G^+(\omega) = \mathbb{I}. \tag{1.38}$$

Finally multiplying with $G_0^+(\omega)$ from the left gives

$$G^+(\omega) = G_0^+(\omega) + G_0^+(\omega)\hat{V}G^+(\omega). \tag{1.39}$$

Equation (1.39) is the famous Dyson equation, first introduced by Freeman Dyson [54], that relates the interacting Green's function G^+ and the non-interacting one G_0^+ in a self-consistent way.

1.2 The self-energy

In this section I introduce the self-energy and its meaning for Green's function theory. To this end, I consider a simple example of the time evolution of a single incoming particle after interaction (scattering) with a single center. For clarity, I work in the following in the reciprocal space, with the plane waves $\phi_{\mathbf{k}}(\mathbf{r}) = \langle \mathbf{r}|\mathbf{k}\rangle = \frac{1}{\sqrt{L^3}} e^{i\mathbf{k}\cdot\mathbf{r}}$, see Mattuck [49] for further reading. For a single scattering center modeled by a potential $\hat{V}(\mathbf{r})$ the probability $W_{\mathbf{k}\longrightarrow\mathbf{q}}$ of scattering an incoming particle $\mathbf{k}$ into a state $\mathbf{q}$ is given by

$$\begin{aligned} W_{\mathbf{k}\longrightarrow\mathbf{q}} &= |\langle \mathbf{q}|U(t-t_0)|\mathbf{k}\rangle|^2 \\ &= |i\langle \mathbf{q}|G^+(t-t_0)|\mathbf{k}\rangle|^2, \end{aligned} \tag{1.40}$$

which gives in the frequency domain

$$\begin{aligned} W_{\mathbf{k}\longrightarrow\mathbf{q}} &= |i\langle \mathbf{q}|G^+(\omega)|\mathbf{k}\rangle|^2 \\ &= |iG^+(\mathbf{k},\mathbf{q};\omega)|^2. \end{aligned} \tag{1.41}$$

Conversely, the probability that the particle passes through unscattered is

$$W_{\mathbf{k}\longrightarrow\mathbf{k}} = |iG^+(\mathbf{k},\mathbf{k};\omega)|^2. \tag{1.42}$$

I now look at a specific case and use for $G^+(\omega)$ the Dyson equation Eq. (1.39). Using the resolution of identity $\sum_{\mathbf{k}} |\mathbf{k}\rangle\langle\mathbf{k}| = \mathbb{I}$ and $G_0^+(\mathbf{k},\mathbf{q};\omega) = G_0^+(\mathbf{k};\omega)\delta_{\mathbf{k},\mathbf{q}}$, one then obtains the expanded Dyson equation

$$\begin{aligned} G^+(\mathbf{k},\mathbf{k};\omega) &= G_0^+(\mathbf{k};\omega) + G_0^+(\mathbf{k};\omega)V_{\mathbf{kk}}G_0^+(\mathbf{k};\omega) \\ &+ \sum_{\mathbf{q}} G_0^+(\mathbf{k};\omega)V_{\mathbf{kq}}G_0^+(\mathbf{q};\omega)V_{\mathbf{qk}}G_0^+(\mathbf{k};\omega) + \ldots \end{aligned} \tag{1.43}$$

with $V_{\mathbf{kq}} = \langle \mathbf{k}|\hat{V}|\mathbf{q}\rangle$.
Equation (1.43) can be represented by a series of Feynman diagrams [55] (see Figure (1.1)), where a double arrow corresponds to the interacting Green's function $G^{+}(\omega)$ and the single arrow to the non-interacting one $G_0^{+}(\omega)$.

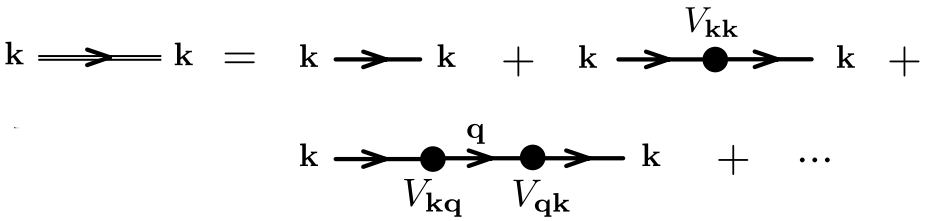

Figure 1.1: The Dyson equation as Feynman diagram summation. The double line represents the full Green's function the single line the non-interacting one. The black dots stand for the perturbing potential.

Defining the quantity $\Sigma(\mathbf{k};\omega)$ as the summation of all terms with intermediate states that are not equal to the in-going and out-going states

$$\Sigma(\mathbf{k};\omega) = V_{\mathbf{k},\mathbf{k}} + \sum_{\mathbf{k}\neq\mathbf{q}} V_{\mathbf{kq}} G_0^{+}(\mathbf{q};\omega) V_{\mathbf{qk}} + \sum_{\substack{\mathbf{q}\neq\mathbf{k} \\ \mathbf{l}\neq\mathbf{k}}} V_{\mathbf{kq}} G_0^{+}(\mathbf{q};\omega) V_{\mathbf{ql}} G_0^{+}(\mathbf{l};\omega) V_{\mathbf{lk}} + \ldots \quad (1.44)$$

The upper equation can be represented in diagrammatic language as shown in Figure (1.2).

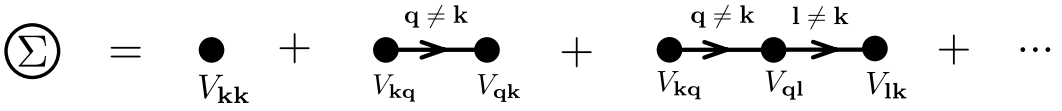

Figure 1.2: The diagrammatic representation of the self-energy as sum over all terms with intermediate states with $\mathbf{k} \neq \mathbf{q}$

Using the definition of $\Sigma(\mathbf{k};\omega)$, one can then rewrite the Dyson equation diagrams in Figure (1.1) as depicted in Figure (1.3)

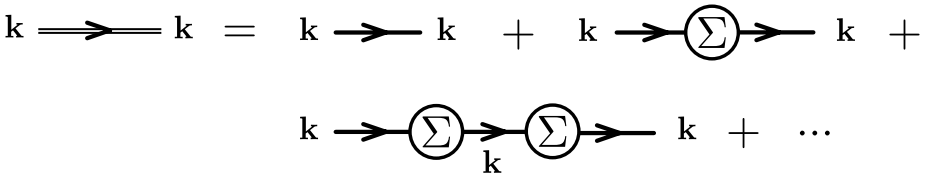

Figure 1.3: The expansion of the Dyson equation using the definition of the self-energy.

which is the expanded Dyson equation corresponding to the one in compact form as given by Eq. (1.39) and the diagrams of Figure (1.4)

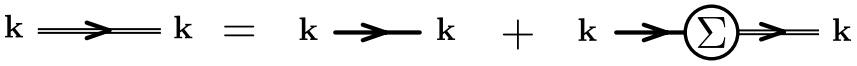

Figure 1.4: Compact form of the Dyson equation in diagrammatic form.

Now all incoming, intermediate and outgoing particles are in the same state $\mathbf{k}$, while all particles that have a different state are included in the definition of $\Sigma(\mathbf{k};\omega)$. $\Sigma(\mathbf{k};\omega)$ is called the self-energy of the particle in state $\mathbf{k}$ and one can rewrite Eq. (1.43) as

$$\begin{aligned} G^+(\mathbf{k},\mathbf{k};\omega) &= G_0^+(\mathbf{k};\omega) + G_0^+(\mathbf{k};\omega)\Sigma(\mathbf{k};\omega)G_0^+(\mathbf{k};\omega) \\ &+ G_0^+(\mathbf{k};\omega)\Sigma(\mathbf{k};\omega)G_0^+(\mathbf{k};\omega)\Sigma(\mathbf{k};\omega)G_0^+(\mathbf{k};\omega) + ..., \end{aligned} \tag{1.45}$$

making it easy to sum the series again

$$\begin{aligned} G^+(\mathbf{k},\mathbf{k};\omega) &= G_0^+(\mathbf{k};\omega)\left[1 + \sum_{n=1}^{\infty}[\Sigma(\mathbf{k};\omega)G_0^+(\mathbf{k};\omega)]^n\right] \\ &= \frac{G_0^+(\mathbf{k};\omega)}{1 - \Sigma(\mathbf{k};\omega)G_0^+(\mathbf{k};\omega)}. \end{aligned} \tag{1.46}$$

Multiplying by $[G_0^+(\mathbf{k};\omega)]^{-1}G_0^+(\mathbf{k};\omega) = 1$ leads to

$$\begin{aligned} G^+(\mathbf{k},\mathbf{k};\omega) &= \frac{1}{[G_0^+(\mathbf{k};\omega)]^{-1} - \Sigma(\mathbf{k};\omega)} \\ &= \frac{1}{\omega - \epsilon_{\mathbf{k}} - \Sigma(\mathbf{k};\omega) + i\delta}. \end{aligned} \tag{1.47}$$

Here $G_0^+(\mathbf{k};\omega)$ is the solution to the non-interacting Schrödinger equation corresponding to the free particle eigenvalues $\epsilon_{\mathbf{k}}$. Equation (1.47) shows that the interaction part of a given system is contained in the self-energy $\Sigma(\mathbf{k};\omega)$, which corrects the free particle energy.

1.3 The quasi-particle concept

In Eq. (1.47) I have derived an expression for the fully interacting Green's function involving the eigenvalues of the non-interacting system, i.e. $\epsilon_{\mathbf{k}}$, and the self-energy. However, a physical meaning for the self-energy is still missing. To clarify the role of the self-energy in the energy spectrum, one has to look at the Fourier transform of Eq. (1.47) to the time domain

$$G^+(\mathbf{k},\mathbf{k},t-t_0) = \frac{i}{2\pi}\int_{-\infty}^{\infty} d\omega \frac{e^{-i\omega(t-t_0)}}{\omega - \epsilon_{\mathbf{k}} - \Sigma(\mathbf{k};\omega)}. \tag{1.48}$$

This integral can be calculated on the complex plane, see Mattuck [49]. Briefly speaking, one needs to avoids the poles of the integrand on the real axis by analytical

continuation into the complex plane. For this, one needs first to find the poles themselves. This means one needs to solve

$$\omega - \epsilon_{\mathbf{k}} - \Sigma(\mathbf{k};\omega) = 0. \tag{1.49}$$

Since $\Sigma(\mathbf{k};\omega)$ is ω-dependent, this is not an easy task and has to be performed using approximations. Once the poles are known, the residues can be calculated using the so-called residue theorem. Assuming, that the imaginary part of the self-energy $|\mathrm{Im}\Sigma(\mathbf{k};\omega)|$ is small, (see appendix (A) for further details on the calculation) one can show that the integral Eq. (1.48) is

$$\begin{aligned} \frac{i}{2\pi}\int_{-\infty}^{\infty} d\omega \frac{e^{-i\omega(t-t_0)}}{\omega - \epsilon_{\mathbf{k}} - \Sigma(\mathbf{k};\omega)} &= -2i\pi Z_{\mathbf{k}} e^{-i[\epsilon_{\mathbf{k}}+\Delta_{\mathbf{k}}-\frac{i}{2}\Gamma_{\mathbf{k}}](t-t_0)} \quad \text{for} \quad t > t_0 \\ &= 0 \quad \text{for} \quad t < t_0, \end{aligned} \tag{1.50}$$

where the different components are given by

$$\begin{aligned} Z_{\mathbf{k}} &= \left(1 - \frac{\partial \mathrm{Re}\Sigma(\mathbf{k};\omega)}{\partial\omega}|_{\omega=\epsilon_{\mathbf{k}}}\right)^{-1} \\ \Delta_{\mathbf{k}} &= \mathrm{Re}\Sigma(\mathbf{k};\epsilon_{\mathbf{k}}) \\ \Gamma_{\mathbf{k}} &= -2Z_{\mathbf{k}}\mathrm{Im}\Sigma(\mathbf{k};\epsilon_{\mathbf{k}}). \end{aligned} \tag{1.51}$$

For Eq. (1.48) one then obtains

$$G^{+}(\mathbf{k},\mathbf{k},t-t_0) = Z_{\mathbf{k}} e^{-i[\epsilon_{\mathbf{k}}+\Delta_{\mathbf{k}}](t-t_0)} e^{-\frac{1}{2}\Gamma_{\mathbf{k}}(t-t_0)}. \tag{1.52}$$

Conversely for the free particle case, i.e. the case without scattering potential, one has

$$G_0^{+}(\mathbf{k},\mathbf{k},t-t_0) = e^{-i\epsilon_{\mathbf{k}}(t-t_0)}. \tag{1.53}$$

Comparing Eq. (1.52) and Eq. (1.53), I observe the following:

1. By the introduction of the scattering potential V, the single particle energy $\epsilon_{\mathbf{k}}$ has been shifted to $\epsilon_{\mathbf{k}} + \Delta_{\mathbf{k}}$.

2. Since the propagator Eq. (1.52) defines the probability amplitude $W_{\mathbf{k}\longrightarrow\mathbf{k}}$ as I have seen in the previous section, one notices, that introducing a scattering potential induces an exponential decay of $W_{\mathbf{k}\longrightarrow\mathbf{k}}$. This is characterized by the life time $\tau_{\mathbf{k}} = \frac{1}{\Gamma_{\mathbf{k}}}$ with a decay rate $\Gamma_{\mathbf{k}}$. Thus, if the decay time is long, corresponding to a long life time, the particle can be considered as being free-particle-like and one speaks of a *quasi-particle*.

3. In addition to the life time, the *quasi-particle* also has an effective mass m^* defined by the *quasi-particle* weight $Z_{\mathbf{k}}$ as

$$\frac{m}{m^*} = Z_{\mathbf{k}}[1 + \frac{1}{d\epsilon_{\mathbf{k}}/d\mathbf{k}}\frac{\partial \mathrm{Re}\Sigma(\mathbf{k};\omega)}{\partial\mathbf{k}}], \tag{1.54}$$

   where m is the mass of the free particle.

Hence, by introducing this quasi-particle concept, the scattering problem can be "mapped" back to a free particle problem with renormalized eigenvalues and masses. Thus, the quasi-particles are weakly coupled to the rest of the system and can be considered as independent particles. This is a useful concept and a way of understanding particle interactions that has proven to be very successful in gaining insight into the complexity of the many-body problem.

1.4 The electron-electron interaction

Up to now I have briefly introduced the one particle Green's function, the Feynman diagram representation and the quasi-particle concept as theoretical tools for treating single particle scattering (non-interacting systems). They reflect a way of approaching the complexity of many-body interactions, that has proven to be very successful. However, one is usually interested in understanding the physics of systems with more that one electron. Hence, the ground state $|0\rangle$ in Eq. (1.35) would be the one of a many-body system. Gell-Mann and Low [56] have shown in their famous theorem, that the ground state of the non-interacting system, $|0_0\rangle$, is connected to the ground state of the many-body system $|0\rangle$ via

$$|0\rangle = \frac{U(0,-\infty)|0_0\rangle}{\langle 0_0|U(0,-\infty)|0_0\rangle}. \tag{1.55}$$

Thus, in the many-body case, the propagator in Eq. (1.35) is given by

$$\begin{aligned} iG(\mathbf{r},\mathbf{r}',t-t_0) &= \langle 0|\psi(\mathbf{r},t)\psi^\dagger(\mathbf{r}',t_0)|0\rangle,\ t>t_0 \\ &= \frac{\langle 0_0|U_\mathrm{I}(\infty,t)\psi_\mathrm{I}(\mathbf{r}',t)U_\mathrm{I}(t,t_0)\psi_\mathrm{I}^\dagger(\mathbf{r},t_0)U_\mathrm{I}(t_0,-\infty)|0_0\rangle}{\langle 0_0|U_\mathrm{I}(\infty,-\infty)|0_0\rangle}, \end{aligned} \tag{1.56}$$

where $\psi_\mathrm{I}(\mathbf{r}',t) = U_0^\dagger(t,0)\psi(\mathbf{r})U_0(t,0)$ and $\psi_\mathrm{I}(\mathbf{r}',t) = U_0^\dagger(t,0)\psi^\dagger(\mathbf{r})U_0(t,0)$. U_0 is the time evolution operator corresponding to the non-interacting Hamiltonian while $U_\mathrm{I}(t,t_0) = U_0^\dagger(t,t_0)U(t,t_0)$. The proof of Eq. (1.56) goes through the adiabatic connection, where one starts from the non-interacting state and adiabatically switches on the two particle potential considered as the perturbation (see the books of Mattuck [49] or Fetter and Walecka [51] for further reading).
Although the expression in Eq. (1.56) looks more complicated than the one for the non-interacting case, Eq. (1.35), Feynman showed that the procedures and recipes available for the non-interacting picture can still be applied for the many-body case. Hence, the very handy Feynman formalism, discussed in the previous section for the non-interacting case, can be directly adopted for the many-body problem.
As mentioned in the introduction to this chapter, electrons "feel" each other trough the Coulomb interaction. The long-ranged nature of the latter is a problem when trying to describe systems with more than one electron. In fact, already two-body interactions, such as the Coulomb interaction depicted in Figure (1.5), are complex enough and a system of electrons that interact herewith can only be described using approximate approaches.

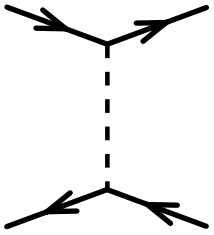

Figure 1.5: The interaction between two electrons (solid lines) via the Coulomb potential (dashed line).

The (Coulomb) electron-electron interaction is strong. Thus, it appears contradictory to perform perturbation expansions in the Coulomb interaction directly. This is because the series will not converge rapidly, which is a requirement for perturbation theory. An there are cases where the series even diverges [57, 58]. To overcome this issue, the way to go is to first choose the relevant interaction that might give an important contribution, using propagator theory, and then expand in this interaction by solving the Dyson equation. Solving the Dyson equation in a self-consistent way (i.e., dressing the propagator), then yields higher order diagrams (i.e., more interactions) that may also be relevant. I am going to present in this section, step by step, the different approximations to the two-body interaction that can be derived from the diagram in Fig. (1.5). Starting from the Hartree [46] interaction, which is the first and the simplest of the two-body interactions, and going through the Hartree-Fock [45] approximation to then introduce the so-called random-phase approximation [47, 48, 43] and the concept of screening. Finally, I will introduce Hedin's equations [40], written in this Green's function language. They are insightful and incorporate higher order interactions via the so called vertex function. The prominent and very successful GW approximation to Hedin's equations will also be discussed.

1.4.1 The Hartree-Fock approximation

The first electron-electron interaction to be included and at the same time the most intuitive one is the so called *Hartree approximation* [46] that can be derived straightforwardly if one closes the two particle diagram Fig. (1.5) as depicted in Figure below.

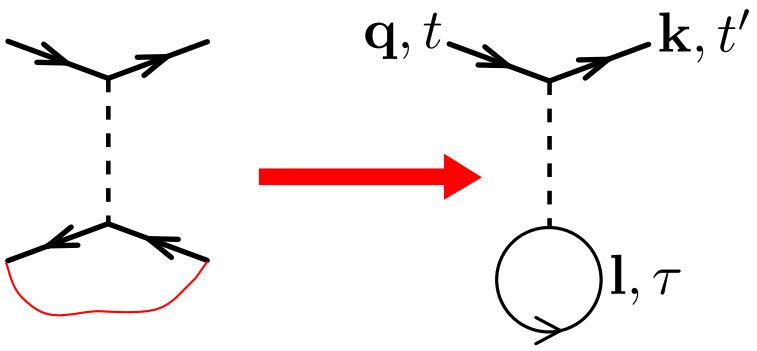

Figure 1.6: Left: A cartoon way the two particle interaction diagram that results in the Hartree diagram. Right: The diagram depicting the resulting Hartree interaction.

The two-particle propagator would have the following expression

$$G_H^+(\mathbf{k},\mathbf{q};t'-t) = -\sum_{\mathbf{l}}^{occ.}\int d\tau G_0^+(\mathbf{k},\mathbf{k};t'-\tau)V_{\mathbf{klql}}G_0^-(\mathbf{l},\mathbf{l};\tau-\tau)G_0^+(\mathbf{q},\mathbf{q};\tau-t), \tag{1.57}$$

where the equal time hole propagator G_0^- gives [49] $G_0^-(\mathbf{l},\mathbf{l};\tau-\tau) = -1$, so that one gets

$$G_H^+(\mathbf{k},\mathbf{q};t'-t) = -\sum_{\mathbf{l}}^{occ.}\int d\tau G_0^+(\mathbf{k},\mathbf{k};t'-\tau)V_{H,\mathbf{kq}}G_0^+(\mathbf{q},\mathbf{q};\tau-t). \tag{1.58}$$

where I have set

$$\begin{aligned}\sum_{\mathbf{l}}^{occ.} V_{\mathbf{klql}} &= \sum_{\mathbf{l}}^{occ.}\int\int d\mathbf{r}_1 d\mathbf{r}_2 \phi_{\mathbf{k}}^*(\mathbf{r}_1)\phi_{\mathbf{l}}^*(\mathbf{r}_2)\frac{1}{|\mathbf{r}_1-\mathbf{r}_2|}\phi_{\mathbf{q}}(\mathbf{r}_1)\phi_{\mathbf{l}}(\mathbf{r}_2) \\ &= \int d\mathbf{r}_1 \phi_{\mathbf{k}}^*(\mathbf{r}_1)V_H(\mathbf{r}_1)\phi_{\mathbf{q}}(\mathbf{r}_1) = V_{H,\mathbf{kq}},\end{aligned} \tag{1.59}$$

with $V_H(\mathbf{r}_1) = \int d\mathbf{r}_2 \frac{\rho(\mathbf{r}_2)}{|\mathbf{r}_1-\mathbf{r}_2|}$ and the electron density given by $\rho(\mathbf{r}_2) = \sum_{\mathbf{l}}^{occ.}|\phi_{\mathbf{l}}(\mathbf{r}_2)|^2$. V_H is essentially the interaction of an incoming electron in state $\mathbf{q}$ with a hole at a state $\mathbf{l}$, that gets annihilated instantaneously, which brings the electron to the state $\mathbf{k}$.

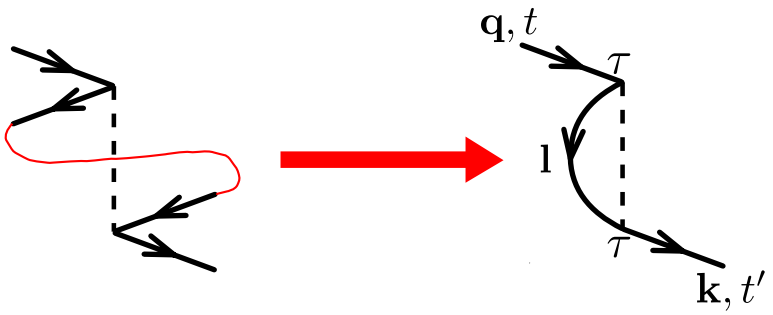

Figure 1.7: Left: A cartoon showing how the two particle interaction diagram should be connected to yield the Fock diagram. Right: The resulting Feynman diagram representing the Fock interaction. It depicts the interaction of an electron with itself, which is a direct result of the indistinguishableness of electrons.

The next possible first order diagram to include is the *exchange (or Fock) approximation* [45]; again looking at the diagram of Figure (1.5), one can choose to connect the lines as shown in Figure (1.7). This corresponds to the propagator

$$G^{+}_{1,X}(\mathbf{k},\mathbf{q};t'-t)=\sum_{\mathbf{l}}^{occ.}\int d\tau G^{+}_{0}(\mathbf{k},\mathbf{k};t'-\tau)V_{\mathbf{lkql}}G^{-}_{0}(\mathbf{l},\mathbf{l};\tau-\tau)G^{+}_{0}(\mathbf{q},\mathbf{q};\tau-t), \tag{1.60}$$

with

$$\begin{aligned}\sum_{\mathbf{l}}^{occ.}V_{\mathbf{lkql}}&=\sum_{\mathbf{l}}^{occ.}\int\int d\mathbf{r}_1 d\mathbf{r}_2\phi^{*}_{\mathbf{l}}(\mathbf{r}_1)\phi^{*}_{\mathbf{k}}(\mathbf{r}_2)\frac{1}{|\mathbf{r}_1-\mathbf{r}_2|}\phi_{\mathbf{q}}(\mathbf{r}_1)\phi_{\mathbf{l}}(\mathbf{r}_2)\\&=\int\int d\mathbf{r}_1 d\mathbf{r}_2\phi^{*}_{\mathbf{k}}(\mathbf{r}_2)V_X(\mathbf{r}_1,\mathbf{r}_2)\phi_{\mathbf{q}}(\mathbf{r}_1)=V_{X,\mathbf{kq}},\end{aligned} \tag{1.61}$$

and $V_X(\mathbf{r}_1,\mathbf{r}_2)=\sum_{\mathbf{l}}^{occ.}\frac{\phi^{*}_{\mathbf{l}}(\mathbf{r}_1)\phi_{\mathbf{l}}(\mathbf{r}_2)}{|\mathbf{r}_1-\mathbf{r}_2|}$. One can then rewrite Eq. (1.60) as

$$G^{+}_{1,X}(\mathbf{k},\mathbf{q};t'-t)=-\int d\tau G^{+}_{0}(\mathbf{k},\mathbf{k};t'-\tau)V_{X,\mathbf{kq}}G^{+}_{0}(\mathbf{q},\mathbf{q};\tau-t). \tag{1.62}$$

depicted by the diagram in Fig. (1.7) and where the "−" sign results from the diagrammatic rules for the propagator $G^{-}_{0}(\mathbf{l},\mathbf{l};\tau-\tau)$ [49]. It represents the indistinguishability of electrons; meaning that, one cannot tell, when an incoming electron gets *exchanged* with another one in the system. So, an electron in state $\mathbf{l}$ can result from the interaction of an electron in state $\mathbf{q}$ with an electron in state $\mathbf{k}$, and the same electron can interact with an electron in state $\mathbf{q}$ to yield an electron in state $\mathbf{k}$. That is why this diagram has the name of exchange diagram. Another way of interpreting the exchange diagram, is by looking at it as being a diagram of an electron interacting with itself.
The Hartree-Fock (HF) self-energy describes both the Hartree and the exchange (or

Fock) interaction and is defined as $\Sigma_{HF}(\mathbf{k},\mathbf{q}) = V_{H,\mathbf{kq}} - V_{X,\mathbf{kq}}$ allowing us to write the Dyson equation for this self-energy in the frequency domain

$$G_{HF}(\mathbf{k},\mathbf{q};\omega) = G_0(\mathbf{k},\mathbf{k};\omega)\delta_{\mathbf{kq}} + \sum_{\mathbf{l}}\sum_{\mathbf{k}'} G_0(\mathbf{k},\mathbf{k}';\omega)\Sigma_{HF}(\mathbf{k}',\mathbf{l})G_{HF}(\mathbf{l},\mathbf{q};\omega). \quad (1.63)$$

The Hartree-Fock self-consistent field equations

The HF eigenfunctions $\psi(\mathbf{r})$ as expansion of a set of basis functions can be written as

$$\psi_\nu(\mathbf{r}) = \sum_{\mathbf{k}} c_{\nu\mathbf{k}}\phi_{\mathbf{k}}(\mathbf{r}), \quad (1.64)$$

where the $c_{\nu\mathbf{k}}$ are the expansion coefficient matrices. Using this expansion it is then possible to write the HF equation in real space

$$\left[-\frac{1}{2m}\nabla^2 - \sum_{\mathbf{R}}\frac{Z}{|\mathbf{r}-\mathbf{R}|} + V_H(\mathbf{r})\right]\psi_\nu(\mathbf{r}) - \int d\mathbf{r}' V_X(\mathbf{r},\mathbf{r}')\psi_\nu(\mathbf{r}') = \epsilon_\nu\psi_\nu(\mathbf{r}), \quad (1.65)$$

with

$$\begin{aligned} V_H(\mathbf{r}_1) &= \sum_{\mu}^{occ.}\int d\mathbf{r}_2 \frac{|\psi_\mu(\mathbf{r}_2)|^2}{|\mathbf{r}_1-\mathbf{r}_2|}, \\ V_X(\mathbf{r}_1,\mathbf{r}_2) &= \sum_{\mu}^{occ.}\frac{\psi^*_\mu(\mathbf{r}_1)\psi_\mu(\mathbf{r}_2)}{|\mathbf{r}_1-\mathbf{r}_2|}. \end{aligned} \quad (1.66)$$

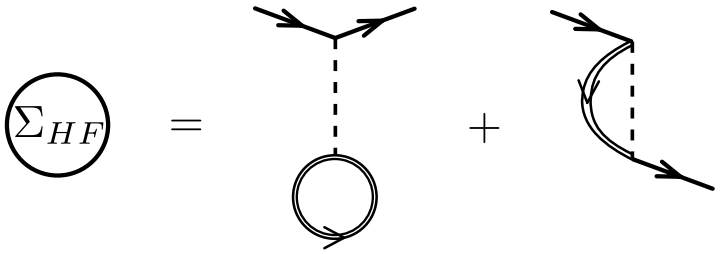

Figure 1.8: The Hartree-Fock self-energy at self-consistency. The double lines refer to G_{HF} obtained from solving the Hartree-Fock equations in a self-consistent way.

Since the potentials V_H and V_X are defined by the orbitals ψ_μ, Eqs. (1.65) and (1.66) define self-consistent equations that have to be iterated until the potentials (fields) do not change anymore. Thus, they define a so called self-consistent field cycle. One can then depict the Hartree-Fock self-energy as shown in Figure (1.8), where the double lines refer to the self-consistent propagators including higher order and more complex processes through the infinite summation in the self-consistency cycle.

1.4.2 The random phase approximation and the concept of screening

The Hartree-Fock approximation is very popular and constitutes a useful starting point to understand complex electron-electron interactions. However, the bare Coulomb interaction contained in the exact exchange term of Hartree-Fock turns out to be problematic. This is especially manifested when one aims to describe metallic systems for which Hartree-Fock theory predicts an insulator even for the simple case of the homogeneous electron gas (see the discussion by Pines [59]). To overcome the issues caused by the bare Coulomb interaction that enters the Hartree-Fock approximation presented in the previous section, one can go a step further and look at second-order diagrams. Even if doing Hartree-Fock self-consistently does include some second-order diagrams in the Coulomb interaction, not all of them are included. The first second-order diagram, that is not included in the self-consistent Hartree-Fock approximation is the one depicted in Fig. (1.9). It is constructed by linking two two-particle diagrams and is called second order since two Coulomb lines

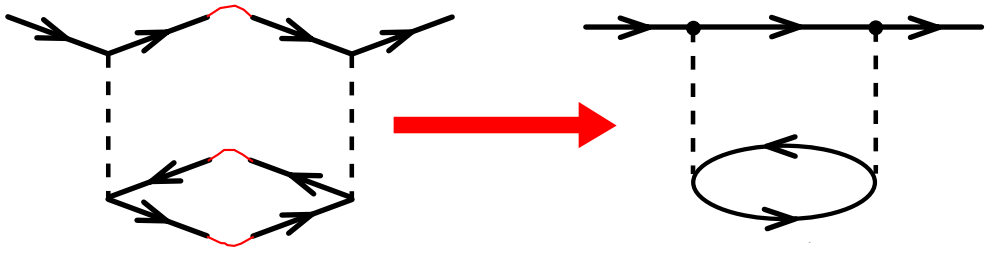

Figure 1.9: A cartoon depicting the construction of the second order diagram from two two-particle interaction diagrams.

(dashed lines) are involved in the self-energy part. This becomes clear, if one writes the corresponding propagator

$$G^{+}(\mathbf{k},\mathbf{q};t'-t) = \sum_{\mathbf{l},\mathbf{n},\mathbf{m}}^{occ.} \int\int d\tau_1 d\tau_2 G_0^{+}(\mathbf{k},\mathbf{k};t'-\tau_1) V_{\mathbf{kmln}} G_0^{+}(\mathbf{n},\mathbf{n};\tau_2-\tau_1) \\ G_0^{-}(\mathbf{m},\mathbf{m};\tau_2-\tau_1) G_0^{+}(\mathbf{l},\mathbf{l};\tau_2-\tau_1) V_{\mathbf{lnqm}} G_0^{+}(\mathbf{q},\mathbf{q};\tau-t), \quad (1.67)$$

where the coulomb matrix element $V_{\mathbf{kmln}}$ occurs twice. The physical meaning of the diagram Fig. (1.9) is, that an incoming particle with state $\mathbf{q}$ creates a particle-hole pair at time τ_1 and is scattered to state $\mathbf{l}$. The particle-hole recombines at time τ_2 and the electron is scattered to state $\mathbf{k}$. The process occurs at different times and is thus of dynamical nature, in contrast to the Hartree-Fock processes, that are occurring instantaneously and thus, are purely static processes.
It is possible to sum these contributions to infinity, which yields higher, more complex interactions.

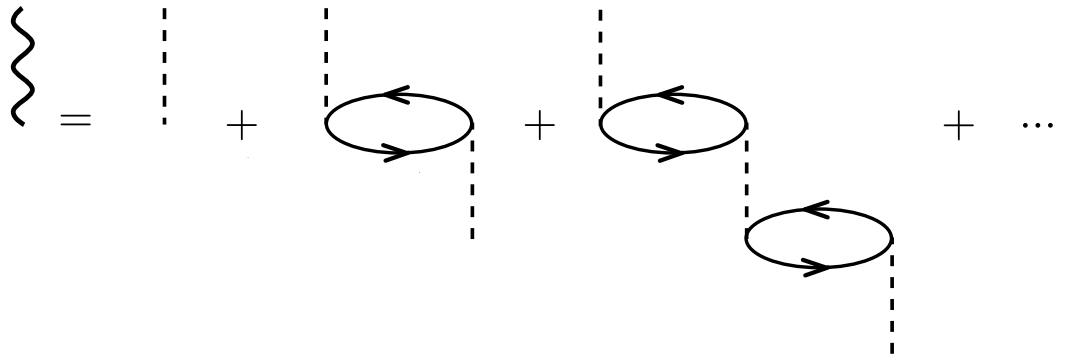

Figure 1.10: The screened Coulomb interaction (double dashed lines) as an infinite sum over bubble diagrams with their Coulomb "legs" (single dashed lines).

A way to perform the summation over second order diagrams is to consider an additional Dyson equation, for the two Coulomb lines and the electron-hole bubble of the second order diagram Fig. (1.9) as shown in Fig. (1.10), where the series defines a screened Coulomb interaction depicted by the double Coulomb lines. Then it is clear that the infinite summation can be written as a geometric series, and thus in the compact form of Fig. (1.11)

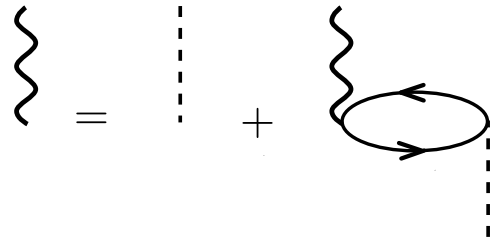

Figure 1.11: Screened Coulomb interaction in Dyson equation form.

Hence, summing up the Coulomb lines with electron-hole bubbles leads to a new "screened" Coulomb interaction consisting of an infinite summation of electron-hole interactions. This way of summing up the Coulomb interaction diagrams is known as the random-phase-approximation (RPA) first introduced by Bohm and Pines [47, 48]. In other words, it renormalizes Fock diagrams so that the bare Coulomb interaction is replaced by the screened one as illustrated by the diagram in Fig. (1.12).

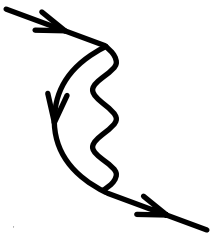

Figure 1.12: The exact exchange diagram with the screened Coulomb interaction from RPA.

The second order diagram becomes the one depicted in Fig. (1.13) and for the corresponding propagator one obtains the expression

$$G^{+}_{1,RPA}(\mathbf{k},\mathbf{k};t'-t) = \sum_{\mathbf{l},\mathbf{q}}^{occ.} \int\int d\tau_1 d\tau_2 G^{+}_0(\mathbf{k},\mathbf{k};t'-\tau_1) V_{\mathbf{q}} G^{+}_0(\mathbf{k}-\mathbf{q},\mathbf{k}-\mathbf{q};\tau_2-\tau_1)$$
$$G^{-}_0(\mathbf{l},\mathbf{l};\tau_2-\tau_1) G^{+}_0(\mathbf{l}+\mathbf{q},\mathbf{l}+\mathbf{q};\tau_2-\tau_1) V_{-\mathbf{q}} G^{+}_0(\mathbf{k},\mathbf{k};\tau_1-t). \tag{1.68}$$

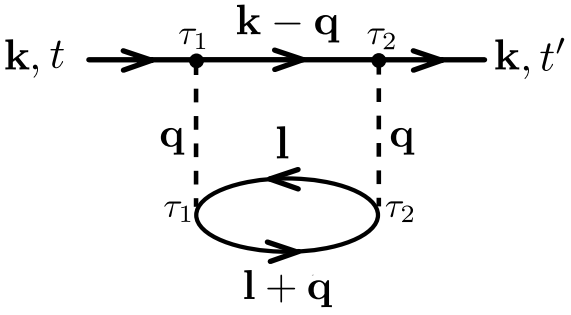

Figure 1.13: The second order diagram for the homogeneous electron gas.

In diagram Fig. (1.13) the electron-hole bubble describing the electron with momentum $\mathbf{l}+\mathbf{q}$ and the hole with momentum $\mathbf{l}$ can be considered as a separated quantity called the polarisability (Π_0):

$$\Pi_0(\mathbf{q};\tau_2-\tau_1) = \sum_{\mathbf{l}} G^{-}_0(\mathbf{l},\mathbf{l};\tau_2-\tau_1) G^{+}_0(\mathbf{l}+\mathbf{q},\mathbf{l}+\mathbf{q};\tau_2-\tau_1), \tag{1.69}$$

that corresponds to the diagram

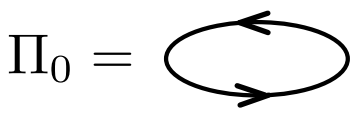

One has then all the ingredients to write the screened Coulomb interaction as the series in Fig. (1.10) illustrates explicitly using the formula for the geometric

series. The screened Coulomb interaction in the frequency domain is then

$$\begin{aligned} W(\mathbf{q},\omega) &= V_{\mathbf{q}} - V_{\mathbf{q}}\Pi_0(\mathbf{q};\omega)V_{\mathbf{q}} + V_{\mathbf{q}}\Pi_0(\mathbf{q};\omega)V_{\mathbf{q}}\Pi_0(\mathbf{q};\omega)V_{\mathbf{q}} - ... \\ &= V_{\mathbf{q}}[1 + \Pi_0(\mathbf{q};\omega)V_{\mathbf{q}}]^{-1} \end{aligned} \tag{1.70}$$

corresponding to the diagrams of Fig. (1.14)

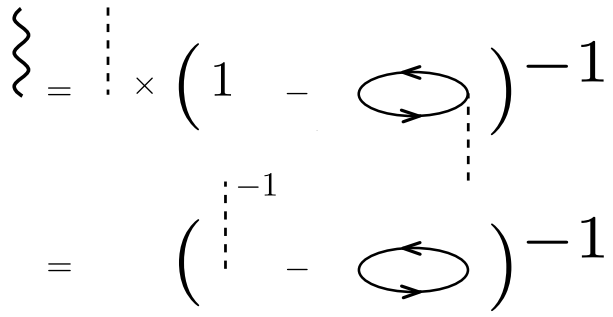

Figure 1.14: Feynman diagram representation of the Screened Coulomb interactions as in Eq. 1.70

The Dyson-like expression Eq. (1.70) is a a key equation in RPA and shows that the screened Coulomb interaction W is an infinite sum over the electron-hole bubble diagrams.

1.4.3 Hedin's equations and the GW approximation

In this section I want to present a well known scheme for writing the general many-body problem of many interacting electrons in terms of self-consistent equations formally describing all the possible interactions that can occur in a many-body system. This Green's function based scheme developed originally by Hedin [40] has become very popular in the electronic structure community, in particular its so-called GW approximation, where the vertex function, describing the complex interactions, has a particularly simple shape. The GW approximation has proven to be very successful in describing spectral features of finite systems and solids [60, 61, 62]. Here I present the formalism as is done in the review paper by Aryasetiawan and Gunnarsson [52]. To start, I consider the many-body Hamiltonian in second quantization

$$\begin{aligned} \hat{H} &= \int d\mathbf{r}dt\psi^\dagger(\mathbf{r},\mathbf{t})h_0(\mathbf{r})\psi(\mathbf{r},\mathbf{t}) \\ &+ \frac{1}{2}\int d\mathbf{r}dt\mathbf{r}'\psi^\dagger(\mathbf{r},\mathbf{t})\psi^\dagger(\mathbf{r}',\mathbf{t})v(|\mathbf{r}-\mathbf{r}'|)\psi^\dagger(\mathbf{r}',\mathbf{t})\psi(\mathbf{r},\mathbf{t}). \end{aligned} \tag{1.71}$$

Using commutator relations for the Fermion field operators $\psi(\mathbf{r},\mathbf{t})$ and the Heisenberg equation of motion for the above Hamiltonian $i\frac{\partial}{\partial t}\psi(\mathbf{r},\mathbf{t}) = [\psi(\mathbf{r},\mathbf{t}),\hat{H}]$, one obtains

$$[i\partial_t - h_0(1)]G(1,2) - \int d3M(1,3)G(3,2) = \delta(1-2), \tag{1.72}$$

where $1 = (\mathbf{r}, t)$, $2 = (\mathbf{r}', t')$ and $3 = (\mathbf{r}_1, t)$ have been defined and the so called quasi-particle mass operator

$$\int d3M(1,3)G(3,2) = -i \int d3v(1-3)\langle 0|\mathbf{T}\{\psi^\dagger(3^+)\psi(3)\psi(1)\psi^\dagger(2)\}|0\rangle, \quad (1.73)$$

is given via the self-energy as $\Sigma = M - V_H$, where V_H is the Hartree potential and $3^+ = (\mathbf{r}_1, t^+)$. The expression above introduces the two-particle propagator $\langle 0|\mathbf{T}\{\psi^\dagger(3^+)\psi(3)\psi(1)\psi^\dagger(2)\}|0\rangle$, that accounts for higher order interactions. As is done by Schwinger [63, 52], one can introduce a time-dependent field $\phi(\mathbf{r}, t)$ as a mathematical tool for generating the self-energy and the vertex. At the end of the formalism $\phi(\mathbf{r}, t)$ is then usually set to zero. One finally obtains the coupled equations

$$\begin{aligned}
\Sigma(1,2) &= i \int d3d4G(1,3^+)W(1,4)\Gamma(3,2,4), && (1.74)\\
G(1,2) &= G_0(1,2) + \int d3d4G_0(1,3)\Sigma(3,4)G(4,2), && (1.75)\\
\Gamma(1,2,3) &= \delta(1-2)\delta(2-3) \\
&+ \int d4d5d6d7 \frac{\delta\Sigma(1,2)}{\delta G(4,5)} G(4,6)G(7,5)\Gamma(6,7,3), && (1.76)\\
\Pi(1,2) &= -i \int d3d4G(1,3)\Gamma(3,4,2)G(4,1^+), && (1.77)\\
W(1,2) &= v(1,2) + \int d3d4v(1,3)\Pi(3,4)W(4,2). && (1.78)
\end{aligned}$$

where Π is the polarizability, W the screened Coulomb interaction and Γ the vertex function. Equations (1.74) - (1.78) are the so-called Hedin's equations. They are connected to each other; this means, if one wants to calculate one quantity, e.g. the Green's function, one needs to know the self-energy and thus the screened Coulomb interaction that is a functional of the polarizability Π, itself a functional of the vertex function Γ.
A more careful look at the equations above, makes it obvious that the vertex function enters all quantities. Hence, one can easily think of approximating this function to simplify the computation of the related other functions. The easiest approximation of the vertex function is to take

$$\Gamma(1,2,3) = \delta(1-2)\delta(2-3). \quad (1.79)$$

This is the so called GW approximation whose name originates from the expression for the self-energy $\Sigma(1,2) = iG(1,2)W(1,2)$. Hedin's equations then simplify to

$$\begin{aligned}
\Sigma(1,2) &= iG(1,2)W(1,2), && (1.80)\\
G(1,2) &= G_0(1,2) + \int d3d4G_0(1,3)\Sigma(3,4)G(4,2), && (1.81)\\
\Pi(1,2) &= -iG(1,2)G(2,1^+), && (1.82)\\
W(1,2) &= v(1,2) + \int d3d4v(1,3)\Pi(3,4)W(4,2). && (1.83)
\end{aligned}$$

Equations (1.80) to (1.83) define a self-consistency cycle that is simpler than the one given by Eqs. (1.74) - (1.78), since the vertex is set to unity. A cartoon depicting the GW self-consistency cycle is shown in Figure (1.15)

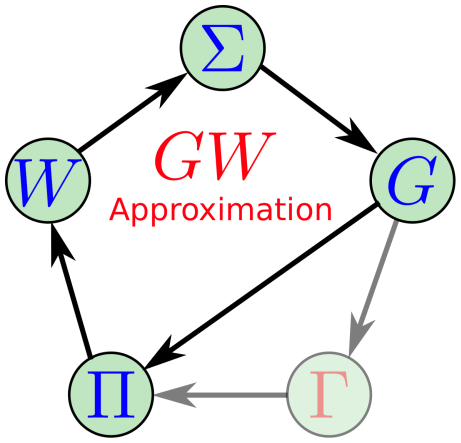

Figure 1.15: Cartoon representing the loop over Hedin's equations. The self-consistency loop for the GW approximation is obtained by computing the polarizability Π directly from the Green's function without vertex correction.

From a diagrammatic point of view, the GW approximation describes exactly the same processes, and hence has the same diagrams as RPA. This is illustrated in the Feynman diagram for the GW self-energy in Fig. (1.16). One can say that the first approximation to the vertex function Γ in Hedin's equations recovers the RPA.

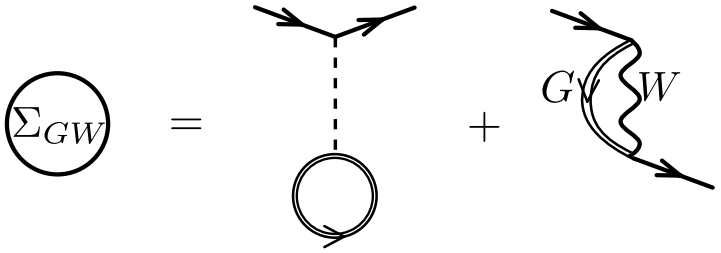

Figure 1.16: The GW self-energy obtained by replacing the bare Coulomb interaction in the Hartree-Fock self-energy by the screened one.

1.4.4 *GW* calculations for real systems

Because of the high computational costs of numerical implementations of fully self-consistent GW, a perturbative approach has been considered known as G_0W_0. One starts with the Green's function of a self-consistent Kohn=Sahm density-functional (see next chapter) or HF calculation, from which one obtains the polarisability $\chi^0(i\omega)$ after the Alder-Wiser formula [64, 65]

$$\chi^0(\mathbf{r},\mathbf{r}',i\omega)=\sum_i^{occ.}\sum_\nu^{unocc.}\frac{\varphi_i^*(\mathbf{r})\varphi_\nu(\mathbf{r})\varphi_\nu^*(\mathbf{r}')\varphi_i(\mathbf{r}')}{i\omega-\epsilon_i-\epsilon_\nu}+c.c., \tag{1.84}$$

where φ_i (φ_ν) are the Kohn-Sham or HF occupied (unoccupied) orbitals and ϵ_i (ϵ_ν) the corresponding eigenvalues. The GW self-energy can then be calculated from Eq. (1.80) via the screened Coulomb interaction W. One can then correct upon the Kohn-Sham eigenvalues $\epsilon_\nu^{\mathrm{KS}}$ as follows

$$\epsilon_\nu^{\mathrm{QP}}=\epsilon_\nu^{\mathrm{KS}}+\Sigma_{GW}^\nu(\epsilon_\nu^{\mathrm{QP}})-v_{\mathrm{XC}}^\nu, \tag{1.85}$$

where $\Sigma_{GW}^\nu(\epsilon_\nu^{\mathrm{QP}})=\int d\mathbf{r}d\mathbf{r}'\psi_\nu(\mathbf{r})\Sigma(\mathbf{r},\mathbf{r}',\epsilon_\nu^{\mathrm{QP}})\psi_\nu^*(\mathbf{r}')$ and the Kohn-Sham exchange-correlation potential $v_{\mathrm{XC}}^\nu=\int d\mathbf{r}\psi_\nu(\mathbf{r})V_{\mathrm{XC}}(\mathbf{r})\psi_\nu^*(\mathbf{r})$. Thus, the unperturbed eigenvalues $\epsilon_\nu^{\mathrm{KS}}$ experience the perturbation $\Sigma_{GW}-V_{\mathrm{XC}}$. With the quasi-particle correction $\Sigma_{GW}^\nu(\epsilon_\nu^{\mathrm{QP}})-v_{\mathrm{XC}}^\nu$. The G_0W_0 gained its reputation mainly from its successful description of electronic excitations in solids [52, 66, 62, 67].

1.5 Wave-function based approaches

As mentioned previously, the electron-electron interaction makes the description of real systems only feasible within approximated approaches. The electronic wave function represents a key quantity in such approaches since it sets the configuration-space within which a given approximation is valid. Hence, schemes that can improve the predictive power of a given theory by improving its wave function are often referred to as wave-function based methods.
The most primitive of such methods is the HF approach as I have introduced in the previous sections from a diagrammatic perspective. In HF the wave function of N interacting electrons is described by a Slater determinant

$$\Psi_0(\{\mathbf{r},\sigma\})=\frac{1}{\sqrt{N!}}\begin{vmatrix}\varphi_i(\mathbf{r}_i,\sigma_i) & \varphi_j(\mathbf{r}_i,\sigma_i) & \cdots & \varphi_N(\mathbf{r}_i,\sigma_i)\\ \varphi_i(\mathbf{r}_j,\sigma_j) & \varphi_j(\mathbf{r}_j,\sigma_j) & \cdots & \varphi_N(\mathbf{r}_j,\sigma_j)\\ \vdots & \vdots & \ddots & \vdots\\ \varphi_i(\mathbf{r}_N,\sigma_N) & \varphi_j(\mathbf{r}_N,\sigma_N) & \cdots & \varphi_N(\mathbf{r}_N,\sigma_N)\end{vmatrix}. \tag{1.86}$$

It is essentially the linear combination of the product of independent electronic wave functions $\varphi_i(\mathbf{r}_i,\sigma_i)$ of spin σ_i with all the possible permutations of their coordinates. Moreover, the Slater determinant satisfies the antisymmetry properties of electrons. Using this wave function, the HF energy can be calculated from

$$E^{\mathrm{HF}}=\langle\Psi_0|\hat{H}_e|\Psi_0\rangle. \tag{1.87}$$

The above formula defines an energy functional of the electronic wave function $E^{\mathrm{HF}}[\{\varphi(\mathbf{r},\sigma)\}]$ that can be minimized using the variational principle [68]. However as mentioned in the previously a major drawback of HF theory is its lack of electronic correlation effects.
To include such effects a treatment of the electron-electron interaction beyond HF

is required. In other words not only occupied states should be considered but also unoccupied ones, allowing for excitations to be taken into account. Hence, a larger configuration-space is needed and the single Slater determinant is not enough anymore. In so called Møller-Plesset perturbation theory (MP2) [69] the second order

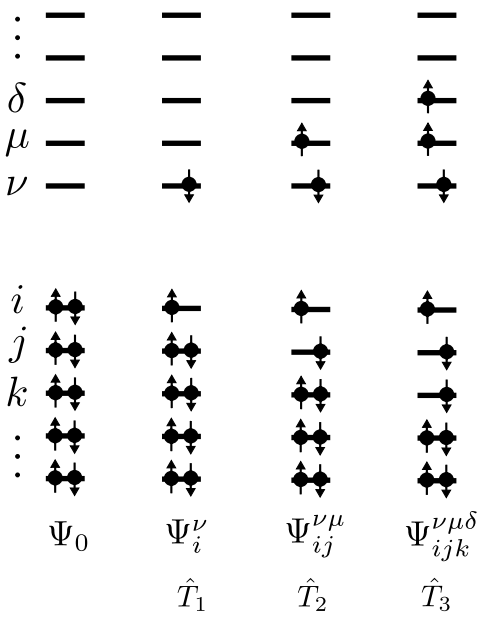

Figure 1.17: Schematic drawing showing an example of the different excitations considered in CC theory. The Latin indexes label occupied states, whereas the Greek one stand for the unoccupied states.

term of the exact exchange from perturbation theory (on the bare Coulomb interaction) is included, yielding the MP2 expression [43]

$$E^{\mathrm{MP2}} = \frac{1}{2}\sum_{ij}^{occ.}\sum_{\mu\nu}^{unocc.}\sum_{\sigma\sigma'}\langle i\nu,\sigma|j\mu,\sigma'\rangle\left[\frac{\langle \nu i,\sigma|\mu j,\sigma'\rangle - \langle \nu i,\sigma|\nu j,\sigma'\rangle\delta_{\sigma\sigma'}}{\epsilon_i^{\sigma}+\epsilon_j^{\sigma'}-\epsilon_\nu^{\sigma}-\epsilon_\mu^{\sigma'}}\right], \tag{1.88}$$

where the Greek indexes, $\nu, \mu, ...$, run over unoccupied states and the Latin ones, $i, j, ...$, over occupied states. The two-electron Coulomb repulsion integrals are given by

$$\langle i\nu,\sigma|j\mu,\sigma'\rangle = \int d\mathbf{r}d\mathbf{r}'\frac{\varphi_i^*(\mathbf{r},\sigma)\varphi_\nu(\mathbf{r},\sigma)\varphi_j^*(\mathbf{r}',\sigma')\varphi_\mu(\mathbf{r}',\sigma')}{|\mathbf{r}-\mathbf{r}'|}. \tag{1.89}$$

The two terms in the brackets [...] in Eq. (1.88) correspond to the second order Coulomb (i.e., Hartree) and second order exchange energy (i.e., Fock), respectively. While MP2 improves upon HF in many aspects [70, 71, 72], it fails for metals with zero direct energy gap. This is because E^{MP2} includes energy differences in the denominator that are zero for such systems and hence E^{MP2} becomes divergent [73]. In another context, Čižek and Paldus [74, 75] introduced the coupled cluster (CC) method. It has been considered as the most reliable and at the same time computationally still affordable method in quantum chemistry [76, 77]. In CC theory one

differentiates between single excitations (Ψ_i^ν) double excitations ($\Psi_{ij}^{\nu\mu}$) triple excitations ($\Psi_{ijk}^{\nu\mu\delta}$) and so on, as shown in Fig. (1.17). Hence, the CC wave function builds on the following ansatz

$$\Psi_{\mathrm{CC}} = \exp(\hat{T})\Psi_0 = \sum_{n=0}^{\infty} \frac{\hat{T}^n}{n!}\Psi_0, \tag{1.90}$$

where Ψ_0 is the single Slater determinant and the cluster operator $\hat{T}$ is given by

$$\hat{T} = \hat{T}_1 + \hat{T}_2 + \hat{T}_3 + ... + \hat{T}_n. \tag{1.91}$$

The indexes $1, 2, ..., n$ refer to the number of excited states introduced by the operator $\hat{T}$. Hence, $\hat{T}_1\Psi_0 = \sum_{i\nu} t_i^\nu \Psi_i^\nu$ introduces the single excitation Ψ_i^ν from the Slater determinant Ψ_0, and $\hat{T}_2\Psi_0 = \sum_{i>j,\nu>\mu} t_{ij}^{\nu\mu}\Psi_{ij}^{\nu\mu}$ includes double excitations $\Psi_{ij}^{\nu\mu}$ and so on. The $t_{ij...}^{\nu\mu...}$ are the CC amplitudes and their determination is the major task in CC calculations [77].
Considering only single (S) and double (D) excitations within the CCSD, the energy is then given by

$$E^{\mathrm{CCSD}} = E^{\mathrm{HF}} + \frac{1}{2}\sum_{i<j}^{occ.}\sum_{\mu>\nu}^{unocc.}\sum_{\sigma\sigma'}(t_{ij}^{\nu\mu} + t_i^\nu t_j^\mu - t_i^\mu t_j^\nu)\left[\langle ij,\sigma|\mu\nu,\sigma'\rangle - \langle ij,\sigma|\nu\mu,\sigma'\rangle\right]. \tag{1.92}$$

The computational cost of CCSD is already very demanding and scales as $\mathcal{O}(N^6)$. Going beyond CCSD and including third order excitations within CCSDT (the "T" here stands for triples) would make the theory scale as $\mathcal{O}(N^8)$. Although the CC theory in all its variants is a very accurate method [78], one can easily see that the computational cost grows extremely fast with the configuration-space i.e., the size of the wave function. This implies that CC is restricted to small systems in the size of small molecules and has only recently been extended to periodic systems [79]. It is then legitimate to think that a theory that depends less, or in another way, on the electronic wave function would be helpful to assess larger systems. In the next chapter I introduce density functional theory, which is the established method for treating realistic systems.

Chapter 2

Kohn-Sham Density Functional Theory

In the previous chapter I have introduced some basic concepts, that are useful for understanding processes related to the many-body nature of condensed matter systems. The relation between the computational scaling and the configuration-space of so-called wave-function based methods was discussed in the last section of Chapter 1. The usefulness of these concepts resides in their ability to capture electronic correlations in a reasonable manner. However, despite the fact, that these methods have, in many cases, proven to be very accurate, their high computational cost limits their applicability to extended systems. The main reason for the high computational cost is the large, configuration-space needed to describe the correlations at the level of these theories. A scheme, that has proven to be very efficient in describing large, realistic systems is Kohn-Sham density functional theory (DFT) [80, 81]. It has been developed, as its name suggests, by Walter Kohn and Lu J. Sham in the 1960s and has become the most widely used quantum-theoretical method for real materials. Its main advantage is that it allows a formulation of the many-body problem, represented by the many-body Schrödinger equation, as a single particle Schrödinger equation. In this new Schrödinger equation all quantities become functionals of the electronic density. The one-to-one connection between the electronic density and the potentials is established by the Hohenberg-Kohn theorems [80] building the mathematical foundation of Kohn-Sham DFT. First in this chapter, I will present Kohn-Sham DFT as a direct result of the Hohenberg-Kohn theorems before I discuss the different approaches to approximate the exchange-correlaton functional. Finally, I will introduce the Sham-Schlüter equation [5] that allows a connection of DFT and many-body schemes and show how the many-body schemes such as the random-phase approximation (RPA), described in the previous chapter, can be used to improve upon DFT.

2.1 The Hohenberg-Kohn theorem

Let us start with the electronic Hamiltonian Eq. (1.4). Discarding the Coulomb interaction between the nuclei, i.e. V_{nn}, one can write the N-electron Hamiltonian

as

$$\hat{H} = \hat{T} + \hat{V}_{ext} + \hat{V}_{ee}. \tag{2.1}$$

The Schrödinger equation corresponding to this Hamiltonian is

$$\hat{H}\psi_n = \epsilon_n \psi_n, \tag{2.2}$$

where $\epsilon_0 < \epsilon_1 < ...$ are the eigenvalues of the many-electron problem. The density related to a particular eigenstate is given by

$$n(\mathbf{r}) = \langle \psi(\mathbf{r}_1, ..., \mathbf{r}_N) | \sum_i \delta(\mathbf{r}_i - \mathbf{r}) | \psi(\mathbf{r}_1, ..., \mathbf{r}_N) \rangle. \tag{2.3}$$

I am now going to present the so called Hohenberg-Kohn (HK) theorems [80], that are the basis of the Kohn-Sham density functional formalism. I do this without any proof and refer the reader to the book by Dreizler and Gross [82]. The main motivation of the HK theorems is to answer the key question of whether two different external potentials $\hat{V}^1_{ext}$ and $\hat{V}^2_{ext}$ can yield two different ground state densities. In a more mathematical language, if one considers the mappings F and $\tilde{F}$ with

$$\begin{aligned} F &: \hat{V}_{ext}(\mathbf{r}) \longmapsto \psi \\ \tilde{F} &: \psi \longmapsto n(\mathbf{r}) \end{aligned} \tag{2.4}$$

and the mapping G

$$F \circ \tilde{F} \equiv G : \hat{V}_{ext}(\mathbf{r}) \longmapsto n(\mathbf{r}), \tag{2.5}$$

which can be depicted as in Figure (2.1), is G an injective (a one-to-one) mapping?

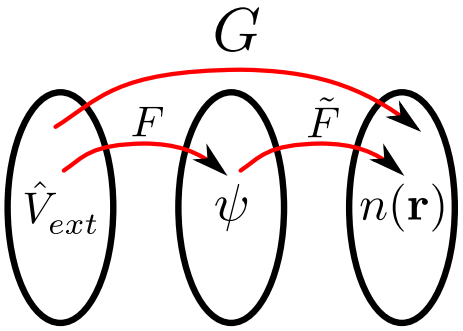

Figure 2.1: Schematic drawing showing the mapping of the external potential into the electronic density $n(\mathbf{r})$

The proof of the injectivity of G [82] implies that different external potentials always lead to different ground state densities. Additionally, from the proof that G is reversible follows that the ground state density $n(\mathbf{r})$ uniquely determines the external potential $\hat{V}_{ext}(\mathbf{r})$ (up to a constant). So, the first of the two HK theorems states:

"The external potential $\hat{V}_{ext}$ is determined, within a trivial additive constant, uniquely by the electron density $n(\mathbf{r})$".

The essence of the **the second** HK theorem is, that

"the exact ground state density $n_0(\mathbf{r})$ can be determined by minimizing the functional "

$$\begin{aligned} E[n] &= \langle\psi_0[n]|\hat{T} + \hat{V}^0_{ext} + \hat{V}_{ee}|\psi_0[n]\rangle \\ E_0 &= \min_{n\neq 0} E[n], \end{aligned}$$

with $\hat{V}^0_{ext}$ being the external potential and $\hat{V}_{ee}$ the electron-electron interaction of a specific system with ground states density $n_0(\mathbf{r})$ and ground state total energy E_0".

The HK theorems set the stage for the development of a set of equations that define the Kohn-Sham density functional scheme.

2.2 The Kohn-Sham equations

As mentioned above, the HK theorems have far reaching consequences. To show what exactly is meant by that, is the main purpose of this section. Let us consider an auxiliary non-interacting (NI) system described by the Hamiltonian

$$\hat{H}^{NI} = \hat{T}^{NI} + \hat{V}_{eff}, \tag{2.6}$$

with the effective potential $\hat{V}_{eff}$. Thus, according to the HK theorems, there exists a unique energy functional

$$E^{NI}[n] = \hat{T}^{NI}[n] + \int d\mathbf{r} n(\mathbf{r})\hat{V}_{eff}(\mathbf{r}), \tag{2.7}$$

so that the variational equation

$$\delta E^{NI}[n] = 0 \tag{2.8}$$

yields the ground state density $n^{NI}(\mathbf{r})$ that corresponds to $\hat{H}^{NI}$.
The key assumption while establishing the Kohn-Sham density functional scheme is considering that

"for any interacting system there exists a non-interacting system with local single-particle effective potential $\hat{V}_{eff}$, such that the exact ground state density $n_0(\mathbf{r})$ of the interacting system equals the ground state density of the auxiliary one"

$$n_0(\mathbf{r}) = n_{NI}(\mathbf{r}). \tag{2.9}$$

The trick is, one can easily calculate the non-interacting electron density $n_{NI}(\mathbf{r})$ of $\hat{H}^{NI}$ using

$$\begin{aligned} n_{NI}(\mathbf{r}) &= \sum_{i}^{occ.} |\psi_i(\mathbf{r})|^2 \\ \left(\hat{T}^{NI}(\mathbf{r}) + \hat{V}_{eff}(\mathbf{r})\right)\psi_i(\mathbf{r}) &= \epsilon_i \psi_i(\mathbf{r}), \end{aligned} \tag{2.10}$$

with the ground state single particle energies ϵ_i.
Following the first HK theorem, $\hat{V}_{eff}(\mathbf{r})$ exists and is a unique functional of the electronic density. From Eq. (2.9) it becomes clear that the single particle orbitals, $\hat{V}_{eff}(\mathbf{r})$ and the kinetic part $\hat{T}^{NI}(\mathbf{r})$ are also unique functionals of the density $n_0(\mathbf{r})$. However, one is usually not interested in the non-interacting case but in the interacting one. Thus, for an interacting system with external potential $\hat{V}_{ext}(\mathbf{r})$ and ground state density $n_0(\mathbf{r})$, the $\hat{V}_{eff}(\mathbf{r})$ that generates $n_0(\mathbf{r})$ can be determined by

$$\begin{aligned} n_0(\mathbf{r}) &= \sum_{i}^{occ.} |\psi_{i,0}(\mathbf{r})|^2 \\ \left(\hat{T}^{NI}(\mathbf{r}) + \hat{V}_{eff}(\mathbf{r})\right)\psi_{i,0}(\mathbf{r}) &= \epsilon_i \psi_{i,0}(\mathbf{r}). \end{aligned} \tag{2.11}$$

While the corresponding energy functional is the following

$$E_0[n] = \langle\psi_0|\hat{T} + \hat{V}_{ee}|\psi_0\rangle + \int d\mathbf{r} n(\mathbf{r})\hat{V}_{ext}(\mathbf{r}). \tag{2.12}$$

If now one adds and subtracts the expression

$$\hat{T}^{NI}[n] + \frac{1}{2}\int d\mathbf{r}d\mathbf{r}' n(\mathbf{r})v(\mathbf{r}-\mathbf{r}')n(\mathbf{r}'), \tag{2.13}$$

where $v(\mathbf{r}-\mathbf{r}')$ is the Coulomb interaction. One can redefine

$$E_0[n] = \hat{T}^{NI}[n] + \int d\mathbf{r} n(\mathbf{r})\hat{V}_{ext}(\mathbf{r}) + \frac{1}{2}\int d\mathbf{r}d\mathbf{r}' n(\mathbf{r})v(\mathbf{r}-\mathbf{r}')n(\mathbf{r}') + E_{\mathrm{XC}}[n]. \tag{2.14}$$

The new last term defined as

$$E_{\mathrm{XC}}[n] = \langle\psi_0|\hat{T} + \hat{V}_{ee}|\psi_0\rangle - \frac{1}{2}\int d\mathbf{r}d\mathbf{r}' n(\mathbf{r})v(\mathbf{r}-\mathbf{r}')n(\mathbf{r}') - \hat{T}^{NI}[n], \tag{2.15}$$

is the so called exchange-correlation energy functional, where the first term corresponds to the contributions from the kinetic and Coulomb potentials for the interacting system, the second term is the corresponding Hartree contribution and the last term the kinetic contribution of the non-interacting system. Here it is worth mentioning, that the kinetic part $\hat{T}^{NI}[n]$ is not a "real" functional of the density since it contains the differential operator ∇, which make it a functional of the single particle orbitals.

The HK variational principle (second HK theorem) ensures that $E_0[n]$ is stationary for small variations around the minimum density $n_0(\mathbf{r})$, which means

$$\begin{aligned} 0 &= \delta E_0[n] = E_0[n_0+\delta n] - E_0[n_0] \\ &= \delta \hat{T}^{NI}[n] + \int d\mathbf{r}\delta n(\mathbf{r})\hat{V}_{ext}(\mathbf{r}) + \int d\mathbf{r}d\mathbf{r}'\delta n(\mathbf{r})v(\mathbf{r}-\mathbf{r}')n(\mathbf{r}') \\ &\quad + \int d\mathbf{r}\hat{V}_{\mathrm{XC}}([n_0];\mathbf{r})\delta n(\mathbf{r}), \end{aligned} \tag{2.16}$$

with the exchange-correlation potential

$$\hat{V}_{\mathrm{XC}}([n_0];\mathbf{r}) = \frac{\delta E_{\mathrm{XC}}[n]}{\delta n(\mathbf{r})}|_{n=n_0} \tag{2.17}$$

Hence, as is explained in [82], performing the minimization with respect to the electron density yields for the kinetic energy term $\delta T^{NI} = -\int d\mathbf{r}\hat{V}_{eff}(\mathbf{r})\delta n(\mathbf{r})$, so that one has for the minimizing effective potential

$$\begin{aligned} \hat{V}_{eff}(\mathbf{r}) &= \hat{V}_{ext}(\mathbf{r}) + \int d\mathbf{r}' v(\mathbf{r}-\mathbf{r}')n(\mathbf{r}') + \hat{V}_{\mathrm{XC}}(\mathbf{r}) \\ &= \hat{V}_{ext}(\mathbf{r}) + \hat{V}_H(\mathbf{r}) + \hat{V}_{\mathrm{XC}}(\mathbf{r}), \end{aligned} \tag{2.18}$$

with the Hartree potential $\hat{V}_H(\mathbf{r})$. Eqs. (2.11) together with (2.17) and (2.19) define the so called **Kohn-Sham theorem:** it can be formulated as follows

> *The exact ground state density $n_0(\boldsymbol{r})$ of an arbitrary interacting system can be obtained by the self-consistent solution of the set of equations*
>
> $$\begin{aligned} n_0(\mathbf{r}) &= \sum_i^{occ.} |\psi_{i,0}(\mathbf{r})|^2, \\ \left[-\frac{\hbar^2}{2m}\nabla^2 + \hat{V}_{ext}(\mathbf{r}) + \hat{V}_H(\mathbf{r}) + \hat{V}_{\mathrm{XC}}(\mathbf{r})\right]\psi_{i,0}(\mathbf{r}) &= \epsilon_i\psi_{i,0}(\mathbf{r}), \end{aligned} \tag{2.19}$$
>
> *with $\epsilon_0 \leq \epsilon_1 \leq \ldots$ and the exchange-correlation potential $\hat{V}_{\mathrm{XC}}(\boldsymbol{r})$ as given by Eq. (2.17).*

It should be pointed out here, that compared to the Hartree-Fock equations, the Kohn-Sham equations in (2.19) represent a local scheme that does not include the exact exchange potential. Instead, exchange and correlation effects are encoded in the multiplicative exchange-correlation potential $\hat{V}_{\mathrm{XC}}(\mathbf{r})$. Moreover, one can obtain from Kohn-Sham theory excited state energies in terms of energy differences. In Hartree-Fock theory, Koopmans' theorem [83] establishes a relation between the Hartree-Fock eigenvalues ϵ_i and the total energy difference between an N-particle ground state and an $N-1$-particle ground state related to the energy needed to remove a particle in state i as

$$\epsilon_i^{HF} = E_{HF}[N] - E_{HF}[N-1_i], \tag{2.20}$$

provided the system remains otherwise unperturbed. An equivalent theorem for Kohn-Sham eigenvalues can be formulated within the so called Janak's theorem [84]: For a Kohn-Sham Hamiltonian $H^{\gamma}\psi_i(\mathbf{r}) = \epsilon_i(\gamma)\psi_i(\mathbf{r})$ with the ground state density $n(\mathbf{r}) = \sum_i^{occ.} \gamma_i |\psi_i(\mathbf{r})|^2$, the Kohn-Sham eigenvalues are proportional to the differential change of the ground state total energy with respect to the fractional occupancies γ_i

$$\epsilon_i(\gamma) = \frac{\partial E(\{\gamma\})}{\partial \gamma_i}. \tag{2.21}$$

The excitation energy $\Delta E(\gamma_i)$ corresponding to the occupation number γ_i is then approximately given by [82]

$$\Delta E(\gamma_i) = E(\gamma_i) - E(\gamma_0), \tag{2.22}$$

and requires two self-consistent calculations, one with occupancy γ_i yielding the total energy $E(\gamma_i)$ and the other with the ground state occupancy γ_0 yielding the total energy $E(\gamma_0)$.
Until now the exchange-correlation potential $\hat{V}_{\mathrm{XC}}(\mathbf{r})$ in Eq. (2.19) remains a mysterious quantity that I have not talked about yet. Thus, Eq. (2.19) is up to now exact but unfortunately, to be able to apply the Kohn-Sham scheme to realistic systems, approximations to $\hat{V}_{\mathrm{XC}}(\mathbf{r})$ have to be made. In the next section I will present the most famous (and also the first) attempt to approach this key quantity, the so called local-density approximation.

2.3 Local and semi-local approximations

The first and at the same time a broadly used approach to evaluate the exchange-correlation potential $\hat{V}_{\mathrm{XC}}(\mathbf{r})$ is to assume a slowly varying electronic density. This assumption may, at first glance, seem unreasonable for atoms and molecules, but is quite plausible for extended systems such as periodic systems, since there the density varies slowly in space (however, in the extreme vicinity of the nuclei, the density still varies quit significantly). This is the main idea behind what is known as the local-density approximation (LDA). In LDA the system is locally approximated as a homogeneous electron gas:

$$E_{\mathrm{XC}}^{\mathrm{LDA}}[n] = \int d\mathbf{r} n(\mathbf{r}) \epsilon_{\mathrm{XC}}^{hom}(\bar{n})|_{\bar{n}=n(\mathbf{r})}, \tag{2.23}$$

with $\epsilon_{\mathrm{XC}}^{hom}(\bar{n})$ being the exchange-correlation energy per particle in the homogeneous system at a constant density $\bar{n}$ given by $\bar{n} = \frac{N}{\Omega}$ for an N-electron system with volume Ω. For the homogeneous electron gas, the form of the exchange part is known analytically [85] and is given by

$$E_{\mathrm{X}}^{\mathrm{LDA}}[n] = -\frac{3}{4}\left(\frac{3}{\pi}\right)^{\frac{1}{3}} \int d\mathbf{r} n(\mathbf{r})^{\frac{4}{3}}. \tag{2.24}$$

The correlation contribution, however, cannot be obtained in analytically and has to be parametrized. Different parameterizations of $\epsilon_{\mathrm{C}}^{hom}$ have been proposed by Perdew and Zunger [1], Perdew and Wang [86] or Vosko, Wilk and Nusair [87]. The LDA exchange-correlation potential is then calculated from $E_{\mathrm{XC}}^{\mathrm{LDA}}$ as

$$\hat{V}_{\mathrm{XC}}^{\mathrm{LDA}}(\mathbf{r}) = \frac{\delta E_{\mathrm{XC}}^{\mathrm{LDA}}[n]}{\delta n(\mathbf{r})}. \tag{2.25}$$

LDA involves the most simple approximations and one would intuitively expect, that LDA is not sufficient enough to describe a lot of systems. However, it has been shown, that it is surprisingly accurate for a multitude of systems where the theory is expected to fail [88, 89]. Even for molecules or atoms it gives reasonable results that are, most of the time, at least of qualitative predictive power [88]. A reason for this unexpected success of LDA lies in its averaged description of the so called exchange hole leading to a sufficiently good approximation to the exchange-correlation energy. An extended and clear discussion of this matter can be found in Ref. [82]. From a quantitative point of view however, it has been shown that LDA has a tendency to overestimate the cohesive energies by $\sim 15-20\%$ while it underestimates lattice constants by $\sim 2-3\%$ especially for metals and insulators [89, 90, 91].
There have been several attempts to improve upon LDA by incorporating some "inhomogeneity". One way of doing this is by accounting for the spin degree of freedom, in the frame of what has been known as local-spin density approximation (LSDA). In the LSDA the density is spin dependent making the exchange-correlation energy functional dependent on the spin-up ($n^{\uparrow}$) and spin-down ($n^{\downarrow}$) densities

$$E_{\mathrm{XC}}^{\mathrm{LSDA}}[n^{\uparrow}, n^{\downarrow}] = \int d\mathbf{r} n(\mathbf{r}) \epsilon_{\mathrm{XC}}(n^{\uparrow}, n^{\downarrow}), \tag{2.26}$$

where $n(\mathbf{r}) = n^{\uparrow}(\mathbf{r}) + n^{\downarrow}(\mathbf{r})$.
Furthermore, one can add the gradient of the density within what is commonly called the generalized gradient approximation (GGA)[92]. The GGA exchange-correlation energy functional is given by[92]

$$E_{\mathrm{XC}}^{\mathrm{GGA}}[n^{\uparrow}, n^{\downarrow}] = \int d\mathbf{r} f(n^{\uparrow}, n^{\downarrow}, \nabla n^{\uparrow}, \nabla n^{\downarrow}). \tag{2.27}$$

$f(n^{\uparrow}, n^{\downarrow}, \nabla n^{\uparrow}, \nabla n^{\downarrow})$, is an analytic function that needs to be parametrized. The most widely used parametrization of f was performed by Perdew, Burke and Ernzerhof [93] leading to an exchange-correlation functional known as the PBE functional. Many other GGA functionals have also been developed [92, 94, 86, 95, 96, 97, 98, 99, 100, 101, 102] such as the empirically parametrized BLYP functional [103, 104] all with different performances compared to LDA [105, 106].

2.4 Hybrid functionals

It has been shown that the thermochemical data obtained from L(S)DA/GGAs can be improved if one adds a fraction of HF exact exchange [107, 108, 109, 110]

giving rise to a hole new rung of functionals called hybrid functionals. From a DFT calculation one obtains Kohn-Sham orbitals building up a unique Slater determinant Ψ_0. In principle a HF exact exchange functional can be defined as

$$E_{\mathrm{EXX}} = \langle \Psi_0 | \hat{V}_{ee} | \Psi_0 \rangle - \frac{1}{2} \int d\mathbf{r}_1 d\mathbf{r}_2 \frac{n(\mathbf{r}_1) n(\mathbf{r}_2)}{|\mathbf{r}_1 - \mathbf{r}_2|}, \tag{2.28}$$

where $\hat{V}_{ee}$ is the electron-electron Coulomb repulsion.
Initially, Becke [111] motivated the construction of hybrid functionals using the adiabatic connection equation [96, 97, 7]

$$E_{\mathrm{XC}} = \int_0^1 d\lambda E_{\mathrm{XC}}(\lambda), \tag{2.29}$$

where $\lambda \in [0, 1]$ and

$$E_{\mathrm{XC}}(\lambda) = \langle \Psi_\lambda | \hat{V}_{ee} | \Psi_\lambda \rangle - \frac{1}{2} \int d\mathbf{r}_1 d\mathbf{r}_2 \frac{n(\mathbf{r}_1) n(\mathbf{r}_2)}{|\mathbf{r}_1 - \mathbf{r}_2|}, \tag{2.30}$$

with $E_{\mathrm{XC}}(\lambda = 0) = E_{\mathrm{EXX}}$ and $E_{\mathrm{XC}}(\lambda = 1) = E_{\mathrm{XC}}^{\mathrm{L(S)DA/GGA}}$. He then proposed what became known as the B3LYP functional [112]

$$E_{\mathrm{BLYP}} = E_{\mathrm{XC}}^{\mathrm{LSDA}} + a_0 (E_{\mathrm{EXX}} - E_{\mathrm{X}}^{\mathrm{LSDA}}) + a_x (E_{\mathrm{X}}^{\mathrm{GGA}} - E_{\mathrm{X}}^{\mathrm{LSDA}}) + a_c (E_{\mathrm{C}}^{\mathrm{GGA}} - E_{\mathrm{C}}^{\mathrm{LSDA}}). \tag{2.31}$$

Here a_0, a_x and a_c are fitted to experimental data. The B3LYP functional has gained a large popularity especially among quantum chemists.
To get rid of the empirically determined parameters Perdew and co-workers [113] developed a functional that contains a fixed fraction α of exact exchange

$$E_{\mathrm{XC}}^{\mathrm{PBE0}} = \alpha E_{\mathrm{X}} + (1 - \alpha) E_{\mathrm{X}}^{\mathrm{PBE}} + E_{\mathrm{C}}^{\mathrm{PBE}}, \text{with } \alpha = \frac{1}{4}. \tag{2.32}$$

This functional became famous under the name of PBE0 [114].
They justified the value of α by considering that the fourth order in perturbation theory is sufficient to produce accurate results for molecules. Adding this fraction of exact exchange indeed improved upon L(S)DA/GGAs in a quite significant manner [113, 115]. Another motivation for considering the HF exact exchange is the so called self-interaction error in the approximated XC density functionals. It occurs when calculating the Hartree energy, given by

$$E_H[n] = \frac{1}{2} \int \int d\mathbf{r}_1 d\mathbf{r}_2 \frac{n(\mathbf{r}_1) n(\mathbf{r}_2)}{|\mathbf{r}_1 - \mathbf{r}_2|}. \tag{2.33}$$

In the case of a one electron system this term would not cancel for L(S)DA/GGAs, which is wrong, since an electron should not interact with itself. In Hartree-Fock theory, the exact exchange part (i.e. Fock part) of the Hamiltonian would correct this by cancellation of the self-interaction. Hence, including a fraction of exact exchange would correct "some" of the self-interaction error.

For periodic systems, on the other hand, the calculation of the exact exchange contribution entering the PBE0 functional turns out to be a numerical bottle-neck that slows down the calculation dramatically. The introduction of range separated functionals provided a solution. The so called Heyd-Scuseria-Ernzerhof (short HSE) functional by Heyd, Scuseria, and Ernzerhof [116] is the most famous [114] range separated functionals and it is constructed by splitting the Coulomb interaction into a short-range (SR) and a long-range (LR) component

$$\frac{1}{|\mathbf{r}-\mathbf{r}'|} = \frac{\mathrm{erfc}(\omega|\mathbf{r}-\mathbf{r}'|)}{|\mathbf{r}-\mathbf{r}'|} + \frac{\mathrm{erf}(\omega|\mathbf{r}-\mathbf{r}'|)}{|\mathbf{r}-\mathbf{r}'|}, \tag{2.34}$$

using the error function $\mathrm{erf}(\omega|\mathbf{r}-\mathbf{r}'|)$ where ω is a numerical parameter that can be adjusted and $\mathrm{erfc}(\omega|\mathbf{r}-\mathbf{r}'|) = 1 - \mathrm{erf}(\omega|\mathbf{r}-\mathbf{r}'|)$. The HSE exchange-correlation functional is then given by

$$\begin{aligned} E_{\mathrm{XC}}^{\mathrm{HSE}} &= \alpha E_{\mathrm{X}}^{\mathrm{HF,\,SR}}(\omega) + (1-\alpha)E_{\mathrm{X}}^{\mathrm{PBE,\,SR}}(\omega) \\ &\quad + E_{\mathrm{X}}^{\mathrm{PBE,\,LR}}(\omega) + E_{\mathrm{C}}^{\mathrm{PBE}}. \end{aligned} \tag{2.35}$$

In fact, by "cutting" the long reaching tail of the Coulomb potential not only improved on the efficiency of the calculation but also has proven to correct upon PBE0, resulting in a better agreement with experiments, as was found for band gaps and binding energies (see Ref. [116] for details).

2.5 Connecting DFT and many-body perturbation theory - The Sham-Schlüter equation

Despite the success of DFT in describing a multitude of systems and its ability to efficiently describe extended systems, the appeal of high level many-body methods based on standard many-body perturbation theory techniques remains omnipresent. This is mainly because many-body methods enable the improvement of accuracy in a systematic and tractable way yielding the inclusion of features that are, while absent in approximated DFT functionals, of high importance when describing condensed matter systems. Dynamical screening or vertex corrections in the RPA or Hedin's equations mentioned in the first chapter of this manuscript, for example, are established and well understood many-body concepts that one would like to merge with the DFT way of performing electronic structure calculations. Additionally, *GW* and related methods are able to accurately describe spectral properties since they include excitations in a natural way. Thus, a connection between both theories is of high interest. The Sham-Schlüter equation [5] establishes the connection between the Kohn-Sham exchange correlation potential $\hat{V}_{\mathrm{XC}}(\mathbf{r})$ and the irreducible self-energy via the one particle Green's function. Starting with the following Dyson equation for the one particle Green's function G

$$G = G_{KS} + G_{KS}\tilde{\Sigma}G, \tag{2.36}$$

where I have defined

$$\tilde{\Sigma}(\mathbf{r},\mathbf{r}';\omega) \equiv \Sigma_{\mathrm{XC}}(\mathbf{r},\mathbf{r}';\omega) - \delta(\mathbf{r}-\mathbf{r}')\hat{V}_{\mathrm{XC}}(\mathbf{r}), \tag{2.37}$$

with exchange and correlation self-energy at a given level of many-body theory, Σ_{XC} and the Kohn-Sham Green's function G_{KS} corresponding to the Kohn-Sham Hamiltonian

$$h_{KS}(\mathbf{r}) = -\frac{\hbar^2}{2m}\nabla^2 + \hat{V}_{ext}(\mathbf{r}) + \hat{V}_H(\mathbf{r}) + \hat{V}_{\text{XC}}(\mathbf{r}), \tag{2.38}$$

so that $(\omega - h_{KS})G_{KS} = 1$. The density $n(\mathbf{r})$ is related to the diagonal part of the Green's function via

$$n(\mathbf{r}) = -i\int \frac{d\omega}{2\pi} \lim_{\mathbf{r}'\longrightarrow\mathbf{r}} G(\mathbf{r},\mathbf{r}';\omega)e^{i0^+}. \tag{2.39}$$

It is then straightforward to derive the Sham-Schlüter equation if one considers the Kohn-Sham condition that same external potentials yield the same density

$$n(\mathbf{r}) = n_{KS}(\mathbf{r}) = -i\int \frac{d\omega}{2\pi} \lim_{\mathbf{r}'\longrightarrow\mathbf{r}} G_{KS}(\mathbf{r},\mathbf{r}';\omega)e^{i0^+}. \tag{2.40}$$

Performing a frequency integration over the Dyson equation (2.36) and using the definition of the self-energy equation (2.37) one readily obtains the Sham-Schlüter equation

$$\begin{aligned}\int d\mathbf{r}'\hat{V}_{\text{XC}}(\mathbf{r})\int d\omega G_{KS}(\mathbf{r},\mathbf{r}';\omega)G(\mathbf{r}',\mathbf{r};\omega) = \\ \int d\mathbf{r}'\int d\mathbf{r}''\int d\omega G_{KS}(\mathbf{r},\mathbf{r}';\omega)\tilde{\Sigma}(\mathbf{r}',\mathbf{r}'';\omega)G(\mathbf{r}'',\mathbf{r};\omega).\end{aligned} \tag{2.41}$$

The corresponding exchange-correlation energy functional is expressed by [117]

$$E_{\text{XC}}[n] = i\text{Tr}\{\ln(1-\tilde{\Sigma}G_{KS}) + \tilde{\Sigma}G\} - i\Phi_{\text{XC}}[n], \tag{2.42}$$

where $\Phi_{\text{XC}}[n]$ represents the sum over all the skeleton diagrams, so that a functional derivative of Eq. (2.42) would yield Eq. (2.41) [82]. The Sham-Schlüter equation was first solved by Godby *et al.* for a *GW* self- energy [118] and tested on the solids Si, GaAs, A1As, and diamond.

2.6 RPA exchange-correlation energy in a DFT framework

The efficiency of DFT functionals due to their reasonable computational scaling, led DFT based approaches to become the methods of choice in chemistry and materials science [114]. On the other hand, the high computational cost of wave-function based approaches such as RPA, mainly due to the dependence on the unoccupied states, reduces there appeal for applications in quantum chemistry and materials science. There have been many attempts to implement RPA, the earliest implementation by Furche [119] had a scaling of $\mathcal{O}(N^6)$ with respect to system size. The use of different techniques (e.g. the resolution of identity (RI) [120] or the plasmon-pole formulation [121]) can reduce the computational costs to $\mathcal{O}(N^4)$ [122, 121]. Recently, an implementation that scales as $\mathcal{O}(N^3)$ has been reported [123]. Hence, the rapid

increase of computer power in the last years, together with the growing interest in the quantum chemistry and materials science community to reduce the scaling of this method with respect to system size, foresee a promising future for RPA. In this section I turn to the formulation of RPA within the Kohn-Sham DFT framework, derived using the adiabatic connection fluctuation dissipation theorem, see Ren *et al.* [124] for details. The RPA correlation energy is then given by [124]

$$E_{\mathrm{C}}^{\mathrm{RPA}} = \frac{1}{2}\int_0^\infty d\omega \mathrm{Tr}[\ln(1-\chi^0(i\omega)v) + \chi^0(i\omega)v] \tag{2.43}$$

with the bare Coulomb potential $v(\mathbf{r}-\mathbf{r}') = \frac{1}{|\mathbf{r}-\mathbf{r}'|}$. The response function $\chi^0(i\omega)$ is given by the Adler-Wieser formula [64, 65] Eq. (1.84). RPA is implemented in the localized numeric atom-centered orbitals code FHI-aims (Fritz-Haber-Institute *ab initio* molecular simulations) [41, 32, 125, 43], together with some beyond RPA schemes, such as RPA+, RPA+SOSEX and RPA+rSE, see Ren *et al.* for details [43, 126]. Figure (2.2), from Ren *et al.* [124], shows the mean absolute percentage errors (MAPEs) for the van-der Waals (vdW) bonded S22 set of molecules. In contrast to approximated DFT functionals, RPA is able to capture vdW interactions. Thus, the MAPEs of the RPA based methods are noticeably reduced compared to PBE or PBE0, see Fig.(2.2).

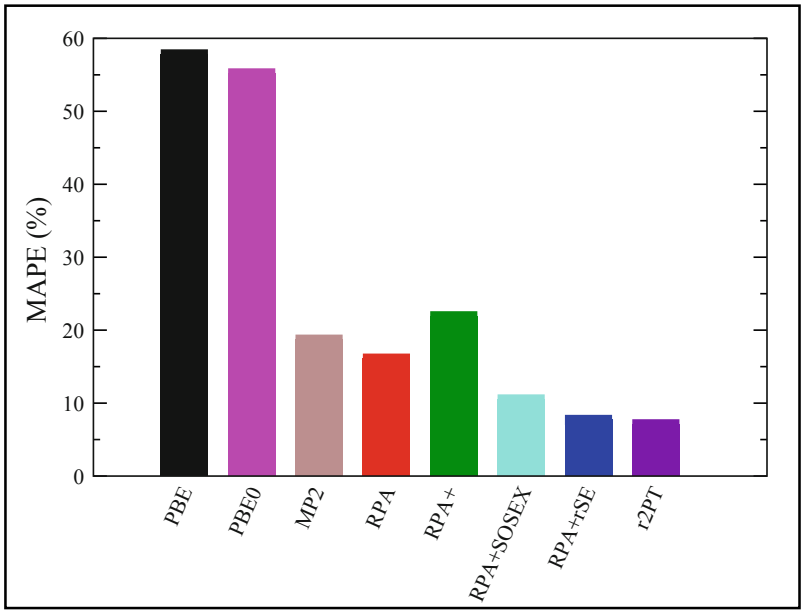

Figure 2.2: The MAPEs for atomization energies of the S22 test set with RPA-based methods. A comparison to PBE, PBE0 and MP2 is made. From Ren *et al.* [124]

2.7 Comparison to *GW*

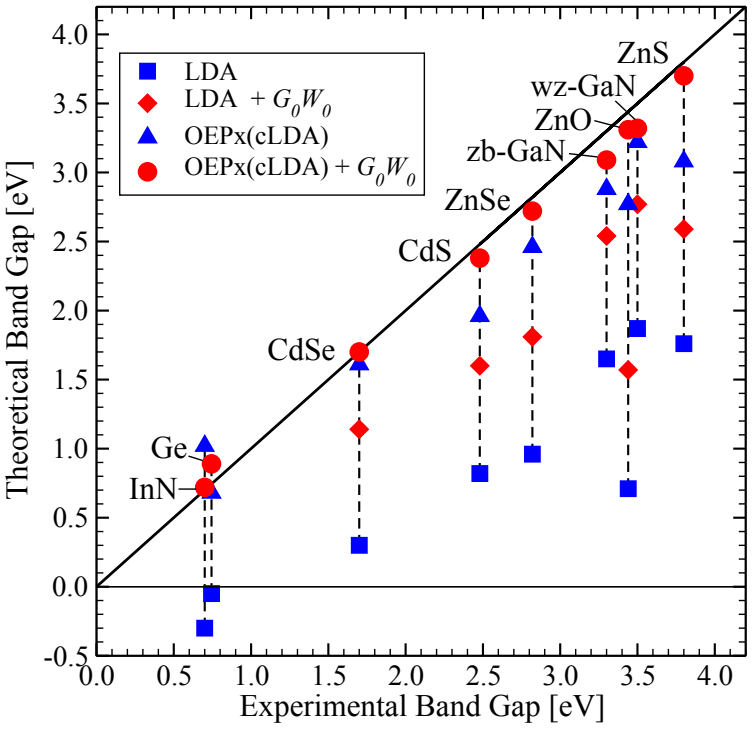

Figure 2.3: Experimental data compared to theoretical calculations. It shows a very good agreement with experiment for OEPx(cLDA)+G_0W_0 and an clear improvement upon LDA for LDA+G_0W_0. The theoretical values are not corrected by the electron-phonon coupling.

In Fig. (2.3), I report the comparison between experimental and theoretical band gaps for a set of nine representative semiconductors as presented in the work of Rinke *et al.* [67]. G_0W_0 improves upon LDA and exact-exchange optimised effective potential with LDA correlation (OEPx(cLDA)), by opening the band gap towards the experimental value.
However, the starting-point dependence of G_0W_0 and the aim to get a GW total energy, together with the improving computational power, some fully self-consistent GW (scGW) implementations for finite systems [60, 127] has emerged in the last years. There the total energy is calculated from the self-consistent Green's function $G(\omega)$ using the Galitskii-Migdal (GM)[128] formula

$$E_{\mathrm{GM}} = -i \int \frac{d\omega}{2\pi} \mathrm{Tr}[(\omega + h_0)G(\omega)]. \tag{2.44}$$

Here h_0 is the sum of the kinetic energy operator and the external potential. Figure (2.4) shows the GM total energy for a set of eleven small molecules, with configuration interaction calculations (CI) as reference. Compared to G_0W_0@HF and G_0W_0@PBE total energies (also computed using E_{GM}) the scGW total energies lie reasonably close to the CI values and do not show starting-point dependence. A

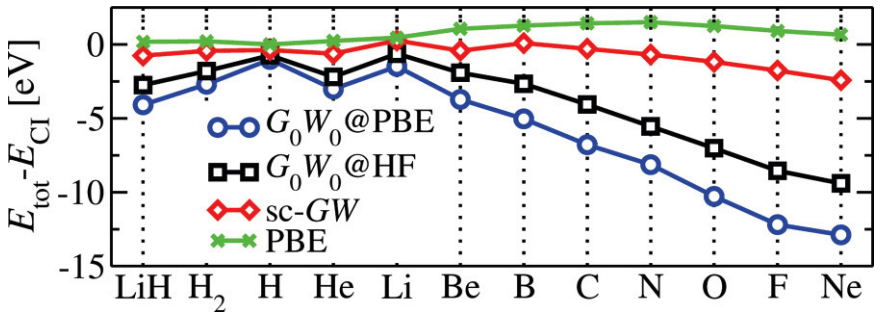

Figure 2.4: Galitskii-Migdal total energies referenced at full CI values E_{CI} for scGW, G_0W_0@HF, G_0W_0@PBE and PBE total energy for comparison. From Caruso *et al.* [127].

more detailed discussion of the scGW implementation in FHI-aims will be given in Chapter 4.

Chapter 3

Embedding Schemes and the Dynamical Mean-Field Theory

One of the main virtues of DFT with its LDA/GGAs functionals is its applicability to large systems. It is the method of choice for the simulation of realistic systems (∼2000 atoms) [129]. State of the art codes [41] allow a linear scaling with system size. Conversely, the aim to treat systems where electronic correlations become more important, such as systems with d- or f-electrons, in a more accurate way has driven people to go back to computationally more demanding theories such as, GW, RPA or even to wave-function based methods such as the full configuration interaction or the coupled cluster method [79], that are able to capture correlation effects at a high level of accuracy. These methods, however, scale at least cubically [123] with system size and are thus limited to small systems, which reduces their attractiveness to real system applications. Hence, one can imagine that a perfect theory would be one that is at the same time efficiently applicable to large systems and provides high accuracy. This conundrum between efficiency and accuracy has given rise to the concept of embedding. Embedding relies on the idea of dividing the system under consideration in two parts: the embedded system (region (I)) and the embedding surrounding (region (II)) where region (II) is treated in a more approximated manner than region (I) (see the schematic picture in Fig. (3.1)). This divide-and-conquer approach should, in an ideal case, allow an extraction of all the "good" features of the embedded region (region (I)) into the embedding surrounding (region (II)).

Many different embedding schemes have been developed in the past [34, 24, 26, 29, 23, 28, 22, 33, 31, 32, 27, 35]. I would like here to present some prominent representatives. This chapter consists of two sections. In the first one I discuss some established embedding schemes for *ab initio* theories, while in the second I address the embedding concept within dynamical mean-field theory (DMFT). Here I first introduce DMFT equations and the related approximations and then briefly discuss "impurity solvers" and some examples for physical quantities where DMFT provides accurate results.

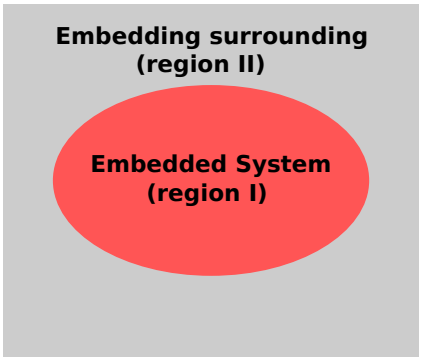

Figure 3.1: Cartoon depicting the embedding concept.

3.1 Conventional embedding schemes

In this section I am going to review some popular embedding approaches used to describe real systems in an *ab initio* way.

3.1.1 The ONIOM model

To overcome the high numerical costs of quantum mechanical (QM) methods with respect to molecular mechanical (MM) approaches, QM:MM embedding schemes were devised [23, 28]. Here the chemically interesting region i.e., region (I) in Fig. (3.1), is treated with QM methods (usually it is DFT), while the rest of the system i.e., region (II) is considered at the molecular mechanical level. The resulting embedding total energy formula is then defined as

$$E = E_{\mathrm{I}}^{\mathrm{high-level}} + E_{\mathrm{II}}^{\mathrm{low-level}} + E_{\mathrm{int}}, \tag{3.1}$$

where $E_{\mathrm{I}}^{\mathrm{high-level}}$ and $E_{\mathrm{II}}^{\mathrm{low-level}}$ are the energies of region (I) and (II) calculated at the high-level (i.e., QM) and low-level (i.e., MM) theory respectively. E_{int} models the interaction energy between the two regions. The challenges facing the QM:MM embedding approaches lie essentially in the way the boundary region (i.e., the region between (I) and (II)) is defined. For covalently bound systems the definition of an embedded region (I) leads to a braking of the saturated covalent bounds. These unsaturated bounds can make the QM calculation of $E_{\mathrm{I}}^{\mathrm{high-level}}$ problematic. Hence, the severed bounds should be saturated using link atoms. In practice any type of link atoms can be considered but usually H atoms are used. On the other hand, for systems where no covalent bounds are cut by the definition of region (I), such as for salvation processes, no saturation is needed. Thus, depending on the system under consideration, many QM:MM embedding schemes have been proposed [130, 131].
A characteristic difference between embedding schemes is the definition of the interaction energy E_{int}. A way to define it is by considering for region (II) a potential that includes at least one center in region (I) [132]. The interaction energy is then the difference between the resulting energy at the low-level theory and the one for region (II) with centers in region (II) only i.e., $E_{\mathrm{low-level}}^{\mathrm{II}}$.
To improve upon MM for the geometry optimization of molecules and include QM

corrections, Maseras and Morokuma [29] proposed a method that they named "our own N-layer integrated molecular orbital molecular mechanics" (ONIOM). In the ONIOM scheme the interaction energy is given by

$$E_{\text{int}} = E_{\text{I+II}}^{\text{low-level}} - (E_{\tilde{\text{I}}}^{\text{low-level}} + E_{\text{II}}^{\text{low-level}}), \tag{3.2}$$

where the subscript ($\tilde{\text{I}}$) stands for region (I) with the link atoms, $E_{\text{I+II}}^{\text{low-level}}$ is the energy of the full system and $E_{\tilde{\text{I}}}^{\text{low-level}}$ and $E_{\text{II}}^{\text{low-level}}$ the energies of region (I) and (II) respectively, all calculated at the low-level theory. Hence, substituting Eq. (3.2) into (3.1) for region (I) with the link atoms yields the ONIOM embedding total energy [132]

$$E_{\text{ONIOM}} = E_{\text{I+II}}^{\text{low-level}} - E_{\tilde{\text{I}}}^{\text{low-level}} + E_{\tilde{\text{I}}}^{\text{high-level}}, \tag{3.3}$$

where $E_{\tilde{\text{I}}}^{\text{high-level}}$ is the energy of region (I) with the link atoms at the high-level theory. Due to the link atoms, each component of the ONIOM total energy Eq. (3.3) can be calculated from a well-defined molecular system. The ONIOM scheme is hence a general approach and is not constrained to a given theory. In principle also a QM low-level theory for the treatment of region (II) can be used within ONIOM(QM:QM).
More recent works by Mayhall *et al.* [133] and Hratchian *et al.* [132] extended the ONIOM(QM:QM) to the electron embedding using Mulliken atomic point charges which allows the polarization of the high level wave function and thus leads to a better description of the charge-charge interaction region. For the low-level theory HF was used whereas Møller-Plesset perturbation theory [69] and the B3LYP functional [134, 104] were considered as high-level theory.

3.1.2 The shell embedded-cluster model

To properly describe solids with localized perturbations of the lattice periodicity, such as defects or adsorbates large supercells are required. This is mainly to eliminate the artificial interactions with periodic images and to reach convergence with respect to the supercell size in particular for charged systems.
To tackle this problem, Berger *et al.* [36] presented recently a QM:MM embedding approach for periodic systems based on the `ChemShell` framework [135, 136]. In this scheme the solid is modeled by a cluster of atoms with the periodicity of the solid under consideration (i.e., an embedded cluster model). This model is divided in multiple concentric regions (shells) as depicted in Fig. (3.2).
Moving further from the center of the cluster, each of these regions is described with more approximate methods. Hence the center is described with QM methods, while the MM region is divided into an inner "active" part, where atoms are allowed to relax and an outer "fixed" part where atoms are constrained to their lattice positions. The outer most shell is constituted of point charges that are fitted to mimic the full electrostatic embedding potential of an infinite bulk reference system [135, 136].
In the same spirit as the link atoms for the ONIOM embedding model, as I have discussed in the previous section, in solid-state embedding, the introduction of an intermediate shell at the QM boundary is necessary to avoid spurious charge transfer

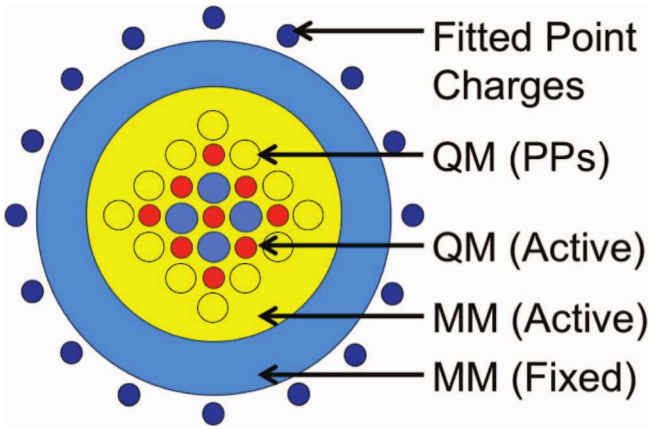

Figure 3.2: Cartoon picture depicting the embedded cluster model used in the QM:MM calculations. The QM central region (red and light blue circles) is treated most accurately. It is surrounded by a region of active (yellow) and a fixed (blue) MM atoms. For ionic systems, an additional embedding (yellow circles) is included in form of atom-centered PPs surrounding the QM region. The outer most shell of points (dark blue) represents the fitted potentials to reproduce the correct long-range electro-static potential of the periodic system. The figure is adapted from Berger *et al.* [36].

from the QM into the MM region. In practice, this is done by replacing all the cations in the intermediate shell by effective core potentials. To this end, Berger *et al.* [36] use norm-conserving pseudopotentials (PPs) of Kleinman-Bylander type [137]. Proceeding as such, the artificial overpolarization of the electronic density trough the neighboring positive MM charges is prohibited. Hence, spurious charge transfer into the MM region is suppressed.
The total energy of the embedded-cluster is then given by

$$E^{\text{tot}} = E^{\text{QM}} + E^{\text{MM}}, \tag{3.4}$$

where E^{MM} is the MM energy obtained from the `ChemShell` package and the E^{QM}, the QM energy, corresponding to a QM Hamiltonian $\hat{H}^{\text{QM}}$, is given by

$$E^{\text{QM}} = \langle \Psi | \hat{H}^{\text{QM}} + \hat{V}^{\text{PP}} + \hat{V}^{\text{MM}} | \Psi \rangle + E^{\text{QM}}_{\text{nuc}} + E^{\text{QM:MM}}_{\text{nuc}}, \tag{3.5}$$

with $\hat{V}^{\text{MM}}$ the fitted external MM embedding potential acting on Ψ, while $E^{\text{QM}}_{\text{nuc}}$ and $E^{\text{QM:MM}}_{\text{nuc}}$ describe the Coulomb interaction between QM nuclei only and between QM and MM nuclei respectively.
As QM calculator Berger *et al.* [36] used the FHI-aims package [41]. The performance of their approach was demonstrated using different functionals, such as PBE, BLYP, B3LYP, PBE0, HSE06 and the XYG3 [138] for the QM region, applied on two examples. The first one being the Fe reduction potential in Fe-substituted ZSM-5 zeolitic framework and the second was the calculation of the adsorption energies of in the water oxidation at defect-free $TiO_2(110)$. They could then confirm, for both cases, the importance of an appropriate description of long-range electrostatics captured by their embedding scheme.

3.1.3 The cluster extrapolation scheme

Addressing the problem of CO adsorption on Cu(111) [18], where the LDA/GGA predicts the wrong site preference (hollow site) compared to experiment (top site). See Fig. (3.3).

Hu, Reuter and Scheffler [31, 139] developed a cluster extrapolation scheme that is

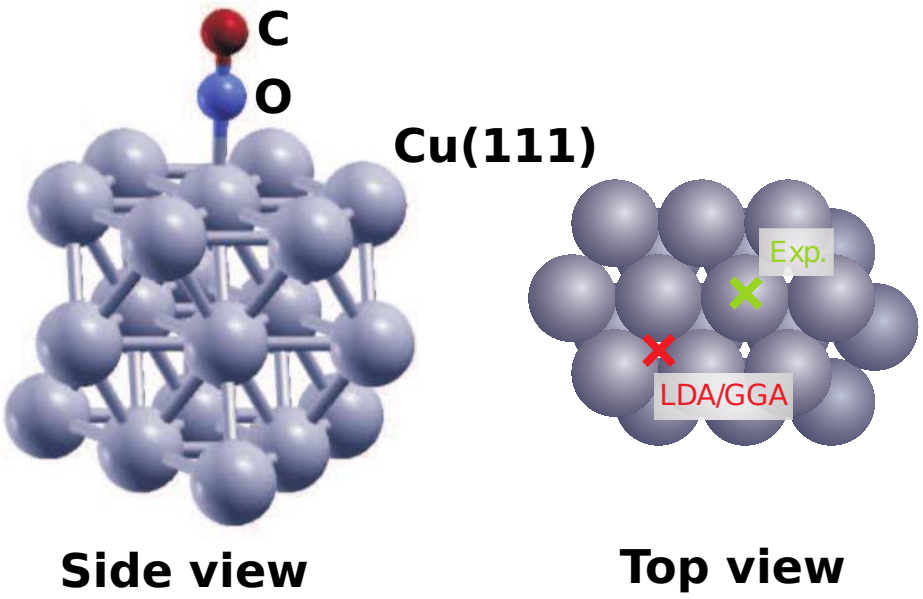

Figure 3.3: Schematic representation of the CO adsorption on a Cu(111) surface. On the top view (right hand side) the experimental site is indicated together with the LDA/GGA predicted one. The figure is a courtesy of Prof. Patrick Rinke.

based on performing a cheap (LDA/GGA) calculation for the periodic system then correcting the resulting total energy by

$$\Delta E_{\mathrm{XC}} = E_{\mathrm{XC}}^{\mathrm{cluster}}[\mathrm{LDA/GGA}] - E_{\mathrm{XC}}^{\mathrm{cluster}}[\text{“better”}], \tag{3.6}$$

where $E_{\mathrm{XC}}^{\mathrm{cluster}}[\mathrm{LDA/GGA}]$ and $E_{\mathrm{XC}}^{\mathrm{cluster}}[\text{“better”}]$ are the cluster XC-energy parts of a cluster calculation with the cheaper (LDA/GGA) and the ”better” theory respectively while the cluster itself is a supercell having the lattice periodicity of the periodic system. The resulting ”better“ total energy $E_{\mathrm{tot}}[E_{\mathrm{xc}}^{\mathrm{better}}]$ is then given by the sum of the LDA/GGA total energy of the periodic system and the correction ΔE_{XC} as

$$E_{\mathrm{tot}}[E_{\mathrm{xc}}^{\mathrm{better}}] = E_{\mathrm{tot}}[E_{\mathrm{xc}}^{\mathrm{LDA}}] + \lim_{\mathrm{cluster}\to\infty} \Delta E_{\mathrm{XC}}, \tag{3.7}$$

Increasing the cluster size, they could then show that the correction ΔE_{XC} converges for relatively small cluster sizes ($\sim$16 atoms) and thus much faster than if one would have considered $E_{\mathrm{XC}}^{\mathrm{cluster}}[\text{”better”}]$ alone in Eq. (3.6).

Using B3LYP and MP2 theories for the ”better“ E_{xc}, they could predict the right site preference for the CO molecule. Finally, it is worth mentioning that a main

difference between the Hu-Reuter-Scheffler [31, 139] cluster extrapolation concept and the ONIOM described above is that link atoms were not used for the cluster calculations.

3.1.4 The embedded cluster theory

Aiming to describe the adsorption of molecules on surfaces Whitten and co-workers [22, 140, 141] developed an embedding scheme that uses the fact that localized electrons/orbitals "exchange more". The surface is modeled by a symmetric cluster of atoms, where the embedded region (i.e., region (I)) constitutes a subspace of atoms within this cluster. Starting with the solution of a Hartree-Fock calculation for the model surface i.e., a single Slater determinant, a localization of the electronic orbitals is performed for region (I) of the system using the maximization of the exchange matrix element with respect to the substrate orbitals in the vicinity of the interaction region (i.e., adsorption region) as criterion. Whitten *et al.* defined the localized orbitals φ_i of region (I) as the ones with maximal exchange interaction with the orbitals ξ_k of region (II). Hence, the following exchange matrix element is to be extremized

$$\gamma_k = \sum_n \langle \varphi_k(\mathbf{r}_i)\varphi_k(\mathbf{r}_j)| \frac{1}{|\mathbf{r}_i - \mathbf{r}_j|} |\xi_n(\mathbf{r}_i)\xi_n(\mathbf{r}_j)\rangle \geq 0. \tag{3.8}$$

The set of delocalized orbitals $\Psi(\{\psi_k\})$ is related to the set of localized ones $\Phi(\{\varphi_k\})$ via the unitary transformation (that leaves the eigenvalue spectrum unchanged) as

$$\Phi(\{\varphi_k\}) = \mathbf{U}\Psi(\{\psi_k\}). \tag{3.9}$$

Thus, for an N electron system the extremal problem reduces to finding the coefficients c_k relating the localized states to the delocalized ones

$$\begin{aligned}
\gamma_1\colon\ \varphi_1 &= \sum_i c_k^1 \psi_k \\
&\vdots \\
\gamma_p\colon\ \varphi_p &= \sum_i c_k^p \psi_k \\
&\vdots \\
\gamma_N\colon\ \varphi_N &= \sum_i c_k^N \psi_k.
\end{aligned}$$

The localized orbitals can then be ordered with respect to their degree of localization as

$$\textbf{most localized}\ \gamma_1 \geq \gamma_2 \geq \ldots \geq \gamma_p \geq \ldots \geq \gamma_N\ \textbf{least localized}. \tag{3.10}$$

Going from point 1 to N the first orbitals are localized inside region (I) then for a given orbital p (with $p < N$), the electrons will be localized at the intermediate region between region (I) and (II). After this point, the orbitals will be mainly

localized in region (II). Overall, one obtains thus less electrons (i.e., $p < N$) in region (I). This hierarchical structure of the localized orbitals is the core idea of this embedding scheme. For the unoccupied states the same localization procedure can be undertaken.
The resulting localized orbitals are then used to construct an embedded Hamiltonian for the adsorbate-substrate system

$$H = -\sum_{i}^{N} \frac{\nabla_i^2}{2} - \sum_{i}^{N}\sum_{\nu}^{M} \frac{Z_\nu}{|\mathbf{r}_i - \mathbf{R}_\nu|} + \sum_{i<j}^{N} \frac{1}{|\mathbf{r}_i - \mathbf{r}_j|} + V^{\text{eff}}, \tag{3.11}$$

with the effective potential V^{eff}

$$\begin{aligned} V^{\text{eff}} = &\sum_{i}^{N} \frac{1}{|\mathbf{r}_i - \mathbf{r}_j|} |\rho(\mathbf{r}_i)\rangle \\ &+ \frac{1}{|\mathbf{r}_i - \mathbf{r}_j|} |\rho(\mathbf{r}_i, \mathbf{r}_j)\rangle \\ &+ \sum_{m} \lambda_m |Q_m\rangle\langle Q_m|, \end{aligned} \tag{3.12}$$

that includes the localized subspace (i.e., $\{\varphi_k, k = 1, \ldots, p\}$) via the density $\rho(\mathbf{r}_i) = \sum_{k}^{p} \varphi_k^*(\mathbf{r}_i)\varphi_k(\mathbf{r}_i)$ and the density matrix $\rho(\mathbf{r}_i, \mathbf{r}_j) = \sum_{k}^{p} \varphi_k^*(\mathbf{r}_i)\varphi_k(\mathbf{r}_j)$. The overlap between core and valence orbitals is treated using a pseudopotential for the valence electrons. This is done in the last term in Eq. (3.12), where $|Q_m\rangle$ are the auxiliary core basis functions introduced to orthogonalize the valence basis functions and λ_m the resulting coefficients. See Ref. [22] for details. The localization of the orbitals in the vicinity of the region of interest (region (I)) allows then to use of configuration interaction to solve the Shrödinger equation defined by the Hamiltonian Eq. (3.11). The method was successfully applied to describe the reaction of methane thiolate on Ni(111), where they could identify the site preference observed in experiment [141, 142].

3.1.5 Potential-functional embedding theory

In the potential-functional embedding scheme developed by Hang and Carter [33], the system is partitioned in two or more subsystems $\mathcal{S}$. The external potential of the total system is constructed as

$$v_{\text{ext}}^{\text{tot}}(\mathbf{r}) = \sum_{\mathcal{S}} v_{\text{ext}}^{\mathcal{S}}(\mathbf{r}). \tag{3.13}$$

Each subsystem is connected to the rest of the system by an embedding potential $u(\mathbf{r})$. This potential can be viewed as an additional external potential, whose role is essentially to replace the interaction between the subsystem and the rest of the system. Huang *et al.* [143] showed that $u(\mathbf{r})$ is unique under the constraint that all subsystems share the same embedding potential for a fixed electron number $N_{\mathcal{S}}$. For a given $u(\mathbf{r})$ and $N_{\mathcal{S}}$ the subsystem's electron density $\rho_{\mathcal{S}}$ can then be calculated

and hence the total density ρ_{tot} is given by $\rho_{\text{tot}} = \sum_{\mathcal{S}} \rho_{\mathcal{S}}$. The Hohenberg-Kohn theorem then guarantees the one-to-one correspondence between $u(\mathbf{r})$, $N_{\mathcal{S}}$ and ρ_{tot}. The key idea of this potential-functional embedding approach is that the problem of finding ρ_{tot} that minimizes the Kohn-Sham total energy functional Eq. (2.14) from Chapter 2, can be translated into a problem of finding $u(\mathbf{r})$ and $N_{\mathcal{S}}$ that minimize a corresponding functional. One can then write

$$\min_{\rho_{\text{tot}}} E_{\text{tot}}[\rho_{\text{tot}}] = \min_{u, N_{\mathcal{S}}} E_{\text{tot}}[\rho_{\text{tot}}[u, N_{\mathcal{S}}]], \tag{3.14}$$

with

$$\begin{aligned} E_{\text{tot}}[\rho_{\text{tot}}[u, N_{\mathcal{S}}]] &= \sum_{\mathcal{S}} E_{\mathcal{S}}[u, N_{\mathcal{S}}] + E_{\text{int}}[u, N_{\mathcal{S}}] \\ &+ \frac{1}{2} \sum_{i \in \mathcal{S}} \sum_{j \in \mathcal{S}' \neq \mathcal{S}} \frac{Z_i Z_j}{|\mathbf{R}_i - \mathbf{R}_j|}. \end{aligned} \tag{3.15}$$

Hence, the resulting energy functional above consists of three term the first one being the subsystem total energy in presence of the embedding potential for a given $N_{\mathcal{S}}$ and is given by

$$E_{\mathcal{S}}[u, N_{\mathcal{S}}] = E^0_{\mathcal{S}}[u, N_{\mathcal{S}}] + \int \rho_{\mathcal{S}}(\mathbf{r}) u(\mathbf{r}) d\mathbf{r}, \tag{3.16}$$

where $E^0_{\mathcal{S}}[u, N_{\mathcal{S}}]$ is a Kohn-Sham like total energy of the bare subsystem (i.e., without the presence of u) and can be written as the Kohn-Sham energy functional Eq. (2.14) from Chapter 2, but using the subsystem's electronic density $\rho_{\mathcal{S}}$ instead of the density of the full system ρ_{tot} and constraining the ion-ion interaction to the ions of the subsystem $\mathcal{S}$, i.e., $\frac{1}{2} \sum_{i \in \mathcal{S}} \sum_{j \in \mathcal{S}, j \neq j} \frac{Z_i Z_j}{|\mathbf{R}_i - \mathbf{R}_j|}$. The last term in Eq. (3.16) represents the ion-ion Coulomb interaction between different subsystems, with $\mathbf{R}_i$ and Z_i the coordinates and nuclear charge of the nucleus i in subsystem $\mathcal{S}$. The interaction energy $E_{\text{int}}[u, \{N_{\mathcal{S}}\}]$ is defined such that the total energy of the full system, i.e., Eq. (2.14), is recovered when adding it to $\sum_{\mathcal{S}} E_{\mathcal{S}}[u, N_{\mathcal{S}}] + E_{\text{int}}[u, N_{\mathcal{S}}]$ and $\frac{1}{2} \sum_{i \in \mathcal{S}} \sum_{j \in \mathcal{S}' \neq \mathcal{S}} \frac{Z_i Z_j}{|\mathbf{R}_i - \mathbf{R}_j|}$ in Eq. (3.16). Hence it is given by

$$E_{\text{int}} = E^0_{\text{int}} - \int \rho_{\text{tot}} u(\mathbf{r}) d\mathbf{r}, \tag{3.17}$$

where

$$\begin{aligned} E^0_{\text{int}} = & \quad T[\rho_{\text{tot}}] - \sum_{\mathcal{S}} T[\rho_{\mathcal{S}}] \\ & + E_{\text{XC}}[\rho_{\text{tot}}] - \sum_{\mathcal{S}} E_{\text{XC}}[\rho_{\mathcal{S}}] + E_{\text{H}}[\{\rho_{\mathcal{S}}\}] \\ & + \sum_{\mathcal{S}} \int \rho_{\mathcal{S}}(\mathbf{r}) \sum_{\mathcal{S} \neq \mathcal{S}'} v^{\mathcal{S}'}_{\text{ext}}(\mathbf{r}) d\mathbf{r}. \end{aligned} \tag{3.18}$$

The minimization of the total energy functional $E_{\text{tot}}[\rho_{\text{tot}}[u, N_{\mathcal{S}}]]$ Eq. (3.16) is done in two steps

(i) for a given u, $E_{\mathcal{S}}$ is minimized with respect to $N_{\mathcal{S}}$.

(ii) Finally, with fixed $N_{\mathcal{S}}$, $E_{\text{tot}}[\rho_{\text{tot}}[u, N_{\mathcal{S}}]]$ is then minimized with respect to u.

The steps (i) and (ii) are repeated until u and $N_{\mathcal{S}}$ do not change any more.
In practice, the kinetic energy density functional $T[\rho_{\mathcal{S}}]$ in Eq. (3.18), is calculated either using optimized effective potentials (OEPs)[144] or approximated methods such as Thomas-Fermi [145, 146] or von Weizsäcker [147]. The XC functionals can be evaluated at the LDA level or using more advanced functionals. This scheme was applied to some diatomic molecules, bulk NaCl and water/MgO(001)[33]. When applying OEP, the embedded total energy Eq. (3.16) reproduces almost exactly the Kohn-Sham benchmark calculations. Moreover, Huang and Carter [33] showed that forces can be obtained by calculating the gradient of the total energy functional with respect to the embedding potential u, which would enable structure optimization.

3.2 Dynamical Mean-Field Theory

Correlated electron systems are often identified as those systems, where the competition between the kinetic and the Coulomb energy is particularly important. In the model Hamiltonian community, Metzner and Vollhardt [25] introduced the limit of infinite dimensions $d \longrightarrow \infty$ (or equivalently infinite number of neighboring lattice sites) to correlated electron systems. They showed that within this limit, the regime where the kinetic and Coulomb energies compete (i.e. where electronic correlations become important) is well described by a momentum independent self-energy $\Sigma(\mathbf{k}, \omega) \xrightarrow{d\longrightarrow\infty} \Sigma(\omega)$. A short time after the work by Metzner and Vollhardt, Georges and Kotliar [27] showed that the Hubbard Hamiltonian [148, 149], one of the most prominent models that describes electronic interactions on a lattice, can be mapped onto an effective Anderson impurity model [37]. Thus, one could map a complex system (that is the Hubbard Hamiltonian) onto a simpler one (that is the Anderson impurity model). This allows the use of very sophisticated and accurate theories to solve the resulting Schrödinger equation. These theories are often referred to as "impurity solvers". They range from iterated perturbation theory [27] to numerically exact ones such as quantum Monte Carlo (QMC) or renormalisation group techniques [150, 151, 152]. In this section I first introduce the DMFT scaling and the resulting DMFT equations before I briefly address impurity solvers and some prominent examples where DMFT gives reasonable results. Here, I mainly orient my self on the review articles by Held [39] and Georges [153] and the work of Georges and Yedidia [154].

3.2.1 Scaling analysis in the limit $d \longrightarrow \infty$

To start, I consider the so called Hubbard model Hamiltonian [148, 149]. For simplicity, I constrain my self to the case of single orbital lattice sites, so that I do not have orbital indices

$$H = -\sum_{ij,\sigma} t_{ij} c^{\dagger}_{i\sigma} c_{j\sigma} + U \sum_{i} n_{i\uparrow} n_{i\downarrow}. \tag{3.19}$$

$n_{i\uparrow} = c^\dagger_{i\uparrow} c_{i\uparrow}$ is the particle number operator, where $c^\dagger_{i\uparrow}$ ($c_{i\uparrow}$) creates (annihilates)

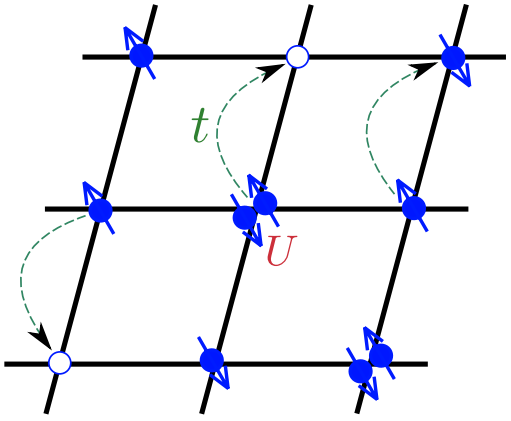

Figure 3.4: Schematic representation of the single orbital Hubbard model. Every site can be filled by at most two electrons with different spins (Pauli principle). The Coulomb interactions between two electrons occupying the same site is described by the matrix element U. Due to the overlap of the orbitals, every electron is free to hop from one site to the other with the probability amplitude t.

an electron with spin up at site i and t_{ij} is the hopping matrix element (essentially modeling the kinetic energy of the problem) between site i and j given by

$$t_{ij} = \int d\mathbf{r} \phi^*(\mathbf{r} - \mathbf{R}_i) \frac{\hbar^2 \nabla^2}{2m} \phi(\mathbf{r} - \mathbf{R}_j), \tag{3.20}$$

with the atomic wave functions $\phi(\mathbf{r} - \mathbf{R}_{i,j})$ at site positions $\mathbf{R}_{i,j}$ and electronic position $\mathbf{r}$. m is the electron mass and U is a general on-site Coulomb interaction probability amplitude given by

$$U = \int d\mathbf{r} d\mathbf{r}' |\phi(\mathbf{r} - \mathbf{R}_i)|^2 V(\mathbf{r} - \mathbf{r}') |\phi(\mathbf{r}' - \mathbf{R}_i)|^2, \tag{3.21}$$

with the bare Coulomb potential $V(\mathbf{r} - \mathbf{r}')$.
One can consider an extended lattice [25, 27, 39], so that one obtains a large number $\mathcal{N}_{|\mathbf{R}_i - \mathbf{R}_j|}$ of neighboring sites j with the same distance $|\mathbf{R}_i - \mathbf{R}_j|$ to site i. In the case of a cubic lattice, one has $\mathcal{N} = 6 = 2d$ nearest neighbors for the dimension $d = 3$. In general the number of nearest neighbors is related to the dimension d via $\mathcal{N}_{|\mathbf{R}_i - \mathbf{R}_j|} \propto d^{|\mathbf{R}_i - \mathbf{R}_j|}$. Thus, considering $\mathcal{N}_{|\mathbf{R}_i - \mathbf{R}_j|} \longrightarrow \infty$ is equivalent to taking $d \longrightarrow \infty$. The interesting question now is, how does the Hamiltonian Eq. (3.19) scale with $\mathcal{N}_{|\mathbf{R}_i - \mathbf{R}_j|} \longrightarrow \infty$.
The second term on the right hand side of (3.19) is purely local. Hence, it scales like

$$\langle U \sum_i n_{i\uparrow} n_{i\downarrow} \rangle \xrightarrow{\mathcal{N}_{|\mathbf{R}_i - \mathbf{R}_j|} \longrightarrow \infty} \text{const.} \tag{3.22}$$

meaning that this term does not diverge but assumes a finite value.
The first term of Eq. (3.19) however is more delicate and requires more attention: it

features a sum over j-equivalent sites. This leads to a divergence of the kinetic energy per site i. This divergence can be overcome by rescaling t_{ij} in the $\mathcal{N}_{|\mathbf{R}_i-\mathbf{R}_j|} \longrightarrow \infty$ limit using the ansatz

$$t_{ij} = \frac{t^*_{ij}}{\sqrt{\mathcal{N}_{|\mathbf{R}_i-\mathbf{R}_j|}}}, \text{ with } t^*_{ij} \xrightarrow{\mathcal{N}_{|\mathbf{R}_i-\mathbf{R}_j|}\longrightarrow\infty} \text{const.} \tag{3.23}$$

The non-interacting Green's function ($U = 0$) is directly related to the hopping matrix element t_{ij} and thus has the same dependence on $\mathcal{N}_{|\mathbf{R}_i-\mathbf{R}_j|}$ as the hopping t_{ij}

$$[G_0(i\omega)]_{ij} = [i\omega + \mu - t]^{-1}_{ij} \propto \frac{1}{\sqrt{\mathcal{N}_{|\mathbf{R}_i-\mathbf{R}_j|}}}. \tag{3.24}$$

This can be best demonstrated if one performs the matrix inversion in the upper expression using the minors method. Then it becomes clear that the off-diagonal terms are a factor $\frac{t_{ij}}{i\omega+\mu-t_{ij}}$ smaller than the diagonal ones. Hence, within the limit of an infinitly large number of neighboring sites these terms can be neglected and one is left with diagonal terms only.
For the full Green's function one can also show that it scales in the same way. Hence, one can write

$$G_{ij}(i\omega) \propto \frac{1}{\sqrt{\mathcal{N}_{|\mathbf{R}_i-\mathbf{R}_j|}}} \xrightarrow{\mathcal{N}_{|\mathbf{R}_i-\mathbf{R}_j|}\longrightarrow\infty} \text{const.}. \tag{3.25}$$

But how does this scaling analysis translate into the language of diagrams?

Localization of Feynman diagrams

In the former subsection I briefly discussed how the Green's functions scale in the limit of infinite neighboring atoms. As I have discussed in Chapter 1, the best way to visualize the meaning of Green functions is to draw Feynman diagrams. Figure (3.5) shows a second order diagram describing an electron from site i interacting with a hole on site j ($i \neq j$). This is a typical non-local diagram. It contains three G_0 lines that, as I discussed above, scale as $\frac{1}{\sqrt{\mathcal{N}_{|\mathbf{R}_i-\mathbf{R}_j|}}}$. In the diagrammatic expansion this term thus scales as $\frac{1}{\sqrt{\mathcal{N}_{|\mathbf{R}_i-\mathbf{R}_j|}}^3}$. Considering that in the sum $\sum_{ij,\sigma} t_{ij}\langle c^\dagger_{i\sigma} c_{j\sigma}\rangle$ there is a factor $\mathcal{N}_{|\mathbf{R}_i-\mathbf{R}_j|}$ for every class of equivalent sites j, one is left with $\frac{\mathcal{N}_{|\mathbf{R}_i-\mathbf{R}_j|}}{\sqrt{\mathcal{N}_{|\mathbf{R}_i-\mathbf{R}_j|}}^3} = \frac{1}{\sqrt{\mathcal{N}_{|\mathbf{R}_i-\mathbf{R}_j|}}}$. This means that the contribution of such a diagram becomes negligible in the limit $\mathcal{N}_{|\mathbf{R}_i-\mathbf{R}_j|} \longrightarrow \infty$. Diagrams like the one in Fig. (3.5) are not the only non-local ones occurring. The left hand side of Fig. (3.6) shows the process of an electron that leaves site i to interact with another electron from site j and then finally comes back to site i. Such a diagram survives the scaling since it only contains two G_0 lines connecting site i and j: it scales as $\frac{\mathcal{N}_{|\mathbf{R}_i-\mathbf{R}_j|}}{\sqrt{\mathcal{N}_{|\mathbf{R}_i-\mathbf{R}_j|}}^2} = (\mathcal{N}_{|\mathbf{R}_i-\mathbf{R}_j|})^0 = 1$. However, this process is already contained in the diagram of the full Green's function (represented by double lines in diagrammatic language) shown in the right hand side of Fig. (3.6). They describe the fact that, within this scaling, an electron can still leave site $\mathbf{R}_i$,

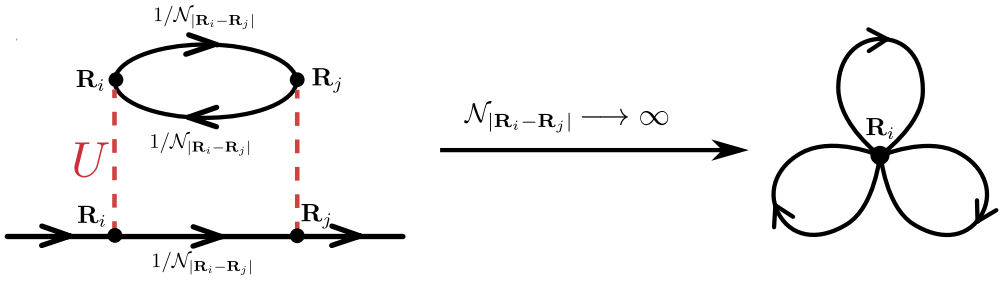

Figure 3.5: Second order diagram of the non-local Green's function. It can be seen as an electron-hole process, where the electron sits on site $\mathbf{R}_i$ and the hole on site $\mathbf{R}_j$. Such a diagram vanishes in the limit $d \longrightarrow \infty$.

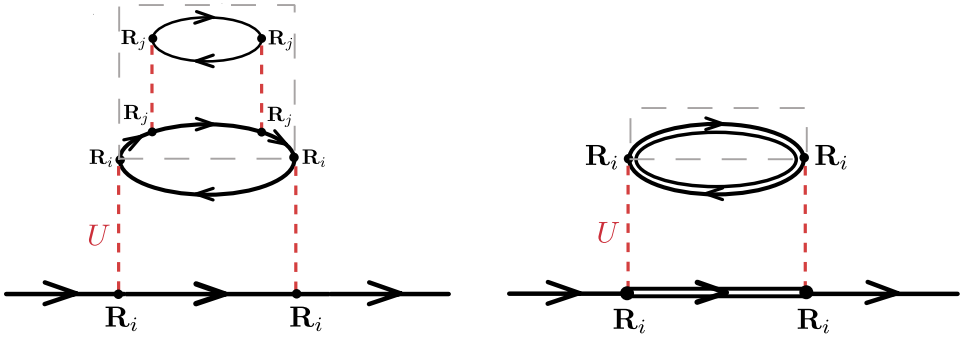

Figure 3.6: Left hand side: Diagrams, where the sites $\mathbf{R}_i$ and $\mathbf{R}_j$ are connected by only two G_0 lines. These diagrams survive the scaling. However, they are all included on the full Green's function diagram shown in the right hand side.

interact on other sites an then come back to site $\mathbf{R}_i$. In Chapter 1, I have shown that the connection between the full (interacting) Green function and the non-interacting one is made through the Dyson equation via the self-energy. Diagrammatically, the self-energy is the sum of all skeleton (amputated) diagrams. These are diagrams such as the ones in Fig. (3.5) or Fig. (3.6) only without the ingoing and outgoing G_0 legs (i.e. the amputated diagrams). Hence, it is obvious that the locality of the full diagrams is automatically translated to the skeleton diagrams. Thus, just as the Green's functions, the self-energy is purely local

$$\Sigma_{ij}(i\omega) \xrightarrow{\mathcal{N}_{|\mathbf{R}_i-\mathbf{R}_j|\longrightarrow\infty}} \delta_{ij}\Sigma(i\omega). \tag{3.26}$$

As a summary one can say that in the DMFT limit only local diagrams are considered, while the lattice of the real problem is approximated by a local on-site problem.See Fig. (3.7). This approximation becomes exact for $d \longrightarrow \infty$.

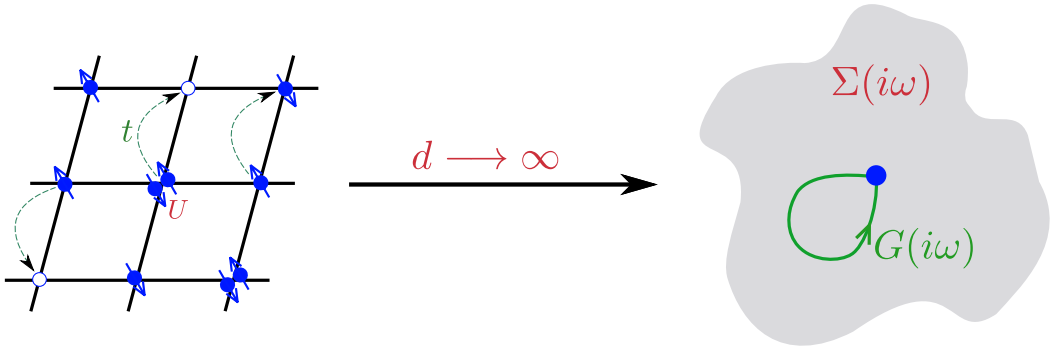

Figure 3.7: Cartoon of the DMFT approximation to the Hubbard model. Within the $d \longrightarrow \infty$ limit the Hubbard lattice can be described by a single lattice on which only local interactions are relevant. While electrons can still interact on other sites, only interactions of electrons that "come back" are taken into account.

3.2.2 Derivation of the dynamical mean-field equations

To start, I again consider the Hubbard model

$$H_\lambda = U\sum_i n_{i\uparrow}n_{i\downarrow} - \lambda\sum_{ij,\sigma} t_{ij}c^\dagger_{i\sigma}c_{j\sigma} \tag{3.27}$$

where the coupling constant $\lambda \in [0,1]$ was introduced to control the non-local hopping term of the Hamiltonian, so that one can distinguish

$$H_\lambda = H_{loc} + \lambda H_{\text{non}-\text{loc}} \tag{3.28}$$

Mapping the Hubbard model onto an impurity model

The mapping is done by constraining the local Green's function $\langle c_i(\tau)c_i^\dagger(\tau')\rangle$ to take a specific value $G(\tau-\tau')$ by introducing the Lagrange multiplier $\Delta(\tau-\tau')$, so that

one can write the free-energy functional for finite temperatures as [153]

$$\Omega_\lambda[G(\omega),\Delta(\omega)] = -\frac{1}{\beta}\ln\int DcDc^\dagger \exp\{\int_0^\beta d\tau(\sum_{i\sigma} c^\dagger_{i\sigma}(-\partial_\tau+\mu)c_{i\sigma} - H_\lambda)+ \int_0^\beta\int_0^\beta d\tau d\tau' \sum_{i\sigma}\Delta(\tau-\tau')[G(\tau-\tau') - c_i(\tau)c_i^\dagger(\tau')]\}, \quad (3.29)$$

where $\beta = \frac{1}{k_B T}$ with temperature T, k_B is the Boltzmann constant and the path integral $\int Dc := \lim_{n\to\infty}\int dc_1 ... \int dc_n$ and the Matsubara frequencies ω are [155] $\omega \equiv \omega_\nu = \frac{(2\nu+1)\pi}{\beta}$.
Usually, one is interested in the stationarity of $\Omega_\lambda[G(\omega),\Delta(\omega)]$ with respect to the Lagrange multiplier $\Delta(\tau-\tau')$ (i.e. $\frac{\partial\Omega}{\partial\Delta} = 0$). This means that for all λ one should have

$$\langle c_i(\tau)c_i^\dagger(\tau')\rangle_{\Delta,\lambda} = G(\tau-\tau'),\ \forall\lambda. \quad (3.30)$$

The upper expression means that the expectation value $\langle c_i(\tau)c_i^\dagger(\tau')\rangle$ should coincide with the local Green's function $G(\tau-\tau')$. This can be easily seen, by explicitly performing the derivative of the free-energy functional Eq. (3.29) and considering the Boltzmann weight $\langle ...\rangle_{\Delta,\lambda}$ defined for a given operator $\hat{\mathcal{O}}$ as

$$\langle\hat{\mathcal{O}}\rangle_{\Delta,\lambda} = \int DcDc^\dagger\hat{\mathcal{O}}\ \exp\{\int_0^\beta d\tau(\sum_{i\sigma} c^\dagger_{i\sigma}(-\partial_\tau+\mu)c_{i\sigma} - H_\lambda)+ \int_0^\beta\int_0^\beta d\tau d\tau' \sum_{i\sigma}\Delta(\tau-\tau')[G(\tau-\tau') - c_i(\tau)c_i^\dagger(\tau')]\}\times \Big[\int DcDc^\dagger\ \exp\{\int_0^\beta d\tau(\sum_{i\sigma} c^\dagger_{i\sigma}(-\partial_\tau+\mu)c_{i\sigma} - H_\lambda)+ \int_0^\beta\int_0^\beta d\tau d\tau' \sum_{i\sigma}\Delta(\tau-\tau')[G(\tau-\tau') - c_i(\tau)c_i^\dagger(\tau')]\}\Big]^{-1} \quad (3.31)$$

Eq. (3.30) implicitly expresses the Green's function as a function of the Lagrange multiplier Δ. One can formally inverse this expression to get an expression of Δ as function of the Green's function $\Delta = \Delta_\lambda[G]$. So that one can then write Eq. (3.29) as functional of the Green's function only

$$\Omega_\lambda[G,\Delta[G]] \equiv \Gamma_\lambda[G]. \quad (3.32)$$

The upper expression is the Legendre transformation of the free energy functional with respect to the local source Δ. Now let me consider the case $\lambda = 0$ corresponding

to the atomic limit where the Hamiltonian is purely local. In this case one can show [153, 154] that the Legendre transform of the free-energy functional is given by

$$\Omega_0[\Delta_0, G] = F_{\text{imp}}[\Delta_0] - \text{Tr}(G\Delta_0), \tag{3.33}$$

with the free-energy of the quantum impurity as functional of the hybridization Δ_0 given by

$$F_{\text{imp}}[\Delta_0] = -\frac{1}{\beta}\ln \int DcDc^\dagger$$
$$\exp\{\int_0^\beta \int_0^\beta d\tau d\tau' \sum_{i\sigma} c^\dagger_{i\sigma}(\tau')[(-\partial_\tau + \mu)\delta(\tau - \tau') - \Delta_0(\tau - \tau')]c^\dagger_{i\sigma}(\tau') + U\int_0^\beta d\tau n_\uparrow(\tau)n_\downarrow(\tau)\}. \tag{3.34}$$

Hence, in the $\lambda = 0$ case the local Green's function is that of a quantum impurity problem (often referred to as the Anderson impurity problem [37] when dealing with the Hubbard model)

$$G = G_{\text{imp}}[\Delta_0]. \tag{3.35}$$

With the hybridization function Δ_0 that defines the bare Green's function of the impurity

$$\mathcal{G}_0^{-1}(i\omega) = i\omega + \mu - \Delta_0(i\omega). \tag{3.36}$$

Thus, since Δ_0 is a dynamical object, it includes retardation in the aspect as the related Green's function.
However, an explicit inversion of (3.35) i.e., $\Delta_0[G] = G_{\text{imp}}$, is not possible in practice without approximations. These numerical approximations are referred to as quantum "impurity solvers" (see section (3.2.5)) and are part of an iterative procedure that has the following steps:

(i) Start with initial condition for Δ_0 or $\mathcal{G}_0$

(ii) Compute interacting Green's function G_{imp} and the related self-energy $\Sigma_{\text{imp}} = \mathcal{G}_0^{-1} - G_{\text{imp}}^{-1}$

(iii) Get new $\mathcal{G}_0^{\text{NEW}}$ as $\mathcal{G}_0^{\text{NEW}} = [\Sigma_{\text{imp}} + G^{-1}]^{-1}$, where G is the local Green's function corresponding to the previous iteration step.

I want now to turn to the explicit form of the local Green's function and the approximation involved therein.

Exact functional of the local Green's function

The $\lambda \neq 0$ terms can be included in the Hubbard Hamiltonian by integrating over the coupling constant λ. Taking the derivative of $\Gamma_\lambda[G]$ in eq. (3.32) with respect to λ, one obtains for the Hubbard Hamiltonian

$$\frac{d\Gamma_\lambda[G]}{d\lambda} = \langle H_{\text{non-loc}}\rangle = -\sum_{ij} t_{ij}\langle c_i^\dagger c_j\rangle|_G = \text{Tr}\sum_{\mathbf{k}} \epsilon_{\mathbf{k}} G_\lambda(\mathbf{k}, i\omega)|_G, \tag{3.37}$$

with $\epsilon_{\mathbf{k}} \equiv \sum_j t_{ij} e^{i\mathbf{k}\cdot(\mathbf{R}_i - \mathbf{R}_j)}$ and where $|_G$ means that the quantities should be expressed as functional of the local Green's function G.
Essentially, Eq. (3.37) is the kinetic energy part of the problem and it establishes a relation between the lattice $G_\lambda(\mathbf{k}, i\omega)$ and the local Green's function G.
Thus, for the exact functional ($\lambda = 1$) one has

$$\begin{aligned}\Gamma[G] &= \Gamma_0[G] + \int_0^1 d\lambda \frac{d\Gamma_\lambda[G]}{d\lambda} \\ &= F_{\text{imp}}[\Delta_0[G]] - \text{Tr}(G\Delta_0[G]) + \mathcal{T}[G],\end{aligned} \tag{3.38}$$

with the kinetic energy functional

$$\mathcal{T}[G] = \int_0^1 d\lambda \text{Tr} \sum_{\mathbf{k}} \epsilon_{\mathbf{k}} G_\lambda(\mathbf{k}, i\omega)|_G. \tag{3.39}$$

The stationarity condition $\frac{\delta\Gamma}{\delta G} = 0$ determines the local Green's function at equilibrium. Recalling that $\frac{\delta\Gamma_0}{\delta G} = -\Delta_0$ one gets the important relation

$$\Delta_0[G(i\omega)] = \frac{\delta\mathcal{T}[G]}{\delta G(i\omega)}, \tag{3.40}$$

that relates the hybridization function to the local Green's function. Equation (3.40) together with (3.35) constitute the fundamental equations of DMFT, where $\Delta_0[G(i\omega)]$ is often referred to as dynamical mean-field hence, giving the method its name. Up to now the theory is general and the only approximations involved are the ones related to the Hubbard Hamiltonian under consideration. However, to obtain the local Green's function one should solve the impurity problem eq. (3.34) with the constraint (3.40). Thus, approximation of the kinetic energy functional $\mathcal{T}[G]$ is necessary. Below I briefly discuss the so called DMFT approximation to the kinetic energy functional.

The DMFT approximation to the kinetic energy functional

The one particle Green's function of the Hubbard Hamiltonian is

$$G(\mathbf{k}, i\omega) = \frac{1}{(i\omega + \mu) - \lambda\epsilon_{\mathbf{k}} - \Delta_\lambda(i\omega) - \Sigma_\lambda(\mathbf{k}, i\omega)}. \tag{3.41}$$

The DMFT approximation is to omit the $\mathbf{k}$ dependence of the self-energy, meaning that the self-energy becomes purely local

$$\Sigma_\lambda(\mathbf{k}, i\omega) \longrightarrow \Sigma_{\lambda=0}(i\omega). \tag{3.42}$$

With $\Sigma_{\lambda=0}[i\omega; G] = \mathcal{G}_0^{-1} - G^{-1} = i\omega + \mu - \Delta_0[i\omega; G] - G^{-1}$. Summing over $\mathbf{k}$ yields

$$G(i\omega) = \int d\epsilon \frac{D(\epsilon)}{\xi(i\omega) - \lambda\epsilon} = \frac{1}{\lambda}\tilde{D}\left(\frac{\xi(i\omega)}{\lambda}\right), \tag{3.43}$$

where $D(\epsilon) = \sum_{\mathbf{k}} \delta(\epsilon - \epsilon_{\mathbf{k}})$ and $\xi(i\omega) = (i\omega + \mu) - \Delta_\lambda(i\omega) - \Sigma_{\lambda=0}(i\omega) = \Delta_0(i\omega) - \Delta_\lambda(i\omega) + G^{-1}$. Introducing R, the inverse function of $\tilde{D}$ given by $\tilde{D}[R(g)] = \frac{\xi(i\omega)}{\lambda} = R(\lambda G(i\omega))$, one can then invert the equation above which enables to write the hybridization function as functional of the local Green's function

$$\Delta_\lambda[i\omega; G] = G^{-1} + \Delta_0[i\omega; G] - \lambda R[\lambda G]. \tag{3.44}$$

Using this expression one can obtain the lattice Green's function as functional of the local Green's function G

$$G_\lambda(\mathbf{k}, i\omega) = \frac{1}{\lambda R[\lambda G] - \lambda \epsilon_{\mathbf{k}}}. \tag{3.45}$$

Now one has all the ingredients to write down the kinetic energy functional in the DMFT approximation. It is given by substituting the upper expression for the lattice Green's function into eq. (3.39)

$$\mathcal{T}_{\mathrm{DMFT}}[G] = \int \sum_0^1 d\lambda \mathrm{Tr}\left[G(i\omega) R[\lambda G(i\omega)] - \frac{1}{\lambda}\right]. \tag{3.46}$$

The resulting full free-energy functional in the DMFT approximation is then

$$\Gamma_{\mathrm{DMFT}}[G] = F_{\mathrm{imp}}[\Delta_0[G]] - \mathrm{Tr}(G\Delta_0[G]) + \mathcal{T}_{\mathrm{DMFT}}[G]. \tag{3.47}$$

the hybridization function then follows from the equilibrium condition $\frac{\delta\Gamma}{\delta G} = 0$

$$\Delta_0[i\omega; G]|_{\mathrm{DMFT}} = R[G(i\omega)] - \frac{1}{G(i\omega)}. \tag{3.48}$$

The local Green's function is then given by

$$G(i\omega) = \int d\epsilon \frac{D(\epsilon)}{\Delta_0[i\omega; G]|_{\mathrm{DMFT}} - R[G(i\omega)]} = \int d\epsilon \frac{D(\epsilon)}{i\omega + \mu - \Sigma_{\mathrm{imp}}(i\omega)}, \tag{3.49}$$

with the impurity self-energy $\Sigma_{\mathrm{imp}} = \mathcal{G}_0^{-1} - G^{-1}$ and $\mathcal{G}_0^{-1} = i\omega + \mu - \Delta_0[i\omega; G]|_{\mathrm{DMFT}}$. Equation (3.49) is in agreement with the constraint that at self-consistency $\Delta_{\lambda=1}[G] = 0$. Thus, within the DMFT approximation the lattice Green's function is given by taking $\Delta_{\lambda=1}[G] = 0$ in eq. (3.41) to finally get

$$G(\mathbf{k}, i\omega)|_{\mathrm{DMFT}} = \frac{1}{i\omega + \mu - \epsilon_{\mathbf{k}} - \Sigma_{\mathrm{imp}}(i\omega)} \tag{3.50}$$

3.2.3 Example of a single impurity Anderson model

To summarize, it is useful to illustrate DMFT for an explicit example. For simplicity I start with the single orbital Hubbard model Eq. (3.19) which models a lattice of single orbital atoms. Orbitals from different lattice sites can overlap so that electrons can hop from one site to the other with probability amplitude t_{ij} as shown in Fig. (3.4). For the isolated atom, i.e. the case where no hopping occurs, the lattice site can have the following eigenstates

- $|0\rangle$, when no electron is occupying the site, with a corresponding eigenvalue 0.
- $|\uparrow\rangle$ (or $|\downarrow\rangle$), when an electron of spin $\uparrow$ (or $\downarrow$) is occupying the site, with eigenvalue ϵ_d
- $|\uparrow\downarrow\rangle$, when two electrons of opposite spin occupy the lattice site, which corresponds to an eigenvalue of $2\epsilon_d + U$ (since every second electron should have enough energy to subdue the barrier given by the Coulomb interaction U).

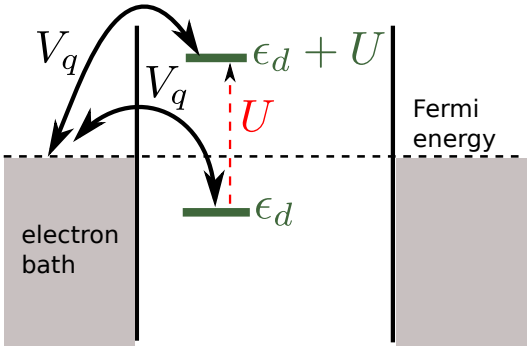

Figure 3.8: Cartoon of the single impurity Anderson model Eq. 3.51. It describes a single electronic level, coupled to an electronic bath. Electrons can hop back and forth between the electronic level and the electronic bath. When the level is half filled (occupied by one electron only) the other electron should should have the energy $\epsilon_d + U$ and an opposite spin to be able to occupy the same level.

As I have shown in the previous section, in dynamical mean-field theory the local Green's function is represented as that of a single atom coupled to an effective bath of electrons as illustrated by Fig. (3.8). The Anderson impurity model (AIM) describes this effective coupling. It is given in the case of a single impurity by

$$H_{\mathrm{AIM}} = H_{\mathrm{atom}} + H_{\mathrm{bath}} + H_{\mathrm{coupling}}, \tag{3.51}$$

where

$$\begin{aligned} H_{\mathrm{atom}} &= U n_\uparrow n_\downarrow + (\epsilon_d - \mu)(n_\uparrow + n_\downarrow), \\ H_{\mathrm{bath}} &= \sum_{q\sigma} \epsilon_q d^\dagger_{q\sigma} d_{q\sigma}, \\ H_{\mathrm{coupling}} &= \sum_{q\sigma} [V_q d^\dagger_{q\sigma} c_\sigma + h.c.], \end{aligned}$$

with $n_{\uparrow,\downarrow} = c^\dagger_{\uparrow,\downarrow} c_{\uparrow,\downarrow}$. $c^\dagger_\uparrow$ creates an electron on the atom with spin up and $d^\dagger_{q\sigma}$ creates a bath electron at state q and spin σ. ϵ_q is the energy of a bath electron at state q and V_q is the hopping amplitude from the atomic level to the bath level q.
In the case of the Anderson model the hybridization function can be derived as

$$\Delta(i\omega) = \sum_q \frac{V_q V_q^*}{i\omega - \epsilon_{\mathbf{q}}} \tag{3.52}$$

The resulting impurity self-energy as functional of the local Green's function is then

$$\begin{aligned}\Sigma_{\text{imp}} &= \mathcal{G}_0^{-1}(i\omega) - G_{\text{imp}}^{-1}(i\omega) \\ &= i\omega + \mu - \epsilon_d - \Delta(i\omega) - G_{\text{imp}}^{-1}(i\omega),\end{aligned} \tag{3.53}$$

with the local impurity Green's function $G_{\text{imp}}^{-1}(i\omega)$. Again the lattice Green's function in the DMFT approximation becomes

$$G(\mathbf{k}, i\omega) = \frac{1}{i\omega + \mu - \epsilon_d - \epsilon_{\mathbf{k}} - \Sigma_{\text{imp}}(i\omega)}. \tag{3.54}$$

Summing over the $\mathbf{k}$ degrees of freedom, the following self-consistency condition

$$\begin{aligned}G^{\text{on-site}}(i\omega) &= \sum_{\mathbf{k}} \frac{1}{\Delta(i\omega) + G_{\text{imp}}^{-1}(i\omega) - \epsilon_{\mathbf{k}}} \\ &= \int d\epsilon \frac{D(\epsilon)}{\Delta(i\omega) + G_{\text{imp}}^{-1}(i\omega) - \epsilon},\end{aligned} \tag{3.55}$$

is obtained. From the upper equation it becomes clear that the self-consistency condition relates the dynamical mean-field $\Delta(i\omega)$ to the local on-site Green's function, at each frequency point. This defines an iterative procedure within which the lattice Hamiltonian is mapped onto a simpler impurity problem. This is the essence of the embedding concept in DMFT: a complex problem is represented as a simple one that is easier and more efficiently solvable one. A sketch of the self-consistency cycle in DMFT is shown in Fig. (3.9). For an initial guess of the impurity self-energy Σ_{imp} a lattice Green function that yields after $\mathbf{k}$-summation the local on-site Green's function resulting in a hybridization function $\Delta(\omega)$. Solving the resulting impurity problem then gives the new impurity self-energy Σ_{imp}, which is related to the local impurity Green's function via Eq. (3.53).

3.2.4 Extending DMFT to *ab-initio* methods: The LDA+DMFT approach

As I have shown in the previous sections, DMFT is a method that has its roots in the model Hamiltonian community. Model Hamiltonians are a common tool in physics because the desired physics can be put by hand and because they are solvable. However, their predictive power for real systems remains limited due to the approximations made and the parameters introduced that are not always obvious to determine. In this section, I briefly present a scheme that merges the *ab-initio* within the model Hamiltonian word. The idea, originally developed by Anisimov *et al.* [156] within the so-called LDA+U framework, is to start with an *ab-initio* Hamiltonian at a given level of theory and to include local interactions by means of the DMFT framework. There have been numerous schemes following the X+DMFT philosophy, where X stands either for Hartree, Hartree-Fock, LDA by Anisimov *et al.* [157] and Lichtenstein and Katsnelson [158] or even *GW* by Biermann *et al.* [159]. Here I shortly address the LDA+DMFT framework since it is the most broadly used one. As its name suggests, the LDA+DMFT approach uses the LDA Hamiltonian

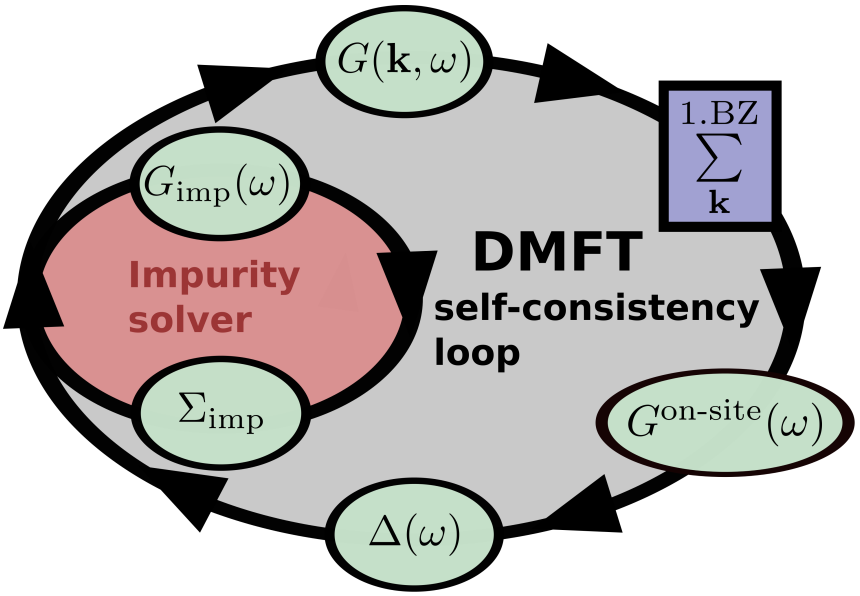

Figure 3.9: Sketch of the DMFT self-consistency cycle. Staring with an initial guess of Σ_{imp} the DMFT Green's-function-mapping onto an effective impurity model is initialized. Solving the resulting impurity problem yields a new impurity self-energy, that serves as a new starting point for the Green's-function-mapping.

as a starting point. On top of this Hamiltonian the local correlation effects from DMFT are added. However, as I have shown in Chapter 2, LDA already contains a correlation part. To avoid double counting, the correlation contribution from LDA should be subtracted. Hence, one ends up with the following Hamiltonian (here I restrict my self to the $J = 0$ case for simplicity, meaning that I am considering single orbital models, where Hund's coupling J is zero and refer the reader to [39]) for details)

$$H_{\mathrm{LDA+DMFT}} = H^{\mathrm{dc}}_{\mathrm{LDA}} + U \sum_{\substack{i,\sigma \\ \nu \in L}} n^{\nu}_{i\sigma} n^{\nu}_{i\bar{\sigma}}, \tag{3.56}$$

where $H^{\mathrm{dc}}_{\mathrm{LDA}}$ is the double counting corrected LDA Hamiltonian given by $H^{\mathrm{dc}}_{\mathrm{LDA}} = H_{\mathrm{LDA}} - \sum_{\substack{i,\sigma \\ \nu \in L}} \Delta\epsilon n^{\nu}_{i\sigma}$, with the double counting correction $\sum_{\substack{i,\sigma \\ \nu \in L}} \Delta\epsilon n^{\nu}_{i\sigma}$ and H_{LDA} the LDA Hamiltonian from an *ab initio* calculation. The sum $\sum_{\nu \in L}$ runs over all locally interacting (with interaction U) orbitals ν. In the lattice Green's function Eq. (3.50) the part describing the electronic surrounding $\epsilon_{\mathbf{k}}$ becomes $\tilde{\epsilon}^{\mathrm{LDA}}_{\mathbf{k}} = \epsilon^{\mathrm{LDA}}_{\mathbf{k}} - \Delta\epsilon$, where $\epsilon^{\mathrm{LDA}}_{\mathbf{k}}$ is the Fourier-transform of the LDA Hamiltonian into reciprocal space.
Additionally to the proper choice of the local manifold (i.e., the correlated states) [160], the calculation of the double counting correction term $\Delta\epsilon$ and the interaction U constitutes a major challenge for LDA+DMFT. The latter can be addressed using the LDA density in the framework of the so-called constrained LDA (cLDA) established by Dederichs *et al.* [161], McMcMahan *et al.* [162] and Gunnarsson *et al.* [163]. It relates $\Delta\epsilon$ and U to the LDA density and makes the formalism completely

parameter free and thus purely of *ab initio* nature. In this thesis, I will not give a detailed description of the cLDA formalism. Instead, I will present the general idea of the method. The basic idea behind cLDA is to choose the localized orbitals of interest, usually these are d- or f- orbitals, then isolate them by setting the hopping between these orbitals and all the others to zero. This means that the electrons on these orbitals cannot leave the site and thus are isolated from the rest of the system. This controls the electron number of the electrons interacting on that site. The total-energy as a function of the electron number for a given localized orbital is then [39]

$$E(n_{d,f}) = E_0 + \frac{1}{2}Un_{d,f}(n_{d,f} - 1) + (\epsilon_{d,f}^{\mathrm{LDA}} + \Delta\epsilon)n_{d,f}. \tag{3.57}$$

Hence, performing cLDA calculations for different occupations (e.g. for $(n_d + 1)$ and $(n_d - 1)$) of the localized orbitals using Janak's theorem [84, 164] yields U and $\Delta\epsilon$. The resulting U and $\Delta\epsilon$ are related to the density $\rho(\mathbf{r})$ and thus, are different for different densities. Here, it is worth mentioning that a number of schemes for calculating the double counting correction $\Delta\epsilon$ have been proposed [156, 165, 166], yielding different values for the U and thus the resulting physical quantities.
The LDA+DMFT approach defines a self-consistency cycle that can be summarized in the following steps

(i) From conventional LDA calculation, obtain a starting LDA density.

(ii) For a given density obtain bandstructure $\epsilon_{\mathbf{k}}^{\mathrm{LDA}}$.

(iii) cLDA then provides the corresponding U and $\Delta\epsilon$.

(iv) The LDA+DMFT Hamiltonian Eq. (3.56) can then be solved using the DMFT self-consistency cycle as in Fig. (3.9).

(v) The resulting impurity self-energy Σ_{imp}, yields a new lattice Green's function Eq. (3.50) and thus a new density. One can then go back to (ii) to restart the procedure until convergence. However, in most applications of LDA+DMFT the density is not updated [167, 39, 153].

Until now I have not explicitly discussed the way to solve the impurity problem and how to calculate the impurity self-energy. This will be the topic of the next section.

3.2.5 Impurity solvers

The embedding aspect of DMFT is manifested by the Green's function mapping. This mapping reduces the full problem of an infinite lattice, where electrons are free to interact on all the lattice sites, to an effective impurity problem as demonstrated by Georges and Kotliar [27] and Jarrell [168]. The resulting impurity problem is then easier to solve. This simplification of the problem allows the use of a multitude of powerful numerical impurity solvers. In fact solving the impurity problem became one of the major challenges in DMFT i.e., how to obtain the right impurity self-energy and the related Hybridization function? Numerous ways to solve

the Anderson impurity problem have been devised and implemented such as exact diagonalization or renormalization group techniques such as Wilson's numerical renormalization group (NRG) [150, 151] or the more recent density matrix renormalization group [169, 170, 152] (for a general idea, the reader is referred to the review article by Schollwöck [152]). All these methods can provide very high accuracy for the estimation of the impurity self-energy. However, due to their exponential scaling with the number of states, they remain restricted to very small systems and dimensionality. For example, NRG has been very successfully applied to impurity models with only one Hubbard band [171, 172] and becomes a serious challenge already for the two band case.

For real systems however, the impurity solver of choice at present is the quantum Monte-Carlo (QMC) method with all the various algorithms [173, 174, 175]. Here the numerical effort grows cubically with a decrease in the electronic temperature, which restricts possible simulations to finite temperatures that lie around room temperature. For a more detailed discussion of the different impurity solvers, the reader can refer to the review paper by Held [39].

There are many applications [176, 166, 167], where DMFT was successfully applied within the LDA+DMFT framework using QMC as impurity solver. Here I want to cite only two examples and refer the reader to the Refs. [39, 153] for further reading. For instance, Lichtenstein *et al.* [166] were able to describe the Ni satellite at -6 eV for the majority-spin spectrum, see Fig. (3.10), a feature, that is completely absent in LDA as can be seen from the density of states in Fig. (3.10).

The other example is the Kondo volume collapse in Ce [177, 178] that was investi-

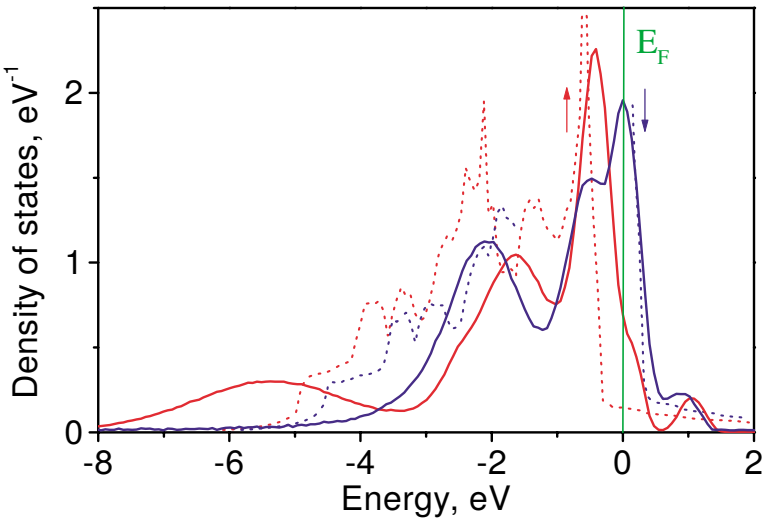

Figure 3.10: LDA+DMFT with QMC solver (solid lines) and spin polarised LDA (doted lines) for both spin directions. From Lichtenstein *et al.* (2001) [166]

gated by many authors [179, 176, 180, 181, 182] using LDA+DMFT. For instance, McMahan *et al.* [176] could reproduce the right evolution of the $4f$-spectral function with change of volume at a temperature $T = 632$ K. The comparison of the calculated LDA+DMFT spectrum and the measured one is shown in Fig. (3.11).

It shows the spectrum corresponding to the λ- (V=29Å^3) and γ- (V=34Å^3) phases. The parameter free LDA+DMFT with QMC impurity solver could reproduce the measured spectra at the α- and γ-phases.

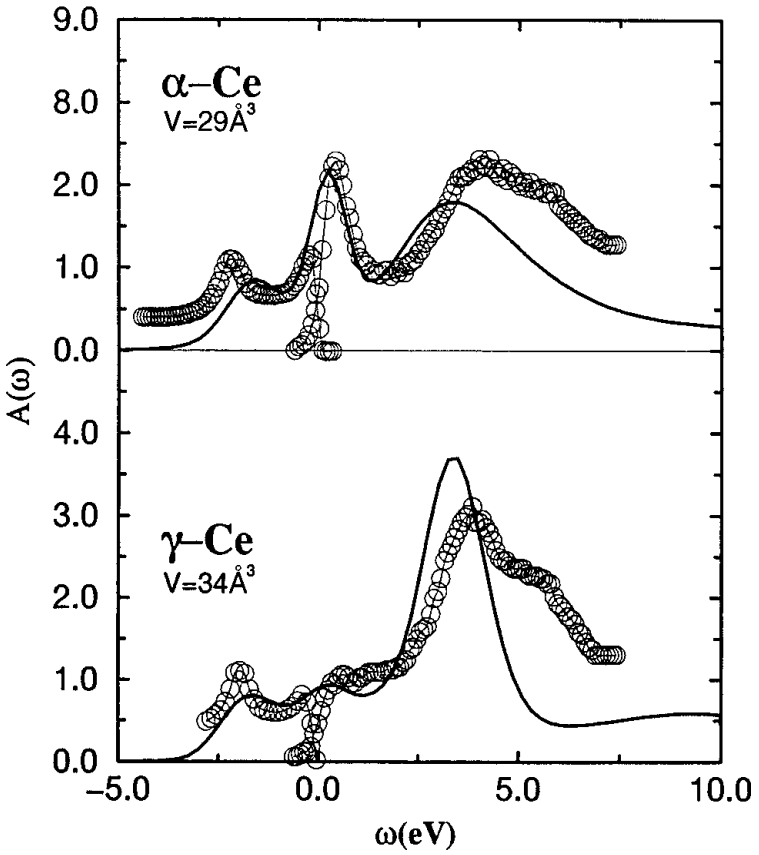

Figure 3.11: Comparison of the LDA+DMFT spectra with QMC solver (solid lines) with experimental data (circles). From McMahan *et al.* (2003) [176]

Chapter 4

Real Space Dynamical Mean-Field Embedding

As I have discussed in the previous chapter, dynamical mean-field theory (DMFT) in its original formulation is a Green's function method for correlated model Hamiltonians. It uses the locality of the electronic interactions to embed a local on-site region of the Hubbard lattice (usually a single d- or f-electron) into a periodic non-interacting electronic bath. This mapping of the Hubbard lattice into an effective localized region coupled to an electronic bath defines a self-consistency cycle.
Furthermore, The local treatment of the on-site region facilitates the use of computationally very demanding and at the same time exact methods, such as continuous time quantum Monte-Carlo [183], exact diagonalization or renormalization group techniques [184]. The localized region is then coupled through a hybridization self-energy to the surrounding electronic bath, which is treated with computationally more efficient methods (see discussion in Chapter 3).
In the last decade DMFT has proven to successfully describe the spectral properties of solids with localized electrons [185, 186, 187, 188]. This success has driven further methodological development such as the extension of the DMFT formulation from a single site to clusters of sites [189, 190], the combination of the DMFT with *ab initio* approaches [157, 158, 191], and the formulation of DMFT for nano-structures [192]. A common feature of all flavors of DMFT, is that the local problem (i.e., single site or cluster of sites) is solved essentially exactly. To allow such exact solvability, a reduction of the electronic degrees of freedom of the local problem to a correlated subspace is imperative. This "down-folding" into a correlated subspace is a highly nontrivial issue that is still being intensively discussed in literature [160].

Conversely, if one does not require that the local problem be solved exactly, then the projection into a correlated subspace is not necessary anymore. The price to pay is that the thus formulated scheme may not be able to properly describe "strong correlation effects" like the Mott-Hubbard metal transition for example. However, there is a large number of problems where typical strong correlation effects are not dominating so that approaches beyond LDA/GGAs are required in order to get quantitatively accurate results. These approaches include quantum chemistry methods [68], advanced exchange-correlation functionals of the 4-th and 5-th rung Jacob's ladder [193], and Green's function many body perturbation theory. All

these schemes treat electronic systems at an *ab initio* level, but are restricted to small systems.

In this chapter I will present an embedding approach for periodic systems that I have developed during my thesis and that I have implemented in the all-electron code FHI-aims [41]. The approach is called *real space dynamical mean-field embedding* (RDMFE) and is based on the concept of DMFT, while formulating it as a Green's function embedding for the above noted *ab initio* approaches. The motivation of RDMFE is to extend the reach of the approaches beyond LDA/GGAs to unprecedented system sizes. As poof-of-concept examples I take hybrid functionals and the *GW* approximation, and consider the unit cell (or any computational super cell that spans the whole space when periodically repeated) as embedded cluster (see Fig. 4.1). For clusters larger than the primitive unit cell, the formulation is similar to cluster DMFT (for a review, see Ref.[190]). in particular the cellular DMFT scheme [194]. As a consequence, the translational symmetry of the original lattice is lost and only that of the supercell is preserved (see discussion in Chapter 5).

Compared to DMFT, in RDMFE the quantum mechanical problem of the cluster is solved only approximatively. This allows the treatment of all electronic degrees of freedom on equal footing. In addition, compared to the conventional embedding approaches that I have discussed in the previous chapter, RDMFE permits charge flow between the localized region and the surrounding and therefore naturally incorporates the boundary between the two regions. Hence, neither special treatment for atoms on the boundary of the embedded region (i.e. localized region) is required, nor is there a problem with the covalent bonds of the boundary atoms.

However, before I present the embedding approach, I first introduce the numeric atom-centered orbitals in FHI-aims to set the stage for the technical discussion of the method and its implementation that will follow in this chapter.

4.1 Numeric atom-centered orbitals in FHI-aims

In *ab initio* electronic structure codes, the basis used is of major importance. It is a quantum mechanical concept, that allows to rewrite the quantum mechanical operators as matrices. This constitutes a big advantage compared to the representation in real-space, since the matrix representation is, from a numerical point of view, easier to handle. For instance, the Kohn-Sham eigenvalue equation for a periodic system is given by

$$\sum_{j}^{N_{\text{basis}}} H_{ij}(\mathbf{k}) c_j^{\nu}(\mathbf{k}) = \epsilon_{\nu}^{\mathbf{k}} \sum_{j}^{N_{\text{basis}}} S_{ij}(\mathbf{k}) c_j^{\nu}(\mathbf{k}), \tag{4.1}$$

where $\mathbf{k}$ is the reciprocal lattice vector and i, j run over the number of basis functions N_{basis}. In FHI-aims these are numeric atom-centered orbitals (NAOs). The index ν labels the Kohn-Sham state corresponding to the eigenvalue $\epsilon_{\mathbf{k}}^{\nu}$. $H_{ij}(\mathbf{k})$ is the

Hamiltonian of the system in matrix representation of the NAO basis given by

$$H_{ij}(\mathbf{k}) = \sum_{\mathbf{R}} \int d\mathbf{r}\varphi_i^*(\mathbf{r})H(\mathbf{r})\varphi_j(\mathbf{r}-\mathbf{R})e^{i\mathbf{k}\cdot\mathbf{R}}$$
$$= \int d\mathbf{r}\varphi_i^*(\mathbf{r})H(\mathbf{r})\varphi_{j\mathbf{k}}(\mathbf{r}), \tag{4.2}$$

where $\varphi_i(\mathbf{r})$ is the NAO basis function with the corresponding Bloch state $\varphi_{i\mathbf{k}}(\mathbf{r}) = \sum_{\mathbf{R}} \varphi_i(\mathbf{r}-\mathbf{R})e^{i\mathbf{k}\cdot\mathbf{R}}$, while $H(\mathbf{r})$ is the Kohn-Sham Hamiltonian and $\mathbf{R}$ are the Bravais lattice vectors. The non-orthogonality of the NAO basis is taken into account by the so-called overlap matrix $S_{ij}(\mathbf{k})$, defined as

$$S_{ij}(\mathbf{k}) = \sum_{\mathbf{R}} \int d\mathbf{r}\varphi_i^*(\mathbf{r})\varphi_j(\mathbf{r}-\mathbf{R})e^{i\mathbf{k}\cdot\mathbf{R}}$$
$$= \int d\mathbf{r}\varphi_i^*(\mathbf{r})\varphi_{j\mathbf{k}}(\mathbf{r}). \tag{4.3}$$

The NAO basis is related to the eigenstate basis of $H(\mathbf{r})$ i.e., the Kohn-Sham basis $\psi_{\nu,\mathbf{k}}(\mathbf{r})$, through the expansion coefficients $c_i^\nu(\mathbf{k})$ via

$$\psi_{\nu,\mathbf{k}}(\mathbf{r}) = \sum_i c_i^\nu(\mathbf{k})\varphi_{i\mathbf{k}}(\mathbf{r}). \tag{4.4}$$

In FHI-aims the NAO basis set $\{\varphi(\mathbf{r})\}$ is of the following form

$$\varphi_i(\mathbf{r}) = \frac{u_i(r)}{r} Y_{lm}(\Omega). \tag{4.5}$$

The so-called radial functions $u_i(r)$ are numerically tabulated and hence fully flexible to choose. To keep $\varphi_i(\mathbf{r})$ real, the complex spherical harmonics have been divided into a real part $Y_{lm}(\Omega)$ for $(m = 0, ..., l)$ and imaginary part for $(m = -l, ..., -1)$. The advantages of NAOs have been already demonstrated in a number of previous implementations [195, 196, 197]. The flexibility of the choice of the radial functions allows the creation of optimized element-dependent basis sets, that can be kept as compact as possible providing a systematically improvable high accuracy for the calculation of physical quantities. Furthermore, each radial function $u_i(r)$ can be localized inside a given radius, allowing a clear separation of the spatial regions. This enables a nearly quadratical $\mathcal{O}(N^2)$ scaling with system size N.
The NAO basis sets in FHI-aims are called *tiers*. With increasing number of *tiers* i.e., *tier*1, *tier*2, ...,*etc.*, the accuracy is improved but also the computational cost grows. For an overview over *tiers* basis sets the reader is referred to Ref. [41].

4.2 The Embedding Green's functions with NAOs

As mentioned above, the embedding formalism I have developed during my thesis, relies on Green's functions. I have implemented this new concept in FHI-aims [41]. Since I will be using operators in the non-orthogonal NAO basis, it makes sense to

first understand and derive the relevant Green's functions in this basis. As I have explained in Chapter 1, the Green's function for the Hamiltonian of an extended crystal $H(\mathbf{r},\mathbf{r}')$ in real space is given by

$$\int d\mathbf{r}'' \left[(i\omega+\mu) - H(\mathbf{r},\mathbf{r}'')\right] G(\mathbf{r}'',\mathbf{r}',i\omega) = \delta(\mathbf{r}-\mathbf{r}'), \tag{4.6}$$

with μ being the chemical potential. Using the expansion of the Green's function

$$G(\mathbf{r},\mathbf{r}',i\omega) = \sum_{\mathbf{k}} \sum_{ij} G_{ij}(\mathbf{k},i\omega)\varphi_{i\mathbf{k}}(\mathbf{r})\varphi^*_{j\mathbf{k}}(\mathbf{r}'), \tag{4.7}$$

in Bloch states of the NAO basis $\varphi_{i,\mathbf{k}}(\mathbf{r})$. Multiplying from left by $\varphi_n(\mathbf{r})$ and integrating over $d\mathbf{r}, d\mathbf{r}''$ yields

$$\sum_{\mathbf{k}} \sum_{ij} [(i\omega+\mu)\varphi^*_{j\mathbf{k}}(\mathbf{r}')S_{ni}(\mathbf{k}) - \varphi^*_{j\mathbf{k}}(\mathbf{r}')H_{ni}(\mathbf{k})]G_{ij}(\mathbf{k},i\omega) = \varphi^*_n(\mathbf{r}'),$$

where I considered the non-orthogonality of the NAO basis i.e., $S_{ij}(\mathbf{k}) = \int d\mathbf{r}\varphi^*_i(\mathbf{r})\varphi^*_{j\mathbf{k}}(\mathbf{r})$. Subsequent multiplication with $\varphi_m(\mathbf{r}')$ and integration over $d\mathbf{r}'$ yields

$$\sum_{\mathbf{k}} \sum_{ij} [(i\omega+\mu)S_{jm}(\mathbf{k})S_{ni}(\mathbf{k}) - S_{jm}(\mathbf{k})H_{ni}(\mathbf{k})]G_{ij}(\mathbf{k},i\omega) = S_{nm},$$

with the NAO overlap matrix $S_{mn} = \int d\mathbf{r}\varphi^*_m(\mathbf{r})\varphi_n(\mathbf{r})$. The lattice Green's function follows if one multiplies with $\sum_{\mathbf{q}} \sum_m S^{-1}_{ml}(\mathbf{q})$ and uses the relation $\sum_m S_{jm}(\mathbf{k})S^{-1}_{ml}(\mathbf{q}) = \delta_{jl}\delta(\mathbf{k}-\mathbf{q})$

$$\sum_{\mathbf{k}} \sum_{i} \left[(i\omega+\mu)S_{ni}(\mathbf{k}) - H_{ni}(\mathbf{k})\right] G_{il}(\mathbf{k},i\omega) = \delta_{nl}. \tag{4.8}$$

I call $G_{il}(\mathbf{k},i\omega)$ the lattice Green's function G^{lat} for the Hamiltonian $H(\mathbf{k}) = H^0(\mathbf{k}) + \Sigma(\mathbf{k},i\omega)$ with H^0 the non-interacting Hamiltonian (i.e., Kohn-Sham Hamiltonian) and interactions described by the lattice self-energy $\Sigma(\mathbf{k},i\omega)$

$$G^{\text{lat}}_{ij}(\mathbf{k},i\omega) \equiv G_{ij}(\mathbf{k},i\omega) = \Big[(i\omega+\mu)S(\mathbf{k}) - H^0(\mathbf{k}) - \Sigma(\mathbf{k},i\omega)\Big]^{-1}_{ij}. \tag{4.9}$$

Relation between the NAO and the Kohn-Sham Green's function

In the Kohn-Sham basis $\{\psi_{\nu\mathbf{k}}\}$, the non-interacting Green's function $G^0_{\nu\mu}$ corresponding to the non-interacting Kohn-Sham Hamiltonian $H^0(\mathbf{k})$ is diagonal and can be written as

$$G^0(\mathbf{r},\mathbf{r}',i\omega) = \sum_{\mathbf{k}} \sum_{\nu} G^0_{\nu}(\mathbf{k},i\omega)\psi_{\nu\mathbf{k}}(\mathbf{r})\psi^*_{\nu\mathbf{k}}(\mathbf{r}'). \tag{4.10}$$

Inserting the NAO expansion Eq. (4.7)

$$G^0(\mathbf{r},\mathbf{r}',i\omega) = \sum_{ij} G^0_{ij}(\mathbf{k},i\omega)\varphi_{i\mathbf{k}}(\mathbf{r})\varphi^*_{j\mathbf{k}}(\mathbf{r}') = \sum_{\nu} G^0_{\nu}(\mathbf{k},i\omega)\psi_{\nu\mathbf{k}}(\mathbf{r})\psi^*_{\nu\mathbf{k}}(\mathbf{r}'), \tag{4.11}$$

and multiplying with $\varphi^*_n(\mathbf{r})\varphi_m(\mathbf{r}')$ yields

$$\sum_{ij} G^0_{ij}(\mathbf{k},i\omega)\varphi^*_n(\mathbf{r})\varphi_{i\mathbf{k}}(\mathbf{r})\varphi^*_{j\mathbf{k}}(\mathbf{r}')\varphi_m(\mathbf{r}') = \sum_{\nu} G^0_{\nu}(\mathbf{k},i\omega)\psi_{\nu\mathbf{k}}(\mathbf{r})\varphi^*_n(\mathbf{r})\psi^*_{\nu\mathbf{k}}(\mathbf{r}')\varphi_m(\mathbf{r}'). \tag{4.12}$$

One can now use the relation $\psi_{\nu,\mathbf{k}}(\mathbf{r}) = \sum_i c^{\nu}_i(\mathbf{k})\varphi_{i\mathbf{k}}(\mathbf{r})$ between the Kohn-Sham and the NAO basis which gives, after integration over $\mathbf{r}$ and $\mathbf{r}'$,

$$\sum_{ij} G^0_{ij}(\mathbf{k},i\omega)S_{ni}(\mathbf{k})S_{jm}(\mathbf{k}) = \sum_{\nu} S_{ni}(\mathbf{k})c^{\nu}_i(\mathbf{k})G^0_{\nu}(\mathbf{k},i\omega)c^{*,\nu}_j(\mathbf{k})S_{jm}(\mathbf{k}). \tag{4.13}$$

To get rid of the overlap matrices, one can again multiply with the inverse overlap matrix to get the final expression

$$G^0_{ij}(\mathbf{k},i\omega) = \sum_{\nu\mu} c^{\nu}_i(\mathbf{k})G^0_{\nu}(\mathbf{k},i\omega)c^{*,\nu}_j(\mathbf{k}) \tag{4.14}$$

For the Kohn-Sham Hamiltonian, $G^0_{\nu}(\mathbf{k},i\omega)$ is diagonal and given by the expression

$$G^0_{\nu}(\mathbf{k},i\omega) = \frac{1}{(i\omega+\mu)-\epsilon^{\nu}_{\mathbf{k}}}, \tag{4.15}$$

with the Kohn-Sham eigenvalues $\epsilon_{\mathbf{k}}$. For the Lattice Green's function Eq. (4.9) however, the corresponding Kohn-Sham Green's function is not diagonal and is given by

$$G_{ij}(\mathbf{k},i\omega) = \sum_{\nu\mu} = c^{\nu}_i(\mathbf{k})\left[(i\omega+\mu)-\epsilon_{\mathbf{k}}\delta_{\nu\mu}-\Sigma_{\nu\mu}(\mathbf{k},i\omega)\right]^{-1} c^{*,\mu}_j(\mathbf{k}) \tag{4.16}$$

As discussed in Chapter 3 for DMFT, the $\mathbf{k}$-dependent lattice Green's function Eq. 4.9 constitutes a key quantity in the present formalism since it explicitly enters the definition of the "on-site" Green's function as I will show in the next section. In the following, I present the embedding Green's functions that maps the real crystal onto an effective system of an on-site region interacting with a surrounding electronic bath, in the same spirit as in DMFT presented in Chapter 3 of this dissertation.

4.2.1 The "on-site" Green's function for a periodic system

I have demonstrated in Chapter 3, that the so-called "on-site" Green's function is a key quantity in DMFT. I want here to derive the "on-site" Green's function from

the lattice Green's function as given by Eq. (4.9). The relation between the unit cells and the **k**-dependent lattice Green's function and self-energy in Eq. 4.9 can be established via the Fourier-transform to real-space,

$$G_{ij}^{\mathrm{lat}}(\mathbf{R}_i - \mathbf{R}_j, i\omega) = \frac{1}{\mathrm{N}_{1.\mathrm{BZ}}} \sum_{\mathbf{k}}^{1.\mathrm{BZ}} e^{i(\mathbf{R}_i - \mathbf{R}_j)\cdot\mathbf{k}} G_{ij}^{\mathrm{lat}}(\mathbf{k}, i\omega)$$
$$\Sigma_{ij}(\mathbf{R}_i - \mathbf{R}_j, i\omega) = \frac{1}{\mathrm{N}_{1.\mathrm{BZ}}} \sum_{\mathbf{k}}^{1.\mathrm{BZ}} e^{i(\mathbf{R}_i - \mathbf{R}_j)\cdot\mathbf{k}} \Sigma_{ij}(\mathbf{k}, i\omega) \tag{4.17}$$

where $\mathbf{R}_i$ and $\mathbf{R}_j$ are Bravais lattice vectors denoting the unit cells in which the basis functions i and j are located. $N_{1.\mathrm{BZ}}$ is the number of **k**-points in the first Brillouin zone (1.BZ). The concept of DMFT is based on the fact that the lattice self-energy becomes local, or **k**-independent, in infinite dimension ($D = \infty$) [25]. For a crystal with translational symmetry this implies (see Chapter 3 for further reading on the DMFT scaling)

$$\Sigma_{ij}(\mathbf{R}_i - \mathbf{R}_j, i\omega) = \Sigma_{ij}^{\mathrm{loc}}(i\omega)\delta_{\mathbf{R}_i,\mathbf{R}_j} \,. \tag{4.18}$$

Thus, the self-energy is non-zero only if the two basis functions originate from the same unit cell. I call this the local (loc) or "on-site" self-energy, following the terminology of the model-Hamiltonian community. In this limit, the whole periodic system can be mapped onto an effective impurity model of a local unit cell dynamically coupled to an effective "external" potential arising from the rest of the crystal.

The first step in establishing this mapping is to define the "on-site" Green's function, i.e., $G_{ij}(\mathbf{R}_i - \mathbf{R}_j, i\omega)$ with $\mathbf{R}_i$=$\mathbf{R}_j$. Using the locality of the self-energy and Eq. (4.9), one obtains the following expression for the on-site Green's function,

$$G_{ij}^{\text{on-site}}(i\omega) = \frac{1}{N_{1.\mathrm{BZ}}} \sum_{\mathbf{k}}^{1.\mathrm{BZ}} G_{ij}^{\mathrm{lat}}(\mathbf{k}, i\omega) =$$
$$\frac{1}{N_{1.\mathrm{BZ}}} \sum_{\mathbf{k}}^{1.\mathrm{BZ}} \left[(i\omega + \mu)S(\mathbf{k}) - H^0(\mathbf{k}) - \Sigma^{\mathrm{loc}}(i\omega)\right]_{ij}^{-1} . \tag{4.19}$$

In the DMFT context this equation is also known as the **k**-integrated Dyson equation. In RDMFE, the environment is treated by KS-DFT in the LDA or PBE. A natural choice of H^0 is thus the KS-Hamiltonian $H^{\mathrm{KS}}(\mathbf{k})$ within LDA or GGA, that contains the kinetic-energy operator, the external potential (v_{ext}), the Hartree potential (v_{H}), and the exchange-correlation (XC) potential (v_{XC})

$$H^{\mathrm{KS}}(\mathbf{k}) = -\frac{1}{2}\nabla^2 + v_{\mathrm{ext}}(\mathbf{k}) + v_{\mathrm{H}}(\mathbf{k}) + v_{\mathrm{XC}}(\mathbf{k}) \,. \tag{4.20}$$

One needs furthermore to define $\Sigma^{\mathrm{loc}}(i\omega)$ in Eq. (4.19). If one starts from $H^{\mathrm{KS}}(\mathbf{k})$, the "on-site" self-energy becomes the difference between the dynamic, complex many-body exchange-correlation self-energy $\Sigma_{\mathrm{XC}}(\mathbf{k}, i\omega)$ and the KS XC potential,

i.e.,

$$\begin{aligned}\Sigma^{\text{loc}}(i\omega) &= \frac{1}{N_{1.\text{BZ}}} \sum_{\mathbf{k}}^{1.\text{BZ}} \left[\Sigma_{\text{XC}}(\mathbf{k}, i\omega) - v_{\text{XC}}^{\text{KS}}(\mathbf{k})\right] \\ &= \Sigma_{\text{XC}}^{\text{loc}}(i\omega) - v_{\text{XC}}^{\text{loc}} \,. \end{aligned} \tag{4.21}$$

Using Eqs. (4.19) and (4.21), one finally obtains

$$\begin{aligned} &G_{ij}^{\text{on-site}}(i\omega) = \\ &\frac{1}{N_{1.\text{BZ}}} \sum_{\mathbf{k}}^{1.\text{BZ}} \left[(i\omega + \mu)S(\mathbf{k}) - H^{\text{KS}}(\mathbf{k}) - \Sigma_{\text{XC}}^{\text{loc}}(i\omega) + v_{\text{XC}}^{\text{loc}}\right]_{ij}^{-1} . \end{aligned} \tag{4.22}$$

RDMFE is thus free from any double-counting ambiguities, because the DFT XC-contribution that has to be subtracted is uniquely defined (see the discussion on double-counting in DMFT in Chapter 3).

4.2.2 The embedded Green's function

In the DMFT formalism (Chapter 3), a periodic system is viewed as a periodically repeated cluster (here the unit or super-cell) which is dynamically embedded into a self-consistently determined environment. The coupling between the embedded subsystem and its surrounding environment is described by a so-called bath Green's function $\mathcal{G}(i\omega)$, connecting the Green's function of the embedded cluster $G^{\text{emb}}(i\omega)$ and the local self-energy via

$$[\mathcal{G}(i\omega)]_{ij}^{-1} = \left[G^{\text{emb}}(i\omega)\right]_{ij}^{-1} + \Sigma_{ij}^{\text{loc}}(i\omega) \,. \tag{4.23}$$

Here the local self-energy $\Sigma^{\text{loc}}(i\omega)$ is the same as introduced in Eq. (4.21). The self-consistency condition of DMFT requires that the Green's function of the embedded cluster $G^{\text{emb}}(i\omega)$ equals the on-site Green's function as given in Eq. (4.19),

$$G^{\text{emb}}(i\omega) = G^{\text{on-site}}(i\omega) \,. \tag{4.24}$$

A more intuitive picture can be alternatively provided if one uses a so-called hybridization function $\Delta(i\omega)$ to describe the coupling between the embedded cluster and its environment. $\Delta(i\omega)$ is closely related to the bath Green's function $\mathcal{G}(i\omega)$,

$$[\mathcal{G}(i\omega)]_{ij}^{-1} \;=\; \left[(i\omega + \mu)S - H_0^{\text{cluster}} - \Delta(i\omega)\right]_{ij} . \tag{4.25}$$

In Eq. (4.25) H_0^{cluster} is the Hamiltonian of the bare cluster describing the non-interacting unit cell i.e., without the $v_{\text{XC}}^{\text{KS}}$ contribution and without the presence of the other atoms from neighboring unit cells (see Fig. (4.1)). This corresponds to the "on-site" term of the Hamiltonian of the periodic system, and in practice can be conveniently obtained from the $\mathbf{k}$-dependent Hamiltonian,

$$H_0^{\text{cluster}} \;=\; \frac{1}{N_{1.\text{BZ}}} \sum_{\mathbf{k}}^{1.\text{BZ}} \left[H^{\text{KS}}(\mathbf{k}) - v_{\text{XC}}^{\text{KS}}(\mathbf{k})\right] . \tag{4.26}$$

Using Eqs. (4.23)-(4.25), one obtains the following expression for the Green's function of the embedded cluster

$$\left[G^{\mathrm{emb}}(i\omega)\right]^{-1}_{ij} = \left[(i\omega+\mu)S - H_0^{\mathrm{cluster}} - \Sigma^{\mathrm{loc}}[G^{\mathrm{emb}}](i\omega) - \Delta(i\omega)\right]_{ij}. \tag{4.27}$$

In the expression above, I have explicitly indicated that the local self-energy is a functional of the embedded Green's function. Thus Eq. (4.27) has to be solved self-consistently, which corresponds to the inner loop of Fig. (4.2). A more detailed discussion of the self-consistency cycle defined be the embedding Green's functions will be provided later in this chapter. The functional dependence of $\Sigma^{\mathrm{loc}}(i\omega)$ on $G^{\mathrm{emb}}(i\omega)$ is given by the actual approximation for the localized region, which will be the topic of the next section. However, already here one sees that the RDMFE approach lends itself to those advanced electronic-structure methods that can be expressed by (self-consistent) Green's functions. Figure (4.1) schematically illustrates a Silicon lattice treated with the RDMFE approach.

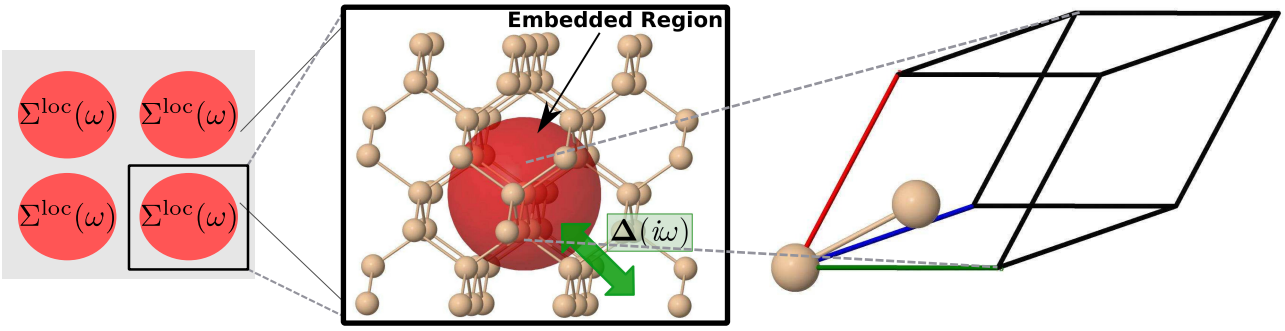

Figure 4.1: The RDMFE concept for a Si lattice. The atoms in the unit cell (red region) constitute the embedded sub-manifold. Each unit cell of the periodic system is treated as a localized region, i.e. only local interactions Σ^{loc} are considered. The unit cells are coupled to the rest of the system via the hybridization self-energy $\Delta(i\omega)$ (green arrow).

4.3 The local self-energy

In an analogous philosophy as for DMFT, one needs to solve the "impurity problem", that is the unit cell coupled to the periodic electronic bath. In other words, one needs to choose an impurity solver. In contrast to DMFT, in RDMFE all the electronic levels that enter a specific system are considered. Hence, QMC or renormalization group techniques are out of the question. Although in principle, one could use any approximation that goes beyond LDA and GGAs, the framework is based on Green's functions. This includes density-matrix and density-based approaches, because both quantities can easily be extracted from the single particle Green's function. In this thesis, two different self-energies have been implemented. The first one is based on

hybrid density functionals that mix a fraction of exact-exchange with GGA semi-local exchange [111, 93, 116], and the second is the GW approximation to the self-energy [40]. In practice, more sophisticated self-energies that go beyond GW are also possible e.g., by including the screened second-order exchange (SOSEX) self-energy that was developed recently [198]. Before I introduce the local self-energy, I want to briefly address the resolution of identity (RI) concept in FHI-aims. This is of particular importance for my work, since all the quantities needed to evaluate the local self-energy use this formalism.

4.3.1 The resolution of identity for NAOs

In an NAO basis the calculation of two-electron four-orbital integrals such as the one for the Coulomb operator V

$$\langle ij|kl\rangle \equiv \langle ij|V|kl\rangle = \int d\mathbf{r}d\mathbf{r}' \frac{\varphi_i(\mathbf{r})\varphi_j(\mathbf{r})\varphi_k(\mathbf{r}')\varphi_l(\mathbf{r}')}{|\mathbf{r}-\mathbf{r}'|}, \tag{4.28}$$

is not an easy task. In contrast to Gaussian based codes, where such integrals have an analytic expression, in the NAO case no analytical solution is possible. Hence, the large number of NAO pairs needed to be stored to evaluate such expressions, requires an important amount of memory (i.e., $\mathcal{O}(N^4)$ with number of basis functions considered in the calculation). This makes four-center integrals numerically very impractical in an NAO framework. The same holds for the evaluation of the polarizability in GW or the related screened Coulomb interaction W. To reduce the numerical costs raised by these integrals, one of the techniques that has been developed over the past years is the resolution of identity (RI)[199, 200, 201, 202, 203, 204]. The RI formalism as it is implemented in FHI-aims [43] enables an efficient evaluation of integrals such as the one in Eq. (4.28) by introducing an auxiliary basis $\{P_\mu(\mathbf{r})\}$ that are defined as an expansion of NAO product basis functions

$$\varphi_i(\mathbf{r})\varphi_j(\mathbf{r}) \approx \sum_{\mu}^{N_{\text{aux}}} C_{ij}^{\mu} P_\mu(\mathbf{r}), \tag{4.29}$$

where μ and ν run over auxiliary basis functions. The auxiliary NAO basis pairs are linear dependent, which makes it possible that the number of auxiliary basis functions N_{aux} can be hold reasonably small and always smaller than the number of NAO basis pairs, that scales as $\mathcal{O}(N_{basis}^2)$. It is this simplification that makes integrals like the one in Eq. (4.28) numerically affordable for NAOs. The determination of the expansion coefficients C_{ij}^{μ} can be performed using the variational approach as reported in Ref.[43]. In this implementation the so-called "RI-V" was used. Here the expansion coefficients are given by

$$C_{ij}^{\mu} = \sum_{\nu} \langle ij|\nu\rangle V_{\mu\nu}^{-1}, \tag{4.30}$$

with $\langle ij|\nu\rangle = \int \varphi(\mathbf{r})_i \varphi(\mathbf{r})_j P_\nu(\mathbf{r}')V(\mathbf{r}-\mathbf{r}')d\mathbf{r}d\mathbf{r}'$ and the matrix elements of the bare Coulomb potential $V(|\mathbf{r}-\mathbf{r}'|)$ in the auxiliary basis

$$V_{\mu\nu} = \int P_\nu(\mathbf{r})V(\mathbf{r}-\mathbf{r}')P_\nu(\mathbf{r}')d\mathbf{r}d\mathbf{r}'. \tag{4.31}$$

For a two particle operator $\mathcal{O}$, one can define the more general expression relating the operator in real space and its matrix element in the auxiliary basis

$$\mathcal{O}(\mathbf{r},\mathbf{r}') = \sum_{\mu\gamma,\nu\delta} P_\mu(\mathbf{r})\tilde{S}^{-1}_{\mu,\gamma}\mathcal{O}_{\gamma\delta}\tilde{S}^{-1}_{\delta,\nu}P_\nu(\mathbf{r}'), \tag{4.32}$$

with the overlap matrix of the auxiliary basis $\tilde{S}_{\mu,\nu} = \int d\mathbf{r} P_\mu(\mathbf{r})P_\nu(\mathbf{r})$, that takes the non-orthogonality of the auxiliary basis into account. Similarly I can write

$$\mathcal{O}_{\mu\nu} = \int d\mathbf{r}d\mathbf{r}' P_\mu(\mathbf{r})\mathcal{O}(\mathbf{r},\mathbf{r}')P_\nu(\mathbf{r}'). \tag{4.33}$$

4.3.2 Hybrid local self-energies

For the hybrid functional based local self-energy, I use the PBE hybrid functional family (PBEh) [205], whose most prominent functional is PBE0 [115]. Furthermore the short-ranged range-separated hybrid functional family HSE [116] will also be used. In PBEh the local self-energy in Eq. (4.21) is given by

$$\begin{aligned}\Sigma^{\mathrm{loc}}_{\mathrm{PBEh}}(\alpha) &= \left[\alpha\Sigma^{\mathrm{loc}}_{\mathrm{X}} + (1-\alpha)v^{\mathrm{loc}}_{\mathrm{X}} + v^{\mathrm{loc}}_{\mathrm{C}}\right] - v^{\mathrm{loc}}_{\mathrm{XC}} \\ &= \alpha\left(\Sigma^{\mathrm{loc}}_{\mathrm{X}} - v^{\mathrm{loc}}_{\mathrm{X}}\right).\end{aligned} \tag{4.34}$$

The PBE0 functional is obtained for α=0.25 [115]. In Eq. (4.34), $v^{\mathrm{loc}}_{\mathrm{X}}$ is the "on-site" part of the GGA exchange, and $\Sigma^{\mathrm{loc}}_{\mathrm{X}}$ is the exact-exchange matrix given by

$$\left[\Sigma^{\mathrm{loc}}_{\mathrm{X}}\right]_{ij} = \sum_{k,l}\langle ik|lj\rangle n^{\mathrm{emb}}_{kl}, \tag{4.35}$$

where n^{emb}_{kl} is the density matrix of the embedded cluster which can be obtained from the embedded Green's function

$$n^{\mathrm{emb}}_{ij} = -\frac{i}{2\pi}\int d\omega\, G^{\mathrm{emb}}(i\omega)_{ij}e^{i\omega\tau^+}. \tag{4.36}$$

$\langle ik|lj\rangle$ are two-electron four-orbital integrals given by

$$\langle ik|lj\rangle \approx \sum_{\mu\nu} C^\mu_{ik}V_{\mu\nu}C^\nu_{lj}, \tag{4.37}$$

where μ,ν are indices of the auxiliary basis functions and $V_{\mu\nu} = \int P_\mu(\mathbf{r})P_\nu(\mathbf{r}')V(\mathbf{r}-\mathbf{r}')d\mathbf{r}d\mathbf{r}'$ is the bare Coulomb potential in the auxiliary basis.
The extension to an HSE [116] type self-energy is straightforward. In HSE, a range-separation parameter is introduced that cuts off the exact-exchange contribution at long distances. The range is controlled via the screening parameter γ so that the local exchange self-energy becomes

$$\Sigma^{\mathrm{loc}}_{\mathrm{X}}(\gamma) = \Sigma^{\mathrm{loc,SR}}_{\mathrm{X}}(\gamma) + \Sigma^{\mathrm{loc,LR}}_{\mathrm{X}}(\gamma), \tag{4.38}$$

with SR and LR denoting the short and long-range part, respectively. If one now replaces $\Sigma^{\mathrm{loc,LR}}_{\mathrm{X}}(\gamma)$ by $v^{\mathrm{loc,LR}}_{\mathrm{X}}$ and introduce the α parameter again, the local HSE self-energy assumes the following form

$$\Sigma^{\mathrm{loc}}_{\mathrm{HSE}}(\alpha,\gamma) = \alpha\left(\Sigma^{\mathrm{SR,loc}}_{\mathrm{X}}(\gamma) - v^{\mathrm{SR,loc}}_{\mathrm{X}}(\gamma)\right), \tag{4.39}$$

defining the local HSE self-energy as I have implemented it for the RDMFE scheme.

4.3.3 The *GW* local self-energy

Furthermore, the *GW* approximation for the local self-energy is used as an "impurity" solver in RDMFE. Here, the computation of the *GW* self-energy for a given input embedded Green's function follows the self-consistent *GW* implementation for finite systems in FHI-aims [43, 206]. On the imaginary time axis, the *GW* self-energy for the embedded unit cell is obtained as

$$[\Sigma^{\mathrm{loc}}_{\mathrm{XC}}(i\tau)]_{ij} = \frac{i}{2\pi}\sum_{lk\mu\nu} M^{\mu}_{ik} M^{\nu}_{lj} G^{\mathrm{emb}}_{kl}(i\tau)[W^{\mathrm{loc}}(i\tau)]_{\mu\nu}\,. \tag{4.40}$$

Here μ, ν indices refer to the auxiliary basis set used to expand the screened Coulomb interaction W^{loc} in the RI approach [43, 206]. Furthermore M^{μ}_{ik} are the 3-index coefficients obtained as,

$$M^{\mu}_{ik} = \sum_{v}(ik|\mu)V^{-1/2}_{\mu\nu}\,. \tag{4.41}$$

For W one thus obtains

$$W^{\mathrm{loc}}_{\mu\nu}(i\omega) = \sum_{\alpha} V_{\mu\alpha}[1 - \Pi^{\mathrm{loc}}(i\omega)]^{-1}_{\alpha\nu} \tag{4.42}$$

where $\Pi^{\mathrm{loc}}(i\omega)$ is the irreducible polarisability, whose Fourier transform in the time domain is directly determined by the embedded Green's function

$$\Pi^{\mathrm{loc}}_{\mu\nu}(i\tau) = -i\sum_{ijlm} M^{\mu}_{il} M^{\nu}_{jm} G^{\mathrm{emb}}_{ij}(i\tau) G^{\mathrm{emb}}_{lm}(-i\tau). \tag{4.43}$$

4.4 The RDMFE self-consistency cycle

In RDMFE, Eqs. (4.27) and (4.35) or (4.40) define an additional "inner" self-consistency loop for a given local self-energy as depicted in Fig. (4.2). It is obvious that the convergence behavior of the iterative loop is dependent on the choice of the theory with which the local self-energy is treated. In fact for the PBE0 self-energy, one only needs to calculate the exact exchange potential and use it to correct a fraction of the KS-DFT exchange. Hence, the convergence of such a cycle is much faster than e.g., the one with a *GW* self-energy, where both the exchange and the correlation parts of the Hamiltonian are updated.

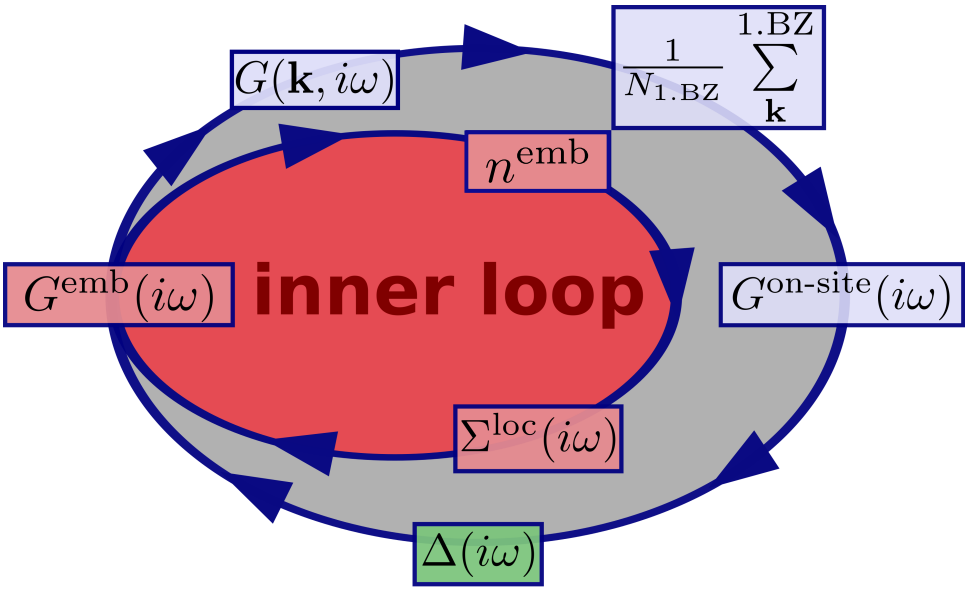

Figure 4.2: The embedded (Eq. 4.27) and the on-site (Eq. 4.19) Green's functions define two Dyson equations that form two nested loops. The two loops are iterated until self-consistency is reached.

Nevertheless, to accelerate convergence of the loop, a linear mixing scheme is used for the self-energy

$$\Sigma^{\mathrm{loc}}_{n+1} = \lambda \Sigma^{\mathrm{loc}}_{n} + (1-\lambda)\Sigma^{\mathrm{loc}}_{n-1}, \tag{4.44}$$

with a mixing parameter λ. Here $\Sigma^{\mathrm{loc}}_{n}$ is the self-energy for the current iteration n, $\Sigma^{\mathrm{loc}}_{n+1}$ denotes the self-energy that is going to be used for the next iteration and $\Sigma^{\mathrm{loc}}_{n-1}$ refers to the one from the previous iteration. Figure (4.3) shows a typical behavior of the number of iterations of the inner loop versus the iterations of the outer loop. For the first and second outer loop iterations, the inner loop iterations increase before they systematically decrease to only one iteration at convergence. I typically choose a mixing parameter of $\lambda = 0.5$.

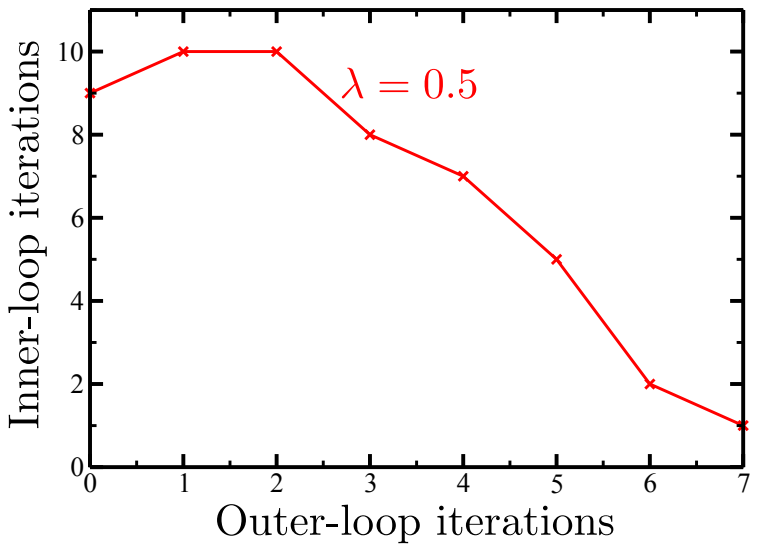

Figure 4.3: Inner loop versus outer loop iterations for a Si bulk with a PBE0 local self-energy. The calculation was performed with a *tier1* basis.

Furthermore, the convergence of the self-consistency cycles is controlled by computing the average deviation δ_{dev} of the embedded (for the inner loop) and the on-site (for the outer loop) Green's functions at each iteration. δ_{dev} is given by

$$\delta_{\text{dev}} = \frac{1}{N_{\text{basis}}^2} \sum_{ij}^{N_{\text{basis}}} \int ||G_{ij}^{n,\text{emb/on-site}}(i\omega) - G_{ij}^{n-1,\text{emb/on-site}}(i\omega)||d\omega, \tag{4.45}$$

with the number of basis functions N_{basis}. The self-consistency cycle is considered converged if δ_{dev} is gets less than a given threshold value. Although strongly system dependent, typically an average deviation of $\delta_{\text{dev}} = 10^{-5}$ is set throughout the hole thesis. I found that for this threshold the convergence of the physical quantities is best. Figure (4.4) shows the evolution of the average deviation with iterations of the outer loop for different values of mixing parameter λ. Increasing the mixing yields slower convergence.

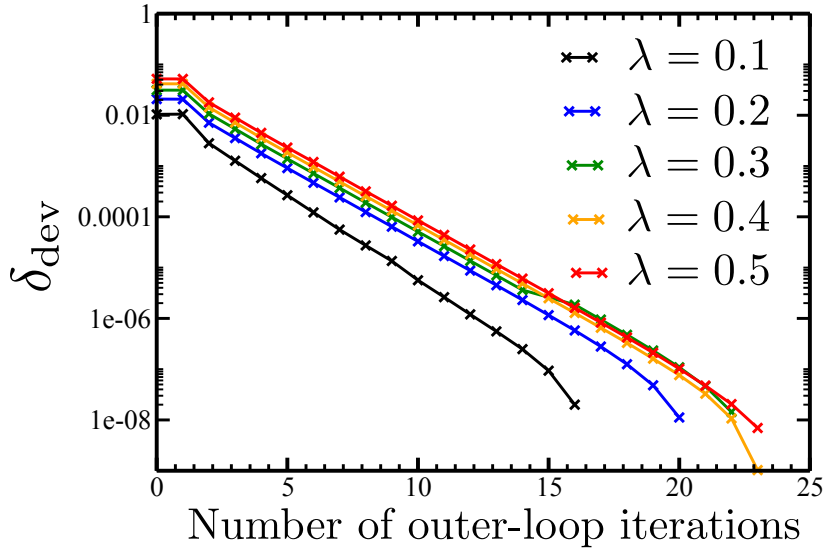

Figure 4.4: The avergave deviation with outer loop iterations for different values of the mixing parameter λ. The calculations was done for bulk Si with a PBE0 self-energy and *tier1* basis.

More elaborate mixing schemes could be implemented as well, but I found that linear mixing works well for the examples presented in this thesis. When the inner loop reaches convergence the resulting Σ^{loc} is fed back into the on-site GF and iterate the main-loop further using the same mixing as for the inner loop. It is worth mentioning, that the on-site Green's function as defined in Eq. (4.19) requires that the Σ^{loc} in the 0-th iteration should be $\Sigma_0^{\mathrm{loc}} = V_{\mathrm{XC}}^{\mathrm{loc}}$. Figure (4.2) shows a sketch of the embedding scheme as described above. The behavior on the embedding Green's functions with iterations of self-consistency cycle is shown in Figs. (4.5)-(4.7). Figure (4.5) illustrates the evolution of an element of the on-site Green's function with outer loop iterations for a PBE0 self-energy. Both the real and imaginary parts of the Green's function are represented and reach their converged values in a reasonable number of iterations. In Figure (4.6) the real part of the embedded Green's function versus iterations of the outer loop (upper panel) and inner loop (lower panel) is depicted. In the upper panel the embedded Green's function at zeroth inner loop iteration for different outer loop iterations is illustrated. In the inner loop the change of the embedded Green's function is less important than it is for the outer loop. However, as shown in Fig. (4.3), the convergence of the inner loop accelerates the outer loop convergence. Finally, the evolution of the imaginary part of the hybridization function $\Delta(i\omega)$ with outer loop iterations is represented in Fig. (4.7).

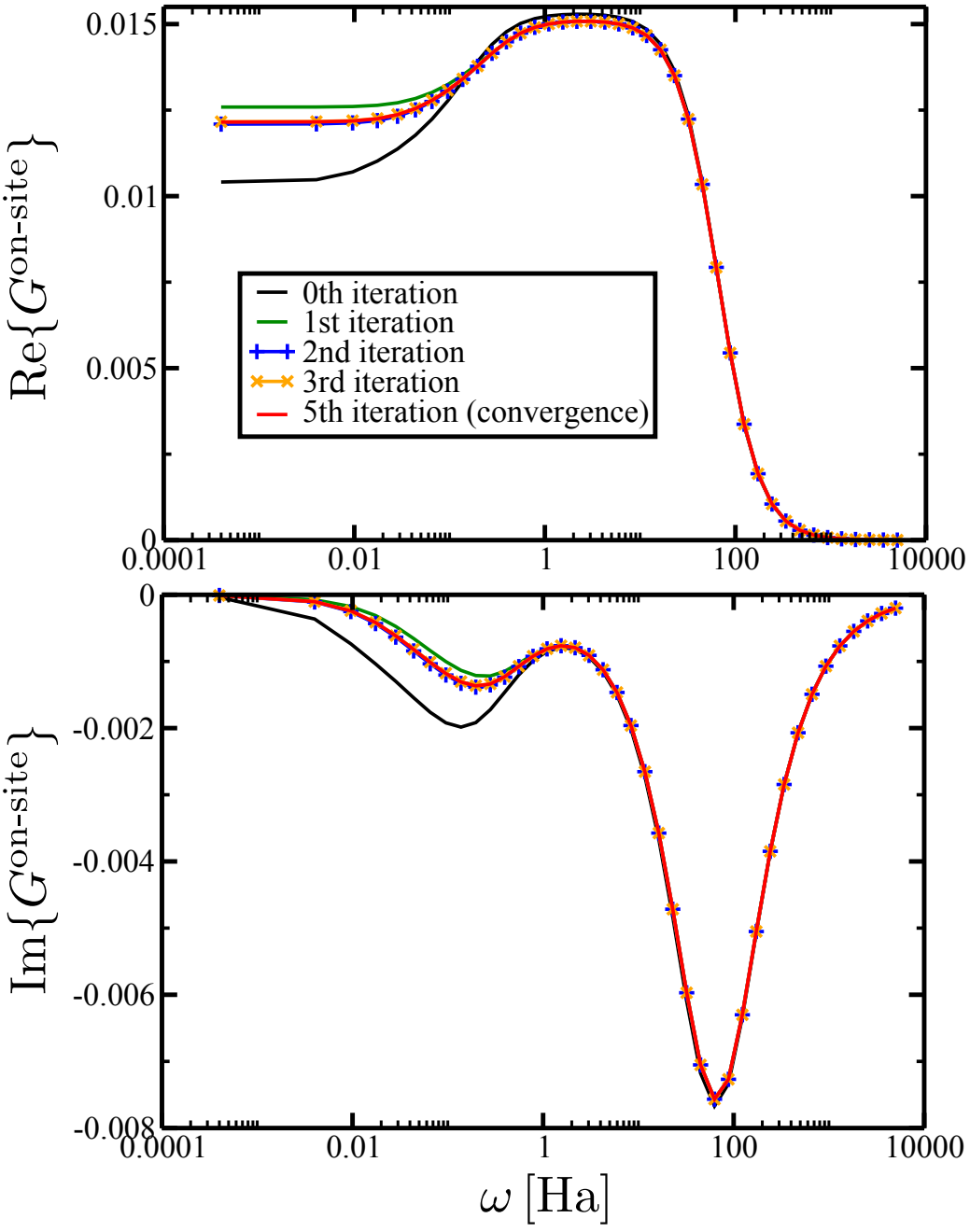

Figure 4.5: Real and imaginary parts of the first diagonal element of the on-site Green's function with a PBE0 self-energy, for bulk Si with two atoms in the unit cell and *tier1* basis. Upper panel: the real part of the on-site Green's function at different iterations of the outer loop. Lower panel: the imaginary part of the on-site Green's function at different iteration of the outer loop.

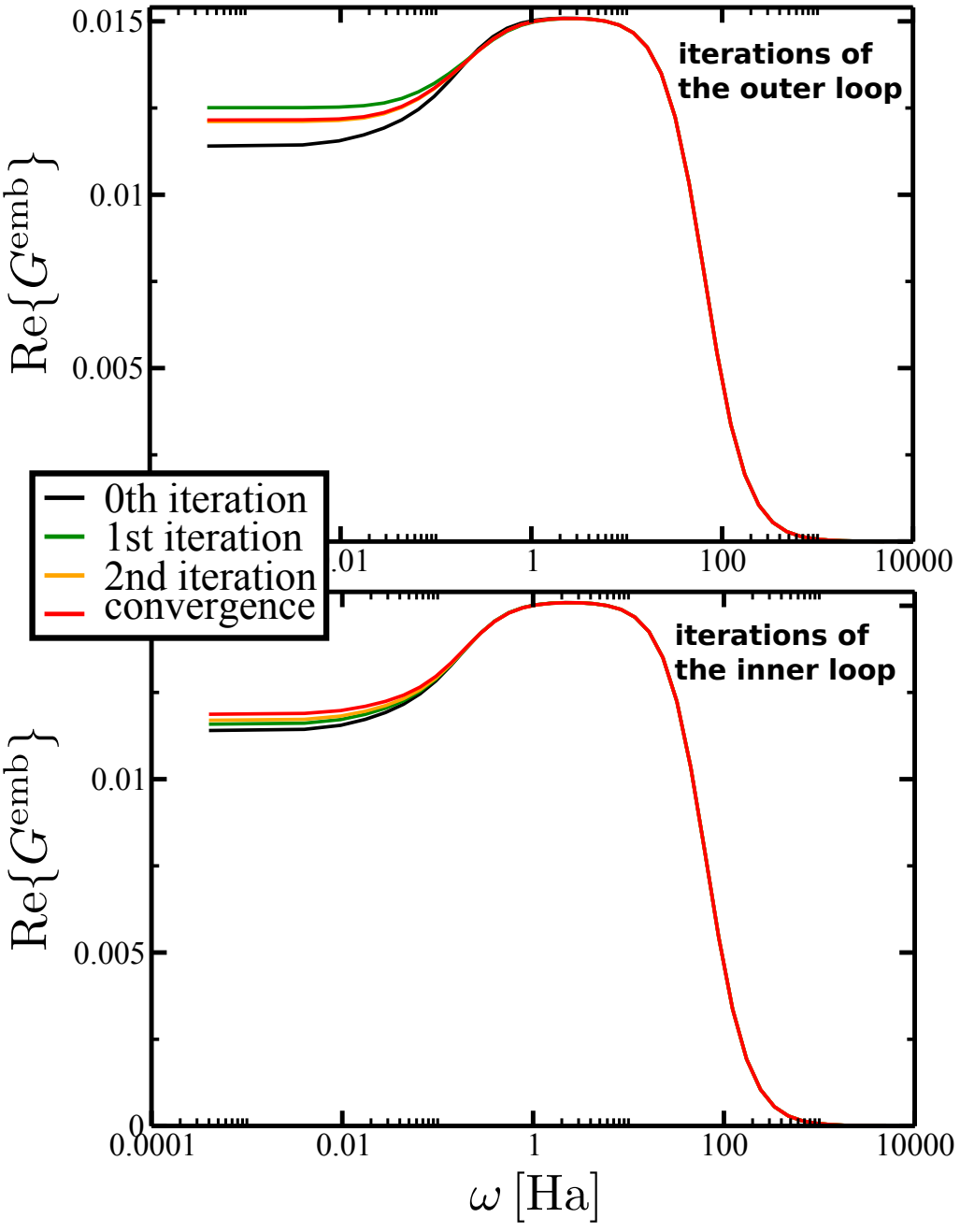

Figure 4.6: Real part of the first diagonal element of the embedded Green's function with a PBE0 self-energy, for bulk Si with two atoms in the unit cell and *tier1* basis. Upper panel: evolution of the embedded Green's function at 0th iteration of the inner loop, with the iterations of the outer loop. Lower panel: evolution of the embedded Green's function with the iteration of the inner loop. The change due to the outer loop iteration is more important, but the convergence of the inner loop accelerates the one of the outer loop.

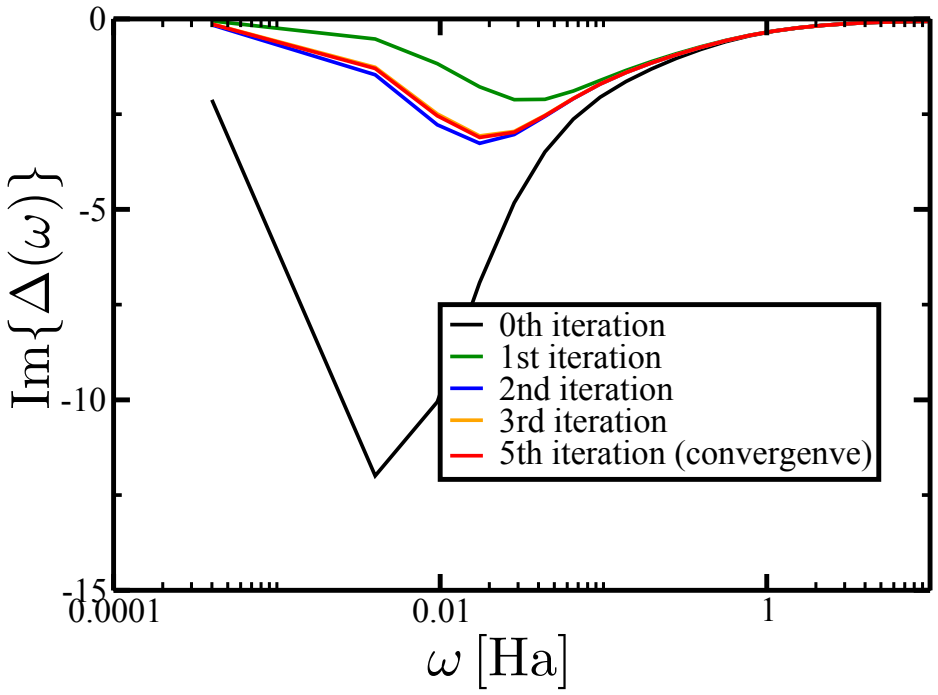

Figure 4.7: Imaginary part of the hybridization function for bulk Si with two atoms in the unit cell and *tier1* basis. The different colors refer to different iterations of the outer loop.

During the self-consistency cycle I compute the particle number N_μ, a quantity that is obtained from the embedded Green's function via

$$N_\mu = -\frac{i}{2\pi}\mathrm{Tr}\int d\omega G_{ij}^{\mathrm{emb}}(\omega,\mu)e^{-i\omega 0^+}. \tag{4.46}$$

To guarantee particle number conservation, one needs to update the electron chemical potential every time one obtains a converged self-energy from the inner loop. I do this using a so-called Richard Brent algorithm for minimization without derivatives [207]. The change in the chemical potential is strongly dependent on the choice of the local self-energy. Figure (4.8) shows a typical behavior of the chemical potential with iterations of the outer loop for bulk Si with two atoms in the unit cell. For the PBE0 self-energy the chemical potential approaches its convergence value already after the first iteration. For the GW self-energy however, it keeps oscillating until it stabilizes around the 13th iteration. I explain this with the fact that for the GW self-energy the exchange as well as the correlation parts are iteratively updated, which leads to a slower convergence of the chemical potential with the number of iterations that for the PBE0 self-energy case, where only a fraction of exact exchange is updated.

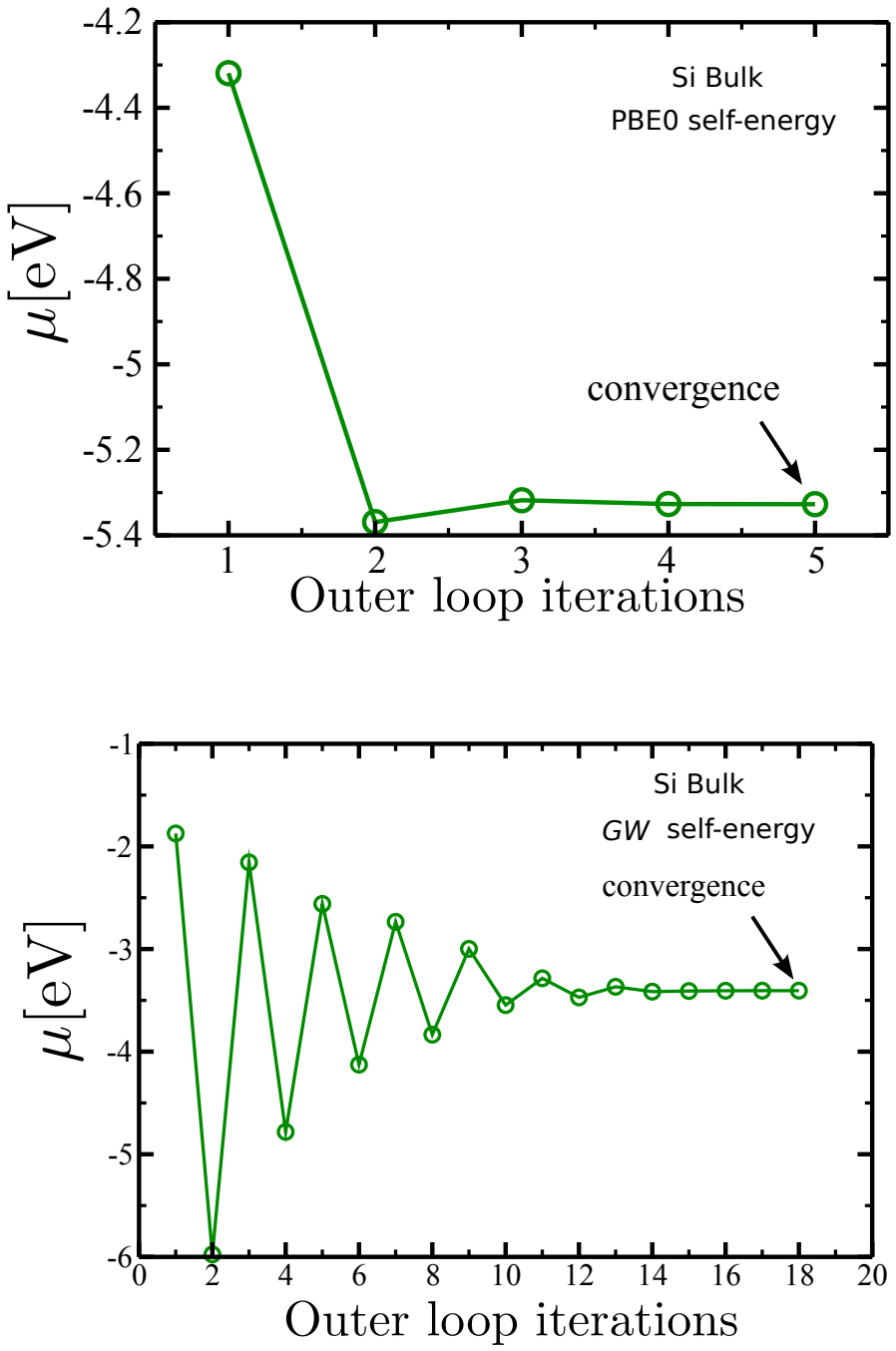

Figure 4.8: Typical change in the chemical potential during the self-consistency cycle for a bulk Si calculation. Upper panel: Calculation for Si bulk with two atoms in the unit cell with a PBE0 self-energy with a *tier1* basis. Convergence is reached after 5 iterations of the outer loop. Already at the second iteration the chemical potential is close to its converged value. Lower panel: Calculation for Si bulk with two atoms in the unit cell with a *GW* self-energy with a *tier3* basis. Convergence is reacjed after 18 iterations of the outer loop. The chemical potential oscillates strongly before it reaches a stable value at iteration ∼13.

4.5 Frequency and time grids

From a general point of view, the non-interacting Green's function for a solid is given by

$$G^0(\mathbf{r},\mathbf{r}',\omega) = \sum_{\nu}\sum_{\mathbf{k}} \frac{\psi_{\nu,\mathbf{k}}(\mathbf{r})\psi_{\nu,\mathbf{k}}(\mathbf{r}')}{\omega+\mu-\epsilon^{\nu}_{\mathbf{k}}}, \tag{4.47}$$

as discussed for Eq. (4.15) and (4.10). Hence, G^0 has poles on the real frequency axis at each $\omega = \epsilon^{\nu}_{\mathbf{k}} - \mu$. These poles have an infinitely peaked δ-shape. The positions of these poles is known in the case of the non-interacting Green's function. For the interacting Green's function however, the poles are still to be determined and need to be properly resolved. Thus, it is clear that very dense frequency grids with up to thousands of frequency points are required to capture such a peaky pole structure. To bypass this issue, one can use a well known trick from complex analysis: If one analytically continues the non-interacting Green's function into the complex frequency domain by replacing $\omega \longrightarrow i\omega$ in Eq. (4.47)

$$G^0(\mathbf{r},\mathbf{r}',i\omega) = \sum_{\nu}\sum_{\mathbf{k}} \frac{\psi_{\nu,\mathbf{k}}(\mathbf{r})\psi_{\nu,\mathbf{k}}(\mathbf{r}')}{i\omega+\mu-\epsilon^{\nu}_{\mathbf{k}}}, \tag{4.48}$$

then G^0 becomes smooth and hence, requires fewer frequency points. As a consequence, the numerical costs are drastically reduced. The one-to-one correspondence between the Green's function on the real and imaginary frequency grids is established through Cauchy's theorem. For further reading on analytic continuation in Green's function theory, the reader is referred to the Refs. [208, 209]. In the RDMFE scheme the analytical continuation becomes important for the local GW self-energy which is frequency dependent and is built from the screened Coulomb interaction W^{loc} and the polarisability Π^{loc}, that are also dynamical quantities. However, physical quantities are usually dependent on the pole structure on the real axis. The practical transformation from the imaginary axis (where the Green's function is smooth) back to the real axis (where the actual poles spectrum is) will be addressed in the next chapter. Moreover, it is worth mentioning that the imaginary frequency grid I am using is not to be confused with the Matsubara [155] frequencies for finite temperature Green's functions.

In this implementation, the discretization of the imaginary time and frequency axes is done on exponentially spaced grids with N_ω frequency points going from $[0, \omega_{\max}]$, and $2N_\tau + 1$ time points ranging from $[-\tau_{\max}, \tau_{\max}]$. The frequency and time grid points ω_n, τ_n and their corresponding integration weights $w(\omega_n), w(\tau_n)$ are given by

$$\begin{aligned} \omega_n &= \omega_0\{e^{(n-1)/h} - 1\} \text{ with the weights } w(\omega_n) = h\omega_0 e^{(n-1)/h} \\ \tau_n &= \omega_0\{e^{n.h} - 1\} \text{ with the weights } w(\tau_n) = h\omega_0 e^{n.h}. \end{aligned} \tag{4.49}$$

h is a constant specified using the condition $\omega_{\max} = \omega_0\left[e^{N_{\omega}h-1}\right]$, while the parameter ω_0 determines the initial grid spacing. The resulting logarithmic grid has dense points close to zero. This is the typical region where the Green's function shows non-trivial behavior. Dense points in this interval helps the resolution of such analytic features. In this thesis, typical values that were adopted are $\omega_{\max} = 7000\mathrm{Ha}$, $\tau_{\max} = 1000\mathrm{Ha}^{-1}$ and $\omega_0 = \tau_0 = 0.01$.

Fourier transforms using poles expansion

For an efficient self-consistent GW self-energy implementation, it is necessary to work in a mixed time and frequency-grid formalism. This is mainly to benefit from the convolution theorem stating that the Fourier transform (FT) of two convoluted functions is equal to the product of their respective FTs. Hence, for the evaluation of the polarisability the computationally demanding calculation of frequency convolutions can be replaced by the simple product of Green's functions in the time domain, as is done in Eq. (4.43). While for solving the Dyson equation, the time integrals over convoluted Green's functions and self-energies can be replaced by the product in frequency space. The embedded Green's functions in time and frequency domains are related via the FTs

$$G^{\text{emb}}(i\tau) = \frac{1}{\sqrt{2\pi}} \int_{-\infty}^{\infty} d\omega G^{\text{emb}}(i\omega) e^{-i\tau\omega} \tag{4.50}$$

$$G^{\text{emb}}(i\omega) = \frac{1}{\sqrt{2\pi}} \int_{-\infty}^{\infty} d\omega G^{\text{emb}}(i\tau) e^{i\tau\omega} \tag{4.51}$$

As it has been done by Caruso *et al.* [61], I use the pole expansion method to evaluates the FTs. It introduces an analytical representation of the frequency dependent Green's function and its FT, reducing thus the grid size in a considerable meaner. The idea here is to expand the embedded Green's function in a set of poles having the shape

$$f_p(i\omega) = \frac{1}{b_p + i\omega}, \tag{4.52}$$

with the corresponding FT

$$f_p(i\tau) = e^{b_p\tau} \left[\theta(-\tau)\theta(b_p) - \theta(\tau)\theta(-b_p)\right], \tag{4.53}$$

where p runs over the number of poles considered in the calculation, N_{poles}, and the parameters b_p are distributed logarithmically in the beginning of the calculation in a range that covers the hole eigenvalues spectrum of the system. Thus, the expansion of the embedded Green's function in this set of poles is

$$G^{\text{emb}}_{ij}(i\omega) = \sum_{p}^{N_{\text{poles}}} \left[\alpha^p_{ij} \text{Re}\{f_p(i\omega)\} + \beta^p_{ij} \text{Im}\{f_p(i\omega)\}\right]. \tag{4.54}$$

The real-valued expansion coefficients α^p, β^p are determined using a linear least square fit for the original Green's function. Once the coefficients α^p, β^p are calculated, the evaluation of the FT of the embedded Green's function is straightforward

$$G^{\text{emb}}(i\tau) = \sum_{p}^{N_{\text{poles}}} \left[\alpha^p_{ij} \text{Re}\{f_p(i\tau)\} + \beta^p_{ij} \text{Im}\{f_p(i\tau)\}\right], \tag{4.55}$$

with the pole-functions $f_p(i\tau)$ given by Eq. (4.53). The FTs of Π^{loc} and W^{loc} and the local GW self-energy Σ^{loc} are performed in an analogous way. Figure (4.10) illustrate the frequency dependent local polarisability (calculated from pole expansion FT of Eq. (4.43) using the pole expansion FT of the embedded Green's function to time frequency) and the resulting local screened Coulomb interaction calculated using Eq. (4.42), at different frequency points. In Fig. (4.9) the same quantities are depicted for a number of poles ranging from 40 to 200. The calculations where performed for a bulk Si with two atoms in the unit cell. Very few poles, in the range of 40, are already sufficient to describe the behavior of the dynamical quantities.

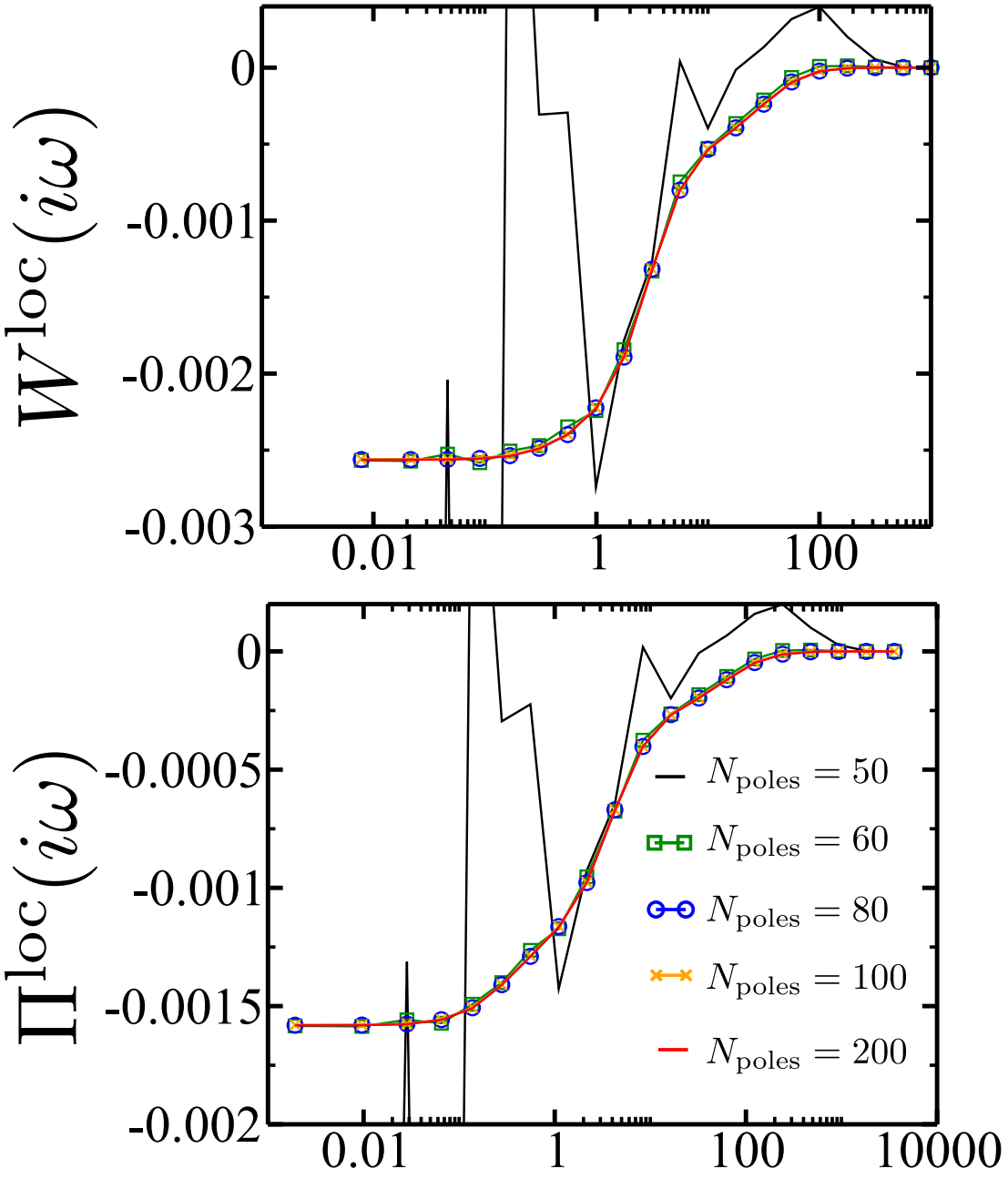

Figure 4.9: Upper panel: the local screened Coulomb interaction calculated using Eq. 4.42, for different poles. Lower panel: the local polarisability calculated from Eq. 4.43 using the FT of the embedded Green's function to time frequency, for different poles. For 80 poles both quantities reach already their converged shape. Calculation was done for Si bulk with 2 atoms in the unit cell and *tier1* basis. The number of frequency points was fixed to 40.

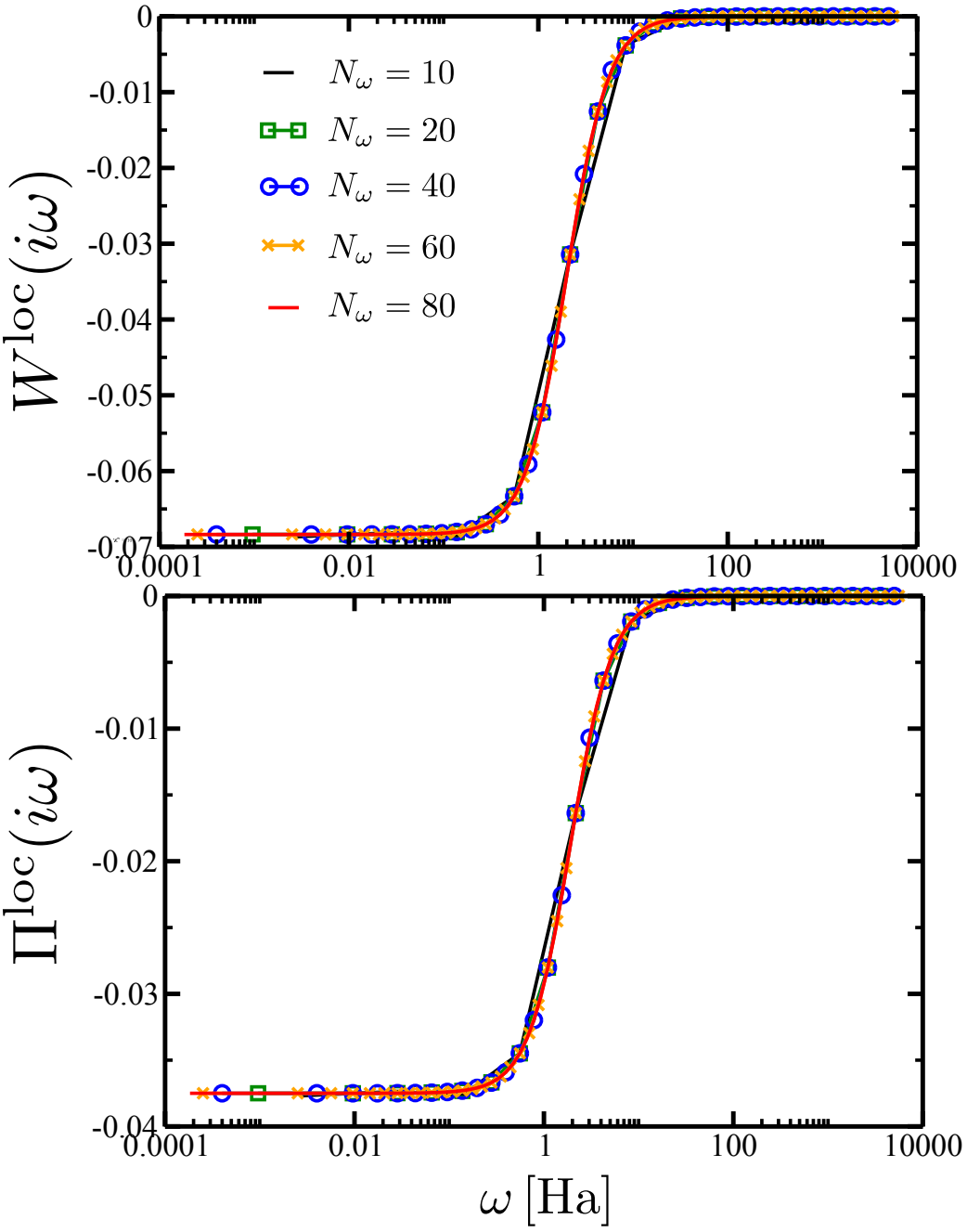

Figure 4.10: Upper panel: the local screened Coulomb interaction calculated using Eq. 4.42, for different frequency points. Lower panel: the local polarisability calculated from Eq. 4.43 using the FT of the embedded Green's function to time frequency, for different frequency points. Calculation was done for He bulk with 2 atoms in the unit cell and *tier2* basis. The number of poles was fixed to 100.

Chapter 5

Exploring Physical Quantities with the Real Space Dynamical Mean-Field Embedding

In This chapter I will first show how physical quantities, such as the density of states and the total energy can be calculated with our RDMFE scheme. Then I will demonstrate that these quantities behave adequately with the related computational parameters and the size of the embedded unit cell.

5.1 Evaluation of the density of states and the spectra

The way the RDMFE density of states (DOS) is calculated depends on the self-energy with which the localized region is treated. For the hybrid case i.e., PBEh and HSE, the self-energy is static (no frequency dependence). Hence, at self-consistency of the RDMFE cycle the local self-energy $\Sigma^{\text{loc}}_{\text{PBEh,HSE}}$ defines a $\mathbf{k}$-dependent embedded Hamiltonian corresponding to the self-consistent lattice Green's function Eq. (4.9)

$$H^{\text{emb}}(\mathbf{k}) = H^{0}(\mathbf{k}) + \Sigma^{\text{loc}}_{\text{PBEh,HSE}}. \tag{5.1}$$

One can then diagonalize the embedded Hamiltonian at each $\mathbf{k}$-point, which yields $\mathbf{k}$-dependent eigenvalues and eigenstates. The resulting embedded DOS $n(\epsilon_{\mathbf{k}})$ is then given by the δ-distribution

$$n(\epsilon_{\mathbf{k}}) = \sum_{\nu} \delta(\epsilon_{\mathbf{k}} - \epsilon^{\nu}_{\mathbf{k}}), \tag{5.2}$$

where ν labels the eigenstates of $H^{\text{emb}}(\mathbf{k})$. Plotting the upper formula would give a very peaky DOS with infinitely high peaked. To allow comparison with experiment, the peaked structure can be made smoother by introducing a Gaussian broadening

$$g_{\nu}(\tilde{\epsilon}) = \int d\mathbf{k} \, \exp\left(-\frac{\tilde{\epsilon} - \epsilon_{\nu}(\mathbf{k})}{\sqrt{2}\sigma}\right)^{2} \tag{5.3}$$

with the broadening σ. The resulting DOS is then given by $N(\tilde{\epsilon}) = \sum_{\nu} g_{\nu}(\tilde{\epsilon})$.

For the local GW self-energy on the other hand, the self-energy is dynamical. Here the spectrum is directly obtained from the Green's function. The $\mathbf{k}$-dependent spectral function is related to the lattice Green's function via the formula

$$A(\mathbf{k},\omega) = -\frac{1}{\pi}\mathrm{Tr}\left[\mathrm{Im}G^{\mathrm{lat}}(\mathbf{k},\omega)\right]. \tag{5.4}$$

As I have explained in the previous chapter, the lattice Green's function is defined on the imaginary axis. To evaluate the spectrum of the lattice Green's function it is necessary to know the poles on the real axis. To this end the analytical continuation of the local GW self-energy back from the imaginary to the real axis is necessary. I do this by fitting each matrix element of the self-energy to a two-pole model[210, 43] given by the formula

$$\Sigma^{\mathrm{loc}}_{GW}(i\omega) \approx \sum_{n}^{2} \frac{\alpha_n}{i\omega - \beta_n}, \tag{5.5}$$

where α_n and β_n are complex fitting parameters that I obtain by performing a least square fitting scheme. I then evaluate Eq. (5.5) for real frequencies and solve the Dyson equation for $G^{\mathrm{lat}}(\mathbf{k},\omega)$. The total spectral function follows then from the $\mathbf{k}$-summation $A(\omega) = \sum_{\mathbf{k}} A(\mathbf{k},\omega)$, which is then convoluted with Gaussians

$$\tilde{A}(\tilde{\omega}) = \int d\omega e^{-\left(\frac{\tilde{\omega}-\omega}{\sqrt{2}\sigma}\right)^2} A(\omega), \tag{5.6}$$

with broadening σ that leads to a DOS $\tilde{A}(\tilde{\omega})$ that can be compared to experiment. To test our implementation and our DOS, I have constructed a test case. For the PBEh self-energy in Eq. (4.34), I consider a hybrid parameter $\alpha = 1$ and discard the local correlation potential correction so that one ends up with a self-energy that contains only the HF exact exchange

$$\Sigma^{\mathrm{loc}}_{\mathrm{PBEh}}(\alpha = 1) = \Sigma^{\mathrm{loc}}_{\mathrm{X}} - v^{\mathrm{loc}}_{\mathrm{XC}}. \tag{5.7}$$

Hence, with the upper self-energy I get a HF Hamiltonian with a Hatree part from Kohn-Sham DFA

$$H^{\mathrm{emb}}(\mathbf{k}) = H^{\mathrm{KS}}(\mathbf{k}) + \Sigma^{\mathrm{loc}}_{\mathrm{X}} - v^{\mathrm{loc}}_{\mathrm{XC}}. \tag{5.8}$$

With this local self-energy one can look at the limiting case of an infinitely large lattice constant. In this limit, the atoms in the unit cell can be considered as an isolated molecule allowing a consistency check of my implementation. Figure (5.1) shows the DOS of He and Na bulks with two atoms in the unit cell, where the lattice constant was extended to 20Å. I then compare the DOS to HF calculation for finite systems. The RDMFE DOS resembles in both cases almost exactly the HF one and is clearly distinct from the PBE DOS, which is the starting DOS in this case. The slight differences between the RDMFE and the HF curves stem from the fact that, in our scheme, the Hartree potential is not updated. Hence, the embedded Hamiltonian still contains the Hartree potential from PBE.

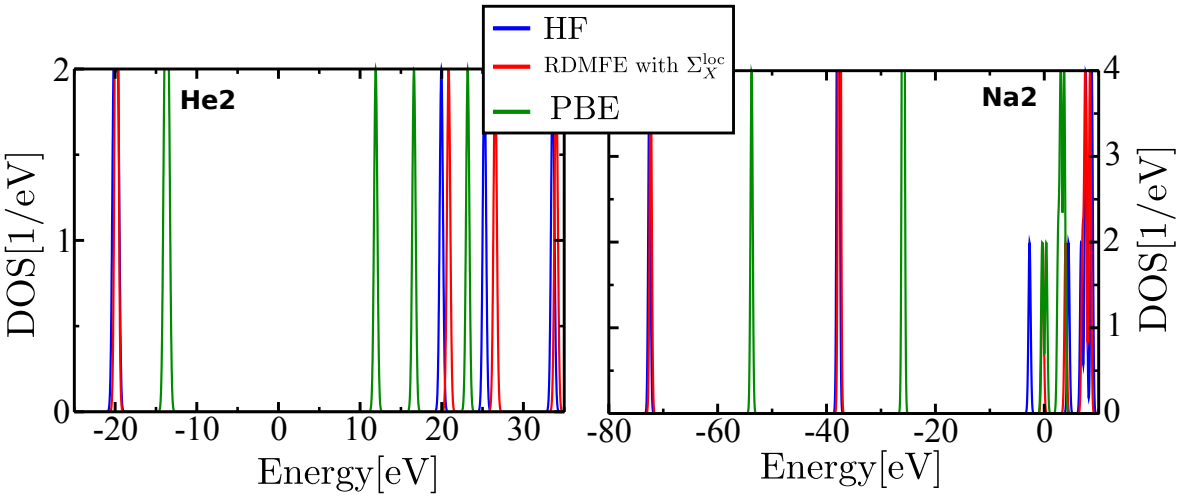

Figure 5.1: Comparison between the RDMFE (red), the HF (blue) and the PBE (green) DOSs for the limit of an infinitely large lattice constant. The left panel shows the DOS for He bulk with two atoms in the unit cell. The right panel shows the DOS for Na with two atoms in the unit cell. The RDMFE DOS resembles the HF one much more that the PBE one, which is the starting calculation. However, since I am not updating the Hartree potential small discrepancies are still noticeable. All the calculations were performed with a *tier*1 basis set. A Gaussian broadening of $\sigma = 0.2$ and a **k**-mesh of $4 \times 4 \times 4$ were used.

5.1.1 Density of states of embedded Si unit cells

Embedded PBE0 self-energy: RDMFE(PBE0)

To investigate the evolution of the DOS with each embedding cycle, for a PBE0 local -self-energy, I calculated the DOS for bulk Si with two atoms in the unit cell at each iteration of the outer loop. Figure (5.2) shows the resulting DOS at different iterations until convergence is reached. The most important change happens already at the first iteration, when moving from PBE to the embedded PBE0 DOS. After the first iteration the changes in the DOS are much smaller. This behavior is consistent with the behavior of the chemical potential for a PBE0 local self-energy shown in the upper panel of Fig. (4.8). The convergence of the embedded DOS with the **k**-mesh and the basis size is shown in Fig. (5.3). Comparing the converged RDMFE(PBE0) DOS for the 2 atom unit cell with the periodic PBE and PBE0 DOSs as shown in Fig. (5.4), One observes that the band gap and the band width are larger than the PBE one and closer to the PBE0 reference. Furthermore, one expects that when increasing the unit cell size, the resemblance between the embedded DOS and the PBE0 reference should become more pronounced. I have done this investigation and considered unit cells of 8 and 32 atoms, see Fig. (5.5). The difference between the embedded DOS and the periodic PBE0 DOS are systematically reduced. A comparison between the resulting RDMFE band gaps for different unit cell sizes with the PBE and PBE0 values is reported in Tab. (5.1), showing that the RDMFE band gap approaches the PBE0 value with increasing unit cell size. With the investigation

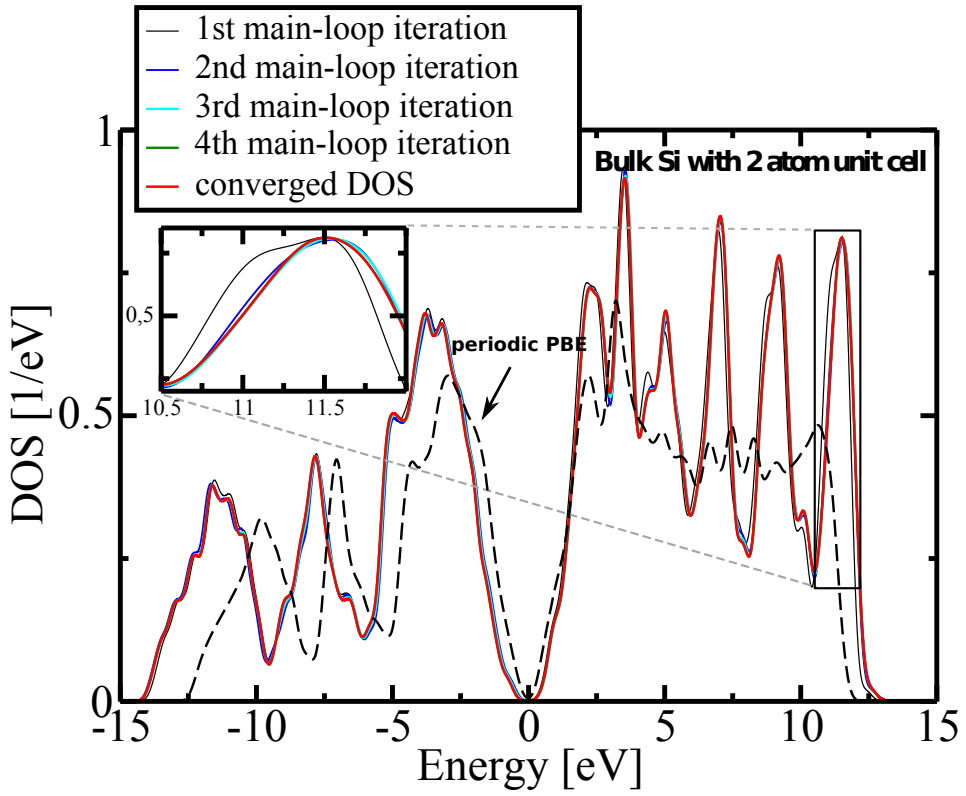

Figure 5.2: DOS comparison at each iteration of the main-loop. Convergence was achieved after 5 main-loop iterations.

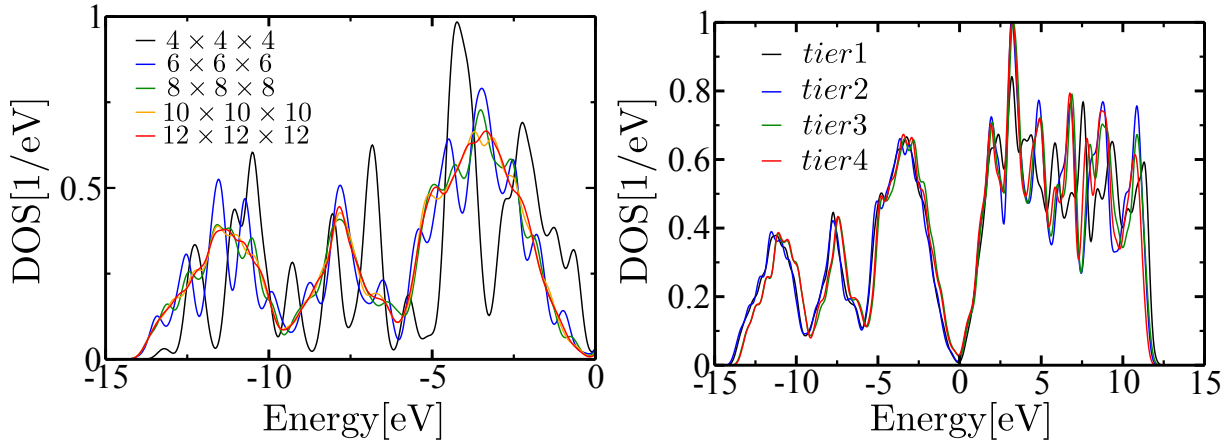

Figure 5.3: Evolution of the embedded DOS for bulk Si with 2 atom unit cell with the computational parameters. Left panel: Valence band with increasing **k**-grid points. Right panel: Valence and conduction bands for different basis set sizes (*tiers*).

			RDMFE(PBE0)			
	PBE	PBE0	2 atoms	8 atoms	16 atoms	exp. (at 300K)[211]
band gap [eV]	0.68	1.85	1.2	1.257	1.569	1.12

Table 5.1: Comparison between PBE, PBE0 and RDMFE for different unit cell sizes for the indirect band gap of silicon. The experimental value [211] is shown for reference.

of the change of the RDMFE DOS with increasing unit cell size I have shown that our embedding scheme behaves adequately by approaching the right limit i.e., the periodic PBE0 reference DOS in this case.

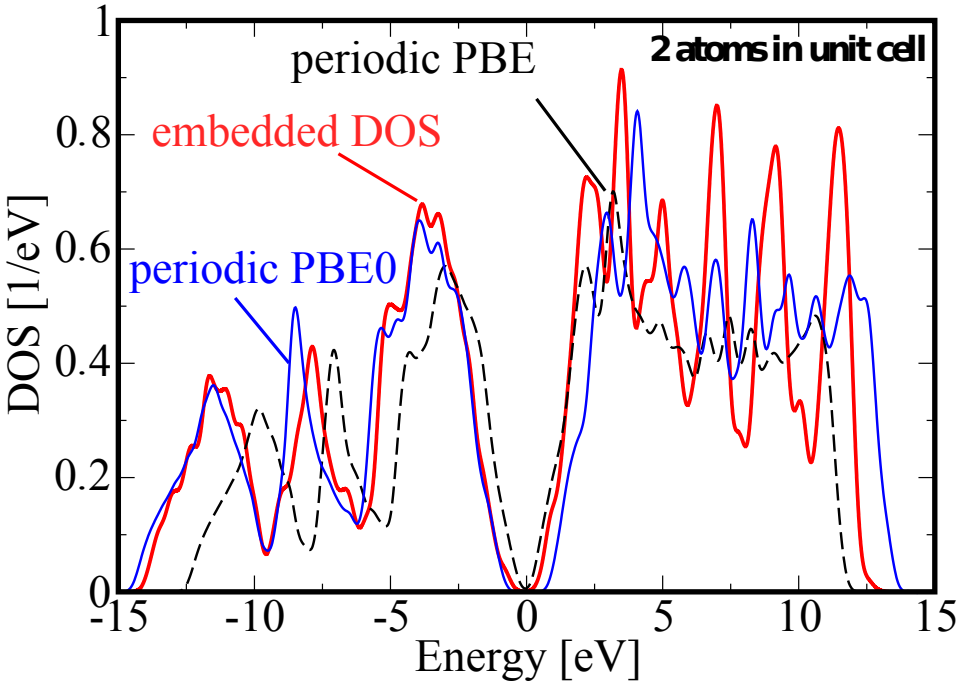

Figure 5.4: Comparison of the embedded DOS, the periodic PBE and the periodic PBE0 DOS for a 2 atom unit cell.

Embedded scGW self-energy: RDMFE(GW)

For the local GW self-energy, I calculated the spectral function as given by Eq. (5.6) from the **k**-summation over the **k**-resolved spectral function given by

$$\begin{aligned} A(\mathbf{k},\omega) &= -\frac{1}{\pi}\mathrm{Tr}\left[\mathrm{Im}G^{\mathrm{lat}}(\mathbf{k},\omega)\right] \\ &= -\frac{1}{\pi}\mathrm{Tr}\frac{|\mathrm{Im}\Sigma^{\mathrm{loc}}_{GW}(\omega)|}{[\omega-\epsilon^{\nu}_{\mathbf{k}}-\mathrm{Re}\Sigma^{\mathrm{loc}}_{GW}(\omega)]^2+[\mathrm{Im}\Sigma^{\mathrm{loc}}_{GW}(\omega)]^2}. \end{aligned} \tag{5.9}$$

Here the trace runs over the Kohn-Sham eigenstate indices ν,μ corresponding to the eigenvalues $\epsilon^{\nu}_{\mathbf{k}}$ and $[\Sigma^{\mathrm{loc}}_{GW}]_{\mu\nu}(\omega)$ is the local GW self-energy obtained from analytic

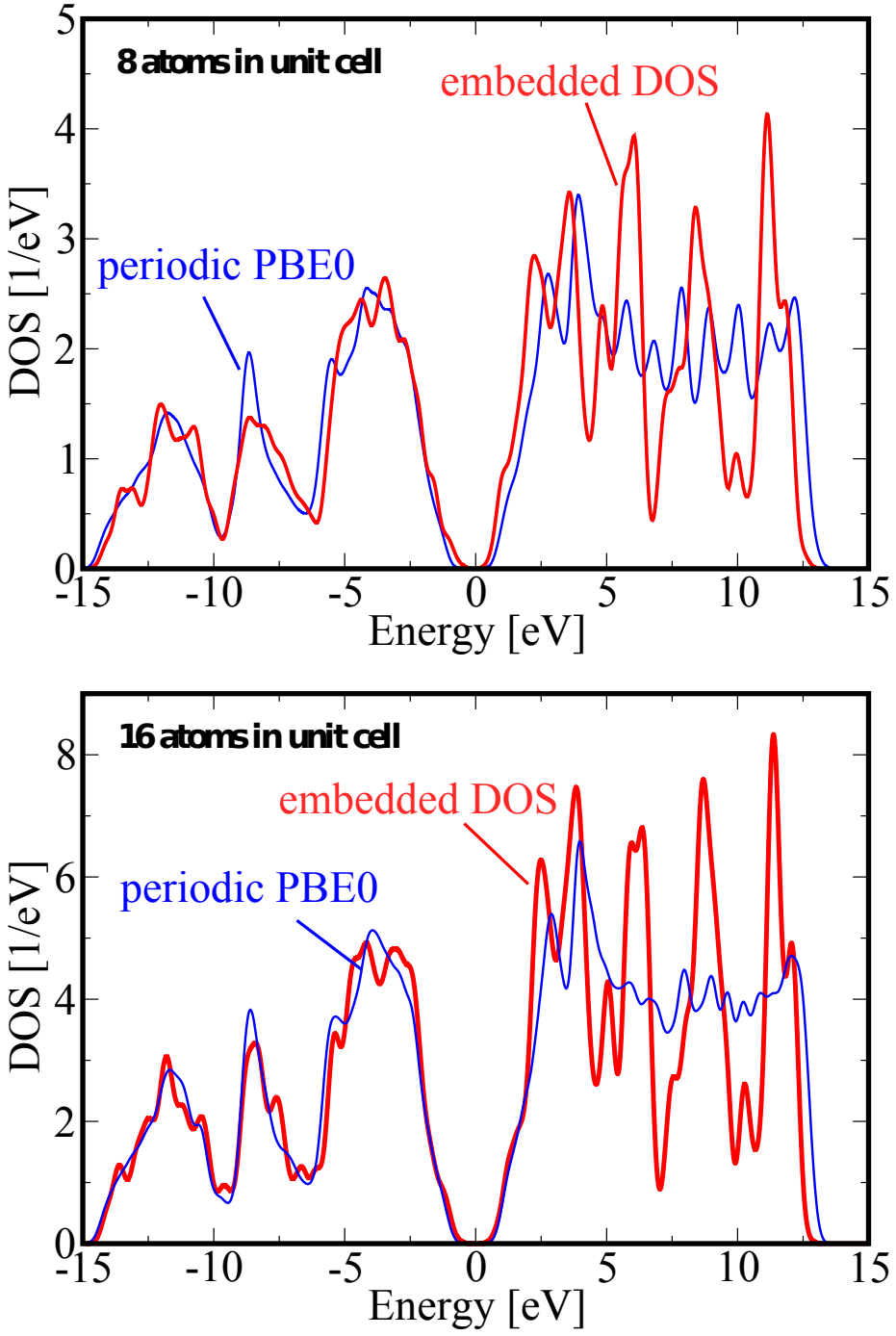

Figure 5.5: Comparison of the embedded DOS, with the periodic PBE0 DOS for an 8 atom unit cell (upper panel) and a 16 atom unit cell (lower panel).

continuation of the imaginary frequency self-energy

$$\Sigma^{\mathrm{loc}}(i\omega) = \Sigma^{\mathrm{loc}}_{GW}(i\omega) - v^{\mathrm{loc}}_{\mathrm{XC}}. \tag{5.10}$$

I first looked at the spectral function at the first iteration of the outer and inner loops. Figure (5.6) shows the embedded GW valence band spectral function at the Γ-point (**k**=0;0;0). A comparison is made for different basis sets up to *tier*3. The direct band

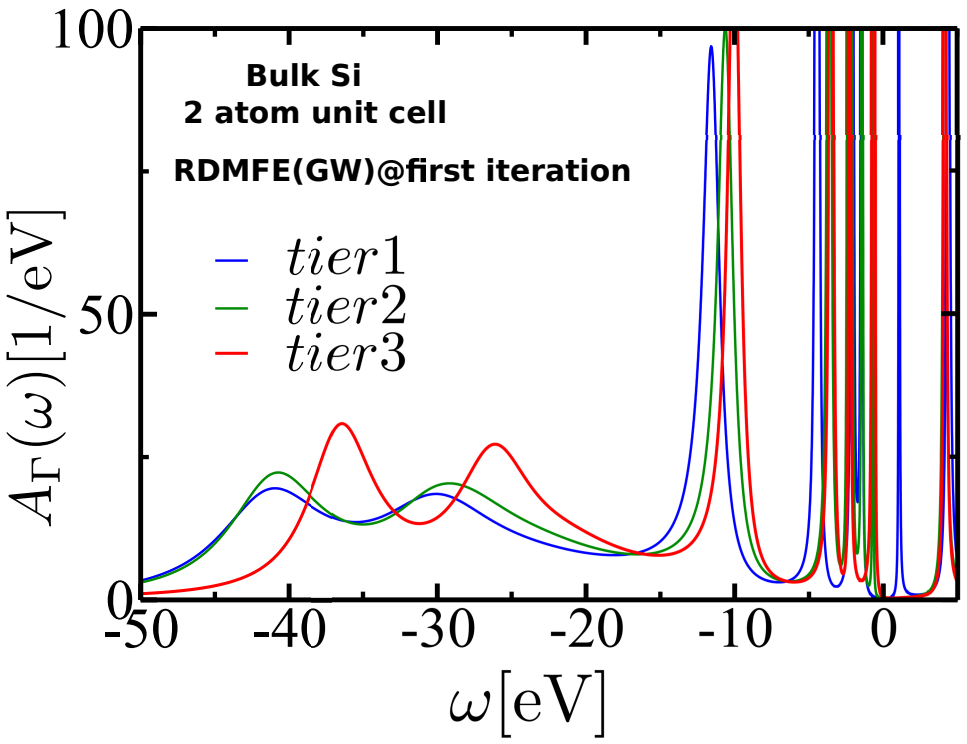

Figure 5.6: The RDMFE(GW) spectral function at the Γ-point for different basis set sizes for bulk Si with 2 atoms in the unit cell. The direct band gap is already converged for the *tier2* basis set. An artificial Gaussian broadening of 0.001eV was used for all spectra.

gap is already converged for a *tier*2 basis set. Moreover, at the bottom of the valence band i.e., at frequencies between -40 and -30 eV a broad peak appears that can be identified as plasmon satellite [212, 213] (See the discussion in the next subsection). The total spectral function (i.e., the **k**-summed one) for bulk Si with 2 atoms in the unit cell at the first iteration and at convergence is shown in Fig. (5.7). Also here the spectrum shows a broad satellite structure between -40 and -30 eV for the spectrum at first iteration. Such satellites are completely absent in KS band structures or when doing GW perturpatively (i.e., G_0W_0), because G_0W_0 only corrects the KS states and does not change the wave function of the states. Since Dyson's equation has been solved once, this spectrum is not equivalent to perturbative G_0W_0 spectra and one would expect to see plasmon satellites. The energy range of the RDMFE satellite agrees well with previous periodic GW calculations [62, 214] and demonstrates that the dynamic, local RDMFE framework can capture non-local phenomena such as plasmon satellites. For scGW the converged DOS is also shown in Fig. (5.7). In

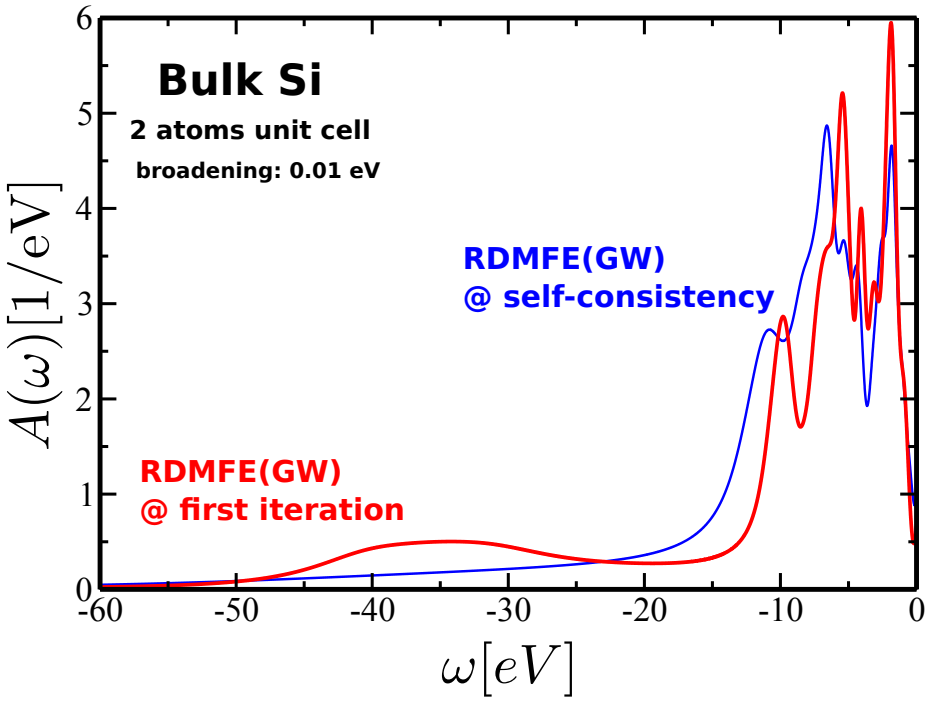

Figure 5.7: Gaussian broadened (with broadening $\sigma = 0.01$ eV) quasiparticle spectrum for the GW self-energy at 1st iteration (red curve) and at self-consistency (blue curve). Only occupied states are shown. Calculation performed using a *tier2* basis set.

agreement with the previous findings by Holm and von Barth [212] and Schöne and Eguiluz [213], the fully self-consistent spectrum shows a broader band width, which can be related to a weight transfer of the plasmon peak to the valence band. I obtain a band gap of ∼0.9 eV for the two atom unit cell, which is close to the experimental value of ∼1.12 eV [215]. This comparison together with the one between the indirect band gap from my calculation and experiment[211] are presented in Tab. (5.2).

band gap	RDMFE(GW)	periodic scGW[216]	QPscGW[217]	exp. (at 300K)
direct (Γ_{15c}) [eV]	3.7	—	3.47	3.4 [211]
indirect (E_g) [eV]	0.9	1.55	1.25	1.12 [215]

Table 5.2: Direct and indirect band gaps as calculated from RDMFE(GW). Comparison is made with the periodic scGW work of Kutepov *et al.*[216] and the quasi particle self-consistent GW calculation of Kotani *et al.*[217] and experiment.

Plasmon satellites in self-consistent *GW* spectra

The effect of self-consistency on the spectral properties in the GW approach have been a matter of debate in the last decade. While fully self-consistent studies have been limited to model [212] and finite systems [61, 60], there is to my knowledge only one work by Kutepov *et al.* [216] that investigates full self-consistency for real periodic systems; although they focus on the evaluation of the total energy rather than spectral features. Schöne and Eguiluz [213] have performed quasi-particle self-consistent GW calculations based on the equivalent shielded-interaction approximation of Baym and Kadanoff [218] that fulfills the conservation laws. They applied it to K and Si and found that, for K, the self-consistent treatment of the correlation yields a bandwidth which is significantly wider than the one obtained from an LDA Green's function in disagreement with the experimental findings. See Fig. (5.8). They connected this band width increase to the spectral weight reduction of the plasmon satellite. Hence, in the non-self-consistent spectrum the plasmon is clearly apparent while for the self-consistent case it is suppressed. These conclusions are in agreement with what Holm and von Barth [212] showed before for the homogeneous electron gas. They demonstrated that full self-consistency in G and W leads to a deterioration in the GW spectral function compared to spectra where G and W are directly computed from the LDA solution or when only G is obtained from the solution of Dyson's equation while W is still evaluated using the Green's function at the LDA level. They argued that the lack of vertex corrections may be the reason behind the bad agreement of the full self-consistent spectrum with the experimental results. Figure (5.9) depicts the spectral function of the homogeneous electron gas from [212]. For the self-consistent calculation, a transfer of the spectral weight from the plasmon peak to the quasi-particle spectrum takes place. As mentioned in the previous subsection, in the RDMFE scheme applied to bulk Si, I have found a satellite structure at the bottom of the valence band for the spectral function corresponding to the GW self-energy evaluated with the Green's function at the Kohn-Sham level. For this spectral function, a plasmon appears also at the top of the conduction band. Figure (5.10) illustrates the valence band and the conduction

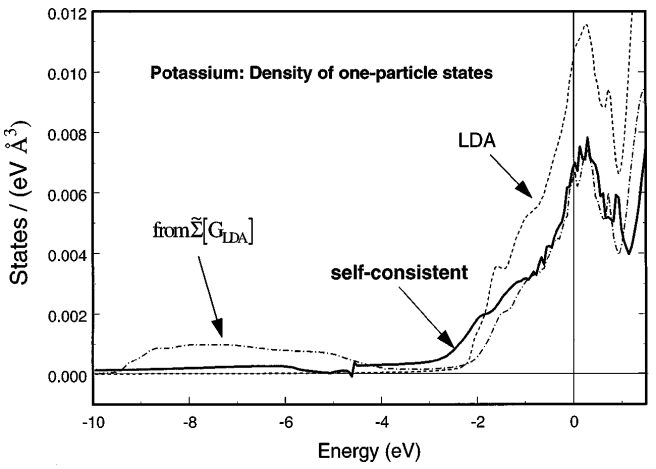

Figure 5.8: Calculated DOS for K. Depicted is the LDA DOS (dashes line), an the results obtained from an LDA Green's function $\tilde{\Sigma}[G_{\mathrm{LDA}}]$ (dot-dashed line) and the self-consistent result (solid line) from [213]. The non self-consistent spectrum shows a satellite structure and a narrower band width than the self-consistent one, where the satellite does not appear.

band plasmons as I calculated them for the embedded 2 atom Si unit cell. Moreover, a closer look at the *GW* correlation self-energy as done in Fig. (5.11) shows that the appearance of the plasmon peak is directly related to the dynamic correlation in the *GW* self-energy. Figigure (5.11) shows that the analytically continued imaginary and real parts of the *GW* correlation self-energy have peak structures at the same energy[1] as the plasmon in the spectral function. Figure (5.12) illustrates the effect of self-consistency on the *GW* correlation self-energy. Self-consistency yields a loss of the sharp structure of the self-energy components resulting in a much smoother shape of the self-energy. This is in agreement with what Holm and von Barth [212] showed for the homogeneous electron gas. Hence, the lack of vertex corrections ind the *GW* approximation can be an explanation to the deterioration of the spectrum at self-consistency. At present this is, however, still a presumption that needs to be checked in future.

5.1.2 Band structure of embedded Si unit cells

For the computation of the DOS, diagonalization at each **k**-point is required. Since it is a **k**-summed quantity relatively few **k**-points are necessary to obtain a reasonable DOS. For the evaluation of the band structure however, a denser **k**-mesh is required to resolve all the relevant bands. Hence, to overcome this ambiguity, the embedded Hamiltonian is reevaluated at the end of the calculation at a denser **k**-points grid, then a diagonalization at each **k**-point of the new grid yields the new **k**-dependent eigenvalues. Next, I consider the band structure for the 2 atom unit cell shown in the upper panel of Fig. (5.15). The same trend as for the DOS is noticeable: the band

[1] Here the little shift between the plasmon peak and the peaks of the self-energy is due to the contributions form the exact exchange and the non-interacting Hamiltonian, included in the spectral function.

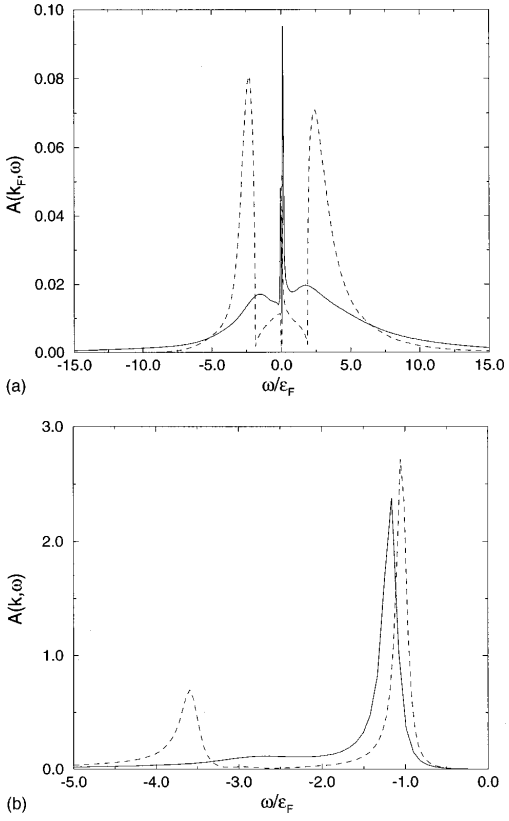

Figure 5.9: The one-electron spectral function resulting from the fully self-consistent *GW* calculation for the homogeneous electron gas (solid line) compared to the corresponding quantity from the partially self-consistent GW_0 calculation (dashes line) [219]. (a) shows the spectral functions at Fermi surface, $\omega = k_{\mathrm{F}}$, while (b) shows the a zoom into the bottom of the band. In both figures the loss of the plasmon satellites in the self-consistent *GW* calculation is clearly noticeable. The band width is also significantly increased for the self-consistent *GW* case.

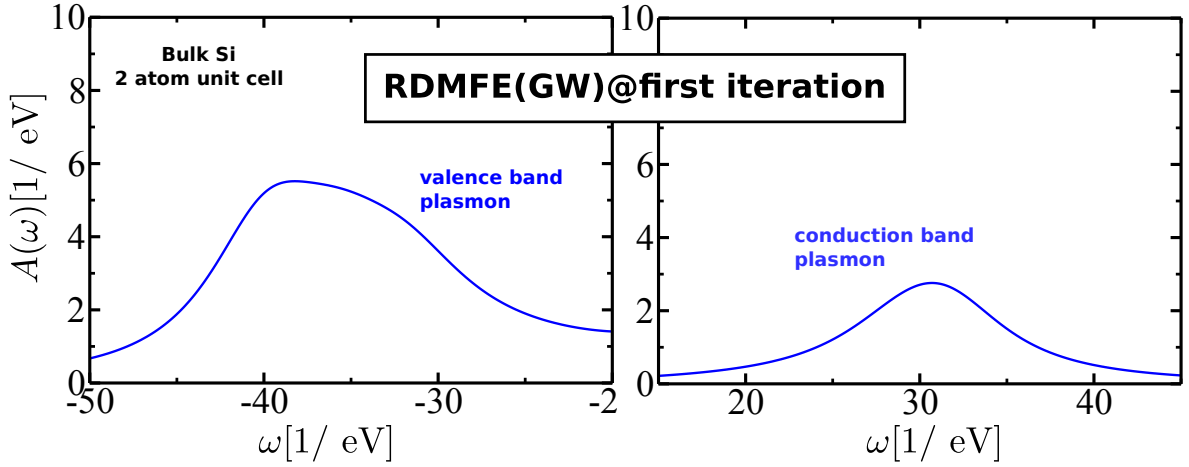

Figure 5.10: A zoom into the plasmon satellite region at the bottom of the valence band (left) and the top of the conduction band (right). The calculation was made with a *tier*2 basis set.

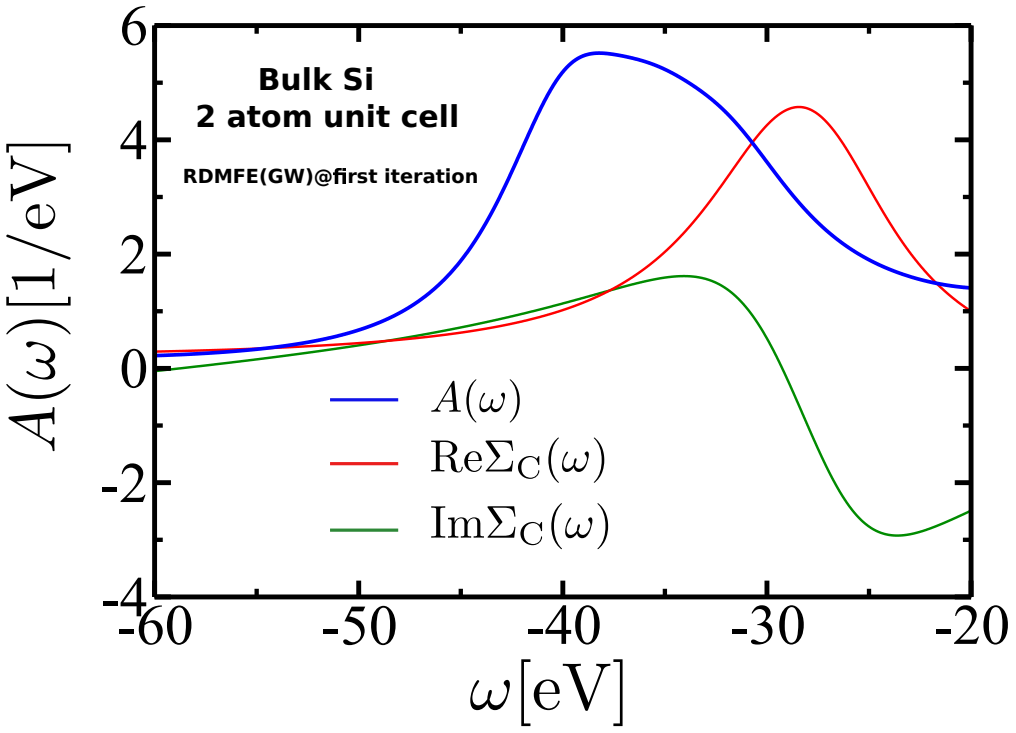

Figure 5.11: The real (green curve) and imaginary (red curve) parts of the *GW* correlation self-energy at the plasmon peak (blue curve) at first iteration of the RDMFE inner and outer loops. The plasmon peak results from the dynamical correlation in the *GW* self-energy.

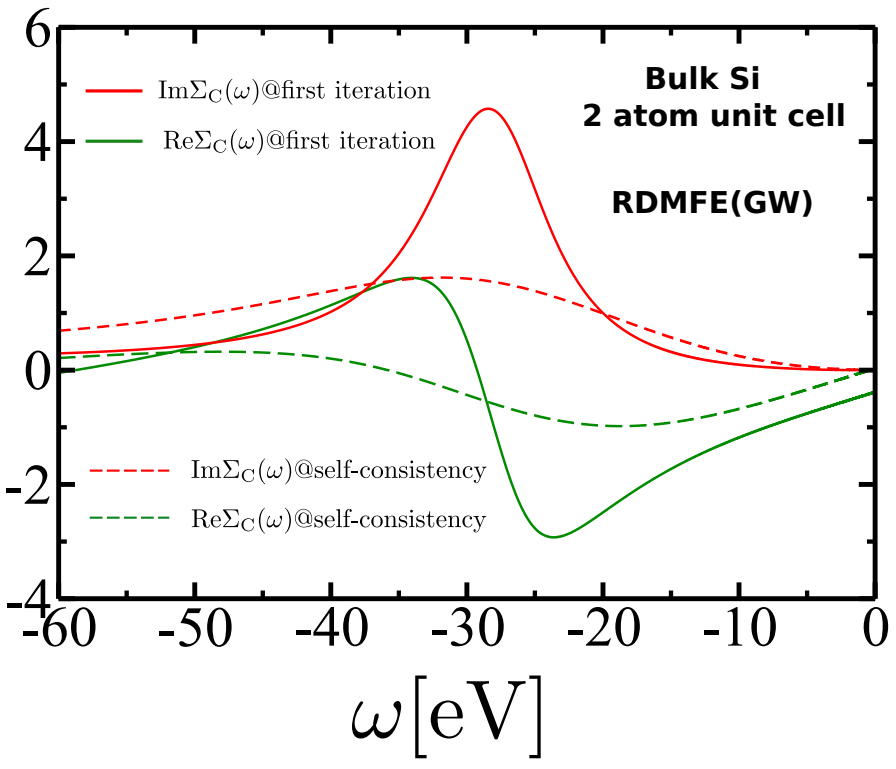

Figure 5.12: Comparison between the real (read curves) and imaginary (green curves) of the correlation self-energy at first iteration (solid lines) and self-consistency (dashed lines). The loss of the sharp features of the self-energy is clearly noticeable for the self-consistent calculation.

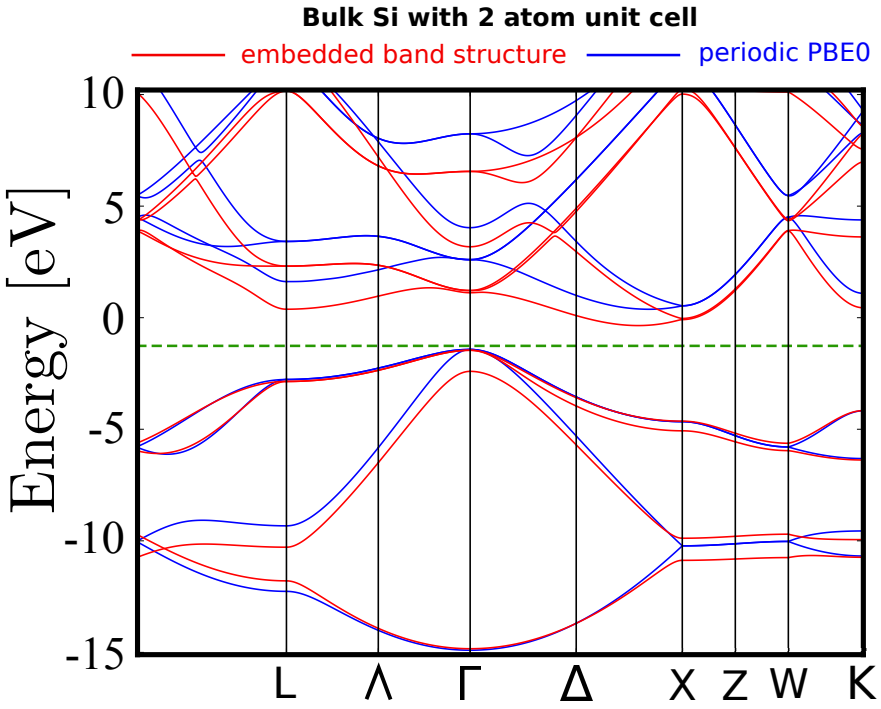

Figure 5.13: The embedded band structure for bulk Si compared to the periodic PBE0 one. The local self-energy breaks the translation symmetry and the degeneracy lifted at some hight symmetry **k**-points

gap and the band width approach PBE0 and so do the bands in general. However, at some high symmetry points the degeneracy of certain bands is lifted. The origin of this degeneracy lifting is the break of the crystal symmetry that is introduce by the local RDMFE self-energy. It is a well known artefact and has been discussed extensively in the context of cellular and cluster DMFT [189, 220]. The local self-energy simply does not "know" about the symmetry of the crystal and can therefore not enforce it. The solution to the problem is then obvious: the approximation of the range of the self-energy needs to be extended. If the self-energy would extend over a larger region (i.e. supercell) it would acquire more information about the crystal symmetry. Then the degeneracy splitting should reduce. This can be made clear when expanding the self-energy of the crystal

$$\Sigma(\mathbf{r},\mathbf{r}';\omega) = \sum_{\mathbf{k}} \sum_{ij} \varphi_{\mathbf{k}i}(\mathbf{r}) \Sigma_{ij}(\mathbf{k},\omega) \varphi^*_{\mathbf{k}j}(\mathbf{r}'), \tag{5.11}$$

where[1] $\Sigma_{ij}(\mathbf{k},\omega) = \int d\mathbf{r} d\mathbf{r}' \varphi^*_{\mathbf{k}i}(\mathbf{r}) \Sigma(\mathbf{r},\mathbf{r}';\omega) \varphi_{\mathbf{k}j}(\mathbf{r}')$, $\mathbf{r}$ and $\mathbf{r}'$ are electronic space coordinates and $\mathbf{k}$ the electronic wave vector, while i,j are basis indices. Expressing the Bloch states in terms of atomic orbitals $\varphi_{\mathbf{R},i}$

$$\varphi_{\mathbf{k}i}(\mathbf{r}) = \sum_{\mathbf{R}} \exp\left[-i\mathbf{k}\cdot\mathbf{R}\right] \varphi_{\mathbf{R},i}(\mathbf{r}), \tag{5.12}$$

with $\mathbf{R}$ being the Bravais lattice vector, I obtain from Eq. (5.11)

$$\begin{aligned}\Sigma(\mathbf{r},\mathbf{r}';\omega) = &\sum_{\mathbf{k}} \sum_{ij} \sum_{\mathbf{R},\mathbf{R}'} \exp\left[-i\mathbf{k}\cdot(\mathbf{R}-\mathbf{R}')\right] \\ &\times \varphi_{\mathbf{R}i}(\mathbf{r}) \Sigma_{ij}(\mathbf{k},\omega) \varphi^*_{\mathbf{R}'j}(\mathbf{r}').\end{aligned} \tag{5.13}$$

I can then divide the sum $\sum_{\mathbf{R},\mathbf{R}'} = \sum_{\mathbf{R}=\mathbf{R}'} + \sum_{\mathbf{R}\neq\mathbf{R}'}$, so that the upper equation becomes

$$\begin{aligned}\Sigma(\mathbf{r},\mathbf{r}';\omega) = &\sum_{ij} \sum_{\mathbf{R}=\mathbf{R}'} \varphi_{\mathbf{R}i}(\mathbf{r}) \Sigma^{\mathrm{loc}}_{ij}(\omega) \varphi^*_{\mathbf{R}'j}(\mathbf{r}') \\ &+ \sum_{\mathbf{k}} \sum_{\mathbf{R}\neq\mathbf{R}'} \exp\left[-i\mathbf{k}\cdot(\mathbf{R}-\mathbf{R}')\right] \varphi_{\mathbf{R}i}(\mathbf{r}) \Sigma_{ij}(\mathbf{k},\omega) \varphi^*_{\mathbf{R}'j}(\mathbf{r}').\end{aligned} \tag{5.14}$$

Here I have set $\Sigma^{\mathrm{loc}}_{ij}(\omega) = \sum_{\mathbf{k}} \Sigma_{ij}(\mathbf{k},\omega)$. The upper equation shows that by approximating the full crystal self-energy by the local one, i.e. only considering the first line of Eq. (5.14), one misses some crystal information that is contained in the second line of Eq. (5.14).

Let us now consider a larger unit cell that I call region $\mathcal{C}$ of primitive unit cells, see Fig. (5.14). I can then define a new local self-energy $\tilde{\Sigma}^{\mathrm{loc}}_{ij}(\omega) = \sum_{\mathbf{k}} \tilde{\Sigma}_{ij}(\mathbf{k},\omega)$ for this

[1] For simplicity I consider here an orthogonal basis so that I can write $\Sigma_{ij}(\mathbf{k},\omega) = \int d\mathbf{r} d\mathbf{r}' \varphi^*_{\mathbf{k}i}(\mathbf{r}) \Sigma(\mathbf{r},\mathbf{r}';\omega) \varphi_{\mathbf{k}j}(\mathbf{r}') = \int d\mathbf{r} d\mathbf{r}' \sum_{nm} \varphi^*_{\mathbf{k}n}(\mathbf{r}) S^{-1}_{ni}(\mathbf{k}) \Sigma(\mathbf{r},\mathbf{r}';\omega) S^{-1}_{jm}(\mathbf{k}) \varphi_{\mathbf{k}m}(\mathbf{r}')$. Of course, the NAO basis I am writing my matrices in, is not orthogonal.

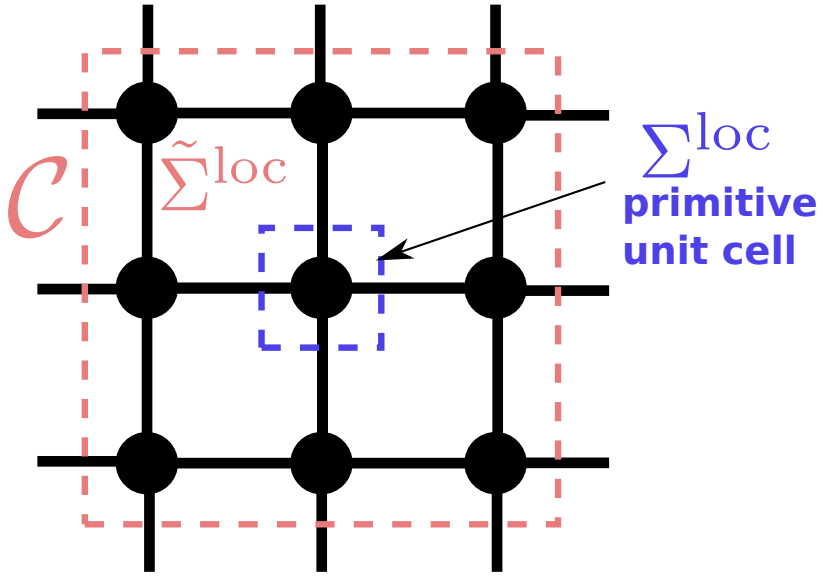

Figure 5.14: Cartoon depicting the primitive unit cell and the larger unit cell $\mathcal{C}$.

region, so that

$$\tilde{\Sigma}_{ij}(\mathbf{k},\omega) = \int d\mathbf{r}d\mathbf{r}'\tilde{\varphi}^{*}_{\mathbf{k}i}(\mathbf{r})\Sigma(\mathbf{r},\mathbf{r}';\omega)\tilde{\varphi}_{\mathbf{k}j}(\mathbf{r}'), \tag{5.15}$$

with the Bloch states defined for region $\mathcal{C}$ as $\tilde{\varphi}_{\mathbf{k}i}(\mathbf{r}) = \sum_{\mathbf{R}\in\mathcal{C}} \exp\left[-i\mathbf{k}\cdot\mathbf{R}\right]\varphi_{\mathbf{R},i}(\mathbf{r})$. Substituting in the upper equation and performing the integration over the electronic coordinates yields the important formula

$$\tilde{\Sigma}_{ij}(\mathbf{k},\omega) = \sum_{\mathbf{R},\mathbf{R}'\in\mathcal{C}} \Sigma_{ij}(\mathbf{R},\mathbf{R}',\omega)\exp\left[i\mathbf{k}\cdot(\mathbf{R}-\mathbf{R}')\right], \tag{5.16}$$

with $\Sigma_{ij}(\mathbf{R},\mathbf{R}',\omega) = \int d\mathbf{r}d\mathbf{r}'\varphi^{*}_{\mathbf{R}i}(\mathbf{r})\Sigma(\mathbf{r},\mathbf{r}';\omega)\varphi_{\mathbf{R}'j}(\mathbf{r}')$.
Equation (5.16) shows that considering a larger unit cell (or cluster) in RDMFE will introduce more information about the crystal symmetry. In the two lower panels of Fig. (5.15), I present an unfolded band structure [221] for the 16 and 32 atom unit cells. Indeed a reduction in the splitting for both the 16 and 32 atom unit cells is observed. However, while the degeneracy is fully restored for some high symmetry points, it is still broken for others such as the X and Z points. The degeneracy lifting occures also for the embedded *GW* self-energy as shown in Fig. (5.16) (a zoom into the plasmon region of the spectral function of Fig. (5.6)). For the spectral function at the Γ-point the plasmon peak shows a splitting that can be related to the local treatment of the embedded self-energy. This splitting does not occure for the total spectral function shown in Fig. (5.7).

5.2 Total energy calculation

For the computation of total energies from Green's functions, the Luttinger-Ward [222] and the Klein [223] functionals are considered to be the functional of choice.

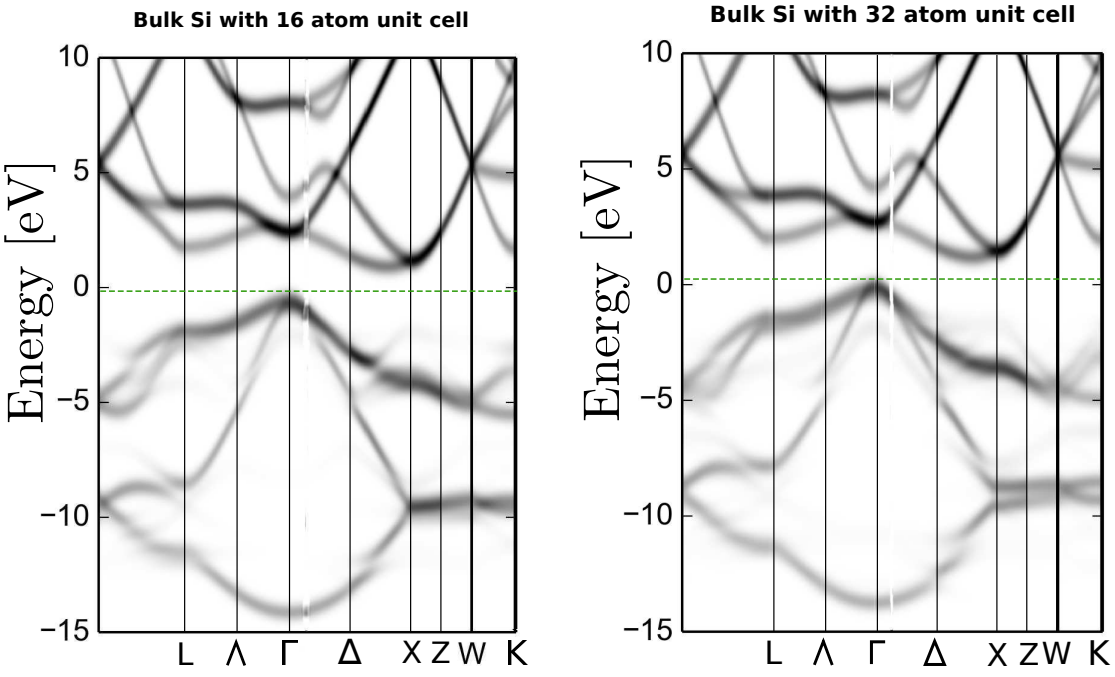

Figure 5.15: Left panel: the embedded unfolded band structure for a 16 atom unit cell. The degeneracy lifting is reduced compared to the 2 atoms case. Right panel: the embedded unfolded band structure for a 32 atom unit cell. Also here the degeneracy is restored in most of the high symmetry points.

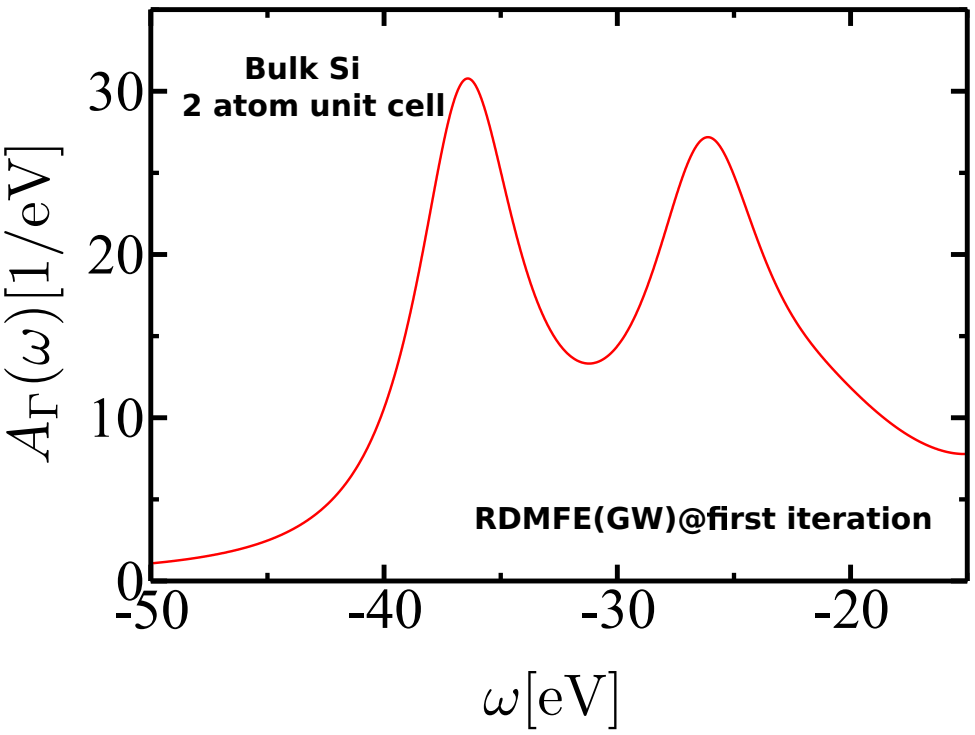

Figure 5.16: A zoom into the plasmon region of the RDMFE(GW) spectral function at first iteration. The splitting in the plasmon peak is an artefact of the local treatment of the RDMFE self-energy.

Their main advantage is that they are variational [224], hence, the Green's function does not have to be the solution of the Dyson equation for them to give accurate total energies. In other words, an approximation to the solution of the Dyson equation (i.e., an approximate Green's function) gives already total energies that are reasonably accurate [60]. On the other hand, the Galitskii-Migdal [128] equation is not variational and is thus only suitable for self-consistent Green's functions that are solutions of the Dyson equation [225, 226, 227]. During this thesis I have investigated a number of ways to compute the total energy from the self-consistent embedded Green's function using the Galitskii-Migdal formula. In this section I will present an analysis of the embedded total energy to justify the definition of the total energy I have chosen for my calculations.

5.2.1 The Galitskii-Migdal equation for local Green's functions

The Galitskii-Migdal formula can be written as [51]

$$E_{\mathrm{GM}} = \frac{1}{2}\int d\mathbf{r} \lim_{\substack{\mathbf{r}'\to\mathbf{r} \\ t\to t^+}} \Big[\partial_t - ih(\mathbf{r})\Big] G(\mathbf{r},\mathbf{r}';t,t'), \tag{5.17}$$

where $h(\mathbf{r})$ is the non-interacting Hamiltonian and $G(\mathbf{r},\mathbf{r}';t,t')$ the fully interacting Green's function. Using the Dyson-equation for the interacting Green's function

$$G(\mathbf{r},\mathbf{r}';t,t') = G_0(\mathbf{r},\mathbf{r}';t,t')+ \int d\mathbf{r}_1\mathbf{r}_2dt_1dt_2G_0(\mathbf{r},\mathbf{r}_1;t,t_1)\Sigma(\mathbf{r}_1,\mathbf{r}_2;t_1,t_2)G(\mathbf{r}_2,\mathbf{r}';t_2,t'), \tag{5.18}$$

and the equation of motion

$$\Big[i\partial_t - h(\mathbf{r})\Big]G_0(\mathbf{r},\mathbf{r}';t,t') = \delta(\mathbf{r}-\mathbf{r}')\delta(\mathbf{t}-\mathbf{t}'), \tag{5.19}$$

one can rewrite eq. (5.17) as follows

$$E_{\mathrm{GM}} = -i\int d\mathbf{r}d\mathbf{r}_2dt_2 \lim_{\substack{\mathbf{r}'\to\mathbf{r}\\ t\to t^+}} \Big[h(\mathbf{r})\delta(\mathbf{r}-\mathbf{r}_2)\delta(t-t_2)+ \tfrac{1}{2}\Sigma(\mathbf{r},\mathbf{r}_2;t,t_2)\Big]G(\mathbf{r}_2,\mathbf{r}';t_2,t'). \tag{5.20}$$

To make the upper expression easier to handle, I divide it into two parts: $E_{\mathrm{GM}} = E_{(1)} + E_{(2)}$, where the first term is given by

$$E_{(1)} = \int d\mathbf{r}d\mathbf{r}_2 \lim_{\substack{\mathbf{r}'\to\mathbf{r}\\ t\to t^+}} h(\mathbf{r})\delta(\mathbf{r}-\mathbf{r}_2)n(\mathbf{r}_2,\mathbf{r}'), \tag{5.21}$$

where I have substituted

$$n(\mathbf{r}_2,\mathbf{r}') = -\frac{i}{2\pi}\int d\omega e^{-i\omega 0^+}G(\mathbf{r}_2,\mathbf{r}',\omega). \tag{5.22}$$

Because of the time dependence of the self-energy, the second term becomes

$$E_{(2)} = -\frac{i}{2}\int d\mathbf{r}d\mathbf{r}_2dt_2 \lim_{\mathbf{r}'\to\mathbf{r}t\to t^+} \Sigma(\mathbf{r},\mathbf{r}_2;t,t_2)G(\mathbf{r}_2,\mathbf{r}';t_2,t'). \tag{5.23}$$

Here, I use the Fourier transform of the time dependent functions $G(t_2,t')$ and $\Sigma(t_2,t')$ to the frequency domain, $G^\sigma(\mathbf{r}_2,\mathbf{r}';t_2,t') = \frac{1}{2\pi}\int d\omega e^{-i\omega(t_2-t')}G^\sigma(\mathbf{r}_2,\mathbf{r}',\omega)$. Recalling the relation for the Dirac δ-distribution $2\pi\delta(\omega-\omega') = \int dt_2 e^{-i(\omega-\omega')t_2}$ I readily obtain

$$E_{(2)} = -\frac{i}{2}\frac{1}{2\pi}\int d\mathbf{r}d\mathbf{r}_2d\omega \lim_{\mathbf{r}'\to\mathbf{r}} \Sigma(\mathbf{r},\mathbf{r}_2;\omega)G(\mathbf{r}_2,\mathbf{r}';\omega)e^{-i\omega 0^+}. \tag{5.24}$$

Since I will be working with a non-orthogonal basis it makes sense to expand $G^\sigma(\mathbf{r}_2,\mathbf{r}',\omega)$ in the basis of NAO Bloch states $\varphi_{i,\mathbf{k}}(\mathbf{r})$

$$G(\mathbf{r}_2,\mathbf{r}',\omega) = \sum_{\mathbf{k}}\sum_{i,j} G_{ij}(\mathbf{k},\omega)\varphi^*_{j,\mathbf{k}}(\mathbf{r}')\varphi_{i,\mathbf{k}}(\mathbf{r}_2), \tag{5.25}$$

where

$$G_{ij}(\mathbf{k},\omega) = \sum_{n,m}\int d\mathbf{r}_2d\mathbf{r}' S^{-1}_{in}(\mathbf{k})\varphi^*_{n,\mathbf{k}}(\mathbf{r}_2)G(\mathbf{r}_2,\mathbf{r}',\omega)\varphi_{m,\mathbf{k}}(\mathbf{r}')S^{-1}_{mj}(\mathbf{k}), \tag{5.26}$$

with the overlap matrix $S_{ij}(\mathbf{k}) = \int d\mathbf{r}\varphi^*_{i,\mathbf{k}}(\mathbf{r})\varphi_{j,\mathbf{k}}(\mathbf{r})$.
Substituting Eq. (5.25) into Eq. (5.22) and (5.24) I obtain the **k**-dependent Galitskii-Migdal formula in the non-orthogonal NAO basis

$$E_{\mathrm{GM}} = \sum_{\mathbf{k}}\sum_{i,j}\left[h_{ji}(\mathbf{k})n_{ij}(\mathbf{k}) - \frac{i}{2}\int\frac{d\omega}{2\pi}\Sigma_{ji}(\mathbf{k},\omega)G_{ij}(\mathbf{k},\omega)e^{-i\omega 0^+}\right]. \tag{5.27}$$

I have not introduced any constraints or approximation yet and the Galitskii-Migdal formula in the upper expression is general. To be able to use the Galitskii-Migdal formula for the RDMFE scheme, however, a few approximations must be introduced

(i) In RDMFE the self-consistent Green's function is local i.e., **k**-independent

$$G(\mathbf{k},\omega) \longrightarrow G^{\mathrm{emb}}(\omega) \tag{5.28}$$

(ii) as a direct result of the locality of the Green's function, the self-energy in RDMFE is local

$$\Sigma(\mathbf{k},\omega) \longrightarrow \Sigma^{\mathrm{loc}}(\omega). \tag{5.29}$$

(iii) Up to now I did not specify the non-interacting Hamiltonian in Eq. (5.27). In our case I define it as

$$h(\mathbf{k}) \approx H^{\mathrm{KS}}(\mathbf{k}) - \frac{1}{2}v^{\mathrm{loc}}_{\mathrm{H}} - v^{\mathrm{loc}}_{\mathrm{XC}} \tag{5.30}$$

where $v^{\mathrm{loc}}_{\mathrm{H}}$ is the local Hartree potential obtained from the Kohn-Sham Green's function via the density matrix $n^{\mathrm{KS}}_{ij} = -\frac{i}{2\pi}\int d\omega\, G^{\mathrm{KS}}(i\omega)_{ij}e^{i\omega\tau^+}$ as

$$[v^{\mathrm{loc}}_{\mathrm{H}}]_{ij} = \sum_{kl}\langle ij|kl\rangle n^{\mathrm{KS}}_{kl}. \tag{5.31}$$

$H^{\mathrm{KS}}(\mathbf{k})$ is the Kohn-Sham Hamiltonian as given in Eq. (4.20), while $v^{\mathrm{loc}}_{\mathrm{XC}}$ is the local XC-potential from Eq. (4.21).

The resulting RDMFE total energy formula is then given by

$$\begin{aligned} E^{\mathrm{RDMFE}}_{\mathrm{GM}} &= \sum_{ij}\sum_{\mathbf{k}} h_{ji}(\mathbf{k})n^{\mathrm{emb}}_{ij} + \frac{1}{2}\int\frac{d\omega}{2i\pi}[\Sigma^{\mathrm{loc}}_{\mathrm{XC}}(i\omega)]_{ji}G^{\mathrm{emb}}_{ij}(i\omega)e^{i\omega 0^+} \\ &= \sum_{ij} H^{\mathrm{KS}}_{ji}n^{\mathrm{emb}}_{ij} - \frac{1}{2}[v^{\mathrm{loc}}_{\mathrm{H}}]_{ji}n^{\mathrm{emb}}_{ij} - [v^{\mathrm{loc}}_{\mathrm{XC}}]_{ji}n^{\mathrm{emb}}_{ij} \\ &+ \frac{1}{2}\int\frac{d\omega}{2i\pi}[\Sigma^{\mathrm{loc}}_{\mathrm{XC}}(i\omega)]_{ji}G^{\mathrm{emb}}_{ij}(i\omega)e^{i\omega 0^+}, \end{aligned} \tag{5.32}$$

where I have defined the **k**-summed Kohn-Sham Hamiltonian $\sum_{\mathbf{k}} H^{\mathrm{KS}}(\mathbf{k}) = H^{\mathrm{KS}}$.
Compared to Eq. (5.27), Eq. (5.32) includes only the local (i.e., **k**-independent) quantities. Furthermore, the non-interacting Hamiltonian $h(\mathbf{k})$ is given by the approximation Eq. (5.30).

To test my total energy implementation, I have performed calculations for the local GW self-energy at the limit of very large lattice constant (i.e., isolated unit cell). This allows a comparison with an implementation for finite systems in FHI-aims [61] where the total energy is computed using the Galitskii-Migdal formula. Table (5.3) shows the components of the Galitskii-Migdal total energy in the RDMFE framework compared to the ones of the scGW calculation for the He atom and the H_2 and the Na_2 molecules[1]. The RDMFE values where all calculated for the corresponding bulks with a lattice constant of 20Å. The RDMFE values reproduce almost to the meV level the scGW values. For the PBE0 case the self-energy is static and is

Term	**He**	**H_2**	**Na_2**
$H^{\mathrm{KS}}n^{\mathrm{emb}}$	-30.971399	-20.082893	-4681.324289
$H^{\mathrm{KS}}n^{scGW}$	-30.976581	-20.084208	-4681.324755
$v_{\mathrm{XC}}^{\mathrm{loc}}n^{\mathrm{emb}}$	-36.283999	-24.105587	-1004.447234
$v_{\mathrm{XC}}^{\mathrm{loc}}n^{scGW}$	-36.286584	-24.106258	-1004.447806
$\frac{1}{2}v_{\mathrm{H}}^{\mathrm{KS}}n^{\mathrm{emb}}$	54.994712	35.697015	4847.058775
$\frac{1}{2}v_{\mathrm{H}}^{\mathrm{KS}}n^{scGW}$	54.996847	35.697851	4847.073781
$\frac{1}{2}\Sigma_{\mathrm{X}}^{\mathrm{loc}}n^{\mathrm{emb}}$	-27.173906	-17.503642	-760.630196
$\frac{1}{2}\Sigma_{\mathrm{X}}^{scGW}n^{scGW}$	-27.181325	-17.505250	-760.632183
$\frac{1}{2}\int\frac{d\omega}{2i\pi}\Sigma_{\mathrm{C}}^{\mathrm{loc}}(i\omega)G^{\mathrm{emb}}(i\omega)e^{i\omega 0^+}$	-1.744578	-2.3053908	-2.457104
$\frac{1}{2}\int\frac{d\omega}{2i\pi}\Sigma_{\mathrm{C}}^{scGW}(i\omega)G^{scGW}(i\omega)e^{i\omega 0^+}$	-1.737910	-2.304200	-2.455707
Total energy $E_{\mathrm{GM}}^{\mathrm{RDMFE}}$	-78.759362	-32.067732	-8808.470968
Total energy E_{GM}^{scGW}	-78.759212	-32.068074	-8808.489963

Table 5.3: Galitskii-Migdal total energy components for a GW total energy (see Eq. (5.32)): a benchmark against the standard scGW implementation for molecules[127]. All energies are in eV. n^{scGW} is the density matrix computed from the scGW Green's function $G^{\mathrm{emb}}(i\omega)$ at self-consistency and $\Sigma_{\mathrm{X}}^{scGW}, \Sigma_{\mathrm{C}}^{scGW}(i\omega)$ are the exchange and correlation GW self-energies at self-consistency.

defined as in Eq. (4.34) for $\alpha = \frac{1}{4}$. Thus, the last term of Eq. (5.32) becomes

$$\begin{aligned}\frac{1}{2}\int\frac{d\omega}{2i\pi}[\Sigma_{\mathrm{XC}}^{\mathrm{loc}}(i\omega)]_{ji}G_{ij}^{\mathrm{emb}}(i\omega)e^{i\omega 0^+} &= \frac{1}{2}[\Sigma_{\mathrm{XC}}^{\mathrm{loc}}(\alpha)]_{ji}n_{ij}^{\mathrm{emb}} \\ &= \frac{1}{2}[\alpha\Sigma_{\mathrm{X}}^{\mathrm{loc}} + (1-\alpha)v_{\mathrm{XC}}^{\mathrm{loc}}]_{ji}n_{ij}^{\mathrm{emb}}. \qquad (5.33)\end{aligned}$$

[1]The chemical potential for the RDMFE calculation had to be adapted to the corresponding value from the finite system calculation to allow optimal comparison. Moreover, additionally to the XC self-energy the Hartree potential should also be updated in the RDMFE self-consistency cycle.

I have computed the different components of the the total energy Eq. (5.32) for the PBE0 self-energy, where I choose bulk Silicon as test system. Figure (5.17) illustrates the evolution of the different components entering the definition of the Galitskii-Migdal formula Eq. (5.32) with increasing unit cell size (up to 32 atoms in the unit cell). The change of all components with respect to the unit cell size is very important. Particularly the change in the local Hartree potential is very large. This is not surprising, since the Hartree potential is a strongly non-local quantity, which cannot be computed from a local density matrix as I am doing in Eq. (5.31). This carries over into the behavior of the total energy shown in Fig.

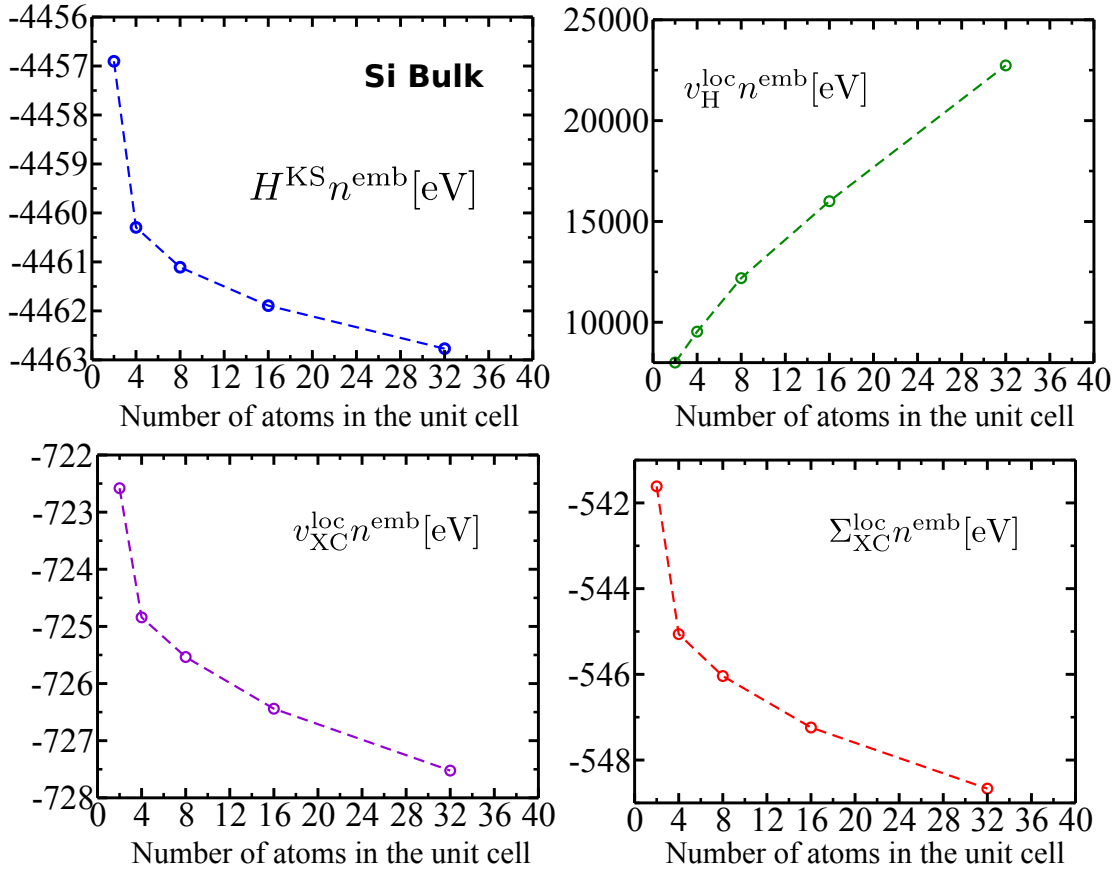

Figure 5.17: The components of the Galitskii-Migdal total energy for the RDMFE Green's function and self-energy as in Eq. 5.32 for bulk Si with increasing unit cell size. All component show strong dependence on the size of the embedded system (i.e., the unit cell). The Hartree contribution (top right) shows an even more pronounced change. All calculation were performed using a *tier1* basis set.

(5.18) that changes drastically with increasing unit cell size. Hence, this strong, nearly divergent, behavior of the total energy, Eq. (5.32), with increasing unit cell size, can be mainly led back to the Hartree contribution (see Fig. (5.17)) that enters the embedded total energy. This observation reinforces the fact that the Hartree potential is a strongly non-local quantity and the local approximation as in Eq. (5.31) is thus too coarse-grained.

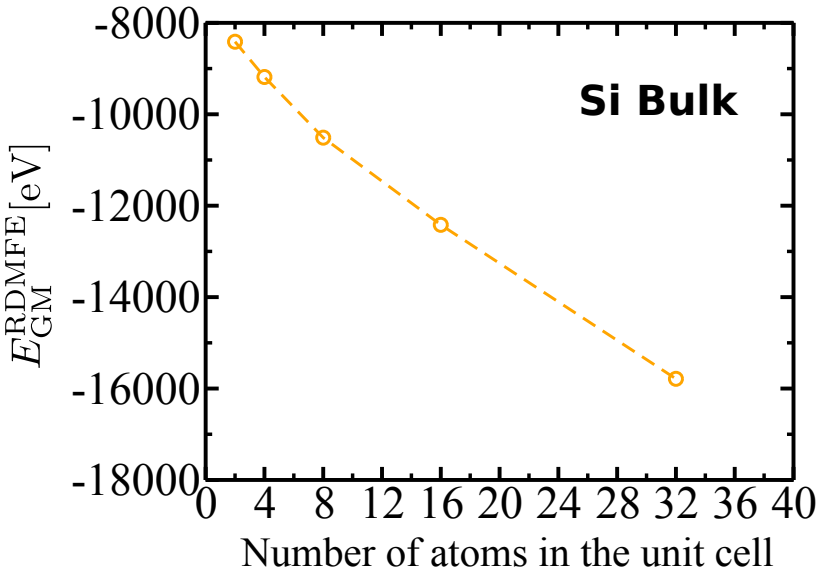

Figure 5.18: The total energy from the Galitskii-Migdal formula Eq. 5.32 with increasing unit cell size for bulk Si. The strong dependence on the size of the embedded system stems mainly from the Hartree contribution. All calculation were performed using a *tier1* basis set.

5.2.2 The embedded total energy as correction to the KS total energy

To reduce the effects introduced by the localisation in the RDMFE approximation, I have thought of rewriting the embedded total energy as a correction to the Kohn-Sham total energy E_{KS}. In FHI-aims the total energy is calculated from the electronic density at self-consistency using the variational Harris formula [228, 229]. It is given, using the equivalent density matrix formalism, by

$$E_{\mathrm{KS}} = \sum_{ij}\sum_{\mathbf{k}} H_{ji}^{\mathrm{KS}}(\mathbf{k}) n_{ij}^{\mathrm{KS}}(\mathbf{k}) - \frac{1}{2}[v_{\mathrm{H}}(\mathbf{k})]_{ji} n_{ij}^{\mathrm{KS}}(\mathbf{k}) - [v_{\mathrm{XC}}(\mathbf{k})]_{ji} n_{ij}^{\mathrm{KS}}(\mathbf{k}) + E_{\mathrm{XC}}[n], \tag{5.34}$$

where n^{KS} is the non-local Kohn-Sham density matrix and $E_{\mathrm{XC}}[n]$ the XC energy functional evaluated at the Kohn-Sham density n of the periodic system. The embedded total energy can then be written as

$$E_{\mathrm{tot}}^{\mathrm{emb}} \approx E_{\mathrm{KS}} + E_{\mathrm{GM}}^{\mathrm{RDMFE}} - E_{\mathrm{KS}}^{\mathrm{loc}}, \tag{5.35}$$

where the local Kohn-Sham total energy $E_{\mathrm{KS}}^{\mathrm{loc}}$ is given by

$$E_{\mathrm{KS}}^{\mathrm{loc}} = \sum_{ij}\sum_{\mathbf{k}} h_{ji}(\mathbf{k}) n_{ij}^{\mathrm{KS}} + E_{\mathrm{XC}}[n]. \tag{5.36}$$

Substituting the upper equation and Eq. (5.32) into Eq. (5.35) one finally arrives at the embedded total energy

$$\begin{aligned} E_{\text{tot}}^{\text{emb}} &= E_{\text{KS}} + \sum_{ij}\sum_{\mathbf{k}} h_{ji}^{\text{RDMFE}}(\mathbf{k})[n_{ij}^{\text{emb}} - n_{ij}^{\text{KS}}] + \frac{1}{2}\int \frac{d\omega}{2i\pi}[\Sigma_{\text{XC}}^{\text{loc}}(i\omega)]_{ji} G_{ij}^{\text{emb}}(i\omega) e^{i\omega 0^+} - E_{\text{XC}}[n] \\ &= E_{\text{KS}} + \sum_{ij} H_{ji}^{\text{KS}}[n_{ij}^{\text{emb}} - n_{ij}^{\text{KS}}] \\ &\quad - \frac{1}{2}[v_{\text{H}}^{\text{loc}}]_{ji}[n_{ij}^{\text{emb}} - n_{ij}^{\text{KS}}] \\ &\quad - [v_{\text{XC}}^{\text{loc}}]_{ji}[n_{ij}^{\text{emb}} - n_{ij}^{\text{KS}}] \\ &\quad + \frac{1}{2}\int \frac{d\omega}{2i\pi}[\Sigma_{\text{XC}}^{\text{loc}}(i\omega)]_{ji} G_{ij}^{\text{emb}}(i\omega) e^{i\omega 0^+} - E_{\text{XC}}[n]. \end{aligned} \tag{5.37}$$

In analogy to the analysis of the Galitskii-Migdal equation in the former section, I analized the components that enter the definition of the embedded total energy Eq. (5.37) for a PBE0 self-energy. I performed calculations on bulk Si with increasing unit cell size. Figure (5.19) depicts the behavior of the different components with respect to increasing the unit cell size. With exception of the Hartree potential, most components change less strongly with increasing unit cell, compared to the "pure" Galitskii-Migdal case Fig. (5.17). The strong change in the Hartree term confirms the assumption, that the Hartree energy cannot be described properly using a local density-matrix. Hence, in the following I will discard this contribution to the embedded total energy. Equation (5.37) then becomes

$$\begin{aligned} E_{\text{tot}}^{\text{emb}} &= E_{\text{KS}} + \sum_{ij} H_{ji}^{\text{KS}}[n_{ij}^{\text{emb}} - n_{ij}^{\text{KS}}] \\ &\quad - [v_{\text{XC}}^{\text{loc}}]_{ji}[n_{ij}^{\text{emb}} - n_{ij}^{\text{KS}}] \\ &\quad + \frac{1}{2}\int \frac{d\omega}{2i\pi}[\Sigma_{\text{XC}}^{\text{loc}}(i\omega)]_{ji} G_{ij}^{\text{emb}}(i\omega) e^{i\omega 0^+} - E_{\text{XC}}[n]. \end{aligned} \tag{5.38}$$

Figure (5.20) shows the embedded total energy as in Eq. (5.38) for bulk Si with increasing unit cell size for a PBE0 self-energy. One would expect that the total energy approaches the periodic PBE0 total energy. However, the embedded total energy goes relatively far below the periodic PBE0 value. In Eq. (5.38) I used in the calculation of the XC energy $E_{\text{XC}}[n]$ the global (i.e., non-local) density of the periodic systems, while the contribution from RDMFE i.e., $\Sigma_{\text{XC}}^{\text{loc}} n^{\text{emb}}$ is purely local. In addition to that, the correction coming from the Kohn-Sham Hamiltonian i.e., the second term in Eq. (5.37), still contains the global Hartree potential corrected with the local density matrix. All this represent inconsistencies in the embedded total energy definition. In the next section I will present the final embedded total energy that overcomes these inconsistencies.

5.2.3 The RDMFE total energy

To recapitulate the findings of the previous section; Eq. (5.38) contains the Kohn-Sham XC-energy part of the full periodic system (i.e., evaluated with the global

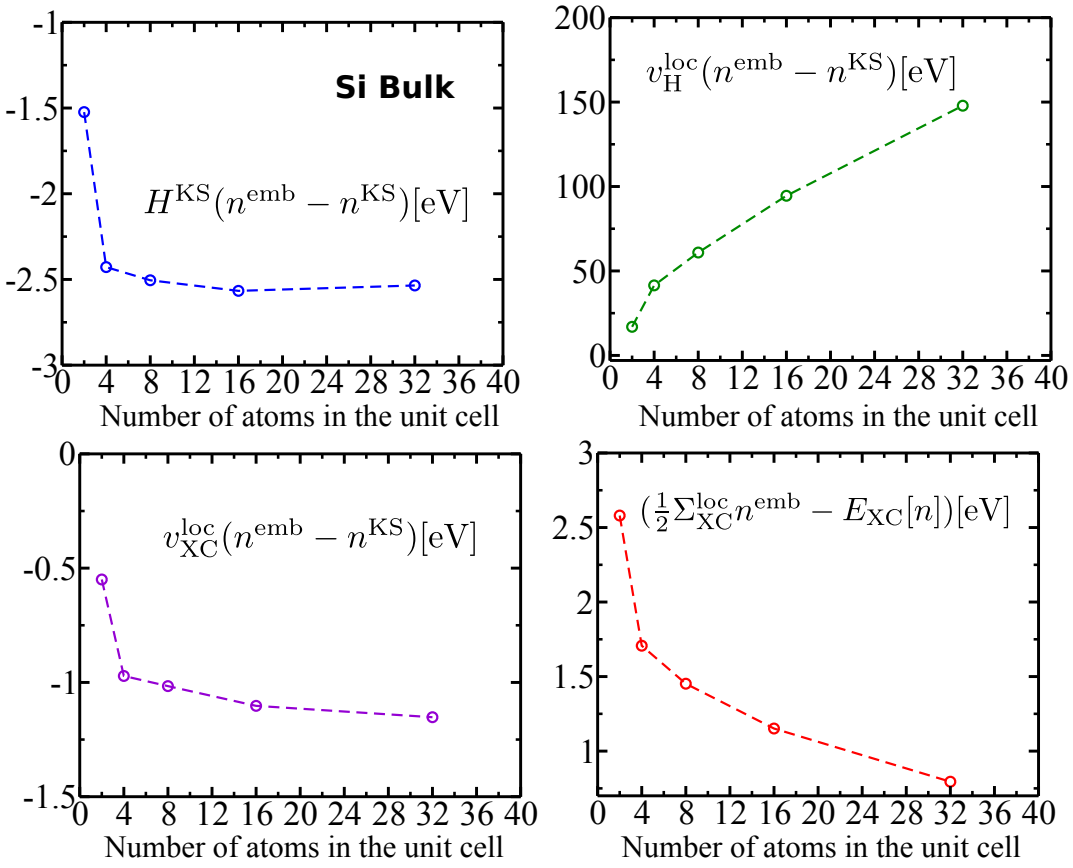

Figure 5.19: The components embedded total energy for the RDMFE Green's function and self-energy as in Eq. 5.38 for bulk Si with increasing unit cell size. Compared to the the Eq. 5.32, the dependence on the embedded system size (i.e., the unit cell) is strongly reduced. For the Hartree contribution (top right), however, this dependence is still important suggesting that the Hartree contribution cannot be properly described using a local density matrix. All calculation were performed using a *tier*1 basis set.

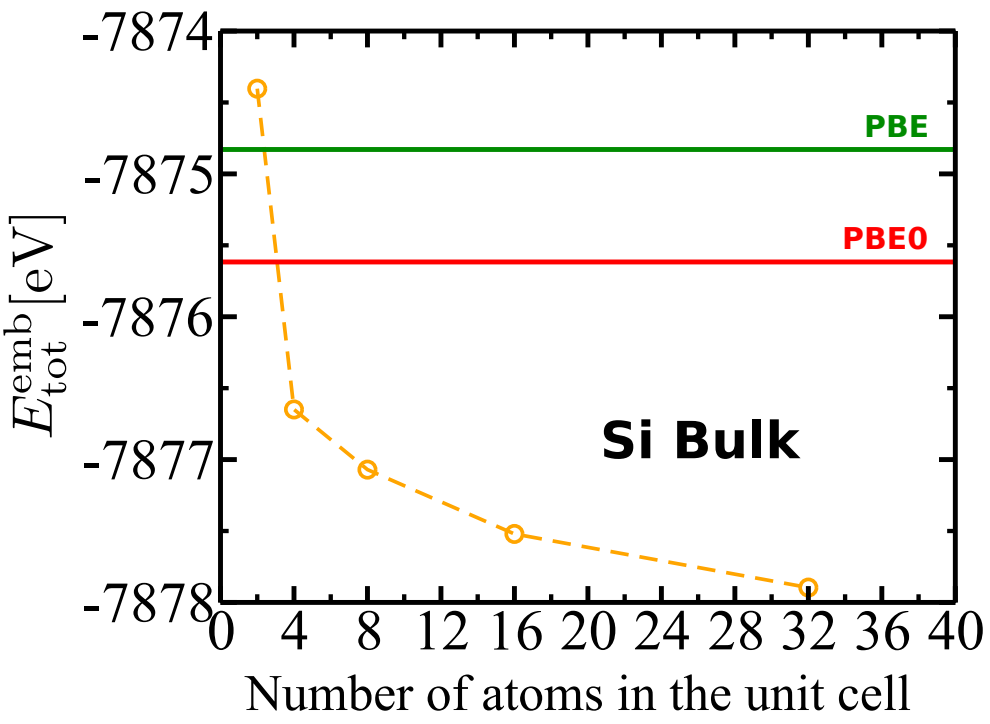

Figure 5.20: The embedded total energy for the RDMFE Green's function and self-energy as in Eq. 5.38 for bulk Si with increasing unit cell size. Comparison is made with the periodic PBE value (green line), i.e., the Kohn-Scham total enegy I am correcting on, and the periodic PBE0 value (red line). For 2 atoms in the unit cell the embedded total energy lies above the PBE value before it drops quite far below the periodic PBE0 total energy for larger unit cells. All calculation were performed using a *tier*1 basis set.

density n). Moreover, to be consistent, the change in the XC-energy contribution of the total energy and the kinetic contribution should be taken together. On the other hand, it is clear that the term

$$\sum_{ij} \left(H^{\mathrm{KS}}_{ji} - [v^{\mathrm{loc}}_{\mathrm{XC}}]_{ji}\right) [n^{\mathrm{emb}}_{ij} - n^{\mathrm{KS}}_{ij}] \tag{5.39}$$

in Eq. (5.38) still includes the Hartree and the external potential parts. To surmount this inconsistency in the definition of the embedded total energy, I have implemented a formula including the kinetic matrix operator explicitly.
For embedded hybrid functionals the total energy expression is given by

$$\begin{aligned} E^{\mathrm{hyb}}_{\mathrm{tot}} \approx E^{\mathrm{KS}}_{\mathrm{tot}} &+ \sum_{ij} t_{ji}(n^{\mathrm{emb}}_{ij} - n^{\mathrm{KS}}_{ij}) \\ &+ E^{\mathrm{hyb}}_{\mathrm{XC}}[n^{\mathrm{emb}}_{ij}] - E^{\mathrm{KS}}_{\mathrm{XC}}[n^{\mathrm{KS}}], \end{aligned} \tag{5.40}$$

with the $\mathbf{k}$-summed kinetic matrix operator $t_{ij} = \frac{1}{N_{1.\mathrm{BZ}}} \sum_{\mathbf{k}} t_{ij}(\mathbf{k})$, where

$$t_{ij}(\mathbf{k}) = -\sum_{\mathbf{R}} \int d\mathbf{r} \varphi^*_i(\mathbf{r}) \frac{\nabla^2}{2} \varphi_j(\mathbf{r} - \mathbf{R}) e^{i\mathbf{k}\cdot\mathbf{R}}. \tag{5.41}$$

The local Kohn-Sham density n^{KS} is obtained from the corresponding local density matrix n^{KS}_{ij} via

$$n^{\mathrm{KS}}(\mathbf{r}) = \sum_{ij} \varphi^*_i(\mathbf{r}) n^{\mathrm{KS}}_{ij} \varphi_j(\mathbf{r}). \tag{5.42}$$

Hence, $E^{\mathrm{KS}}_{\mathrm{XC}}[n^{\mathrm{KS}}]$ is restricted to the embedded region. The contribution from the embedded hybrid calculation is given by

$$E^{\mathrm{hyb}}_{\mathrm{XC}}[n^{\mathrm{emb}}_{ij}] = \frac{1}{2} \sum_{ij} \alpha [\Sigma^{\mathrm{loc}}_{\mathrm{X}}]_{ji} n^{\mathrm{emb}}_{ij} + (1-\alpha) E^{\mathrm{KS}}_{\mathrm{X}}[n^{\mathrm{KS}}] + E^{\mathrm{KS}}_{\mathrm{C}}[n^{\mathrm{KS}}], \tag{5.43}$$

where $E^{\mathrm{KS}}_{\mathrm{X}}[n^{\mathrm{emb}}], E^{\mathrm{KS}}_{\mathrm{C}}[n^{\mathrm{emb}}]$ are respectively, the Kohn-Sham exchange and correlation total energy contribution evaluated with the local embedded density n^{emb} calculated from the corresponding density matrix n^{emb}_{ij}

$$n^{\mathrm{emb}}(\mathbf{r}) = \sum_{ij} \varphi^*_i(\mathbf{r}) n^{\mathrm{emb}}_{ij} \varphi_j(\mathbf{r}). \tag{5.44}$$

For the embedded GW calculation the total energy is given in an analogous fashion

$$\begin{aligned} E^{GW}_{\mathrm{tot}} \approx E^{\mathrm{KS}}_{\mathrm{tot}} &+ \sum_{ij} t_{ji}(n^{\mathrm{emb}}_{ij} - n^{\mathrm{KS}}_{ij}) \\ &+ E^{GW}_{\mathrm{XC}}[G^{\mathrm{emb}}_{ij}(i\omega)] - E^{\mathrm{KS}}_{\mathrm{XC}}[n^{\mathrm{KS}}]. \end{aligned} \tag{5.45}$$

Besides the explicit calculation of the kinetic operator contribution, a key advantage of the total energy formulation Eq. (5.43) and (5.45) is that, instead of evaluating the full $E^{\mathrm{hyb}}_{\mathrm{XC}}[n_{ij}(\mathbf{k})]$, I only compute the change of $E^{\mathrm{hyb}/GW}_{\mathrm{XC}}$ with respect to the

local or semi-local (LDA or GGA) energy in the embedded region (i.e., $E_{\mathrm{XC}}^{\mathrm{KS}}[n^{\mathrm{KS}}]$). This is the main approximation of our approach, which is consistent with the spirit of the local self-energy correction in the RDMFE scheme, and is suggested by the near-sightedness of the XC energy of a bulk system [210]. To test my implementation, I have benchmarked the components of the RDMFE total energy Eq. (5.40) in the limit of large lattice constants, to finite systems calculations. For different hybridization parameter α I expect to recover the PBE values for $\alpha = 0$, while for $\alpha = 1$ the total energy components should equal the HF ones[1]. The resulting comparison is presented in Tab. (5.4) for the He atom and the H_2 molecule. The RDMFE calculation was performed at a lattice constant of 20Å. The Kohn-Sham kinetic energy and XC components tn^{KS} and $E_{\mathrm{XC}}[n^{\mathrm{KS}}]$ are always equal to the corresponding PBE value. This should be the case, since I am starting from a PBE calculation and hence have a PBE Kohn-Sham density n^{KS}. On the other hand, the embedded kinetic and XC components tn^{emb} and $E_{\mathrm{XC}}^{\mathrm{hybr}}[n^{\mathrm{emb}}]$ are almost identical to the corresponding PBE value (for $\alpha = 0$) and HF (for $\alpha = 1$). To see how the

He

	RDMFE(PBEh)			
	$\alpha = 0$	$\alpha = 1$	PBE	HF
tn^{KS}	75.30373823	75.30373823	75.30451969	78.62114201
tn^{emb}	75.30373823	78.61837539	—	—
$E_{\mathrm{XC}}[n^{\mathrm{KS}}]$	-26.47122999	-26.47122999	-26.471861714	-27.85312715
$E_{\mathrm{XC}}[n^{\mathrm{emb}}]$	-26.47122999	-27.08958449	—	—
$E_{\mathrm{XC}}^{\mathrm{hyb}}[n^{\mathrm{emb}}]$	-30.17622890	-27.85233473	—	—

H2

	RDMFE(PBEh)			
	$\alpha = 0$	$\alpha = 1$	PBE	HF
tn^{KS}	31.04311147	30.17349743	31.04214324	30.81157936
tn^{emb}	31.04311147	30.80868329	—	—
$E_{\mathrm{XC}}[n^{\mathrm{KS}}]$	-18.78311417	-18.78311417	-18.782194209	-17.81992246
$E_{\mathrm{XC}}[n^{\mathrm{emb}}]$	-18.78311417	-17.92711806	—	—
$E_{\mathrm{XC}}^{\mathrm{hyb}}[n^{\mathrm{emb}}]$	-19.01981400	-17.81950266	—	—

Table 5.4: Total energy components for the RDMFE(PBEh) total energy for the cases $\alpha = 0$ and $\alpha = 1$ in the limit of a very large lattice constant (isolated unit cell). Comparison is made with the corresponding PBE and HF components.

new total energy expression behaves with the iterations of the outer RDMFE loop,

[1] To allow optimal comparison with HF, I have set the local correlation part in Eq. (5.43) to zero.

I have considered bulk Si with two atoms in the unit cell as test case. Figure (5.21) depicts the evolution of the embedded total energy for the embedded PBE0 and GW self-energies as in Eqs. (5.40) and (5.45), respectively. For the PBE0 case, the total energy reaches its converged value already after 8 iterations, while for the GW self-energy 18 iterations were necessary to converge the total energy. This is not surprising and can be related to the fact that the PBE0 self-energy contributes only a fraction of exact exchange (that is $\alpha = \frac{1}{4}$) to the embedded Hamiltonian, while the GW self-energy contributes the full exact exchange self-energy additionally to the dynamical correlation self-energy. Hence, the embedded GW total energy needs more iterations to stabilize to its converged value. For the same system, I have in-

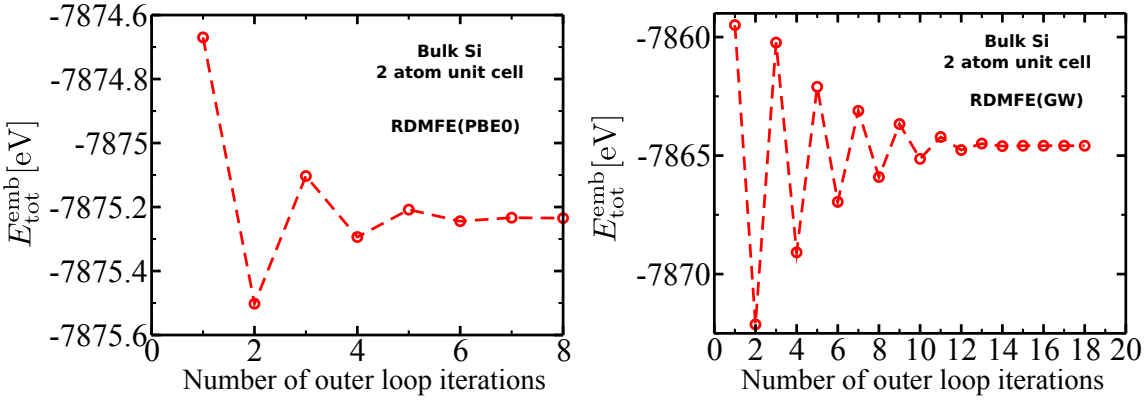

Figure 5.21: The evolution of the RDMFE(PBE0) total energy (left panel) and the RDMFE(GW) total energy (right panel) for bulk Si with a 2 atom unit cell with the iteration of RDMFE the outer loop. The RDMFE(PBE0) total energy approaches its convergence value already after 6 iterations, while the RDMFE(GW) needs 12 iteration to stabilize. The RDMFE(PBE0) calculations were performed with a *tier*1 basis set, while for the RDMFE(GW) I used a *tier*3 basis set.

vestigated the dependence of the embedded total energy on the number of **k**-points in the calculation. Figure (5.22) shows the evolution of the RDMFE total energy for the PBE0 and the GW self-energies, RDMFE(PBE0) and RDMFE(GW). In the case of RDMFE(PBE0), the total energy reaches a reasonably converged value for a **k**-mesh of 6×6×6 points, while for RDMFE(GW) convergence is reached for 10×10×10 **k**-points. The convergence with respect to the basis set is shown in Fig. (5.23) for the RDMFE(PBE0) total energy. While the total energy still changes quite significantly the cohesive energy shows much smaller changes with the basis set size. For the RDMFE(GW) case, the total energy converges only for a *tier*3 basis or higher, as is illustrated in Fig. (5.24). To investigate how the RDMFE total energy Eq. (5.40) behaves with the size of the embedded system, I have performed RDMFE(PBE0) calculations for bulk Si again at increasing unit cell size. Figure (5.25) illustrates the evolution of the components of the embedded total energy coming from the kinetic and the XC contributions. Both components behave in an opposite way i.e., with increasing unit cell size the contribution from the kinetic part becomes more positive in the same way the XC contribution becomes more negative. This is consistent with the fact that the kinetic and XC contributions are

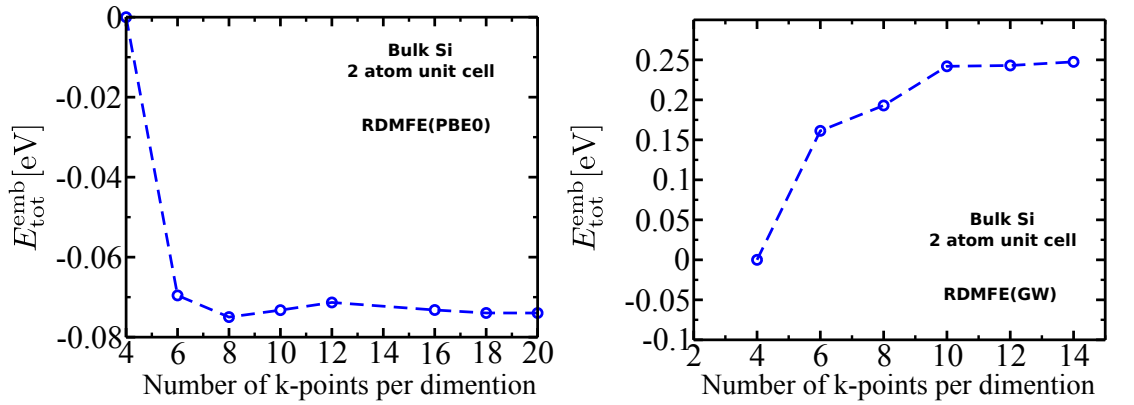

Figure 5.22: RDMFE(PBE0) total energy (left panel) and RDMFE(GW) total energy (right panel) for bulk Si with a 2 atom unit cell at different numbers of **k**-points in the grid. The energy zero is set at the value of the **k**=4×4×4 mesh. The RDMFE(PBE0) calculations were performed with a *tier*1 basis set, while for the RDMFE(GW) I used a *tier*3 basis set.

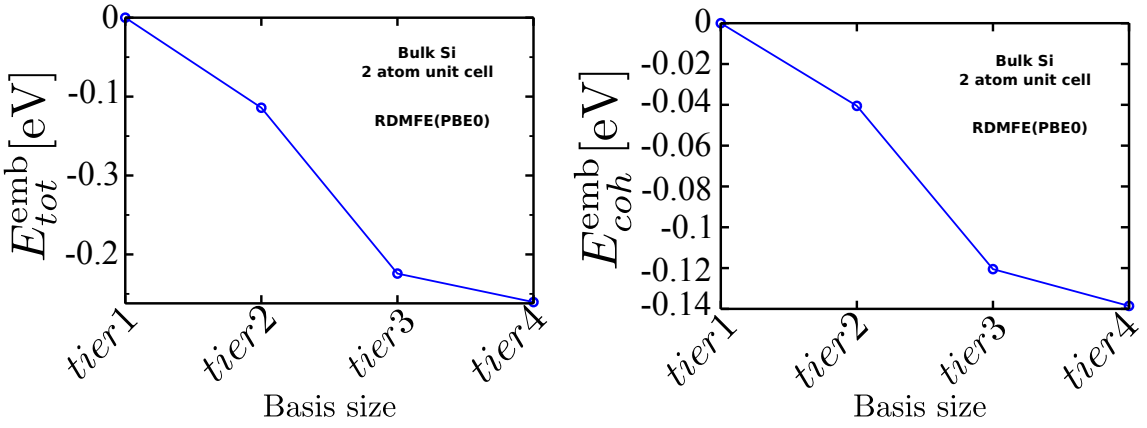

Figure 5.23: RDMFE(PBE0) total energy (left panel) and cohesive energy (right panel) for bulk Si with a 2 atom unit cell as function of the basis size. The energy zero is set at the value of the *tier*1 basis.

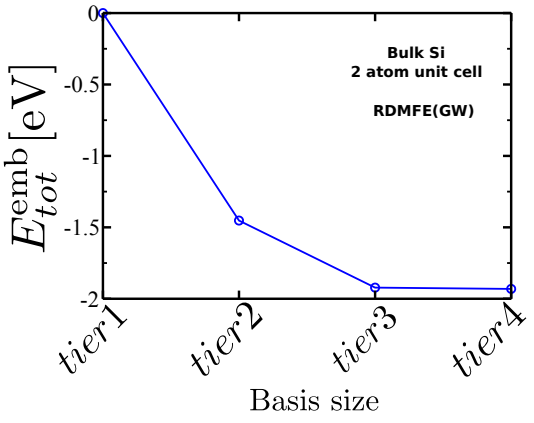

Figure 5.24: RDMFE(GW) total energy for bulk Si with a 2 atom unit cell as function of the basis size. The energy zero is set at the value of the *tier*1 basis.

correlated to each other and should always be considered together.

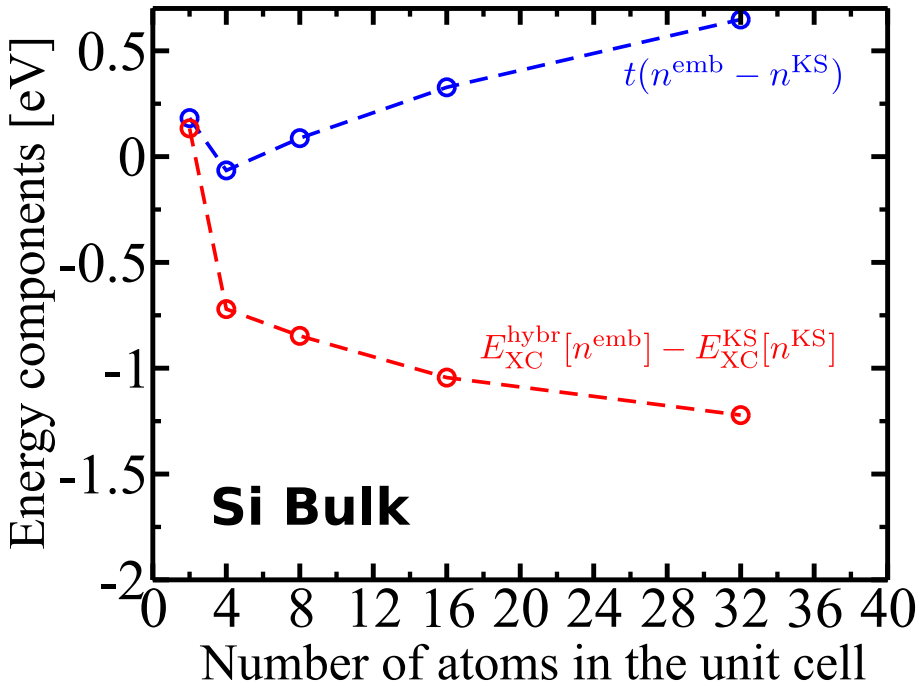

Figure 5.25: Components of the RDMFE(PBE0) total energy for bulk Si with increasing unit cell size. The change in the kinetic contribution (blue line) goes in an opposite way to the one from the XC contribution (red line). The calculations were performed using a *tier1* basis set.

The resulting RDMFE(PBE0) total energy is depicted in Fig. (5.26). For the 2 atom unit cell the RDMFE total energy lies above the periodic PBE0 value ($E_{\mathrm{tot}}^{\mathrm{KS}}$ in Eq. (5.40)) that is the starting calculation. On the other hand, going to larger unit cells, the RDMFE total energy shifts to values below the periodic PBE0 total energy. Recalling Eq. (5.40), one can see however, that the RDMFE total energy corrects up on the Kohn-Sham kinetic and XC contributions, while leaving the electrostatic part of the Kohn-Sham total energy unchanged. Hence, in the RDMFE(PBE0) total energy the electrostatic energy is still the one from PBE. This can be seen when comparing to a periodic PBE0 total energy where the electrostatic part is taken from the PBE calculation. The RDMFE(PBE0) total energy approaches this new value in a systematic way. Analogously, the evolution of the cohesive energy with respect to an increase of the embedded region is illustrated in Fig. (5.27). In the same spirit as for the RDMFE(PBE0) total energy, I have investigated the size dependence of the RDMFE(GW) total energy for bulk He. The small size of the system allows me to consider unit cells with up to 64 atoms. The total energy reaches a converged value for the 48 atom unit cell however, for RDMFE(GW) case I lack of periodic reference with which I could compare my results to.

To summerise, I have investigated the embedded RDMFE total energy as given by Eqs. (5.40) and (5.45) for the embedded PBE0 and GW self-energies. I have shown that it behaves well with the computational parameters and I have demonstrated that the RDMFE(PBE0) total energy converges to the right limit with increasing

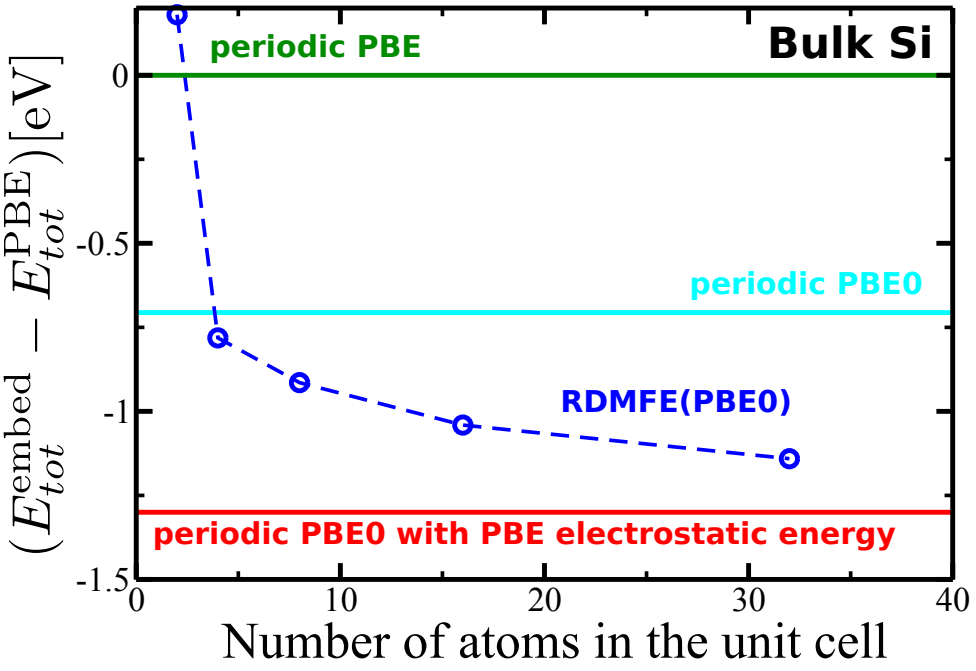

Figure 5.26: The RDMFE(PBE0) total energy for bulk Si with increasing unit cell size. For the 2 atom unit cell, the RDMFE total enegy lies above the periodic PBE reference (green line), while increasing the unit cell size, the RDMFE total energy drops bellow the periodic PBE0 value but approaches systematically the periodic PBE0 with PBE electrostatic energy one. The calculations were performed using a *tier*1 basis set.

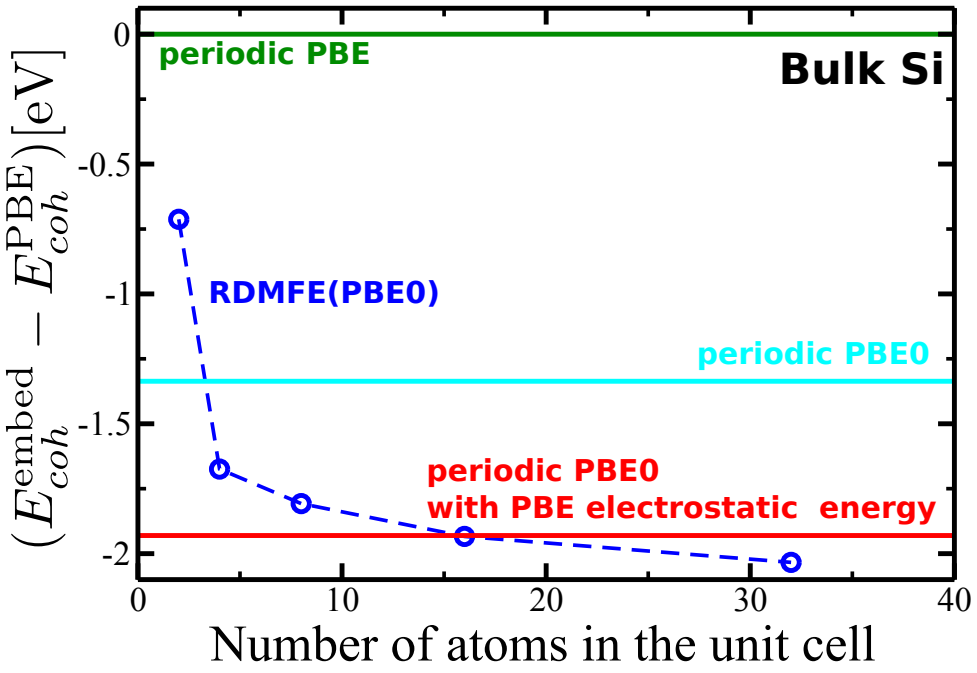

Figure 5.27: The RDMFE(PBE0) cohesive energy for bulk Si with increasing unit cell size. The RDMFE enegy lies between the periodic PBE reference (green line) and the periodic PBE0 with PBE electrostatic energy values. The calculations were performed using a *tier*1 basis set.

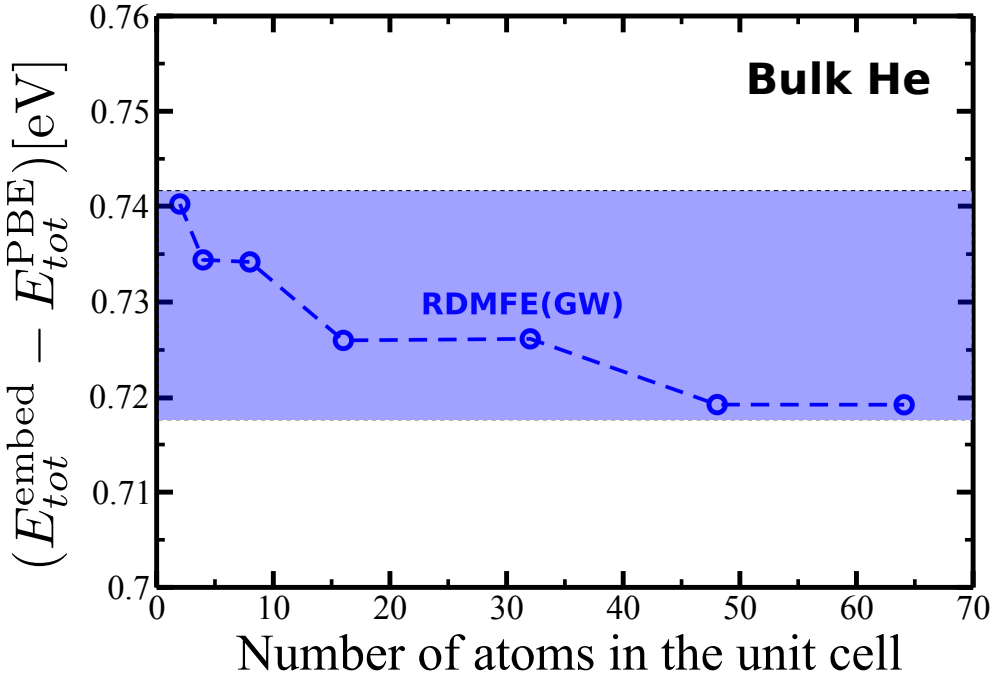

Figure 5.28: The RDMFE(GW) total energy for bulk He for increasing unit cell size, where the blue region indicates a change in the range of $\sim$ 20 meV. Both curves are referenced to the PBE total energy.

size of the embedded region.

5.2.4 Correlating the required size of the unit cell with the range of the interaction

In large systems, electronic screening plays a crucial role. In particular periodic systems cannot be accurately described with a theory that lacks on screening effects. Thus, as I have discussed in the first chapter, the exact exchange self-energy from HF theory includes the bare (unscreened) Coulomb interaction. For my total energy test, however, I have used the PBE0 self-energy that includes a fraction (i.e., 0.25) of exact exchange. One can easily think that this is not the optimal choice for the embedded self-energy in RDMFE, since I am replacing the PBE exchange for the periodic system (that contains some screening effects) with a local exact exchange that does not include any screening. To investigate the screening effect on the RDMFE total energy I have performed a RDMFE calculation with an embedded HSE [116] self-energy as in Eq. (4.39), where the screening can be tuned by the so-called screening parameter γ. The resulting RDMFE total energy can then be written as

$$E_{\mathrm{XC}}^{\mathrm{hyb}}[n_{ij}^{\mathrm{emb}},\alpha,\gamma] = \frac{1}{2}\sum_{ij}\alpha[\Sigma_{\mathrm{X}}^{\mathrm{SR,loc}}(\gamma)]_{ji}n_{ij}^{\mathrm{emb}} + (1-\alpha)E_{\mathrm{X}}^{\mathrm{KS}}[n^{\mathrm{KS}}] + E_{\mathrm{C}}^{\mathrm{KS}}[n^{\mathrm{KS}}], \quad (5.46)$$

with the short range exact exchange self-energy $\Sigma_{\mathrm{X}}^{\mathrm{SR,loc}}(\gamma)$.
In principle γ is just a numerical tool and does not necessary have a physical meaning. To relate the screening parameter to my embedded scheme I have defined the radius R_{sphere} enclosing the embedded region (i.e., the embedded unit cell). The screening parameter is then given by this radius as $\gamma = 1/R_{\mathrm{sphere}}$. Figure (5.29) illustrates the change of the screening parameter with respect to the unit cell volume and the corresponding sphere radius for the 2, 4 , 8 and 16 atom bulk Si unit cells. For

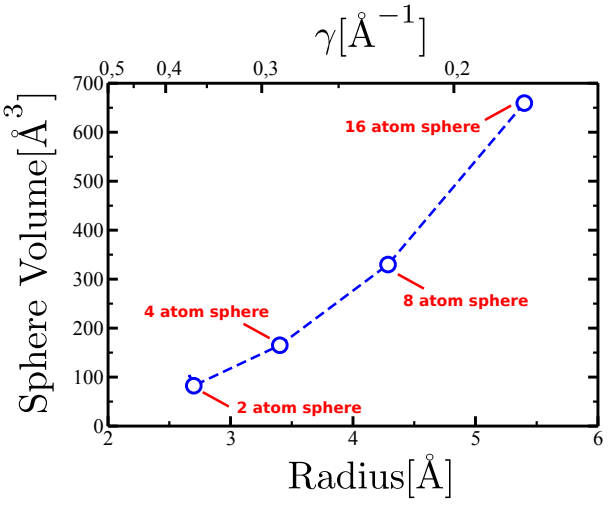

Figure 5.29: An illustration of the relation between the radius of a sphere enclosing the Si unit cell, the sphere volume and the corresponding screening parameter.

different screening parameters I have then performed RDMFE(HSE) calculations for bulk Si. For each given γ I have carried out a calculation with increasing unit cell size from the 2 up to the 32 atom unit cell. The resulting total energy extrapolation is depicted in Fig. (5.30). When compared to the RDMFE(PBE0) curve, the change of the RDMFE(HSE) total energy is reduced, when going from one unit cell to the other. Furthermore, the curve with the smallest radius (largest screening parameter γ) changes the least with increasing unit cell size and reaches a converged value for the 8 atom unit cell.

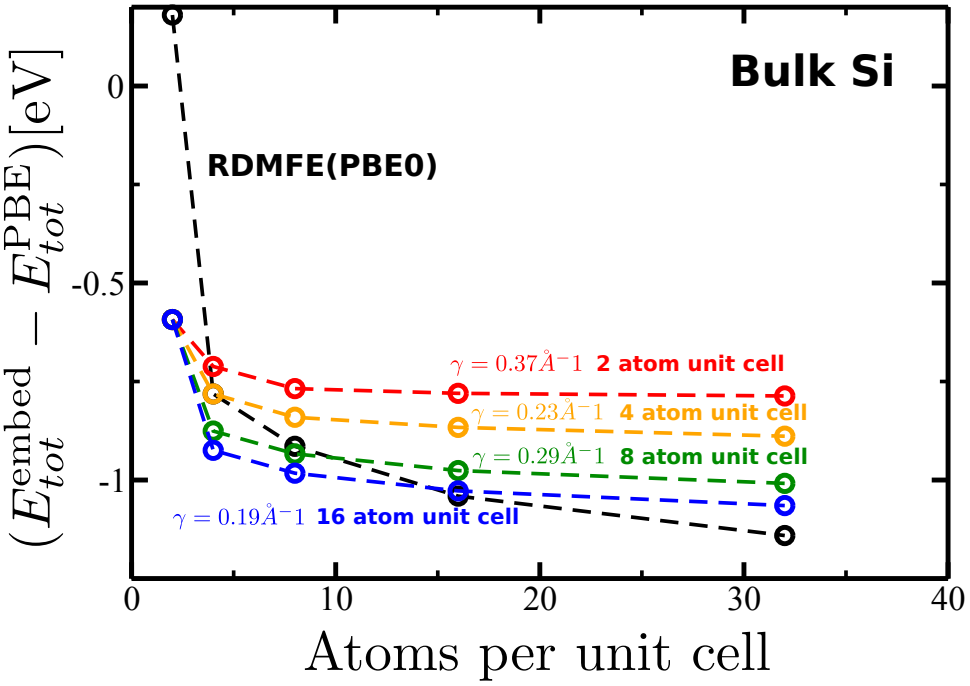

Figure 5.30: The RDMFE(HSE) total energy for bulk He for increasing unit cell size for bulk Si for different screening parameters. Comparison is made with the RDMFE(PBE0) calculation (black line). The dependence on the size of the embedded region is much less pronounced for the RDMFE(HSE). Calculation with a screening of $\gamma = 0.37\text{Å}^{-1}$ shows convergence for the 8 atom unit cell.

This investigation demonstrates that the relatively strong dependence of the RDMFE(PBE0) total energy on the size of the embedded region can be related to the long ranged nature of the exact exchange self-energy. Hence, for self-energies that involve screening, such as the *GW* self-energy, the dependence on the unit cell size should be reduced. This is supported as shown in Fig. (5.28) for bulk He. Furthermore, this study shows that for RDMFE(HSE) the same behavior is possible as for RDMFE(PBEh) with a corresponding α. One can then perform size-converged RDMFE calculations and with PBE0 like total energies and spectra.

5.2.5 Calculating cohesive properties with RDMFE

To finalize my analysis of physical quantities calculated with RDMFE, I want to discuss cohesive bulk properties. Again considering bulk Si as a test system I have

performed RDMFE calculations with embedded PBE0 and GW self-energies. The resulting total energy as function of the lattice constant for RDMFE(PBE0) is shown in Fig. (5.29). For the 2 atom unit cell the equilibrium lattice constant lies already bellow the periodic PBE one, that is the starting point calculation. Increasing the unit cell size to 8 atoms in the unit cell, the equilibrium lattice constants takes a value below the periodic PBE0 one. For the RDMFE(GW) calculation I have performed a

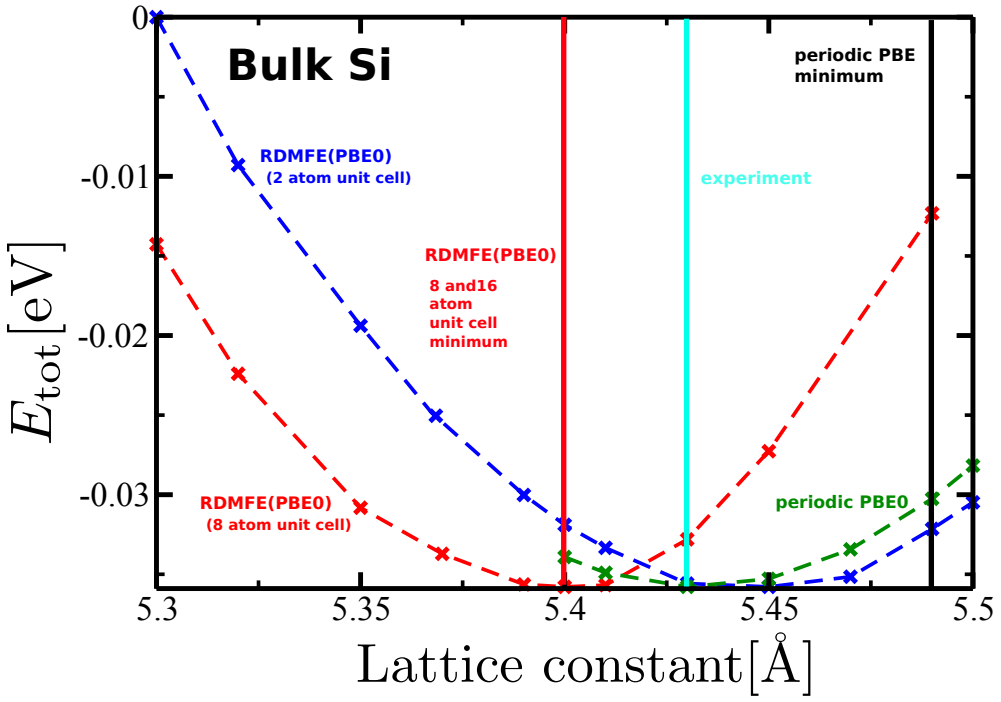

Figure 5.31: RMDFE(PBE) total energy as function of the lattice constant for the 2 (blue dashed line) and the 8 (red dashed line) atom unit cell the equilibrium lattice constant for the 8 and 16 atom unit cells are indicate by the red vertical solid line. Comparison is made with the periodic PBE0 reference (green line). The experimental value (turkis vertical line) and the periodic PBE (black vertical line) are also shown.

2 atom unit cell calculation and compared the resulting equilibrium lattice constant with the only reference at hand, which is the work of Kutepov *et al.* [230]. Figure (5.32) shows this comparison. Also here, the equilibrium lattice constant of 5.43Å lies below the starting point values (i.e., periodic PBE) going towards the experimental result. Moreover, it is reasonably close to the periodic self-consistent GW reference value of 5.39Å. Furthermore, I performed a Birch-Murnaghan [231] fit of the total energy curves to extract the bulk moduli for RDMFE(PBE0) and RDMFE(GW) using the equation of state

$$E(V) = E_0 + \frac{9V_0B_0}{16}\left(\left[\left(\frac{V_0}{V}\right)^{\frac{2}{3}} - 1\right]^3 B_0' + \left[\left(\frac{V_0}{V}\right)^{\frac{2}{3}} - 1\right]^2\left[6 - 4\left(\frac{V_0}{V}\right)^{\frac{2}{3}}\right]\right), \tag{5.47}$$

where $E(V)$ is the total energy at lattice constant a and V_0 the unit cell volume at equilibrium lattice constant a_0, while B_0' is the first derivative of the bulk modulus

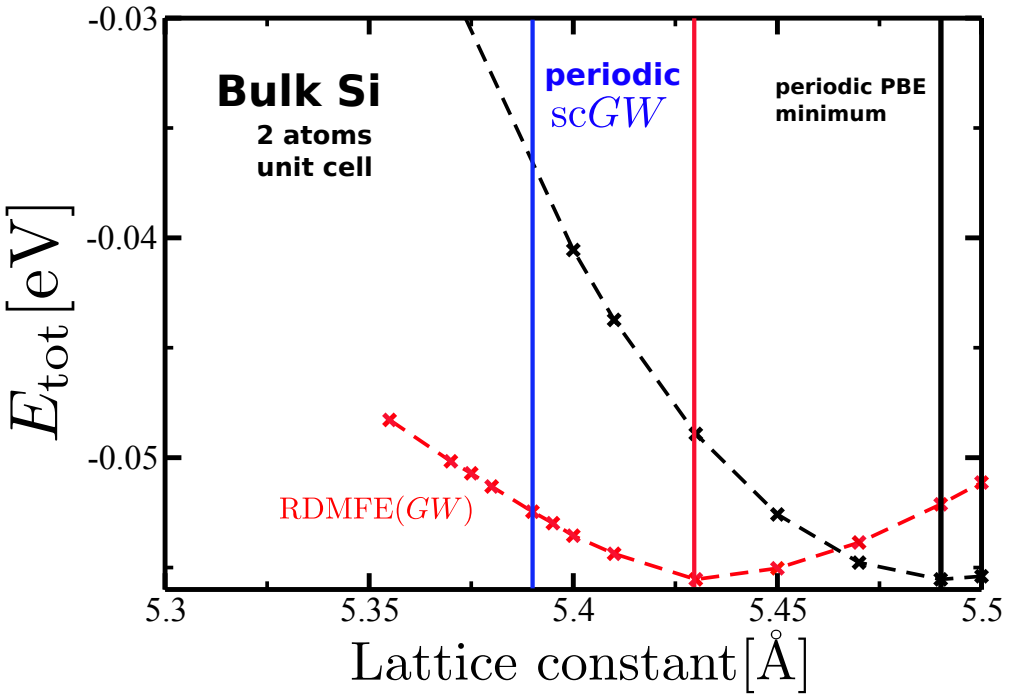

Figure 5.32: RMDFE(GW) total energy as function of the lattice constant for the 2 atom unit cell (blue line). Comparison is made with the periodic PBE reference (black line).

B_0 with respect to the pressure.

The resulting values are reported in Tabs. (5.5) and (5.6). RDMFE tends

	RDMFE(GW)	periodic scGW [230]	experiment
unit cell size	2 atoms	—	—
lattice constant [Å]	5.43	5.39	5.43[232]
bulk modulus B_0 [GPa]	80.37	100.7	99[233]

Table 5.5: Bulk Si RDMFE(GW) equilibrium lattice constant and bulk moduli B_0. Comparison is made with the periodic scGW work of Kutepov *et al.* [230] and experiment [232, 233]

.

to overestimate the bulk moduli for RDMFE(PBE0) compared to the values from periodic PBE0, while for RDMFE(GW) the bulk moduli are significantly below the periodic scGW reference and experiment.

5.3 Physical properties for metals from RDMFE

In this section of the chapter I will present RDMFE calculations of some relevant physical quantities for metalic systems. I consider here bulk Na and Al as representatives.

	RDMFE(PBE0)			periodic PBE0	experiment
unit cell size	2 atoms	8 atoms	16 atoms	2 atoms	—
lattice constant [Å]	5.45	5.4	5.4	5.43	5.43[232]
bulk modulus B_0 [GPa]	95.14	129.07	101.33	84	99[233]

Table 5.6: Bulk Si RDMFE(PBE0) equilibrium lattice constant and bulk moduli B_0. Comparison is made with periodic PBE0 performed with FHI-aims and experiment [232, 233]

.

5.3.1 Cohesive properties for metals from RDMFE(GW)

To verify whether RDMFE is still applicable to non-local systems, I have carried out RDMFE(GW) total energy calculations for metals. For bulk Na with 2 atoms in the unit cell (i.e., primitive unit cell) I looked at the behavior of the total energy with change of the lattice constant. This is shown in Fig. (5.33). The equilibrium lattice constant from RDMFE(GW) compares well to the periodic scGW calculation of Kutepov *et al.* [230]. However, the change of the total energy with the lattice constant is important, suggesting a large bulk modulus as shown in Tab. (5.7). For bulk Al with 4 atoms in the unit cell (i.e., primitive unit cell), the same calculation has been carried out. Here the resulting RDMFE(GW) lattice constant agrees less with the periodic scGW reference. The change in the total energy with respect to the lattice constant appears to be important which is reflected in the bulk modulus (see Tab. (5.7)).

Going to larger unit cell sizes, however, reduces the bulk modulus significantly as shown in Tab. (5.7) for the 8 atom unit cells. This observation is not unexpected. Metals have very delocalized electrons hence, the localization approximation introduced by RDMFE is not well justified. For larger enough unit cells, however, the embedded region would capture enough non-locality so that reasonable results can be produced. The equilibrium lattice constant of bulk Na is converged for the 8 atom unit cell. For bulk Al it is still different from the one of the primitive unit cell calculation but approaches the periodic reference. This observation suggests that, for bulk Al, one needs to go to even larger unit cells to converge out the equilibrium lattice constant.

5.3.2 Band structures for metals from RDMFE(PBE0)

To explore the translation symmetry breaking of RDMFE, discussed in the previous section for bulk Si, I have carried out RDMFE(PBE0) calculations on bulk Na and Al for different unit cell sizes. I then evaluated the unfolded band structures [221] and investigated the behavior of the degeneracy lifting with unit cell size. Figure (5.35) illustrates a comparison of the RDMFE(PBE0) band structure to the periodic PBE0 one for Na the primitive unit cell. The degeneracy lifting, due to the symmetry breaking in RDMFE, is clearly apparent e.g., for the high symmetry **k**-points X, Z and W. The degeneracy is nearly fully restored already for the 4 and 8 atom unit cells, as shown for the unfolded band structures in Fig. (5.36). This is also the case for the 16 atom unit cell unfolded band structure depicted in Fig. (5.37).

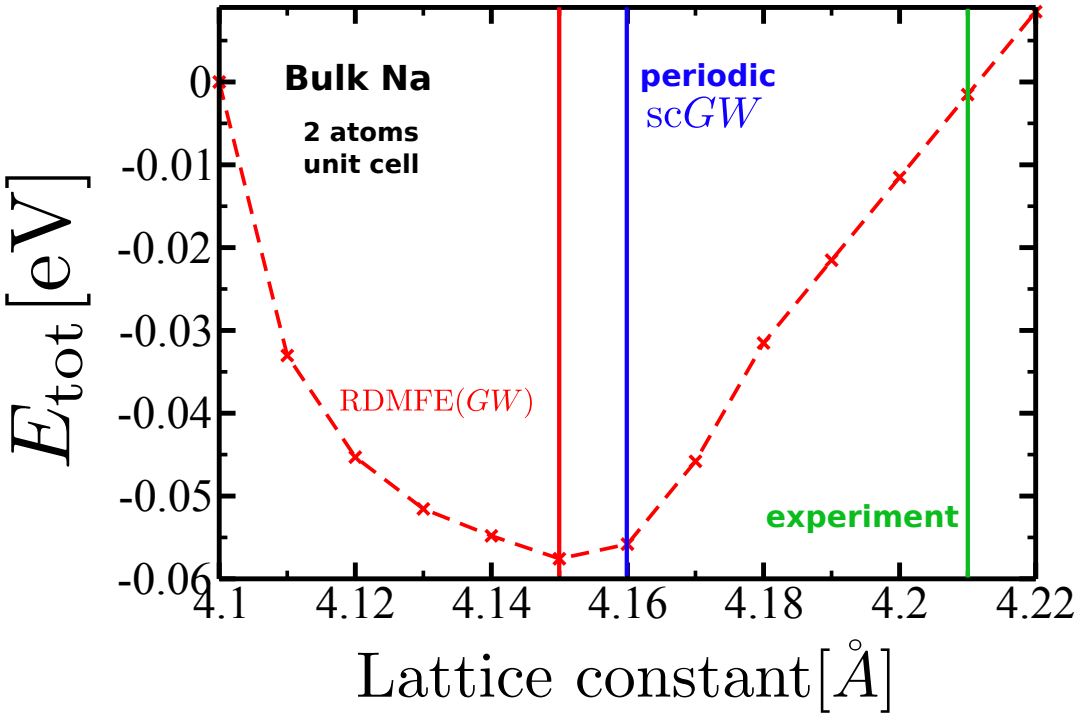

Figure 5.33: RMDFE(GW) total energy as function of the bulk Na lattice constant for the 2 atom unit cell (red dashed line). Comparison is made with the periodic scGW reference from Kutepov *et al.* [230] (blue line) and experiment (green line). The calculations were performed using a *tier*3 basis set and a (10×10×10) **k**-mesh.

I did the same investigation for bulk Al. The comparison between the RDMFE(PBE0) calculation and the periodic PBE0 one for the primitive unit cell case is depicted in Fig. (5.38). Also here the band structure shows degeneracy lifting. The 8 atom unit cell unfolded band structure still shows degeneracy lifting at high symmetry **k**-points as illustrated in the left panel of Fig. (5.39). Going to the 16 atom unit cell, however, reduces the degeneracy lifting drastically, in agreement with my previous findings for bulk Si (see right panel of Fig. (5.39)).

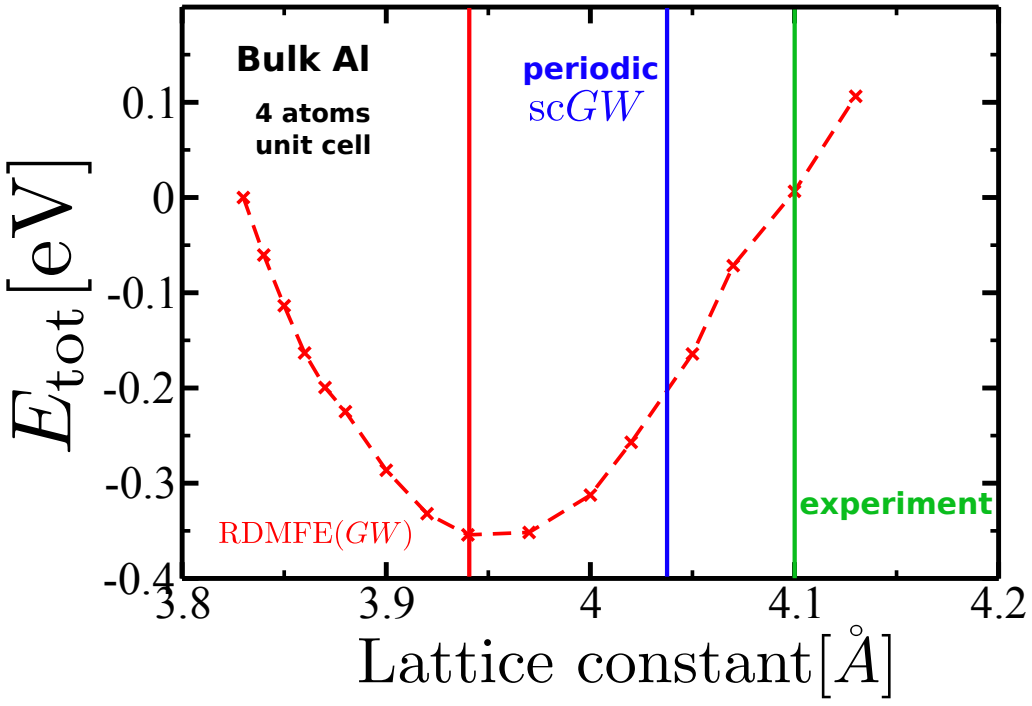

Figure 5.34: RMDFE(GW) total energy as function of the bulk Al lattice constant for the 4 atom unit cell (red dashed line). Comparison is made with the periodic scGW reference from Kutepov *et al.* [230] (blue line) and experiment (green line). The calculations were performed using a *tier*3 basis set and a (10×10×10) **k**-mesh.

	Na		Al	
	a_0[Å]	B_0[GPa]	a_0[Å]	B_0 [GPa]
PBE	4.0	78.62	4.03	159.4
RDMFE(GW) primitive unit cell	4.15	203.47	3.94	206.68
RDMFE(GW) 8 atom unit cell	4.15	104.46	3.99	105.71
periodic scGW [230]	4.16	69.9	4.04	86.5
experiment [233, 234]	4.21	68.1	4.05	72.16

Table 5.7: Comparison between the equilibrium lattice constant (a_0) and the bulk modulus (B_0) calculated with RDMFE(GW), PBE, periodic scGW and experiment for bulk Na and bulk Al. The primitive unit cell for Na contains 2 atoms, while it contains 4 for Al. I considered a larger unit cell with 8 atoms for Na and Al. The calculations were performed using a *tier*3 basis set and a (10×10×10) **k**-mesh.

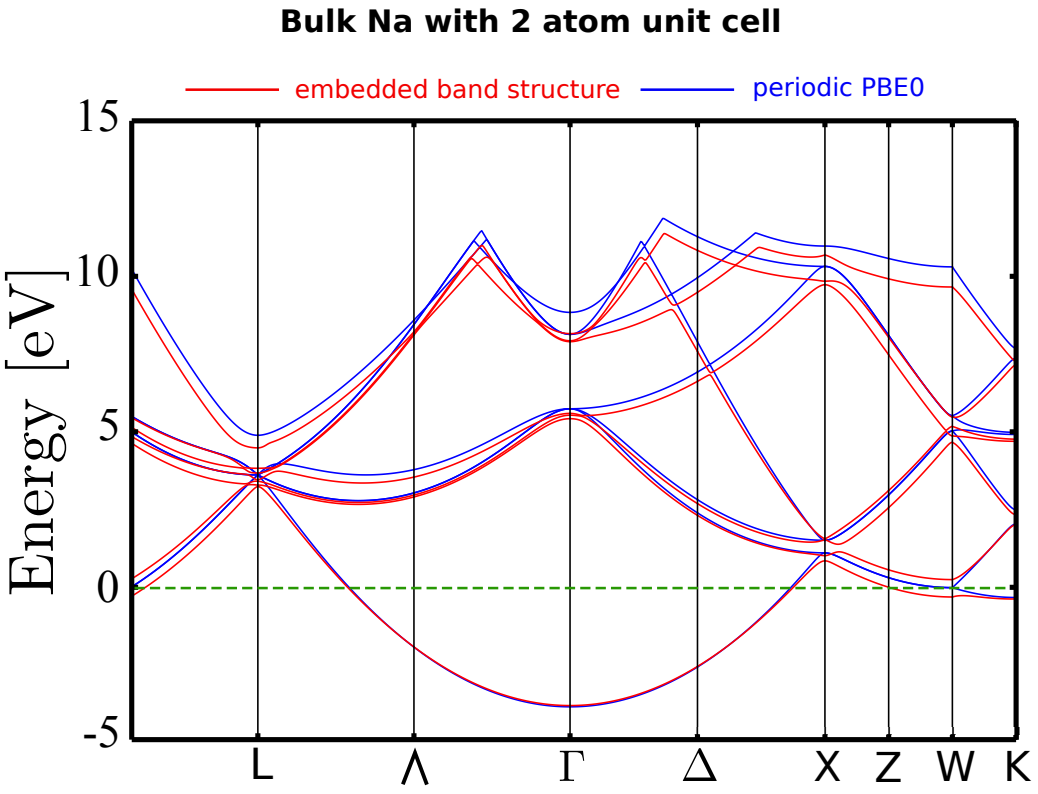

Figure 5.35: The RDMFE(PBE0) band structure for bulk Na, with 2 atoms in the unit cell, compared to the periodic PBE0 one. The local self-energy breaks the translation symmetry and the degeneracy lifted at some hight symmetry **k**-points. The calculations were performed using a *tier*1 basis set and a (10×10×10) **k**-mesh.

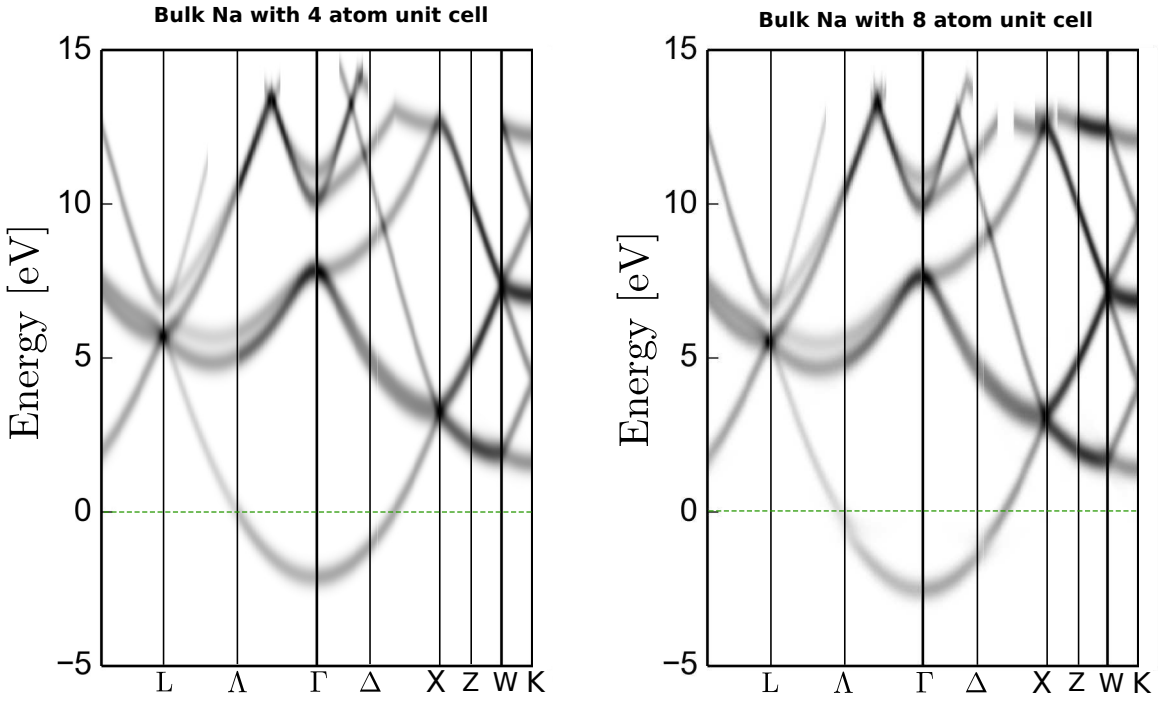

Figure 5.36: Left panel: the RDMFE(PBE0) unfolded band structure for a 4 atom bulk Na unit cell. The degeneracy lifting is reduced compared to the 2 atoms case. Right panel: the embedded unfolded band structure for a 8 atom unit cell. Also here the degeneracy is restored in most of the high symmetry points.

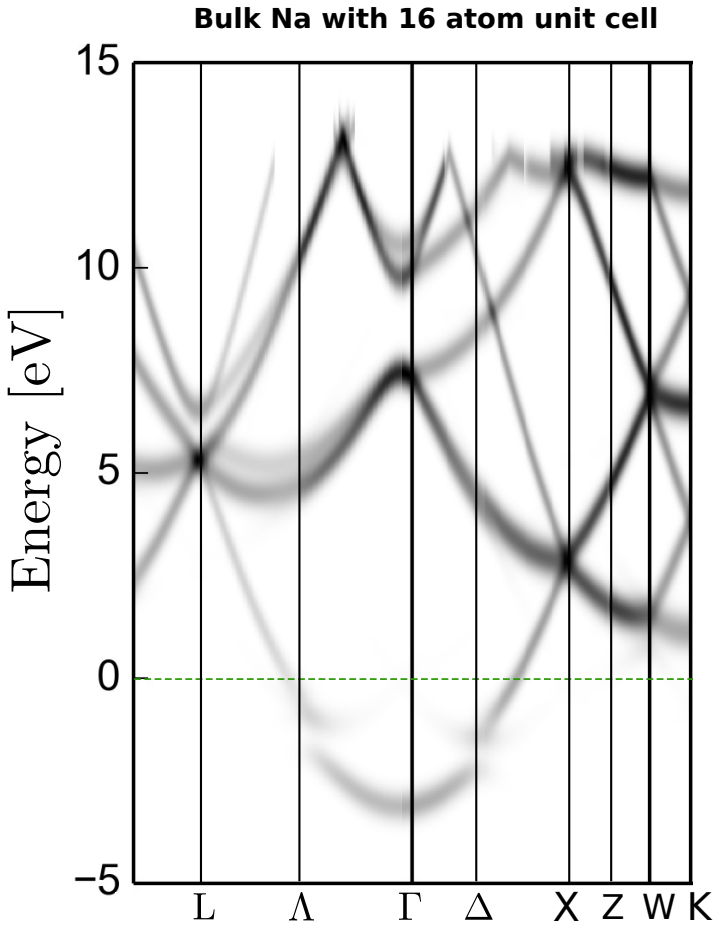

Figure 5.37: The RDMFE(PBE0) unfolded band structure for a 16 atom unit cell. Also here the degeneracy is restored in most of the high symmetry points.

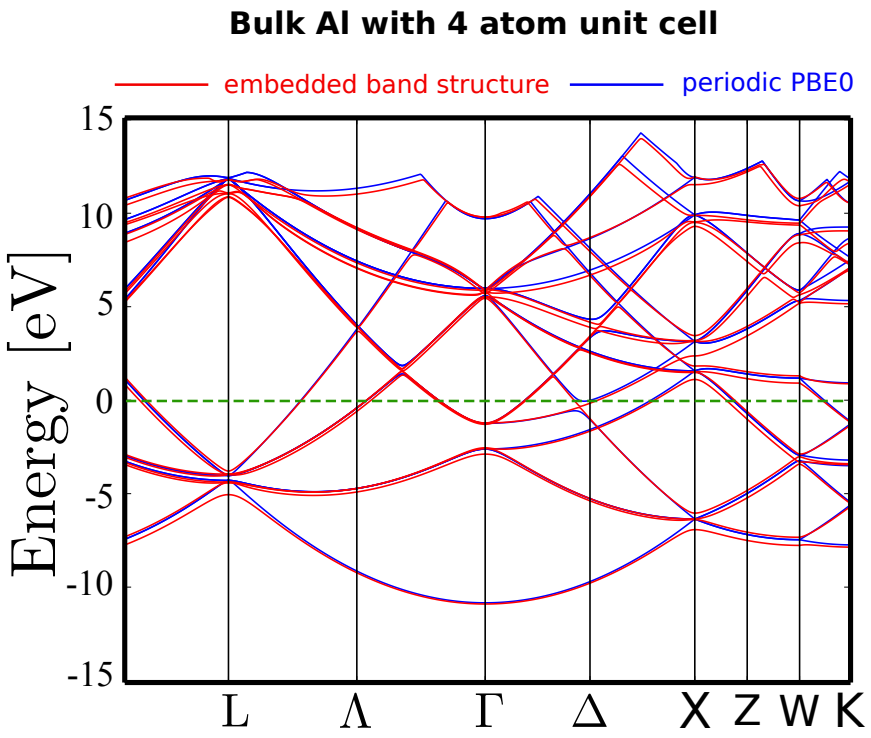

Figure 5.38: The RDMFE(PBE0) band structure for bulk Al, with 4 atoms in the unit cell, compared to the periodic PBE0 one. The local self-energy breaks the translation symmetry and the degeneracy lifted at some hight symmetry **k**-points. The calculations were performed using a *tier*1 basis set and a (10×10×10) **k**-mesh.

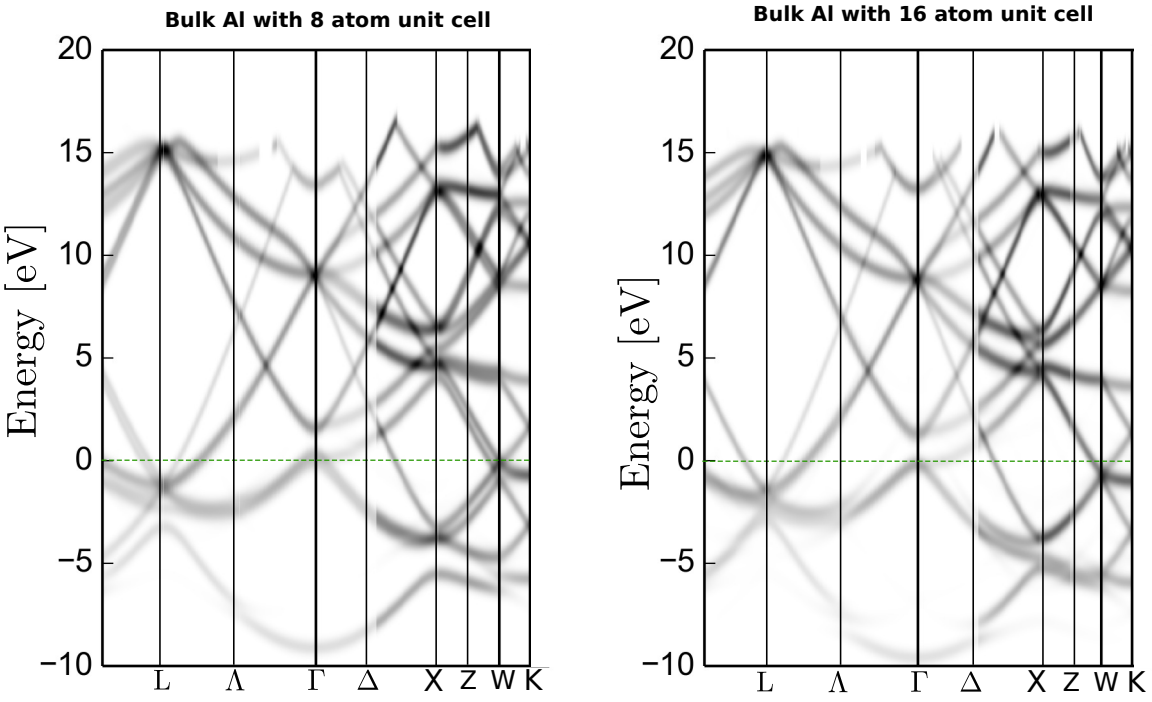

Figure 5.39: Left panel: the RDMFE(PBE0) unfolded band structure for a 8 atom bulk Al unit cell. The degeneracy lifting minimally reduced compared to the 4 atoms case. Right panel: the embedded unfolded band structure for a 16 atom unit cell. Here the degeneracy is restored in most of the high symmetry points.

Conclusions and Perspectives

In this thesis I have presented a real space dynamical mean-field embedding (RDMFE). It is an embedding scheme for periodic systems that builds on dynamical mean-field theory (DMFT). In RDMFE the electrons interacting across periodically repeated unit cells are mapped onto a cluster problem, where only electronic interactions within the cluster are explicitly considered. These locally interacting electrons are then dynamically coupled to a self-consistently determined bath of electrons. While the bath is treated using more efficient methods, such as LDA/GGAs, the embedded cluster is calculated using the computationally more demanding hybrid functionals or the *GW* approximation. The coupling between the embedded system and the surrounding is constructed naturally by means of Green's functions, allowing electronic exchange between the two regions.
Within RDMFE, the translational symmetry with respect to the computational supercell is preserved, making the method most suitable for systems with periodic boundary conditions.
An intrinsic feature of DMFT in RDMFE, is the **k**-dependent self-energy. It has as a consequence that the non-local exchange-correlation (XC) coupling between neighboring unit cells (or computational supercells) is included only at the Kohn-Sham level and neglected in the more advanced (here hybrid functionals or *GW*) treatment. This constitutes the only approximation introduced in RDMFE. The approximated treatment of the localized region, allows that in RDMFE no down-folding into a correlated subspace is required, which constitutes a major difference to DMFT.

By computing physical quantities from RDMFE, for bulk Si as test case, I have demonstrated that the density of states and total energies systematically converge to the periodic limit with increasing size of the embedded system. For the total energies, I moreover showed that the amount of locality in the embedded region can be related to a screening parameter that controls the long-range exact-exchange part of the local self-energy. I argue that this analysis is a proof that the functionality of RDMFE is guaranteed as far as the correct amount of interaction is captured within the embedded region. Moreover, I demonstrated that the problem of the breaking of the translational symmetry due to the different treatment of the inter- and intra-cluster interactions, can be remedied by systematically increasing the embedded cluster size.
An evidence that RDMFE rapidly captures the main features of the "better" theory, was given in the example of the plasmon satellite that already appears in the RDMFE(*GW*) calculation for the primitive unit cell (2 atom unit cell). Hence, the

non-locality of the self-energy in RDMFE is transfered into a frequency dependence, which is a concept that has been proposed previously by Gatti *et al.* [235] and the spectral density functional theory of Kotliar *at al.* [236]. Finally, a test on RDMFE(GW) of some representative metals shows that the theory can still be successfully applied to non-local systems.

Despite all the considerable insight that I have gained in my analysis of RDMFE, the door for further development is still wide open. For instance, the Hartree-potential can be updated self-consistently by feeding the local density from a RDMFE cycle into a Kohn-Sham (i.e., LDA/GGAs) periodic calculation. This will result in a new non-interacting Hamiltonian with which a new RDMFE calculation can be carried out.
On a different aspect, in the present status of my implementation I calculate the RDMFE total energy using the local density-matrix $n(\mathbf{r}) = n(\mathbf{r}, \mathbf{r})$ as given by Eqs. (5.42) and (5.44). An interesting alternative would be to use the density-matrix $n(\mathbf{r}, \mathbf{r}')$ in real space, while the integration in Eqs. (5.42) and (5.44) would go only over $\mathbf{r}, \mathbf{r}'$ that are in the embedded region. Proceeding as such would provide more non-locality into the total energy which could translate into an improved convergence behavior of the total energy with respect to the size of the embedded cluster. In the same spirit but from the point of view of the self-energy, the non-locality, expressed by the $\mathbf{k}$-dependence of the self-energy, can be restored if one follows the scheme proposed in the dynamical cluster approximation [190]. The self-energy would have a $\mathbf{k}$-dependence only within the embedded cluster. Admittedly, however, the development of such approach would require a more involved effort.

To conclude, this proof-of-concept analysis surely shows that RDMFE is a promising embedding scheme that has the potential to make sophisticated and computationally expensive *ab initio* theories accessible for periodic systems. Moreover, the fact that the approach is still in its infancy paves the way for creative development and predicts a multitude of usage possibilities.

Appendix A

The self-energy integral

Here I want to clarify how Fourier transform integrals such as the one in Eq. 1.48 in Chapter 1 is calculated. It is essentially given by

$$\int_{-\infty}^{\infty} d\omega g(\omega), \tag{A.1}$$

where

$$g(\omega) = \frac{e^{-i\omega t}}{\omega - \epsilon - \Sigma(\omega)}. \tag{A.2}$$

Here, the self-energy $\Sigma(\omega)$ is a complex function

$$\Sigma(\omega) = \mathrm{Re}\Sigma(\omega) + i\mathrm{Im}\Sigma(\omega). \tag{A.3}$$

For ω_0 being the *complex* solution of

$$\omega - \epsilon - \Sigma(\omega) = 0, \tag{A.4}$$

$g(\omega)$ has a pole at $\omega = \omega_0$.
Using the residue theorem, one can perform the integral in the lower-half plane for $t > 0$ as shown in Fig. A.1 for $\mathrm{Im}\Sigma(\omega) < 0$.

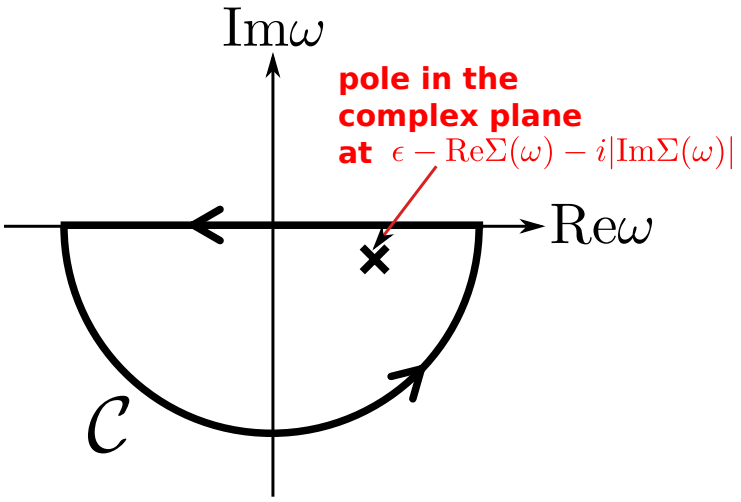

Figure A.1: Closing the contour $\mathcal{C}$ in the lower half-plane.

The purpose is to calculate the residue z_1 given by

$$z_1 = [(\omega - \omega_0)g(\omega)]|_{\omega=\omega_0}. \tag{A.5}$$

This can be done by assuming that $\Sigma(\omega)$ is analytical, so that its Taylor expansion around the pole $\omega = \omega_0$ gives

$$\Sigma(\omega) = \Sigma(\omega_0) + \frac{\partial\Sigma(\omega)}{\partial\omega}|_{\omega=\omega_0}(\omega - \omega_0) + \mathcal{O}\{(\omega - \omega_0)^2\}. \tag{A.6}$$

The expansion above can be substituted into $g(\omega)$ in Eq. A.5 to give

$$\lim_{\omega\to\omega_0}(\omega - \omega_0)g(\omega) = \lim_{\omega\to\omega_0}\frac{(\omega - \omega_0)e^{-i\omega t}}{\omega - \epsilon - \Sigma(\omega_0) - \frac{\partial\Sigma(\omega)}{\partial\omega}|_{\omega=\omega_0}(\omega - \omega_0) - \mathcal{O}\{(\omega - \omega_0)^2\}}. \tag{A.7}$$

Considering the fact that $g(\omega)$ has a pole at ω_0 i.e.,

$$\epsilon - \Sigma(\omega_0) = \omega_0, \tag{A.8}$$

one can rewrite

$$\begin{aligned}\lim_{\omega\to\omega_0}(\omega - \omega_0)g(\omega) &= \lim_{\omega\to\omega_0}\frac{e^{-i\omega t}}{1 - \frac{\partial\Sigma(\omega)}{\partial\omega}|_{\omega=\omega_0} - \mathcal{O}\{(\omega - \omega_0)^2\}} \\ &= \frac{e^{-i\omega_0 t}}{1 - \frac{\partial\Sigma(\omega_0)}{\partial\omega}|_{\omega=\omega_0}}.\end{aligned} \tag{A.9}$$

For the self-energy integral for $t > 0$[1] this results in

$$\int_{-\infty}^{\infty} d\omega\frac{e^{-i\omega_0 t}}{\omega - \epsilon - \Sigma(\omega)} = -2\pi i\frac{e^{-i\omega t}}{1 - \frac{\partial\Sigma(\omega)}{\partial\omega}|_{\omega=\omega_0}}; \text{for } t > 0 \tag{A.10}$$

[1] for $t < 0$ one can show that by closing the integral in the upper half-plane the integral vanishes.

Quasi-particles have usually a very short life-time which, equivalently, means that for quasi-particles $|\mathrm{Im}\Sigma(\omega)| \ll 1$. Hence, considering $\omega = \tilde{\omega}$ the real solution of $\omega - \epsilon - \mathrm{Re}\Sigma(\omega) = 0$, one can make the following approximation

$$\begin{aligned} \mathrm{Im}\Sigma(\omega) &\approx \mathrm{Im}\Sigma(\tilde{\omega}) \\ \mathrm{Re}\Sigma(\omega) &\approx \mathrm{Re}\Sigma(\tilde{\omega}) + \frac{\partial \mathrm{Re}\Sigma(\tilde{\omega})}{\partial \omega}|_{\omega=\tilde{\omega}}(\omega - \tilde{\omega}). \end{aligned} \tag{A.11}$$

The pole expansion then becomes

$$\begin{aligned} \omega - \epsilon - \Sigma(\omega) &= \omega - \epsilon - \mathrm{Re}\Sigma(\tilde{\omega}) + \frac{\partial \mathrm{Re}\Sigma(\tilde{\omega})}{\partial \omega}|_{\omega=\tilde{\omega}}(\omega - \tilde{\omega}) - i\mathrm{Im}\Sigma(\tilde{\omega}) \\ &= 0. \end{aligned} \tag{A.12}$$

Again, using $\epsilon - \mathrm{Re}\Sigma(\tilde{\omega}) = \tilde{\omega}$ yields

$$\begin{aligned} \omega - \tilde{\omega} - \frac{\partial \mathrm{Re}\Sigma(\tilde{\omega})}{\partial \omega}|_{\omega=\tilde{\omega}}(\omega - \tilde{\omega}) - i\mathrm{Im}\Sigma(\tilde{\omega}) &= 0 \\ \omega - \tilde{\omega} &= \frac{i\mathrm{Im}\Sigma(\tilde{\omega})}{1 - \frac{\partial \mathrm{Re}\Sigma(\tilde{\omega})}{\partial \omega}|_{\omega=\tilde{\omega}}}. \end{aligned} \tag{A.13}$$

The complex solution ω_0 is then given by

$$\begin{aligned} \omega_0 &= \tilde{\omega} + \frac{i\mathrm{Im}\Sigma(\tilde{\omega})}{1 - \frac{\partial \mathrm{Re}\Sigma(\tilde{\omega})}{\partial \omega}|_{\omega=\tilde{\omega}}} \\ &= \tilde{\omega} - \frac{i}{2}\Gamma, \end{aligned} \tag{A.14}$$

where I defined $\Gamma = \frac{2|\mathrm{Im}\Sigma(\tilde{\omega})|}{1 - \frac{\partial \mathrm{Re}\Sigma(\tilde{\omega})}{\partial \omega}|_{\omega=\tilde{\omega}}}$.
Finally, one arrives at the following expression for the self-energy integral

$$\begin{aligned} \int_{-\infty}^{\infty} d\omega \frac{e^{-i\omega t}}{\omega - \epsilon - \Sigma(\omega)} &= -2\pi i \frac{e^{-i(\tilde{\omega} - \frac{i}{2}\Gamma)t}}{1 - \frac{\partial \mathrm{Re}\Sigma(\omega)}{\partial \omega}|_{\omega=\tilde{\omega}}}; \text{for } t > 0 \\ &= -2\pi i Z_{\tilde{\omega}} e^{-i(\tilde{\omega} - \frac{i}{2}\Gamma)t}, \end{aligned} \tag{A.15}$$

with the quasi-particle weight $Z_{\tilde{\omega}} = (1 - \frac{\partial \mathrm{Re}\Sigma(\omega)}{\partial \omega}|_{\omega=\tilde{\omega}})^{-1}$ and $\tilde{\omega} = \epsilon + \mathrm{Re}\Sigma(\tilde{\omega})$.

Bibliography

[1] J.P. Perdew and Alex Zunger. Self-interaction correction to density-functional approximation for many-electron systems. *Phys. Rev. B*, 23:5048, 1981.

[2] John P. Perdew, Robert G. Parr, Mel Levy, and Jose L. Balduz. Density-functional theory for fractional particle number: Derivative discontinuities of the energy. *Phys. Rev. Lett.*, 49:1691–1694, Dec 1982.

[3] Paula Mori-Snchez, Aron J. Cohen, and Weitao Yang. Many-electron self-interaction error in approximate density functionals. *The Journal of Chemical Physics*, 125(20):–, 2006.

[4] J.P. Perdew and M. Levy. Physical content of the exact kohn-sham orbital energies: Band gaps and derivative discontinuities. *Phys. Rev. Lett.*, 51:1884, 1983.

[5] L.J. Sham and M. Schlüter. Density-functional theory of the energy gap. *Phys. Rev. Lett.*, 51:1888, 1983.

[6] Paula Mori-Sánchez, Aron J. Cohen, and Weitao Yang. Localization and delocalization errors in density functional theory and implications for band-gap prediction. *Phys. Rev. Lett.*, 100:146401, Apr 2008.

[7] O. Gunnarsson and B. I. Lundqvist. Exchange and correlation in atoms, molecules, and solids by the spin-density-functional formalism. *Phys. Rev. B*, 13:4274, 1976.

[8] John F. Dobson and Jun Wang. Successful test of a seamless van der waal density functional. *Phys. Rev. Lett*, 82:2123, 1999.

[9] Alexandre Tkatchenko and Matthias Scheffler. *Phys. Rev. Lett.*, 102:073005, 2009.

[10] I. D. White, R. W. Godby, M. M. Rieger, and R. J. Needs. Dynamic image potential at an al(111) surface. *Phys. Rev. Lett.*, 80:4265, 1997.

[11] Kristian S. Thygesen and Angel Rubio. Renormalization of molecular quasiparticle levels at metal-molecule interfaces: Trends across binding regimes. *Phys. Rev. Lett.*, 102:046802, 2009.

[12] C. Freysoldt, P. Rinke, and M. Scheffler. Controlling polarization at insulating surfaces: Quasiparticle calculations for molecules adsorbed on insulator films. *Phys. Rev. Lett.*, 103:056803, 2009.

[13] T. C. Leung, X. W. Wang, and B. N. Harmon. Band-theoretical study of magnetism in sc_2cuo_4. *Phys. Rev. B*, 37:384–388, Jan 1988.

[14] J. Zaanen, O. Jepsen, O. Gunnarsson, A.T. Paxton, O.K. Andersen, and A. Svane. What can be learned about hightc from local density theory? *Physica C: Superconductivity*, 153155, Part 3(0):1636 – 1641, 1988. Proceedings of the International Conference on High Temperature Superconductors and Materials and Mechanisms of Superconductivity Part {II}.

[15] Warren E. Pickett. Electronic structure of the high-temperature oxide superconductors. *Rev. Mod. Phys.*, 61:433–512, Apr 1989.

[16] L. F. Mattheiss. Electronic structure of the 3*d* transition-metal monoxides. i. energy-band results. *Phys. Rev. B*, 5:290–306, Jan 1972.

[17] L. F. Mattheiss. Electronic structure of the 3*d* transition-metal monoxides. ii. interpretation. *Phys. Rev. B*, 5:306–315, Jan 1972.

[18] P. J. Feibelman, B. Hammer, J. K. Nørskov, F. Wagner, M. Scheffler, R. Stumpf, R. Watwe, and J. Dumestic. *J. Phys. Chem. B*, 105:4018, 2001.

[19] Imed Mehdaoui and Thorsten Klner. Bonding of co and no to nio(100): a strategy for obtaining accurate adsorption energies. *The Journal of Physical Chemistry A*, 111(50):13233–13237, 2007.

[20] Imed Mehdaoui and Thorsten Klüner. Understanding surface photochemistry from first principles: The case of co-nio(100). *Phys. Rev. Lett.*, 98:037601, Jan 2007.

[21] Imed Mehdaoui and Thorsten Klner. New mechanistic insight into electronically excited co-nio(100): a quantum dynamical analysis. *Phys. Chem. Chem. Phys.*, 10:4559–4564, 2008.

[22] J. L. Whitten and Tapani A. Pakkanen. Chemisorption theory for metallic surfaces: Electron localization and the description of surface interactions. *Phys. Rev. B*, 21:4357–4367, May 1980.

[23] Matthias Scheffler, Jean Pol Vigneron, and Giovanni B. Bachelet. Total-energy gradients and lattice distortions at point defects in semiconductors. *Phys. Rev. B*, 31:6541–6551, May 1985.

[24] U. Chandra Singh and Peter A. Kollman. A combined a b initio quantum mechanical and molecular mechanical method for carrying out simulations on complex molecular systems: Applications to the ch&1 + c1- exchange reaction and gas phase protonation of polyethers. *J. Comp. Chem.*, 7:718, 1986.

[25] Walter Metzner and Dieter Vollhardt. Correlated lattice fermions in $d = \infty$ dimensions. *Phys. Rev. Lett.*, 62:324–327, Jan 1989.

[26] Martin J. Field, Paul A. Bash, and Martin Karplus. A combined quantum mechanical and molecular mechanical potential for molecular dynamics simulations. *J. Comp. Chem.*, 11:700, 1990.

[27] Antoine Georges and Gabriel Kotliar. Hubbard model in infinite dimensions. *Phys. Rev. B*, 45:6479–6483, Mar 1992.

[28] J. Bormet, J. Neugebauer, and M. Scheffler. Chemical trends and bonding mechanisms for isloated adsorbates on al(111). *Phys. Rev. B*, 49:17242–17252, Jun 1994.

[29] F. Maseras and K. Morokuma. *J. Comp. Chem.*, 16:1170, 1995.

[30] Walter Metzner and Dieter Vollhardt. *Rev. Mod. Phys.*, 68:13, 1996.

[31] Q.-M. Hu, K. Reuter, and M. Scheffler. Towars and exact treatment of exchange and correlation in materials: Application to the "co adsorption puzzle" and other systems. *Phys. Rev. Lett*, 98:176103, 2007.

[32] X. Ren, P. Rinke, and M. Scheffler. Exploring the random phase approximation: Application to co adsorbed on cu(111). *Phys. Rev. B*, 80:045402, 2009.

[33] Chen Huang and Emily A. Carter. Potential-functional embedding theory for molecules and materials. *J. Chem. Phys.*, 135:194104, 2011.

[34] Dominika Zgid and Garnet Kin-Lic Chan. Dynamical mean-field theory from a quantum chemical perspective. *J. Chem. Phys.*, 134:094115, 2011.

[35] G. Knizia and Garnet Kin-Lic Chan. *Phys. Rev. Lett.*, 109:186404, 2012.

[36] Daniel Berger, Andrew J. Logsdail, Harald Oberhofer, Matthew R. Farrow, C. Richard A. Catlow, Paul Sherwood, Alexey A. Sokol, Volker Blum, and Karsten Reuter. Embedded-cluster calculations in a numeric atomic orbital density-functional theory framework. *The Journal of Chemical Physics*, 141(2):–, 2014.

[37] P. W. Anderson. Localized magnetic states in metals. *Phys. Rev.*, 124:41–53, Oct 1961.

[38] G. Kotliar, S. Savrasov, K. Haule, V. Oudovenko, O. Parcollet, and C. Marianetti. *Rev. Mod. Phys.*, 78:865, 2006.

[39] K. Held. Electronic structure calculations using dynamical mean field theory. *Advances in Physics*, 56(6):829–926, 2007.

[40] L. Hedin. *Phys. Rev.*, 139:A796, 1965.

[41] V. Blum, F. Hanke, R. Gehrke, P. Havu, V. Havu, X. Ren, K. Reuter, and M. Scheffler. Ab-initio molecular simulations with numeric atom-centered orbitals. *Comp. Phys. Comm.*, 180:2175, 2009.

[42] V. Havu, V. Blum, P. Havu, and M. Scheffler. Efficient o(n) integration for all-electron electronic structure calculation using numeric basis functions. *J. Comp. Phys.*, 228:8367, 2009.

[43] X. Ren, P. Rinke, V. Blum, J. Wieferink, A. Tkatchenko, A. Sanfilippo, K. Reuter, and M. Scheffler. *New J. Phys.*, 14:053020, 2012.

[44] M. Born and R. Oppenheimer. Zur quantentheorie der molekeln. *Annalen der Physik*, 389(20):457–484, 1927.

[45] V. Fock. A comment on the virial relation. *Zs. Phys.*, 63:11–12, 1930.

[46] D. R. Hartree. The wave mechanics of an atom with a non-coulomb central field. part i. theory and methods. *Mathematical Proceedings of the Cambridge Philosophical Society*, 24:89–110, 1 1928.

[47] D. Bohm and D. Pines. A collective description of electron interactins: Iii. coulomb interaction in a degenerate electron gas. *Phys. Rev.*, 92:609, 1953.

[48] P. Nozières and D. Pines. Correlation energy of free-electron gas. *Phys. Rev.*, 111:442, 1958.

[49] Richard D. Mattuck. *A Guide to Feynman Diagrams in the Many-Body Problem.* McGraw-Hill, New York, 1976.

[50] Geert Brocks. *Advanced Quantum Mechanics.* Faculty of Applied Physics, University of Twente, Twente, 2002.

[51] Alexander L. Fetter and John Dirk Walecka. *Quantum Theory of Many-Particle Systems.* McGraw-Hill, New York, 1971.

[52] Ferdi Aryasetiawan and O. Gunnarsson. The *gw* method. *Rep. Prog. Phys.*, 61:237, 1998.

[53] G. Green *English mathematician from the first half of the 19th century,*.

[54] F. J. Dyson. The *s* matrix in quantum electrodynamics. *Phys. Rev.*, 75:1736–1755, Jun 1949.

[55] R. P. Feynman. The theory of positrons. *Phys. Rev.*, 76:749–759, Sep 1949.

[56] Murray Gell-Mann and Francis Low. Bound states in quantum field theory. *Phys. Rev.*, 84:350–354, Oct 1951.

[57] F. J. Dyson. Divergence of perturbation theory in quantum electrodynamics. *Phys. Rev.*, 85:631–632, 1952.

[58] L. N. Lipatov. Divergence of the Perturbation Theory Series and the Quasiclassical Theory. *Sov. Phys. JETP*, 45:216–223, 1977. [Zh. Eksp. Teor. Fiz.72,411(1977)].

[59] David Pines. *The Many-Body Problem: A Lecture Note and Reprint Volume*. Benjamin, New York, 1961.

[60] Dahlen N. E. Stan, A. and R. , van Leeuven. Fully self-consistent gw calculations for atoms and molecules. *Europhys. Lett.*, 76:298, Dec 2006.

[61] Fabio Caruso, Patrick Rinke, Xinguo Ren, Angel Rubio, and Matthias Scheffler. Self-consistent *gw*: All-electron implementation with localized basis functions. *Phys. Rev. B*, 88:075105, Aug 2013.

[62] Matteo Guzzo, Giovanna Lani, Francesco Sottile, Pina Romaniello, Matteo Gatti, Joshua J. Kas, John J. Rehr, Mathieu G. Silly, Fausto Sirotti, and Lucia Reining. Valence electron photoemission spectrum of semiconductors: *Ab Initio* description of multiple satellites. *Phys. Rev. Lett.*, 107:166401, Oct 2011.

[63] J. Schwinger. *Proc. Natl. Acad. Sci. USA*, 37:455, 1971.

[64] Stephen L. Adler. Quantum theory of the dielectric constant in real solids. *Phys. Rev.*, 126:413, 1962.

[65] Nathan Wiser. Dielectric constant with local field effect included. *Phys. Rev.*, 129:62, 1963.

[66] Giovanni Onida, Lucia Reining, and Angel Rubio. Electronic excitations: density-functional versus many-body green's function approaches. *Rev. Mod. Phys.*, 74:601, 2002.

[67] P. Rinke, A. Qteish, J. Neugebauer, and M. Scheffler. Exciting prospects for solids: Exact-exchange based functionals meet quasiparticle energy calculations. *phys. stat. sol. (b)*, 245:929, 2008.

[68] Attila Szabo and Neil S. Ostlund. *Modern Quantum Chemistry: Introduction to Advanced Electronic Structure Theory*. McGraw-Hill, New York, 1989.

[69] C. Møller and M. S. Plesset. *Phys. Rev.*, 46:618, 1934.

[70] Paul R. Rablen, Jeffrey W. Lockman, and William L. Jorgensen. Ab initio study of hydrogen-bonded complexes of small organic molecules with water. *The Journal of Physical Chemistry A*, 102(21):3782–3797, 1998.

[71] L. A. Curtiss, P. C. Redfern, K. Raghavachari, and J. A. Pople. Assessment of gaussian-2 and density functional theories for the computation of ionization potentials and electron affinities. *J. Chem. Phys.*, 109:42, 1998.

[72] Larry A. Curtiss, Paul C. Redfern, Krishnan Raghavachari, and John A. Pople. Gaussian-3x (g3x) theory: Use of improved geometries, zero-point energies, and hartreefock basis sets. *The Journal of Chemical Physics*, 114(1), 2001.

[73] Matthew L. Leininger, Wesley D. Allen, Henry F. Schaefer, and C. David Sherrill. Is mo/llerplesset perturbation theory a convergent ab initio method? *The Journal of Chemical Physics*, 112(21), 2000.

[74] J. Cízek. *J. Chem. Phys.*, 45:4256, 1966.

[75] J. iek and J. Paldus. Correlation problems in atomic and molecular systems iii. rederivation of the coupled-pair many-electron theory using the traditional quantum chemical methodst. *International Journal of Quantum Chemistry*, 5(4):359–379, 1971.

[76] C. David Sherrill and Henry F. Schaefer III. The configuration interaction method: Advances in highly correlated approaches. volume 34 of *Advances in Quantum Chemistry*, pages 143 – 269. Academic Press, 1999.

[77] Rodney J. Bartlett and Monika Musiał. Coupled-cluster theory in quantum chemistry. *Rev. Mod. Phys.*, 79:291, 2007.

[78] A. K. Rapp and E. R. Bernstein. Ab initio calculation of nonbonded interactions: are we there yet? *The Journal of Physical Chemistry A*, 104(26):6117–6128, 2000.

[79] George H. Booth, Andreas Grüneis, Georg Kresse, and Ali Alavi. Towards an exact description of electronic wavefunctions in real solids. *Nature*, 493:365, 2013.

[80] P. Hohenberg and W. Kohn. *Phys. Rev.*, 136:B864, 1964.

[81] W. Kohn and L. J. Sham. *Phys. Rev.*, 140:A1133, 1965.

[82] R.M. Dreizler and E.K.U. Gross. *Density Functional Theory- an Approach to the Quantum Many-Body Problem*. Springer-Verlag, Berlin, 1990.

[83] T Koopmans. ber die zuordnung von wellenfunktionen und eigenwerten zu den einzelnen elektronen eines atoms. *Physica*, 1(16):104 – 113, 1934.

[84] J. F. Janak. Proof that $\frac{\partial e}{\partial n_i} = \epsilon$ in density-functional theory. *Phys. Rev. B*, 18:7165–7168, Dec 1978.

[85] P. A. M. Dirac. Note on exchange phenomena in the thomas atom. *Mathematical Proceedings of the Cambridge Philosophical Society*, 26:376–385, 7 1930.

[86] John P. Perdew and Wang Yue. Accurate and simple density functional for the electronic exchange energy: Generalized gradient approximation. *Phys. Rev. B*, 33:8800–8802, Jun 1986.

[87] S. H. Vosko, L. Wilk, and M. Nusair. Accurate spin-dependent electron liquid correlation energies for local spin density calculations: a critical analysis. *Can. J. Phys.*, 58:1200, 1980.

[88] R. O. Jones and O. Gunnarsson. The density functional formalism, its applications and prospects. *Rev. Mod. Phys.*, 61:689–746, Jul 1989.

[89] Viktor N. Staroverov, Gustavo E. Scuseria, Jianmin Tao, and John P. Perdew. Tests of a ladder of density functionals for bulk solids and surfaces. *Phys. Rev. B*, 69:075102, Feb 2004.

[90] Gábor I. Csonka, John P. Perdew, Adrienn Ruzsinszky, Pier H. T. Philipsen, Sébastien Lebègue, Joachim Paier, Oleg A. Vydrov, and János G. Ángyán. Assessing the performance of recent density functionals for bulk solids. *Phys. Rev. B*, 79:155107, Apr 2009.

[91] Judith Harl, Laurids Schimka, and Georg Kresse. Assessing the quality of the random phase approximation for lattice constants and atomization energies of solids. *Phys. Rev. B*, 81:115126, Mar 2010.

[92] David C. Langreth and John P. Perdew. *Solid State Commun.*, 17:1425, 1975.

[93] John P. Perdew, Kieron Burke, and Matthias Ernzerhof. Generalized gradient approximation made simple. *Phys. Rev. Lett*, 77:3865, 1996.

[94] David C. Langreth and John P. Perdew. Exchange-correlation energy of a metal surface: Wave-vector analysis. *Phys. Rev. B*, 15:2884, 1977.

[95] A. D. Becke. Density functional calculations of molecular bond energies. *The Journal of Chemical Physics*, 84(8), 1986.

[96] John P. Perdew, J. A. Chevary, S. H. Vosko, Koblar A. Jackson, Mark R. Pederson, D. J. Singh, and Carlos Fiolhais. Atoms, molecules, solids, and surfaces: Applications of the generalized gradient approximation for exchange and correlation. *Phys. Rev. B*, 46:6671–6687, Sep 1992.

[97] John P. Perdew, J. A. Chevary, S. H. Vosko, Koblar A. Jackson, Mark R. Pederson, D. J. Singh, and Carlos Fiolhais. Erratum: Atoms, molecules, solids, and surfaces: Applications of the generalized gradient approximation for exchange and correlation. *Phys. Rev. B*, 48:4978–4978, Aug 1993.

[98] Takao Tsuneda, Toshihisa Suzumura, and Kimihiko Hirao. A new one-parameter progressive collesalvetti-type correlation functional. *The Journal of Chemical Physics*, 110(22), 1999.

[99] A. Daniel Boese, Nikos L. Doltsinis, Nicholas C. Handy, and Michiel Sprik. New generalized gradient approximation functionals. *The Journal of Chemical Physics*, 112(4), 2000.

[100] A. Daniel Boese and Nicholas C. Handy. A new parametrization of exchangecorrelation generalized gradient approximation functionals. *The Journal of Chemical Physics*, 114(13), 2001.

[101] Yan Zhao and Donald G. Truhlar. Construction of a generalized gradient approximation by restoring the density-gradient expansion and enforcing a tight lieboxford bound. *The Journal of Chemical Physics*, 128(18):–, 2008.

[102] J. P. Perdew, A. Ruzsinszky, G. I. Csonka, L. A. Constantin, and J. Sun. Workhorse semilocal density functional for condensed matter physics and quantum chemistry. *Phys. Rev. Lett.*, 103:026403, 2009.

[103] A. Becke. *Phys. Rev. A*, 38:3098, 1988.

[104] Chengteh Lee, Weitao Yang, and Robert G. Parr. Development of the colle-salvetti correlation-energy formula into a functional of the electron density. *Phys. Rev. B*, 37(2):785–789, Jan 1988.

[105] U von Barth. Basic density-functional theoryan overview. *Physica Scripta*, 2004(T109):9, 2004.

[106] R. O. Jones. Density functional theory: Its origins, rise to prominence, and future. *Rev. Mod. Phys.*, 87:897–923, Aug 2015.

[107] Vincenzo Barone. Inclusion of hartree-fock exchange in the density functional approach. benchmark computations for diatomic molecules containing h, b, c, n, o, and f atoms. *Chemical Physics Letters*, 226(34):392 – 398, 1994.

[108] Charles W. Bauschlicher Jr. A comparison of the accuracy of different functionals. *Chemical Physics Letters*, 246(12):40 – 44, 1995.

[109] Jon Baker, Jan Andzelm, Max Muir, and Peter R. Taylor. {OH} + {H2} {H2O} + h. the importance of exact exchange in density functional theory. *Chemical Physics Letters*, 237(12):53 – 60, 1995.

[110] Ralf Neumann and Nicholas C. Handy. Investigations using the becke95 correlation functional. *Chemical Physics Letters*, 252(12):19 – 22, 1996.

[111] Axel D. Becke. A new mixing of hartreefock and local densityfunctional theories. *The Journal of Chemical Physics*, 98(2), 1993.

[112] Axel D. Becke. Density-functional thermochemistry. iii. the role of exact exchange. *J. Chem. Phys*, 98:5648, 1993.

[113] John P. Perdew, Matthias Ernzerhof, and Kieron Burke. Rationale for mixing exact exchange with density functional approximations. *The Journal of Chemical Physics*, 105(22), 1996.

[114] Aron J. Cohen, Paula Mori-Snchez, and Weitao Yang. Challenges for density functional theory. *Chemical Reviews*, 112(1):289–320, 2012. PMID: 22191548.

[115] Carlo Adamo and Vincenzo Barone. Toward reliable density functional methods without adjustable parameters: The pbe0 model. *The Journal of Chemical Physics*, 110(13):6158–6170, 1999.

[116] Jochen Heyd, Gustavo E. Scuseria, and Matthias Ernzerhof. Hybrid functionals based on a screened coulomb potential. *J. Chem. Phys.*, 118:8207, 2003.

[117] L. J. Sham. Exchange and correlation in density-functional theory. *Phys. Rev. B*, 32:3876–3882, Sep 1985.

[118] R. W. Godby, M. Schlüter, and L. J. Sham. Self-energy operators and exchange-correlation potentials in semiconductors. *Phys. Rev. B*, 37:10159–10175, Jun 1988.

[119] Filipp Furche. Molecular tests of the random phase approximation to the exchange-correlation energy functional. *Phys. Rev. B*, 64:195120, 2001.

[120] Henk Eshuis, Julian Yarkony, and Filipp Furche. Fast computation of molecular random phase approximation correlation energies using resolution of the identity and imaginary frequency integration. *J. Chem. Phys.*, 132:234114, 2010.

[121] Filipp Furche. Developing the random phase approximation into a practical post-kohnsham correlation model. *J. Chem. Phys.*, 129:114105, 2008.

[122] Gustavo E. Scuseria, Thomas M. Henderson, and Danny C. Sorensen. The ground state correlation energy of the random phase approximation from a ring coupled cluster doubles approach. *J. Chem. Phys.*, 129:231101, 2008.

[123] Merzuk Kaltak, Ji Klime, and Georg Kresse. Low scaling algorithms for the random phase approximation: Imaginary time and laplace transformations. *Journal of Chemical Theory and Computation*, 10(6):2498–2507, 2014.

[124] X. Ren, P. Rinke, C. Joas, and M. Scheffler. Random-phase approximation and its applications in computational chemistry and materials science. *J. Mater. Sci.*, 47:7447, 2012.

[125] X. Ren, Alexandre Tkatchenko, P. Rinke, and M. Scheffler. Beyond the random phase approximation for the electron correlation energy: The importance of single excitations. *Phys. Rev. Lett.*, 106:153003, 2011.

[126] J. Paier, X. Ren, P. Rinke, G. E. Scuseria, A. Grüneis, G. Kresse, and M. Scheffler. *New J. Phys.*, 14:043002, 2012.

[127] F. Caruso, P. Rinke, X. Ren, M. Scheffler, and A. Rubio. Unified description of ground and excited states of finite systems: The self-consistent gw approach. *Phys. Rev. B*, 86:081102(R), 2012.

[128] V. M. Galitskii and A. B. Migdal. *Sov. Phys.-JETP*, 7:96, 1958.

[129] Lydia Nemec, Volker Blum, Patrick Rinke, and Matthias Scheffler. Thermodynamic equilibrium conditions of graphene films on sic. *Phys. Rev. Lett.*, 111:065502, Aug 2013.

[130] Thom Vreven, K. Suzie Byun, Istvn Komromi, Stefan Dapprich, John A. Montgomery, Keiji Morokuma, and Michael J. Frisch. Combining quantum mechanics methods with molecular mechanics methods in oniom. *Journal of Chemical Theory and Computation*, 2(3):815–826, 2006.

[131] Vreven Thom and Morokuma Keiji. *Chapter 3 Hybrid Methods: ONIOM(QM:MM) and QM/MM*, volume Volume 2, pages 35–51. Elsevier, 2006.

[132] Hrant P. Hratchian, Priya V. Parandekar, Krishnan Raghavachari, Michael J. Frisch, and Thom Vreven. Qm:qm electronic embedding using mulliken atomic charges: Energies and analytic gradients in an oniom framework. *The Journal of Chemical Physics*, 128(3):–, 2008.

[133] Nicholas J. Mayhall, Krishnan Raghavachari, and Hrant P. Hratchian. Oniom-based qm:qm electronic embedding method using lwdin atomic charges: Energies and analytic gradients. *The Journal of Chemical Physics*, 132(11):–, 2010.

[134] A. Becke. *J. Chem. Phys.*, 88:2547, 1988.

[135] Paul Sherwood, Alex H. de Vries, Martyn F. Guest, Georg Schreckenbach, C.Richard A. Catlow, Samuel A. French, Alexey A. Sokol, Stefan T. Bromley, Walter Thiel, Alex J. Turner, Salomon Billeter, Frank Terstegen, Stephan Thiel, John Kendrick, Stephen C. Rogers, John Casci, Mike Watson, Frank King, Elly Karlsen, Merethe Sjvoll, Adil Fahmi, Ansgar Schfer, and Christian Lennartz. Quasi: A general purpose implementation of the qm/mm approach and its application to problems in catalysis. *Journal of Molecular Structure: {THEOCHEM}*, 632(13):1 – 28, 2003.

[136] Alexey A. Sokol, Stefan T. Bromley, Samuel A. French, C. Richard A. Catlow, and Paul Sherwood. Hybrid qm/mm embedding approach for the treatment of localized surface states in ionic materials. *International Journal of Quantum Chemistry*, 99(5):695–712, 2004.

[137] Leonard Kleinman and D. M. Bylander. Efficacious form for model pseudopotentials. *Phys. Rev. Lett.*, 48:1425–1428, May 1982.

[138] Ying Zhang, Xin Xu, and William A. Goddard. Doubly hybrid density functional for accurate descriptions of nonbond interactions, thermochemistry, and thermochemical kinetics. *Proceedings of the National Academy of Sciences*, 106(13):4963–4968, 2009.

[139] Qing-Miao Hu, Karsten Reuter, and Matthias Scheffler. Erratum: Towards an exact treatment of exchange and correlation in materials: Application to the

"co adsorption puzzle" and other systems [phys. rev. lett. **98** , 176103 (2007)]. *Phys. Rev. Lett.*, 99:169903, Oct 2007.

[140] J.L. Whitten. Theoretical studies of surface reactions: embedded cluster theory. *Chemical Physics*, 177(2):387 – 397, 1993.

[141] J. L. Whitten and H. Yang. Theoretical studies of surface reactions on metals. *International Journal of Quantum Chemistry: Quantum Chemistry Symposium*, 29:41–47, 1995.

[142] T. S. Rufael, D. R. Huntley, D. R. Mullins, and J. L Gland. Adsorption and reaction of dimethyl disulfide on the ni(111) surface. *The Journal of Physical Chemistry B*, 102(18):3431–3440, 1998.

[143] Chen Huang, Michele Pavone, and Emily A. Carter. Quantum mechanical embedding theory based on a unique embedding potential. *The Journal of Chemical Physics*, 134(15):–, 2011.

[144] Yue Wang and Robert G. Parr. Construction of exact kohn-sham orbitals from a given electron density. *Phys. Rev. A*, 47:R1591–R1593, Mar 1993.

[145] L. H. Thomas. The calculation of atomic fields. *Mathematical Proceedings of the Cambridge Philosophical Society*, 23:542–548, 1 1927.

[146] E. Fermi. Un metodo statistico per la determinazione di alcune priopriet dell'atomo. *Rend. Accad. Naz. Lincei*, 6:602–607, 1927.

[147] C.F.v. Weizsäcker. Zur theorie der kernmassen. *Zeitschrift fr Physik*, 96(7-8):431–458, 1935.

[148] J. Hubbard. The description of collective motions in terms of many-body perturbation theory. *Proc. Roy. Soc. (London)*, A240:539, 1957.

[149] J. Hubbard. The description of collective motions in terms of many-body perturbation theory: Ii. the correlation energy of a free-electron gas. *Proc. Roy. Soc. (London)*, A243:336, 1957.

[150] Kenneth G. Wilson. The renormalization group: Critical phenomena and the kondo problem. *Rev. Mod. Phys.*, 47:773–840, Oct 1975.

[151] Ralf Bulla, Theo A. Costi, and Thomas Pruschke. Numerical renormalization group method for quantum impurity systems. *Rev. Mod. Phys.*, 80:395–450, Apr 2008.

[152] U. Schollwöck. The density-matrix renormalization group. *Rev. Mod. Phys.*, 77:259–315, Apr 2005.

[153] Antoine Georges. Strongly correlated electron materials: Dynamical meanfield theory and electronic structure. *AIP Conference Proceedings*, 715(1), 2004.

[154] A Georges and J S Yedidia. How to expand around mean-field theory using high-temperature expansions. *Journal of Physics A: Mathematical and General*, 24(9):2173, 1991.

[155] Takeo Matsubara. A new approach to quantum-statistical mechanics. *Progress of Theoretical Physics*, 14(4):351–378, 1955.

[156] V. I. Anisimov, J. Zaanen, and O. K. Andersen. Band theory and mott insulator: Hubbard u instead of stoner i. *Phys. Rev. B*, 44:943, 1991.

[157] V I Anisimov, A I Poteryaev, M A Korotin, A O Anokhin, and G Kotliar. First-principles calculations of the electronic structure and spectra of strongly correlated systems: dynamical mean-field theory. *Journal of Physics: Condensed Matter*, 9(35):7359, 1997.

[158] A. I. Lichtenstein and M. I. Katsnelson. *Ab initio* calculations of quasiparticle band structure in correlated systems: Lda++ approach. *Phys. Rev. B*, 57:6884–6895, Mar 1998.

[159] S. Biermann, F. Aryasetiawan, and A. Georges. First-principles approach to the electronic structure of strongly correlated systems: Combining the *GW* approximation and dynamical mean-field theory. *Phys. Rev. Lett.*, 90:086402, Feb 2003.

[160] Kristjan Haule, Chuck-Hou Yee, and Kyoo Kim. Dynamical mean-field theory within the full-potential methods: Electronic structure of ceirin$_5$, cecoin$_5$, and cerhin$_5$. *Phys. Rev. B*, 81:195107, May 2010.

[161] P. H. Dederichs, S. Blügel, R. Zeller, and H. Akai. Ground states of constrained systems: Application to cerium impurities. *Phys. Rev. Lett.*, 53:2512–2515, Dec 1984.

[162] A. K. McMahan, Richard M. Martin, and S. Satpathy. Calculated effective hamiltonian for la$_2$cuo$_4$ and solution in the impurity anderson approximation. *Phys. Rev. B*, 38:6650–6666, Oct 1988.

[163] O. Gunnarsson, O. K. Andersen, O. Jepsen, and J. Zaanen. Density-functional calculation of the parameters in the anderson model: Application to mn in cdte. *Phys. Rev. B*, 39:1708–1722, Jan 1989.

[164] John C. Slater. *Quantum Theory of Atomic Structure*. McGraw-Hill Book Co., Inc., New York, 1960.

[165] A. I. Lichtenstein, M. I. Katsnelson, and G. Kotliar. *edited by A. Gonis (Kluwer, New York)*, 2004.

[166] A. I. Lichtenstein, M. I. Katsnelson, and G. Kotliar. Finite-temperature magnetism of transition metals: An *ab initio* dynamical mean-field theory. *Phys. Rev. Lett.*, 87:067205, Jul 2001.

[167] X. Ren, I. Leonov, G. Keller, M. Kollar, I. Nekrasov, and D. Vollhardt. Lda+dmft computation of the electronic spectrum of nio. *Phys. Rev. B*, 74:195114, Nov 2006.

[168] M. Jarrell. Hubbard model in infinite dimensions: A quantum monte carlo study. *Phys. Rev. Lett.*, 69:168–171, Jul 1992.

[169] Steven R. White. Density matrix formulation for quantum renormalization groups. *Phys. Rev. Lett.*, 69:2863–2866, Nov 1992.

[170] Eric Jeckelmann. Ground-state phase diagram of a half-filled one-dimensional extended hubbard model. *Phys. Rev. Lett.*, 89:236401, Nov 2002.

[171] R. Bulla. Zero temperature metal-insulator transition in the infinite-dimensional hubbard model. *Phys. Rev. Lett.*, 83:136–139, Jul 1999.

[172] R. Bulla, T. A. Costi, and D. Vollhardt. Finite-temperature numerical renormalization group study of the mott transition. *Phys. Rev. B*, 64:045103, Jun 2001.

[173] J. E. Hirsch and R. M. Fye. Monte carlo method for magnetic impurities in metals. *Phys. Rev. Lett.*, 56:2521–2524, Jun 1986.

[174] A. N. Rubtsov, V. V. Savkin, and A. I. Lichtenstein. Continuous-time quantum monte carlo method for fermions. *Phys. Rev. B*, 72:035122, Jul 2005.

[175] Philipp Werner and Andrew J. Millis. Hybridization expansion impurity solver: General formulation and application to kondo lattice and two-orbital models. *Phys. Rev. B*, 74:155107, Oct 2006.

[176] A. K. McMahan, K. Held, and R. T. Scalettar. Thermodynamic and spectral properties of compressed ce calculated using a combined local-density approximation and dynamical mean-field theory. *Phys. Rev. B*, 67:075108, Feb 2003.

[177] D.G. Koskimaki and K.A.G. Jr. *Handbook on the Physics and Chemistry of Rare Earths*. North-Holland, Amsterdam, Amsterdam, 1978.

[178] Marco Casadei, Xinguo Ren, Patrick Rinke, Angel Rubio, and Matthias Scheffler. Density-functional theory for f-electron systems: The alpha-gamma phase transition in cerium. *Phys. Rev. Lett.*, 109:146402, 2012.

[179] M. B. Zölfl, I. A. Nekrasov, Th. Pruschke, V. I. Anisimov, and J. Keller. Spectral and magnetic properties of α- and γ-ce from dynamical mean-field theory and local density approximation. *Phys. Rev. Lett.*, 87:276403, Dec 2001.

[180] Kristjan Haule, Viktor Oudovenko, Sergej Y. Savrasov, and Gabriel Kotliar. The $\alpha \rightarrow \gamma$ transition in ce: A theoretical view from optical spectroscopy. *Phys. Rev. Lett.*, 94:036401, Jan 2005.

[181] A. K. McMahan, R. T. Scalettar, and M. Jarrell. Screening of $4f$ moments and delocalization in the compressed light rare earths. *Phys. Rev. B*, 80:235105, Dec 2009.

[182] S. V. Streltsov, E. Gull, A. O. Shorikov, M. Troyer, V. I. Anisimov, and P. Werner. Magnetic susceptibility of cerium: An lda+dmft study. *Phys. Rev. B*, 85:195109, May 2012.

[183] Philipp Werner, Armin Comanac, Luca de' Medici, Matthias Troyer, and Andrew J. Millis. Continuous-time solver for quantum impurity models. *Phys. Rev. Lett.*, 97:076405, Aug 2006.

[184] Dominika Zgid, Emanuel Gull, and Garnet Kin-Lic Chan. Truncated configuration interaction expansions as solvers for correlated quantum impurity models and dynamical mean-field theory. *Phys. Rev. B*, 86:165128, Oct 2012.

[185] Savrasov S. Y. and Kotliar G. and Abrahams E. *Nature*, 410(6830):793–795, apr 2001. 10.1038/35071035.

[186] K. Held, A. K. McMahan, and R. T. Scalettar. Cerium volume collapse: Results from the merger of dynamical mean-field theory and local density approximation. *Phys. Rev. Lett.*, 87:276404, Dec 2001.

[187] B. Amadon, S. Biermann, A. Georges, and F. Aryasetiawan. *Phys. Rev. Lett.*, 96:066402, Feb 2006.

[188] Jan M. Tomczak, Ferdi Aryasetiawan, and Silke Biermann. *Phys. Rev. B*, 78:115103, Sep 2008.

[189] G. Biroli, O. Parcollet, and G. Kotliar. Cluster dynamical mean-field theories: Causality and classical limit. *Phys. Rev. B*, 69:205108, 2004.

[190] Thomas Maier, Mark Jarrell, Thomas Pruschke, and Matthias H. Hettler. Quantum cluster theories. *Rev. Mod. Phys.*, 77:1027, 2005.

[191] S. Biermann, F. Aryasetiawan, and A. Georges. *First-Principles Approach to the Electronic Structure of Strongly Correlated Systems: Combining the GW Approximation and Dynamical Mean-Field Theory*, 90:086402, 2003.

[192] Serge Florens. *Nanoscale Dynamical Mean-Field Theory for Molecules and Mesoscopic Devices in the Strong-Correlation Regime*, 99:046402, 2007.

[193] J. P. Perdew and K. Schmidt. In V. Van Doren, C. Van Alsenoy, and P. Geerlings, editors, *Density Functional Theory and its Application to Materials* . AIP, Melville, NY, 2001.

[194] G. Biroli and G. Kotliar. *Phys. Rev. B*, 65:155112, 2002.

[195] F. W. Averill and D. E. Ellis. An efficient numerical multicenter basis set for molecular orbital calculations: Application to fecl4. *The Journal of Chemical Physics*, 59(12), 1973.

[196] Alex Zunger and A. J. Freeman. Ground- and excited-state properties of lif in the local-density formalism. *Phys. Rev. B*, 16:2901–2926, Sep 1977.

[197] Andrew P. Horsfield. Efficient ab initio tight binding. *Phys. Rev. B*, 56(11):6594–6602, Sep 1997.

[198] X. Ren, N. Marom, F. Caruso, P. Rinke, and M. Scheffler. submitted.

[199] S. F. Boys and I. Shavitt. *Univeristy of Wisconsin Rept. WIS-AF-13.*, 1959.

[200] J. L. Whitten. Coulomb potential energy integrals and approximations. *J. Chem. Phys.*, 58:4496, 1973.

[201] B. I. Dunlap, J. W. D. Connolly, and J. R. Sabin. On some approximations of xα method. *J. Chem. Phys*, 71:3396, 1979.

[202] Florian Weigend, Marco Häser, Holger Patzelt, and Reinhart Ahlrichs. Ri-mp2: optimized auxiliary basis sets and demonstration of efficiency. *Chem. Phys. Lett.*, 294:143, 1998.

[203] Florian Weigend. A fully direct ri-hf algorithm: Implementation, optimised auxiliary basis sets, demonstration of accuracy and efficiency. *Phys. Chem. Chem. Phys.*, 4:4285, 2002.

[204] M. Feyereisen, G. Fitzgerald, and A. Komornicki. Use of approximate integrals in ab initio theory, an application in mp2 energy calculations. *Chem. Phys. Lett.*, 208:359, 1993.

[205] Matthias Ernzerhof and Gustavo E. Scuseria. Assessment of the perdewburkeernzerhof exchange-correlation functional. *The Journal of Chemical Physics*, 110(11):5029–5036, 1999.

[206] F. Caruso, P. Rinke, X. Ren, M. Scheffler, and A. Rubio. Self-consistent gw: All-electron implementation with localized basis functions. *Phys. Rev. B*, 88:075105, 2013.

[207] Richard P. Brent. *Algorithms for minimization without derivatives.* Prentice-Hall series in automatic computation. Englewood Cliffs, N.J. Prentice-Hall, 1973.

[208] B. Farid, R. Daling, D. Lenstra, and W. van Haeringen. *GW* approach to the calculation of electron self-energies in semiconductors. *Phys. Rev. B*, 38:7530–7534, Oct 1988.

[209] G. E. Engel, Behnam Farid, C. M. M. Nex, and N. H. March. Calculation of the *GW* self-energy in semiconducting crystals. *Phys. Rev. B*, 44:13356–13373, Dec 1991.

[210] H. N. Rojas, R. W. Godby, and R. J. Needs. Space-time method for *ab initio* calculations of self-energies and dielectric response functions of solids. *Phys. Rev. Lett.*, 74:1827, 1995.

[211] Ioffedatabase.

[212] B. Holm and U. von Barth. Fully self-consistent *gw* self-energy of the electron gas. *Phys. Rev. B*, 57:2108, 1998.

[213] Wolf-Dieter Schöne and Adolfo G. Eguiluz. Self-consistent calculations of quasiparticle states in metals and semiconductors. *Phys. Rev. Lett.*, 81:1662–1665, Aug 1998.

[214] Johannes Lischner, Derek Vigil-Fowler, and Steven G. Louie. Physical origin of satellites in photoemission of doped graphene: An *Ab Initio gw* plus cumulant study. *Phys. Rev. Lett.*, 110:146801, Apr 2013.

[215] Safa O. Kasapa and Peter Capper. Springer handbook of electronic and photonic materials. *Springer*, pages 54,327, 2006.

[216] Andrey Kutepov, Sergey Y. Savrasov, and Gabriel Kotliar. Ground-state properties of simple elements from gw calculations. *Phys. Rev. B*, 80:041103, Jul 2009.

[217] Takao Kotani, Mark van Schilfgaarde, and Sergey V. Faleev. Quasiparticle self-consistent *gw* method: A basis for the independent-particle approximation. *Phys. Rev. B*, 76:165106, Oct 2007.

[218] Gordon Baym and Leo P. Kadanoff. Conservation laws and correlation functions. *Phys. Rev.*, 124:287, 1961.

[219] Ulf von Barth and Bengt Holm. Self-consistent gw_0 results for the electron gas: Fixed screened potential w_0 within the random-phase approximation. *Phys. Rev. B*, 54:8411–8419, Sep 1996.

[220] A. I. Lichtenstein and M. I. Katsnelson. Antiferromagnetism and d-wave superconductivity in cuprates: A cluster dynamical mean-field theory. *Phys. Rev. B*, 62:9283(R), 2000.

[221] Unit cells larger than the primitive unit cell give rise to a folded band structure. To cast the band structure back onto the Brillouin zone of the 2 atom unit cell we use the unfolding approach of L. Nemec.

[222] J. M. Luttinger and J. C. Ward. Ground-state energy of a many-fermion system. ii*. *Phys. Rev.*, 118:1417, 1960.

[223] Abraham Klein. Perturbation theory for an infinite medium of fermions. ii*. *Phys. Rev.*, 121:950, 1961.

[224] Robert van Leeuwen, Nils Erik Dahlen, and Adrian Stan. Total energies from variational functionals of the green function and the renormalized four-point vertex. *Phys. Rev. B*, 74:195105, Nov 2006.

[225] Gordon Baym. Self-consistent approximations in many-body systems. *Phys. Rev.*, 127:1391, 1962.

[226] Nils Eric Dahlen, Robert van Leeuwen, and Ulf von Barth. Variational energy functionals of the green function and of the density tested on molecules. *Int. J. Quantum Chem.*, 101:512, 2005.

[227] Nils Eric Dahlen, Robert van Leeuwen, and Ulf von Barth. Variational energy functionals of the green function and of the density tested on molecules. *Phys. Rev. A*, 73:012511, 2006.

[228] J. Harris. Simplified method for calculating the energy of weakly interacting fragments. *Phys. Rev. B*, 31:1770–1779, Feb 1985.

[229] W. Matthew C. Foulkes and Roger Haydock. Tight-binding models and density-functional theory. *Phys. Rev. B*, 39:12520–12536, Jun 1989.

[230] Andrey Kutepov, Kristjan Haule, Sergey Y. Savrasov, and Gabriel Kotliar. Electronic structure of pu and am metals by self-consistent relativistic *gw* method. *Phys. Rev. B*, 85:155129, Apr 2012.

[231] Francis Birch. Finite elastic strain of cubic crystals. *Phys. Rev.*, 71:809–824, Jun 1947.

[232] T. Hom, W. Kiszenik, and B. Post. Accurate lattice constants from multiple reflection measurements. II. Lattice constants of germanium silicon, and diamond. *Journal of Applied Crystallography*, 8(4):457–458, Aug 1975.

[233] C. O. Rodriguez, V. A. Kuz, E. L. Peltzer y Blanca, and O. M. Cappannini. Structural properties of tetrahedrally coordinated crystals from first-principles calculations of pressure and total energies. *Phys. Rev. B*, 31:5327–5334, Apr 1985.

[234] V. L. Moruzzi, J. F. Janak, and K. Schwarz. Calculated thermal properties of metals. *Phys. Rev. B*, 37:790–799, Jan 1988.

[235] Matteo Gatti, Valerio Olevano, Lucia Reining, and Ilya V. Tokatly. Transforming nonlocality into a frequency dependence: A shortcut to spectroscopy. *Phys. Rev. Lett.*, 99:057401, Aug 2007.

[236] S. Y. Savrasov and G. Kotliar. Spectral density functionals for electronic structure calculations. *Phys. Rev. B*, 69:245101, Jun 2004.

Acknowledgments - Danksagung

First and foremost I would like to thank Matthias Scheffler for giving me the opportunity to carry out my PhD at the theory department of the Fritz-Haber Institute and for always being helpful and supportive during the work on this thesis. I also want to express my gratitude to Patrick Rinke, my direct supervisor, for the incredible support he gave me during my PhD period, for his experience from which I learned a lot and for the great time we had together in Berlin. Many thanks go to Xinguo Ren, my co-supervisor, who gave me great encouragement and from whom I learned how to deal with unpredictable situations in method development and how to be patient when doing method development. I also thank Heiko Appel, Sergey Levchenko, Igor Ying Zhang and Christian Carbogno for the helpful discussions. Thanks go also to Arvid Ihrig for the inspiring discussions about everything related to computers. Furthermore, I thank all my friends at the Fritz (in alphabetical order) Arvid, Björn, Fabio, Franz, Johannes, Lydia, Marco, Mariana, Nicola, Tanja, Victor, Viktor, Vivek and my room mates Honghui and Markus for the great time we had together and for keeping the atmosphere at the Fritz so enjoyable. I would like to thank my family in Casablanca for the great encouragement. Infinite thanks go to my wonderful wife for the inexhaustible support and for always standing by my side and my daughter for being so happy to see me when I came back home every evening.